Diss. ETH No. 15733

Growth and Properties of Optoelectronic Structures Based on IV-VI Materials

A dissertation submitted to the

SWISS FEDERAL INSTITUTE OF TECHNOLOGY (ETH) ZURICH

For the degree of

DOCTOR OF NATURAL SCIENCES

presented by

Dmitry Zimin

Graduated Engineer in Microelectronics and Semiconductor Devices

Yaroslavl State University, Russia

Born April 22, 1977 in Yaroslavl, Russia

citizen of Russia

Accepted on the recommendation of

Prof. Dr. G. Kostorz, examiner

Prof. Dr. M. Tacke, co-examiner

PD Dr. H. Zogg, co-examiner

Zurich, 2004

Contents

Summary

The main purpose of this work was to make and characterize thin layers, low-dimensional structures and devices based on IV-VI materials. Narrow band gap IV-VI semiconductors, mainly binary PbSe, PbTe and their ternary alloys with Eu ($Pb_{1-x}Eu_xSe$, $Pb_{1-x}Eu_xTe$, $0 \leq x \leq 1$) were epitaxially grown with molecular beam epitaxy on (111) oriented BaF_2 and (100) and (111) oriented Si substrates. Owing to their direct narrow band gaps in the range of $0.15 \div 0.32$ eV, the main applications of lead chalcogenides are mid-infrared optoelectronic devices such as detectors and emitters.

Dislocation densities ρ_{disl} of heteroepitaxial IV-VI layers were determined by several methods. The densities vary within a broad range from $\rho_{disl} \approx 5 \times 10^6$ cm^{-2} for 11 µm thick PbTe homostructures grown on Si (111) to $\rho_{disl} \approx 10^9$ cm^{-2} for thin PbSe layers grown on Si (100). But as shown in this work, despite lattice and thermal mismatches with the above mentioned substrates, lead chalcogenide thin film homostructures as well as multistacks exhibit sufficient structural quality to be applied for devices.

Content of europium atoms in IV-VI alloys was determined by different methods. Advantages and disadvantages of these methods are discussed.

Several low-dimensional structures with different dimensionalities (zero-, one- and two-dimensional) were investigated.

Self-assembled PbSe quantum dots grown on PbTe (111) quasi-substrates, where the latter were grown on Si (111), show a width of the size distribution as low as 2%. This value is lower than any other reported size distribution width of self-assembled dots. The result is explained in this work by nonoverlapping diffusion radii for most of the dots and their nucleation occurring mainly at defects.

Under certain conditions, long parallel or perpendicular CaF_2 stripes of nanometer width and height were grown on Si (100). This system might be an attractive anisotropic template for epitaxial growth of IV-VI nanowires.

PbSe and PbTe quantum wells were embedded in ternary $Pb_{1-x}Eu_xSe$ or $Pb_{1-x}Eu_xTe$ layers.

Bragg mirrors consisting of alternating IV-VI/BaF$_2$ quarter wavelength layers were grown. A few such layer pairs of a thickness corresponding to quarter wavelength suffice to get high reflectivities R>99% owing to the very high refractive index contrast between these materials.

PbSe/Pb$_{1-x}$Eu$_x$Se and PbTe/Pb$_{1-x}$Eu$_x$Te optically pumped edge-emitting lasers show laser emission in the 3÷5 μm range up to 250 K. Growth procedures, design and mirror manufacturing of these lasers are discussed.

Wavelength transformers consisting of a PbSe/Pb$_{1-x}$Eu$_x$Se active resonant cavity with integrated top and bottom Bragg mirrors were manufactured. They convert the incoming 0.9 μm pump radiation to a narrow mid-infrared emission peak, the wavelength of which is given by the design of the transformer. This is the first device of such type for mid-IR grown with IV-VI materials.

The resonant cavity infrared detectors with a bottom Pb$_{1-x}$Eu$_x$Se/BaF$_2$ Bragg mirror, a cavity with a thin active Pb$_{1-y}$Eu$_y$Se absorption layer and a Pb blocking contact which acts as a top mirror were made. The spectral response measurements show a very narrow resonance peak, which position and width are given by the design.

Zusammenfassung

Der wesentliche Zweck dieser Arbeit war es, dünne Schichten, niederdimensionale Strukturen und Bauelemente basierend auf IV-VI Materialien herzustellen und zu charakterisieren. Die auf IV-VI Materialien basierenden Schmalbandhalbleiter, überwiegend binäres PbSe, PbTe und ihre ternären Legierungen mit Eu ($Pb_{1-x}Eu_xSe$, $Pb_{1-x}Eu_xTe$, $0 \leq x \leq 1$) wurden epitaktisch mittels Molekularstrahl Epitaxie auf (111)-orientierte BaF_2, (100)- und (111)-orientierte Siliziumsubstrate abgeschieden. Aufgrund ihrer direkten Bandlücke im Bereich von $0.15 \div 0.32$ eV liegt die Hauptanwendung dieser Bleichalkogenide bei optoelektronischen Bauelementen für das mittlere Infrarot, wie zum Beispiel Detektoren und Emitter.

Die Versetzungsdichten ρ_{disl} der heteroepitaktischen IV-VI Schichten wurden mit unterschiedlichen Meßmethoden bestimmt. Die erhaltenen Versetzungsdichten variierten in einem weiten Bereich von $\rho_{disl} \approx 5 \times 10^6$ cm^{-2} für 11 µm dicke auf Si (111) abgeschiedene PbTe Homostrukturen bis zu $\rho_{disl} \approx 10^9$ cm^{-2} für dünne auf Si (100) abgeschiedene PbSe Schichten. Aber wie in dieser Arbeit gezeigt wird, können trotz der Gitter- und thermischen Fehlpassung auf den oben erwähnten Substraten, sowohl Homo-, als auch Mehrschichtsysteme in ausreichender Qualität für Bauelemente hergestellt werden.

Der Europiumanteil in den IV-VI Legierungen wurde mit verschiedenen Methoden bestimmt und deren Vor- und Nachteile diskutiert.

Verschiedene niederdimensional Strukturen mit unterschiedlichen räumlichen Ausdehnungen (Null-, Ein- und Zweidimensional) wurden untersucht.

Selbstorganisierte PbSe Quantenpunkte zeigen eine sehr schmale Höhenverteilung von etwa 2%. Diese Quantenpunkte wurden auf PbTe (111) Quasisubstrate abgeschieden, wobei letztere wiederum auf Si (111) hergestellt wurden. Dies ist der bisher kleinste berichtete Wert einer Größenverteilung von selbstorganisierten Quantenpunkten. In der vorliegenden Arbeit wird dieses Ergebnis anhand von nicht überlappenden Diffusionsradien, welches für die meisten Quantenpunkte zutrifft und überwiegender Nukleation an Defekten erklärt.

Unter bestimmten Bedingungen können auf Si (100) lange parallele oder senkrechte Streifen aus CaF$_2$, deren Abmessung sowohl in der Breite als auch in der Höhe im Nanometerbereich liegen, abgeschieden werden. Diese Anordnung könnte als viel versprechendes System für die Herstellung von IV-VI Quantendrähten dienen.

PbSe and PbTe Quantentöpfe wurden in ternäre Pb$_{1-x}$Eu$_x$Se bzw. Pb$_{1-x}$Eu$_x$Te Schichten eingebettet.

Braggspiegel bestehend aus alternierenden Viertel Wellenlängen IV-VI/BaF$_2$ Schichten wurden mittels Molekularstrahl Epitaxie hergestellt. Nur wenige solcher Schichtpaare mit einer Dicke, die einem Viertel der Wellenlänge entspricht, reichen dank des hohen Brechungsindex-Kontrastes zwischen diesen Materialien aus, um Reflektivitäten R>99% zu erhalten.

PbSe/Pb$_{1-x}$Eu$_x$Se und PbTe/Pb$_{1-x}$Eu$_x$Te optisch gepumpte Kantenemitter zeigen Laseremission im 3÷5 μm Bereich bis 250 K. Die Herstellung, Aufbau und Spiegelherstellung dieser Laser werden eingehend beschrieben.

Weiterhin wurden Wellenlängenwandler bestehend aus einer PbSe/Pb$_{1-x}$Eu$_x$Se aktiven resonanten Kavität, welche in einem oberen und unteren Braggspiegel integriert ist, hergestellt. Diese konvertieren das einfallende 0.9 μm Pumplicht zu einer schmalen im mittleren infrarot liegenden Emissionslinie, deren Wellenlänge durch den Aufbau des Wandlers gegeben ist. Dies ist der erste Wellenlängenwandler aus IV-VI Materialien für den Bereich des mittleren Infrarots.

Des weiteren werden die Herstellung und Eigenschaften eines resonanten Kavität Infrarot Detektors bestehend aus einem unteren Pb$_{1-x}$Eu$_x$Se/BaF$_2$ Braggspiegel, einer Kavität aus einer dünnen aktiven Pb$_{1-y}$Eu$_y$Se Absorptionsschicht und mit einem Blei Sperrkontakt, welcher als oberer Spiegel benutzt wird, beschrieben. Spektrale Absorptionsmessungen zeigen eine sehr schmalbandige Absorptionslinie, deren Position und Breite durch das Design gegeben sind.

List of abbreviations and symbols

Abbreviations and acronyms

AFM	atomic force microscopy
AES	Auger electron spectroscopy
DH	double heterostructure
EDX	energy dispersive X-ray analysis
ETHZ	Swiss Federal Institute of Technology Zurich
FIB	focused ion beam
FM	Frank-van der Merwe (layer-by-layer) growth
FTIR	Fourier transform infrared spectroscopy
FWHM	full widths at half maximum
IR	infrared
LTHM	low temperature Hall mobility
MBE	molecular beam epitaxy
ML	monolayer
PVD	physical vapour deposition
QCM	quartz crystal deposition monitor
QD	quantum dot
QW	quantum well
QWi	quantum wire
RBS	Rutherford backscattering spectroscopy
RCD	resonant cavity detector
RHEED	reflection high-energy electron diffraction
RIE	reactive ion etching
SEM	scanning electron microscopy
SIM	scanning ion microscopy
SIMS	secondary ion mass spectroscopy
SK	Stranski-Krastanow (layer-plus-island) growth
std	standard deviation
TD	threading dislocation
UHV	ultra high vacuum

VCSED   vertical cavity surface-emitting device
VCSEL   vertical cavity surface-emitting laser
VW   Volmer-Weber (island) growth
XF_2 fluorite
XPS   X-ray photospectroscopy
XRD   X-ray diffraction

Roman symbols

a_o lattice constant
A_e area of the orifice
b Burgers vector
B magnetic field
D diffusion constant
d layer thickness
d_o atomic distance
d_{act} thickness of the active layer
e elementary charge
E electric field
E energy
E_d surface diffusion energy
E_g band gap energy
F_L Lorentz force
F_q resonance frequency
G electrical conductance
h height
I electric current or intensity
J_{imp} impinging deposition rate
J_{reevap} reevaporation rate
k wave vector
k_B the Boltzmann´s constant
k_f reciprocal vector of the X-ray scattered beam
k_i reciprocal vector of incident

L	mean distance between two defects or cavity length or laser length
L_{diff}	mean diffusion length
L_{disl}	mean distances between dislocations
m	mass or effective mass or mode number
M	molecular mass
n	refractive index or charge carrier density (electrons)
n_d	point defect density
n_H	optical layer with high refractive index
n_i	density of cluster i
n_L	optical layer with low refractive index
p	charge carrier density (holes)
P_v	vapour pressure of the material inside the cell
p_s	sheet carrier density
q	electric charge
R	electrical resistance or radius of the AFM tip
R_c	cluster radius
R_H	Hall coefficient
R_S	sheet resistance
T	temperature
t	time
T_{cell}	temperature of the cell
T_m	melting point
T_w	substrate temperature
V	voltage
V_H	Hall voltage
W	width
ΔW	broadening of the AFM image
x	europium concentration
Y	input optical admittance

Greek symbols

α_v	evaporation coefficient
β	mean number of atoms in a cluster
β_{exp}	linear thermal expansion coefficient
β_{FWHM}	full widths at half maximum (for X-ray measurements)
δ	difference in path length or phase shift
ε	dielectric constant
Φ	flux
γ	surface energy
Γ_{eff}	rate of molecules emitted from the cell into the environment
η	quantum efficiency or optical admittance
$\hbar$	Planck's constant divided by 2π
φ	phase shift
κ	positive integer number
λ	wavelength
λ_o	target wavelength
λ_a	mean diffusion length
λ_c	de Broglie wavelength
$\lambda_{cut\text{-}off}$	cut-off wavelength
μ	carrier mobility
μ_{sat}	Low temperature saturation Hall mobility
ν	wavenumber
ν_a	jump frequency
θ	incidence angle
ρ	density or electrical resistivity
ρ_{disl}	dislocation density
ρ_E	density of states
σ	shear modulus or electrical conductivity
σ_i	capture number
τ	minority carrier lifetime

τ_a	adsorption time
τ_c	capture time
τ_n	nucleation time
υ	velocity
ω_x	mean island size

Crystallographical symbols

< >	set of equivalent directions
{ }	set of equivalent lattice planes
[ ]	specific direction
( )	specific lattice plane

Chapter 1

Introduction

Multi-purpose miniature devices, which can solve more than one task, are in the focus of the contemporary scientific and technological research. Infrared detectors grown on active substrates with read-out electronics [1] or light emitting diodes with varying colours [2] can be taken as examples of multi-task devices.

The present work is mainly devoted to tunable optoelectronic devices. They are applied in the mid-infrared range (3÷5 µm) for performing tasks at multiple or changing wavelengths. Different wavelengths are used in spectroscopic gas analysis to cover different absorption lines. Several possibilities are available to employ only one radiation source and detector for operation at multiple wavelengths. For light emitting devices, this might be achieved by an external cavity and/or by use of the temperature dependence of properties of alloys.

During the last 15 years, the development of III-V materials (including nitrides) for optoelectronic applications has mainly covered the very important wavelength range from soft ultraviolet to near infrared (0.2÷1.5 µm). Still longer wavelengths can be emitted and detected with these materials as well [3, 4].

In the present work, growth and properties of IV-VI narrow gap compounds for the 3÷5 µm wavelength range are described. The main advantage of IV-VI compounds is their capability to be tuned chemically over a large wavelength range, and in addition, the band gap energy changes strongly with the temperature. These materials exhibit a direct narrow band gap, which gives an opportunity to use interband transition in detection or emission of radiation. This is contrary to some III-V infrared devices, where intraband transitions are employed. The narrow direct band gap of the IV-VI materials gives much freedom in design of optoelectronic structures and makes them simple to manufacture. Moreover, lead chalcogenides have a lower Auger recombination rate than gallium arsenide based (GaAs) semiconductors [5, 6]. The spectral detectivities of III-V and IV-VI materials are comparable [4].

Therefore, IV-VI semiconductor devices are of considerable interest for investigation of their radiation emission and detection properties. Such properties are described in this work. Presented here are infrared emitting structures based on lead selenide (PbSe), lead telluride (PbTe) and their

alloys with europium (Eu) which are optically pumped. This gives even more space for structure engineering, because there is no need to apply low ohmic contacts and p-n junctions as needed for electrical excitation. In the course of the present investigation, different types of infrared emitters have been produced such as edge-emitting structures operating above laser threshold and vertical cavity surface-emitting devices (VCSEDs) which operate below threshold. All emitters are excited by optical pumping using commercially available, inexpensive and miniature III-V near infrared laser diodes.

Resonant cavity detectors (RCDs) are presented in this thesis as an example of photovoltaic detectors for the 3÷5 μm range. These detectors are constructed in a manner that they are sensitive to the desired wavelengths only. Experiments show that the desired wavelength range can be very narrow (< 1%).

As mirror structures, distributed Bragg reflectors, made of alternating quarter wavelength ($\lambda/4$) layers were used for the RCD and VCSED. In addition, $\lambda/4$ grooves were fabricated by focused ion beam (FIB) for mirrors of some edge-emitting devices.

All the above-mentioned devices were grown by molecular beam epitaxy (MBE); the thicknesses of the layers d vary from several monolayers to 10 μm. There is no need to assert the importance of epitaxy and its influence on device performance. Thus, considerable attention is paid to the growth procedure, investigation of properties and quality control. All optoelectronic elements are described here first and foremost from the point of view of growth and subsequent film characterization. The influence of the high number of dislocations appearing in the layers because of the lattice and thermal expansion mismatch is discussed as well.

An additional issue is the growth of low-dimensional structures. Reduced dimensionalities lead to better device performances, especially for lasers [7]. In this work, quantum well (QW) lasers are compared with double heterostructure (DH) lasers regarding their structural issues and device performance. Moreover, we investigated growth properties of self-assembled one- and zero-dimensional structures, quantum wires (QWis) and quantum dots (QDs). PbSe quantum dots were grown on PbTe quasi-substrates with a very narrow dot size distribution of 2÷3% (which seems to be the lowest value for all quantum dot investigations up to now). With such structures, very low threshold QD infrared lasers are expected.

The present PhD thesis is organized as follows. Chapter 2 describes material properties of the lead chalcogenide compounds (mainly PbSe and

PbTe) and their alloys with europium (Eu), europium chalcogenides (EuSe) and substrates like silicon (Si) or barium fluoride (BaF_2).

Chapter 3 includes basics of growth and characterization for the structures grown by molecular beam epitaxy (MBE). Starting with the nucleation theory, this chapter further deals with the MBE set-up and growth conditions for structures with different dimensions. Characterization methods like atomic force microscopy (AFM), X-ray diffraction (XRD), low temperature Hall mobility (LTHM) measurements and infrared spectroscopy are described.

The determination of the europium concentration x in $Pb_{1-x}Eu_xSe$ and $Pb_{1-x}Eu_xTe$ layers, which is important for device manufacturing, is outlined in Chapter 4. These measurements include cut-off wavelength determination by Fourier transform infrared spectroscopy (FTIR) as well as the dependence of Hall mobility from the Eu concentration.

Structural quality of IV-VI layers and determination of dislocation densities with different methods are described in Chapter 5.

Zero-dimensional structures (PbSe quantum dots on PbTe/Si (111)) are presented in Chapter 6. The size distribution of the quantum dots is very narrow under certain growth conditions. An explanation is given for this behaviour.

Self-assembled fluoride stripes grown on Si (100) are presented in Chapter 7.

In Chapter 8, applications of IV-VI compounds for optoelectronic devices are discussed. Bragg mirrors are discussed in the beginning of the chapter. In Section 8.2, edge-emitting lasers grown on different substrates, their properties and different ways of mirror manufacturing are described. VCSED structures were fabricated and operated below threshold. Resonant cavity infrared diodes are discussed further, and then a subchapter on the comparison of the devices performance follows.

A short outlook of possible future work according to the present results is given at the end.

Chapter 2

Material properties

In this chapter the main structural and physical properties of lead chalcogenides, europium chalcogenides, fluorites (XF_2) and silicon are described. Particular attention will be given to lattice mismatch between different materials and band gap values, characteristics important for epitaxy and optoelectronic device manufacturing (Fig. 2.1).
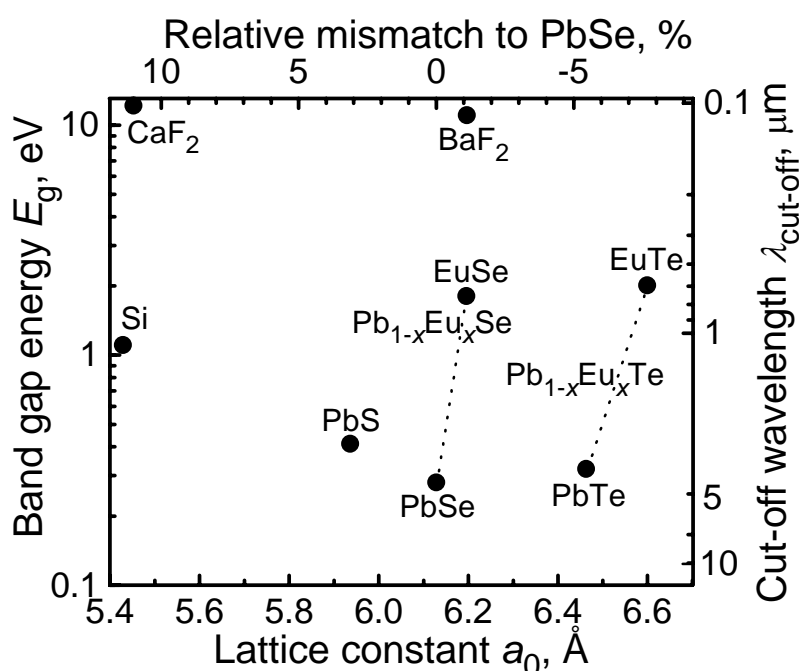
Fig. 2.1. Lattice constants, cut-off wavelengths and energy band gaps of IV-VI, XF_2 materials and Si (see also Table 2.1). T=300 K.

2.1 Crystal structure

2.1.1 Silicon

Silicon exhibits the diamond structure. The diamond structure has two interpenetrating face-centred cubic lattices which are offset with respect to one another along the body-diagonal of the cube by one quarter of its length (Fig. 2.2). The bonding is covalent.
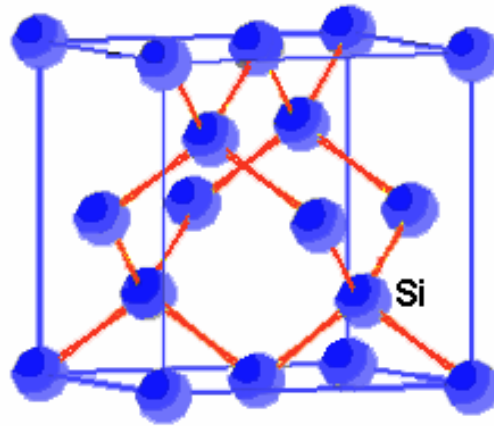
Fig. 2.2. Diamond crystal structure of silicon.

2.1.2 Fluorites

In the fluoride structure, it is the cation (Ca^{2+}) which forms a closest packed cubic layer (Fig. 2.3). The fluoride ions fill all of the tetrahedral holes. The coordination number of Ca^{2+} is eight.
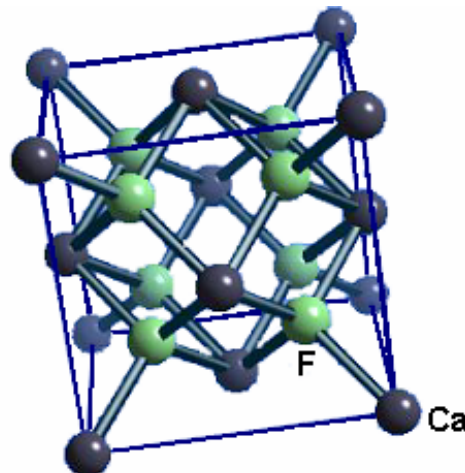

Fig. 2.3. Crystal structure of fluorides. From [8] with the kind permission of the author.

2.1.3 Lead chalcogenides and europium chalcogenides

The lead chalcogenide and europium chalcogenide structures consist of closest packed Se^{2-} or Te^{2-} ions with the Pb^{2+} (or Eu^{2+}) ions filling the octahedral holes (NaCl type). There are two face centred cubic lattices which are separated by one half of the body diagonal of the unit cube. The coordination number of both the Pb^{2+} and Se^{2-} ions is six (Fig. 2.4).

In the lead chalcogenides a Pb vacancy is the source of two holes, a chalcogen vacancy a source of two electrons. A Pb interstitial atom is a

source of one electron and a chalcogen interstitial atom is practically neutral [9].
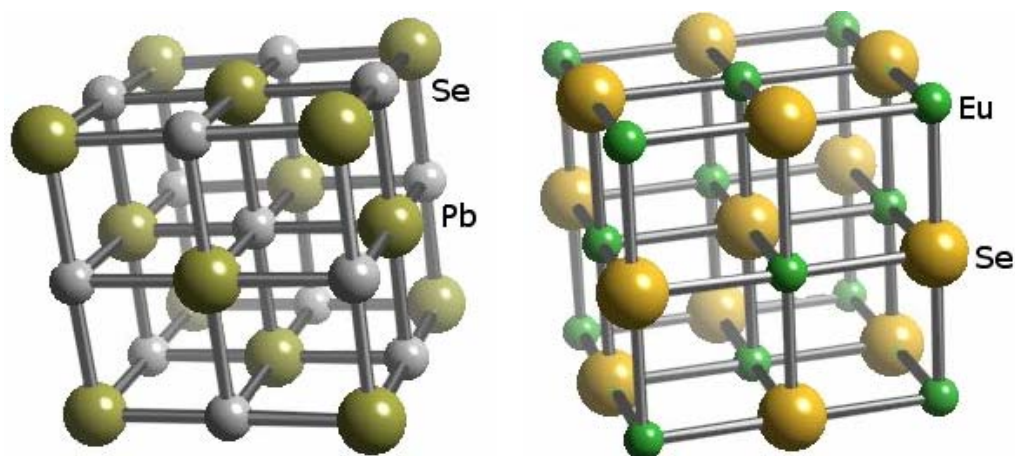

Fig. 2.4. Crystal structure of the lead salts (PbSe is shown as an example, left) and europium chalcogenides (EuSe lattice, right). From [8] with the kind permission of the author.

2.2 General properties of chalcogenides, fluorites and silicon

General material properties are shown in Table 2.1. Narrow band gap, very high refractive index, high dielectric constant and very low thermal conductivity are the main characteristic features of IV-VI materials. CaF_2

Table 2.1. General material properties of some chalcogenides, fluorites and silicon. The values were taken from [10], [11], [12], [13], [14], [15], [16], [17].

	PbSe	PbTe	EuSe	CaF_2	BaF_2	Si
Lattice constant a_o (Å)	6.125[10]	6.461[10]	6.191[10]	5.46[10]	6.19[10]	5.43[10]
Density ρ (kg/m³)	8150[10]	8164[10]	6450[17]	3180[10]	4890[10]	2330[10]
Melting point T_m (K)	1338[10]	1190[10]	2573[10]	1696[10]	1628[10]	1958[10]
Refractive index n ($\lambda \approx 5$ µm, 300 K)	4.92[14]	5.79[14]	2.31[12]	1.40[11]	1.45[11]	3.42[11]
Band gap energy E_g (300 K)	0.27[13]	0.31[13]	1.8[12]	12.1[16]	11[16]	1.107[10]
Dielectric constants ε (300 K) ε_∞ (300 K)	206[15] 22.9[15]	380[15] 32.8[15]	9.5[12] 5.35[12]	6.81[17]	7.32[17]	11.9[17]
Thermal conductivity (W/mK) (300 K)	1.7[10]	2.3[10]	0.24[10]	9.7[10]	10.9[10]	124[17]
Linear thermal expansion coeff. β_{exp} (10^{-6} K^{-1}) (300 K)	19.4[13]	19.8[13]		19.1[13]	19.8[13]	2.6[13]

and BaF$_2$ are dielectrics with low refractive index. Europium chalcogenides (EuSe, EuTe) belong to the class of magnetic semiconductors (they have antiferromagnetic order) with wide band gap. Silicon (Si) parameters are interesting from the side of epitaxy: Mostly this material together with CaF$_2$/BaF$_2$ combinations was used for epitaxy as a substrate.

2.3 Band structure

IV-VI materials and their alloys have some peculiar electronic and structural properties compared with other semiconductors. They have a direct narrow band gap, where the valence band maximum and the conduction band minimum states are situated at the L point of the Brillouin zone (Fig. 2.5). PbSe and PbTe have four equivalent valleys along the <111> directions [18].
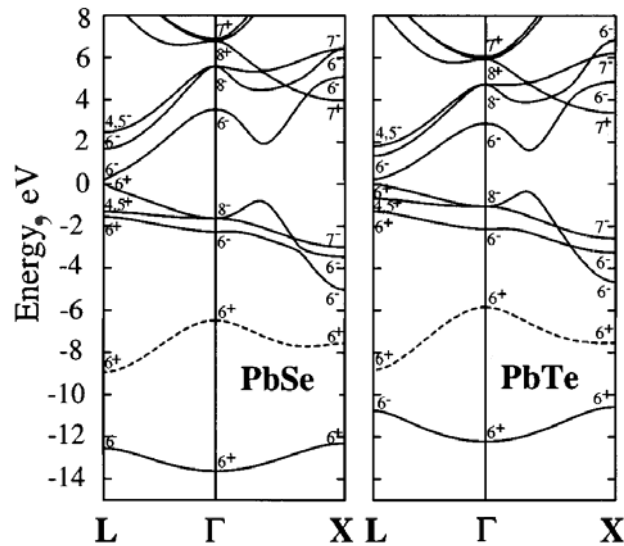

Fig. 2.5. Calculated electronic band structure of PbSe (left) and PbTe (right). After [18] with the kind permission of the author.

The values E_g in the lead chalcogenides and lead europium chalcogenides increase with an increase of temperature (positive temperature coefficient). This is contrary to the behaviour of most other semiconductors. These changes are appreciable, the band gaps of PbTe and PbSe increase by a factor of two from 0 K to 300 K. The temperature dependence of the band gap is described by

$$E_g[\text{meV}] = 171.5 + \sqrt{163.84 + 0.1936 \cdot (T + 20)^2} \; , \tag{2.1}$$

$$E_g[\text{meV}] = 125 + \sqrt{400 + 0.256 T^2} \; , \tag{2.2}$$

for PbTe and PbSe, respectively [19]. These temperature dependences are shown in Fig. 2.6, where the band gap E_g and the cut-off wavelength $\lambda_{cut-off}$ are correlated as:

$$E_g [eV] = \frac{1.24}{\lambda_{cut-off} [\mu m]}. \tag{2.3}$$

The band gaps have negative pressure coefficients, they decrease when pressure is applied. Usually, the band gap decreases with the atomic number of the anion. However, for the IV-VI compounds, the following order of the band gaps is observed [18]:

$E_g(PbS)($ E_g=410 meV at 300 K [13]) > $E_g(PbTe)$ > $E_g(PbSe)$.

The band gap of PbSe and PbTe are interchanged from the point of view of refractive index n: Typically materials with smaller band gaps have higher refractive indices.
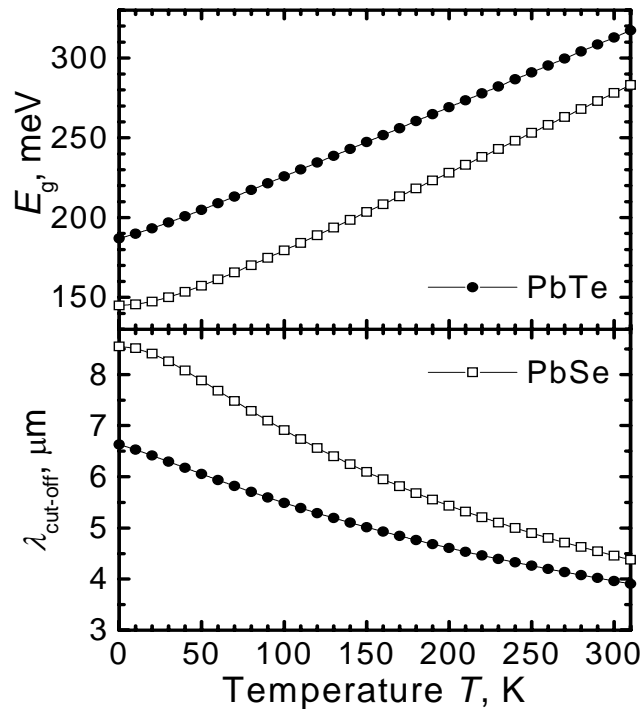
Fig. 2.6. Cut-off wavelength (bottom) and band gap energy (top) as functions of temperature.

2.4 Pb$_{1-x}$Eu$_x$Se and Pb$_{1-x}$Eu$_x$Te ternary alloys

There are several chemical elements which are used to change the physical properties of the lead chalcogenides when they replace a Pb atom. The band gap is increased by alloying PbSe or PbTe with strontium (Sr), europium (Eu), calcium (Ca), barium (Ba) and cadmium (Cd), which

therefore shifts the cut-off wavelength to the blue. On the contrary, tin (Sn) makes the band gap energy smaller (red shift). To achieve semimagnetic properties, ternary lead chalcogenide alloys containing manganese (Mn), europium (Eu), uranium (U), chromium (Cr) or gadolinium (Gd) are taken into consideration [20]. For the optoelectronic device design (for example lasers or resonant cavities) the refractive indices play an important role. Adding europium or strontium decreases the refractive index.

By changing the Eu content in $Pb_{1-x}Eu_xSe$ and $Pb_{1-x}Eu_xTe$ ternary alloys, the energy gap, lattice constant and refractive index of the layers are altered. Lead selenide and lead telluride have the same behaviour of the physical properties concerning the Eu content: With increasing europium concentration x the band gap E_g and lattice constant a_o are increasing while the refractivity index n is decreasing. As an example, the dependences of E_g and a_o from different x in $Pb_{1-x}Eu_xTe$ are presented in Fig. 2.7 [21], in $Pb_{1-x}Eu_xSe$ ternary alloys in Fig. 2.8 [10, 12, 22, 23, 24, 25] and the behaviour of n for $Pb_{1-x}Eu_xSe$ in Fig. 2.9 [12, 14, 22, 26].
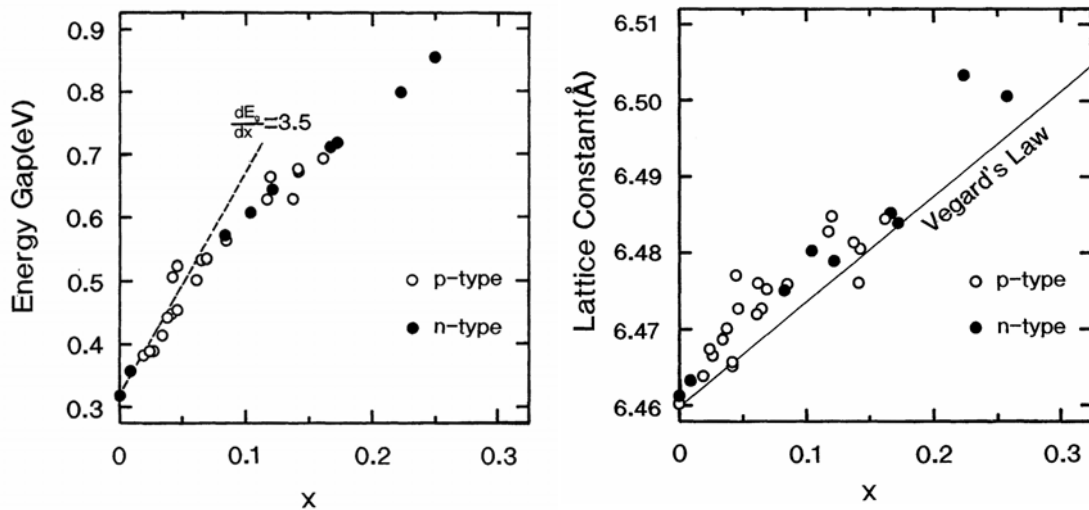

Fig. 2.7. The dependence of the energy gap (left) and the lattice constant (right) of $Pb_{1-x}Eu_xTe$ on the composition ratio x at 300 K. After [21] with the kind permission of the author.

As follows from the graphs, E_g, a_o and n do not have a linear dependence on the Eu concentration x. For example, the lattice constant does not follow Vegard's law [27]. The temperature dependence of the energy band gap of europium containing IV-VI ternary alloys changes in the same way as binary IV-VIs [22, 28, 29]. For $Pb_{1-x}Eu_xTe$ the temperature dependence for low x values is [28]

$$E_g(x,T) = 189.7 + \frac{0.48T^2}{T+29}(1-7.56x) + 4480x, \ (x{<}0.05) \qquad (2.4)$$
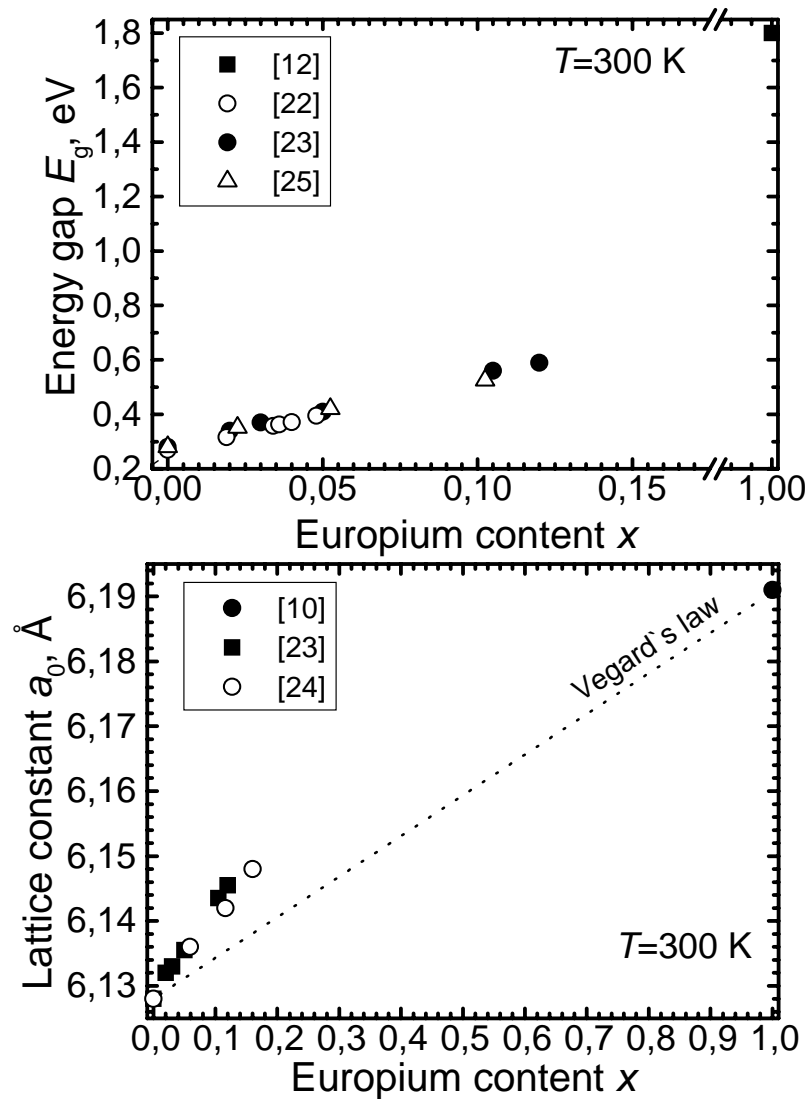
Fig. 2.8. Lattice constant (top) and energy band gap (bottom) at T=300 K as functions of Eu content in Pb$_{1-x}$Eu$_x$Se ternary alloys [10, 12, 22, 23, 24, 25].

Fig. 2.9. Refractive index n as a function of Eu concentration x after [12, 14, 22, 26]. The values are taken at the cut-off wavelengths.

Fig. 2.10. Refractive index of PbSe and Pb$_{1-x}$Eu$_x$Se with different *x* content at different temperatures. Eu concentrations are ● 0.019, ● 0.034, ● 0.036, ● 0.04, ● 0.048. After [22] with the kind permission of the author.

and for $Pb_{1-x}Eu_xSe$

$$E_g(x,T) = 146.3 + \frac{0.475T^2}{T+40.7}(1-3x) + 3000x \qquad (2.5)$$

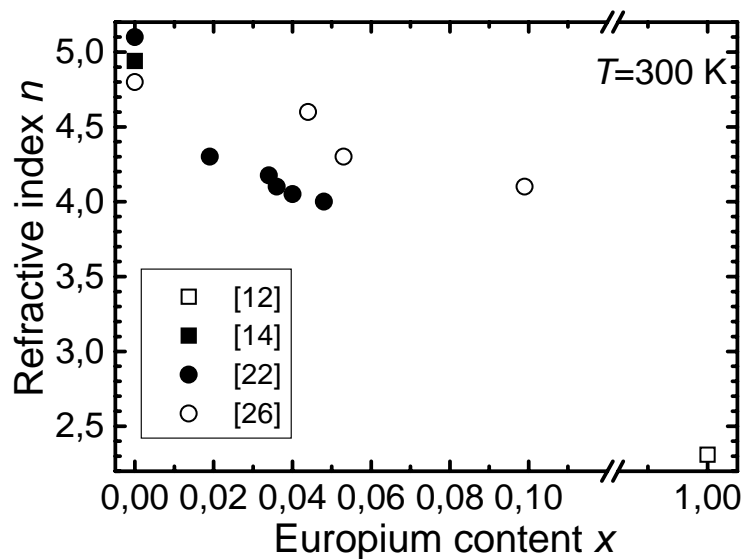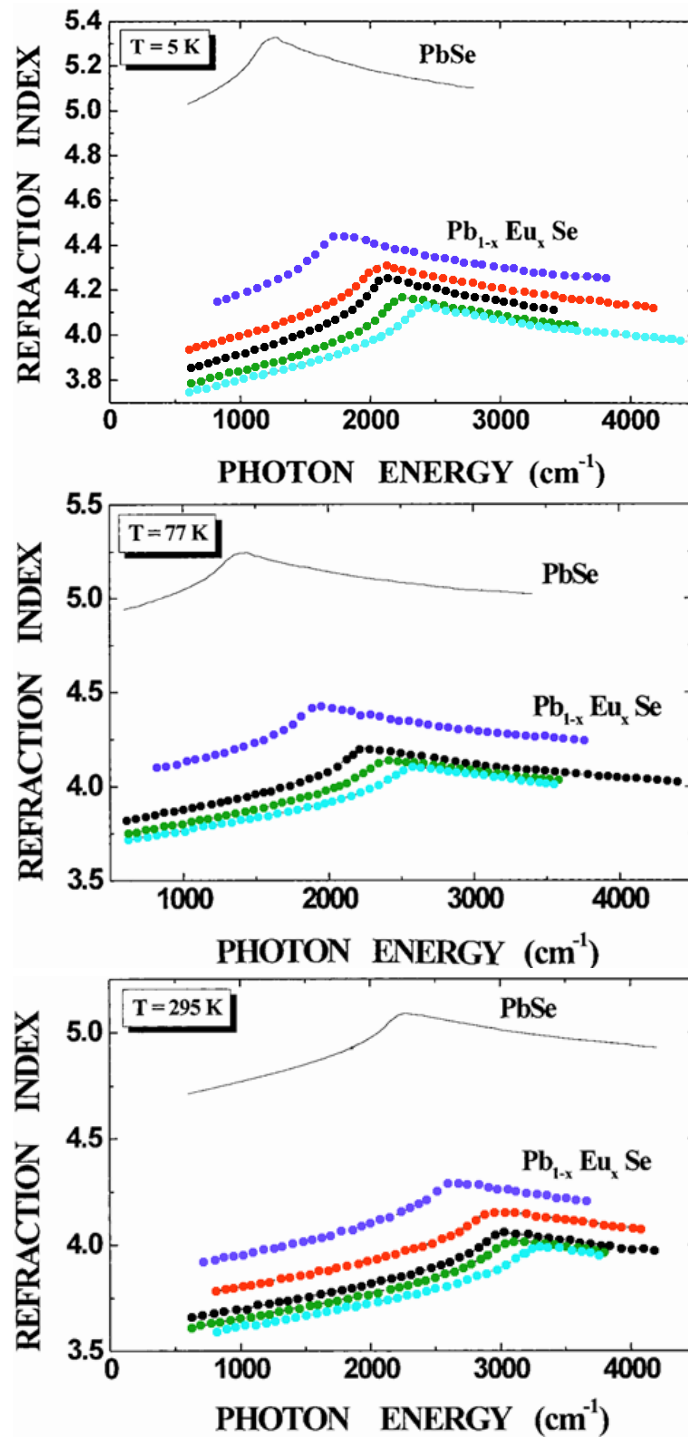(modified formula from [30], used for the calculations in Chapter 4) after [22]. For both formulas E_g is in meV and T in K.

The refractive index of $Pb_{1-x}Eu_xSe$ decreases with increasing x very quickly for low concentrations (see Fig. 2.10):

$$n \cong 4.95 - 27.3x, \; (x<0.05) \qquad (2.6)$$

and then the decrease factor is rather low:

$$n \cong 3.98 - 1.67x, \; (0.05<x<1). \qquad (2.7)$$

These formulas were approximated after [12, 22].

2.5 Dislocations in IV-VI films

There are twelve different $a/2$<110> type Burgers vectors $\vec{b}$ for lead salt compounds (Fig. 2.11). For the (111) growth direction, six of these twelve $\vec{b}$ vectors are inclined by 54.7° out of the surface and six vectors lie in the (111) surface [e.g. 31]. The primary glide planes are {100} in IV-VIs and the critical resolved shear stresses are low for these planes (while the second glide system of {110}-type glide planes exhibits much higher stresses) [32].
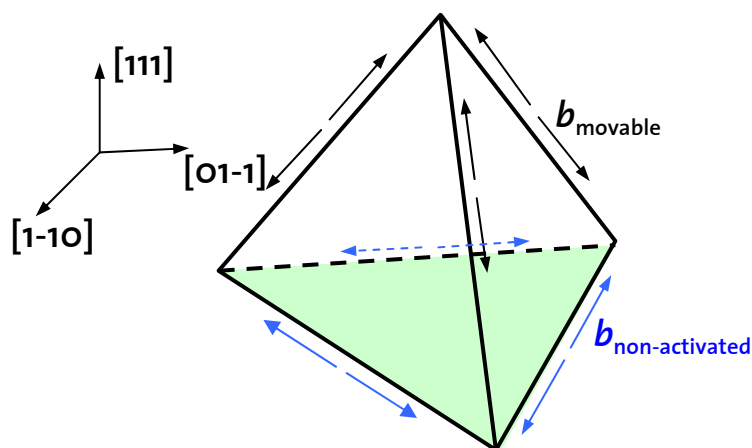
Fig. 2.11. Arrangement of the twelve possible a/2<110>-type Burgers vectors. Dislocations with the vectors shown black are movable, with the blue vectors-non-activated under applied stress along [111] direction.

The six vectors lying in the (111) plane are arranged along the sides of the tetrahedron base (shown blue in Fig. 2.11). They lie parallel to the surface, their Schmid factor is zero. The corresponding dislocations therefore are not moved. The other six vectors are inclined to the surface (shown black)

and the Schmid factor is not zero. Dislocations within these inclined directions may move under applied uniaxial stress along [111] direction [33].

2.5.1 Dislocations in IV-VI films grown on silicon

Since the lattice constants of lead chalcogenides and fluorides are higher than that of silicon, a compressive strain is expected in the layers. Most of this strain is already relaxed at growth temperatures. For such highly mismatched systems the critical thickness of misfit dislocation formation is very small. On cool down, tensile strain appears owing to the thermal expansion coefficient difference of the materials (see Table 2.1). This tensile strain is $\approx$0.8% at room temperature and $\approx$1.2% at 77 K for the layers grown at growth temperature T_w=673 K [31, 34].

The relaxation mechanism can be explained from the microscopic point of view. Glide steps are visible along the <110> directions, which are the intersection of the {100} glide planes with the (111) interface. A {100}<110> glide system for a NaCl type IV-VI (111) oriented layer on Si (111) is shown in Fig. 2.12. Glide of the threading ends of misfit dislocations occurs at each temperature change to compensate for strains. A moving threading dislocation (TD) can intersect other dislocations. The intersection probability of two dislocations is quite high for the high dislocation
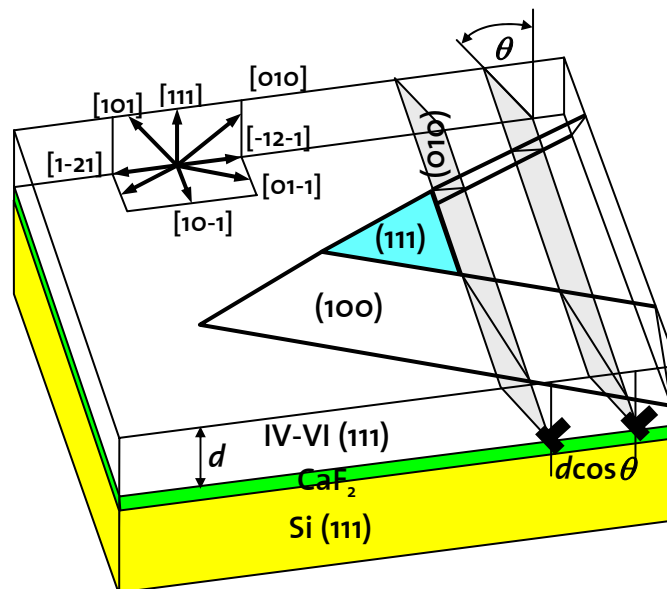

Fig. 2.12. {100}<110> glide system for (111) oriented IV-VI films on Si (111).

densities (10^7-10^8 cm^{-2}). A moving TD (m) is able to react with a non-activated TD (na) forming a new moving TD (m+na$\rightarrow$m). By interaction of two moving dislocations a dislocation experiencing zero stress may be

formed (m+m→na) [33]. In high quality IV-VI films no blocking occurs when dislocations react. Therefore, there are always enough dislocations available that can be moved and dislocation reactions decrease TD density on each temperature change.
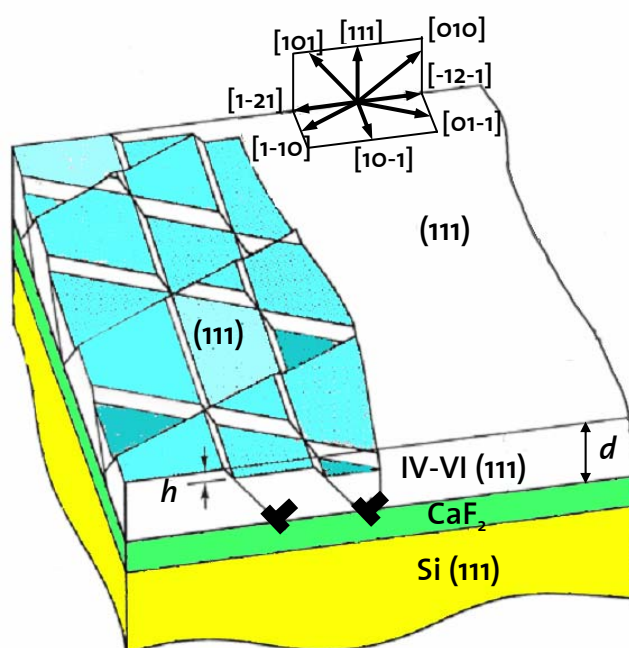
Fig. 2.13. Surface morphology of (111) oriented IV-VI layers on Si (111) due to the dislocation gliding.

Owing to the glide in the {100}<110> glide system equilateral triangle terraces form on the (111) surface (three equivalent <110> directions) (Fig. 2.13) [35]. These terraces can be observed by optical methods, electron scanning microscopy and atomic force microscopy (Fig. 2.14). The typical step height on the surface for PbTe layers on Si (111) is ≈14 Å [36].
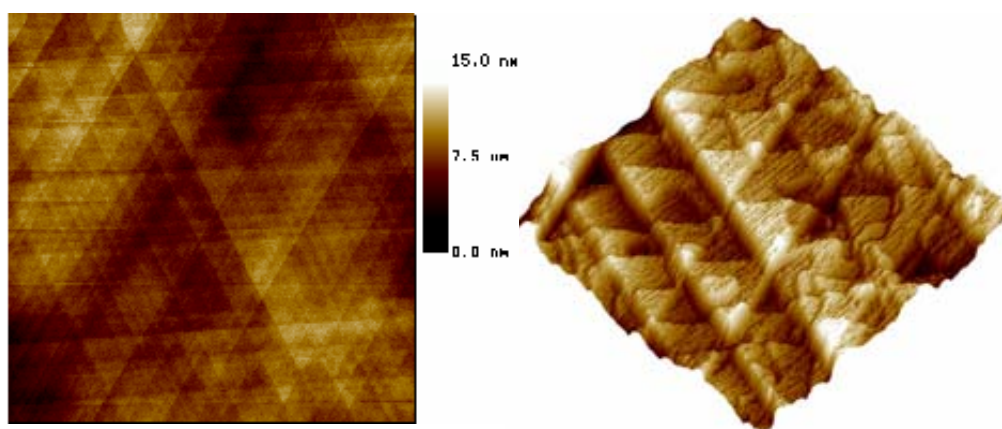
Fig. 2.14. AFM images of a PbTe layer on Si (111). Steps and triangles as a result of dislocation gliding can be seen. The AFM image sizes are 5×5 μm² (left) and 1×1 μm² (right). The step heights are 1.4 nm.

Contrary to (111) oriented structures, (100) oriented IV-VI layers "relax" by cracking if their thickness exceeds about 2 µm. Cracking occurs on cool down to room temperature after growth or to cryogenic temperatures. For the primary {100}<110> glide system in (100) lead chalcogenide layers Schmidt factors are zero and therefore, the secondary {110}<011> system is responsible for strain relaxation. But this system seems to be not active enough to prevent cracks [31]. These cracks make IV-VI layers useless for many applications, but on the other hand they can bring some advantages as well (for a detailed description of (100) film cracking see Appendix B).

A third glide system in IV-VI materials, induced by electron beam thermal stress, the {111}<110> system, was reported by Foitzik [37]. But plastic deformation of single crystals with the second and the third glide systems appears at higher stress than with the first.

2.5.2 Dislocations in IV-VI films grown on BaF$_2$ (111)

Similar layers grown on bulk BaF$_2$ (111) substrates do not show triangular shaped surfaces. This can be explained by the fact that the thermal expansion mismatch between IV-VI layers and barium fluoride is much smaller than for IV-VI/Si pairs. The threading ends of the dislocations are of a screw type character [38]. Dislocations which already originate during growth to relieve the lattice mismatch are hardly visible because they are continually overgrown: A single screw type TD would produce a semi-infinite step on the surface. Owing to the high TD density in the epitaxial layer these surface steps are always terminated by a second dislocation with opposite normal component of $\vec{b}$ [32, 38].

With increasing thickness of the IV-VI layers, the TD density rapidly decreases. Since the curvature of the surface steps at the dislocations remains constant, more and more complete turns of step spirals are formed. At layer thicknesses of more than 1 µm the surface is completely covered by large growth spirals. Taking into consideration the presence of left- as well as right-handed growth spirals corresponding to anti-parallel Burgers vectors $\vec{b}$, these dislocations attract each other and annihilation might occur. It was shown by Ueta [39] that the TD density decreases by three orders of magnitude down to 10^6 cm^{-2} when the thickness of the IV-VI layer on BaF$_2$ increases from 0.1 to 10 µm.

Chapter 3
Characterization and growth

In this chapter the main features of nucleation and further epitaxial growth will be discussed. Some points concerning IV-VI growth on different substrates will be covered as well. This chapter also describes equipment and techniques that were used for epitaxy and characterization.

3.1 Nucleation and growth

3.1.1 Nucleation theory

Nucleation and growth of thin films include processes on time and length scales that extend over many orders of magnitude [40]. Molecules can move on length scales of nanometers, the typical atomic vibrations (order of 10^{-13} sec) reflect short time scales and quantum dots can consist of a few atoms. From another point of view, a typical optoelectronic device might be dozens and hundreds of micrometers in size, its growth takes hours with the reevaporation rate of 10^{11} molecules/cm^{2}sec. The main aim of a nucleation theory is to combine these scales in one appropriate model. There are a variety of different models, including mean field rate equations [41], atomistic kinetic Monte Carlo [42] and level set (island dynamics) models [43].

3.1.1.1 Nucleation and start of growth

Epitaxial growth of thin films and nucleation can be generally described as shown in Fig. 3.1 [after 40]. Molecules of the flux Φ (yellow and green balls indicate the same substance, but different colours are taken for different layers) are impinging on the surface (grey balls) (1). There are many possibilities for atoms when they reach the surface. Atoms can diffuse with a diffusion constant D (2). Atoms can meet to form a dimer (3) or can be attached to existing islands (4). Moreover, atoms can detach from the island edge (5) or diffuse along the edge (6). (7) and (8) show the possibility of deposition on the top of islands. And finally, atoms can reevaporate from the surface with the rate J_{reevap} (9).
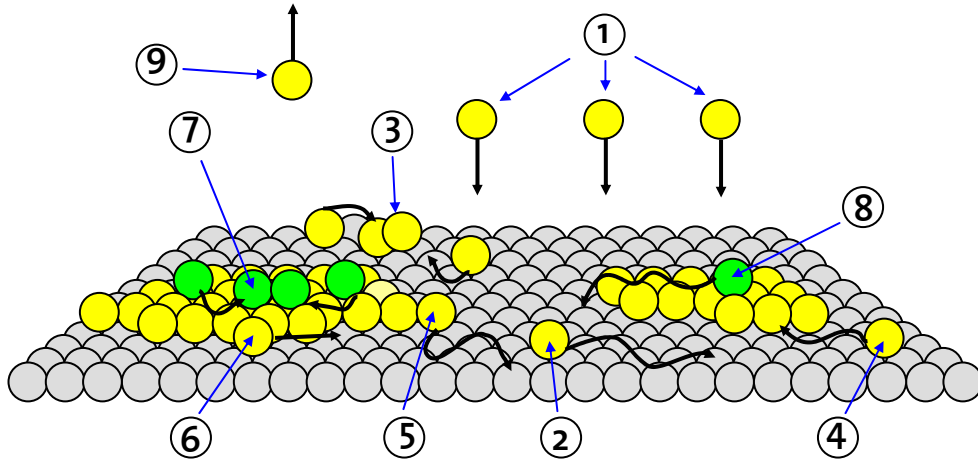
Fig. 3.1. Schematic drawing of epitaxial growth (surface atoms are grey).
(1) Flux from the source, (2) Diffusion on the surface, (3) Formation of dimer,
(4) Attachment to an existing island, (5) Detachment from the edge of an
island, (6) Diffusion along the island, (7) Deposition of adatoms on the top of
the island, (8) Sliding down from the island, (9) Reevaporation.

For some theories the idea of a critical nucleus is important. The main principles are shown in Fig. 3.2. By the arrival with an input flux Φ, atoms (2-d density n_1) can form dimers with density n_2 (nucleation time τ_n) with another single atom, can be captured by the cluster consisting of x atoms with the density n_x (τ_c for capture) or reevaporated (τ_a for desorption):

$$\frac{dn_1}{dt} = \Phi - \frac{n_1}{\tau}, \text{ where}$$

$$\frac{1}{\tau} = \frac{1}{\tau_a} + \frac{1}{\tau_n} + \frac{1}{\tau_c} + \dots \tag{3.1}$$

The dimer n_2 can be detached back to single atom n_1 or produce a bigger cluster density n_i with i atoms. Clusters with the number of atoms x equal or more than a critical amount s ($x \geq s > i$) are called stable and grow by diffusive capture and at a later stage by impingement. The rate equation for the atom number in stable clusters with the mean island size ω_x is presented as

$$\frac{d(n_x \omega_x)}{dt} = n_1 \left(\frac{1}{\tau_n} + \frac{1}{\tau_c} \right) + \Phi \sum_{s>i} k_s n_s a_s \ , \tag{3.2}$$

where all relevant growth processes are included in the first term. The second term corresponds to direct impingement onto all stable clusters of area a_s with a geometrical correction factor k_s [44].

The island density on the surface can be estimated from

$$N_{\text{Island}} = C_0 \left(\frac{D}{\Phi} \right)^{-\frac{1}{3}}, \tag{3.3}$$

where C_o is a dimensionless quantity that is determined by the geometrical factors and parameters that describe the capture efficiency of the islands [45].
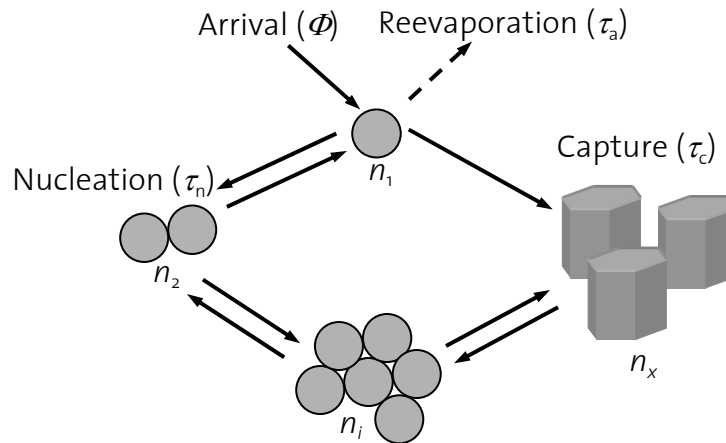

Fig. 3.2. The critical island size model.

3.1.1.2 Nucleation at point defects

The random location of point defects is the most important factor in determining the cluster size distribution and the character of cluster density [46]. The nucleation mechanism is assumed to be that of an infinitely long chain reaction

$$n_d + n_1 \Leftrightarrow n_{1d},$$

$$n_{1d} + n_1 \Leftrightarrow n_{2d},$$

...

$$n_{id} + n_1 \Leftrightarrow n_{(i+1)d}, \tag{3.4}$$
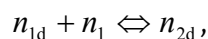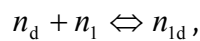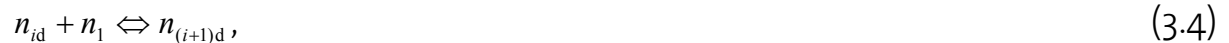
where n_d is point defect density, n_1 is a single atom density and n_{id} is a density of clusters consisting of i atoms which are formed on a point defect (see also Fig. 3.3).

In this case the total nucleation rate is the sum of the nucleation rate on the defect free surface and at the defects [40]

$$\frac{dn_x}{dt} = \sigma_i D n_1 n_i + \sigma_{id} D n_1 n_{id} \tag{3.5}$$

where σ_i and σ_{id} are corresponding capture numbers.

The size distribution function $N(i, t)$ is different under various experimental conditions. In a small temperature region, where the cluster radius is much smaller than the mean diffusion length, and the distance
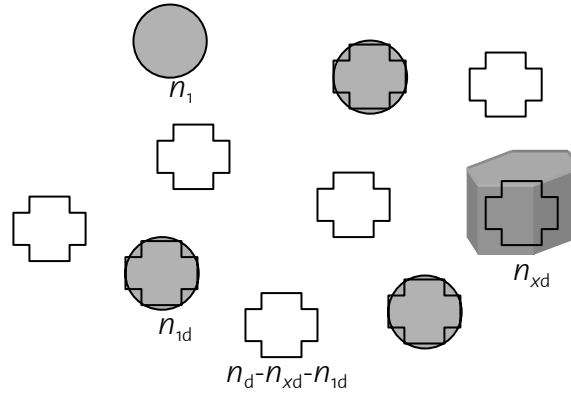
Fig. 3.3. Nucleation on defects (crosses) of the density n_d.

between two defects is larger than the mean diffusion length $R_c \ll \lambda_a$, $L > \lambda_a$ (see Fig. 3.4 for symbol definitions), the cluster growth rate

$$\frac{di}{dt} = \frac{2\pi\Phi\lambda_a^2}{\ln\left(\dfrac{\lambda_a}{R_c}\right)}$$

(3.6)

depends weakly on the cluster size and therefore the size distribution follows approximately the Poisson distribution law

$$N(i,t) = \frac{n_d \beta^i e^{-\beta}}{i!},$$

(3.7)

provided that a single atom adsorbed on a point defect is a stable cluster. At sufficiently large i, equation (3.7) turns into the Gaussian distribution law
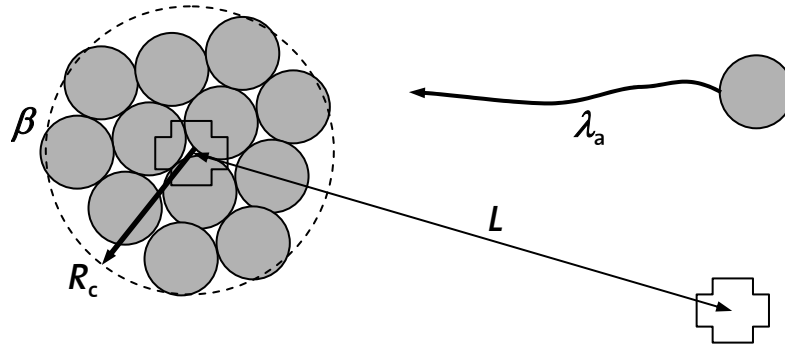
Fig. 3.4. Main definitions of symbols: cluster radius R_c, mean diffusion length λ_a, mean size of the clusters β (number of atoms), and mean distance between two defects L.

$$N(i,t) = \frac{n_d}{\sqrt{2\pi\beta}} \exp\left[-\frac{(i-\beta)^2}{2\beta}\right].$$

(3.8)

Taking into account the inequality $R_c \ll \lambda_a < L$ it can be concluded that a significant part of a substrate remains uncovered by the diffusion zones

and in this case random nucleation n_i is comparable with selective nucleation n_{id} and is described by equation (3.5). In the case of significant overlapping of diffusion zones $L<\lambda_a$ in the beginning of nucleation there is no deactivating of neighbour defects by the "fixed on the defect" atom, while it does not change the capture efficiency of its defect. Larger clusters consisting of 10 or more atoms have larger capture cross sections, so that they are likely to deactivate the nearest point defects provided that no atoms have yet been trapped on them. If the surface is partially covered by clusters consisting of e.g. β=10 atoms, then the probability of finding a free point defect (not covered by clusters) on the surface is proportional to e^{-10} [46].

When $L<\lambda_a$, the fluctuations in point defect density influence the growth rate of the clusters. If the cluster shape does not change during growth, the size distributions for a hemispherical shape of radius R_c and mean radius $R_{c,m}$ can be written as

$$N(R_c) = n_d \frac{3R_c^2}{R_{c,m}^3} \exp\left[\frac{-R_c^3}{R_{c,m}^3}\right], \quad \lambda_a \gg L,$$
(3.9)

$$N(R_c) = n_d \frac{6R_c^5}{R_{c,m}^6} \exp\left[\frac{-R_c^6}{R_{c,m}^6}\right], \quad \frac{L}{2\lambda_a} \approx 1.$$
(3.10)

If $L>2\lambda_a$, the distribution becomes very narrow:

$$N(R_c) = n_d \sqrt{\frac{3}{R_{c,m}^3}} R_c^2 \exp\left[\frac{-\pi(R_c^3 - R_{c,m}^3)^2}{3R_{c,m}^3}\right], \quad 2\lambda_a < L.$$
(3.11)

3.1.2 Growth modes

The particular growth mode for a given system depends on the interface energies and on the lattice mismatch. In the equilibrium theory of heteroepitaxial growth three growth modes are traditionally distinguished [47], (Fig. 3.5):

1. Frank-van der Merwe (FM) or layer-by-layer growth.
2. Volmer-Weber (VW) or island growth.
3. Stranski-Krastanow (SK) or layer-plus-island growth.

Bauer was the first to systematize these growth modes in thermodynamic terms. Consider γ_A and γ_S the surface energies of the depositing material and the surface, and γ^* the interfacial energy. If one deposits material A on a substrate S, then if

$$\gamma_A + \gamma^* < \gamma_S$$
(3.12a)

layer growth will take place, and if

$$\gamma_A + \gamma^* > \gamma_S \tag{3.12b}$$

island growth occurs.
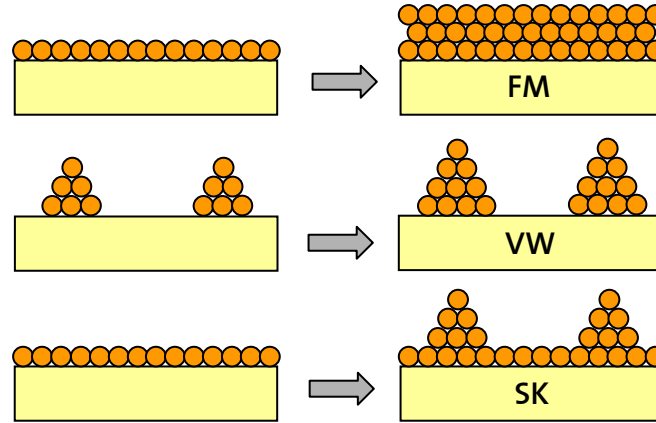
Fig. 3.5. Growth modes for heteroepitaxial systems. From top to bottom: Frank-van der Merwe; Volmer-Weber; Stranski-Krastanow.

The Frank-van der Merwe growth mode arises because the atoms of the deposited material are more strongly attracted to the substrate than to themselves and a two dimensional (2-d) film growth results. In the opposite case, where the deposited atoms are more strongly bound to each other than to the substrate, the Volmer-Weber mode results and a layer grows in three dimensions (3-d). If the strain energy is large, the Stranski-Krastanow mode arises. This happens because the interfacial energy γ^* increases as the layer thickness increases; typically this layer is strained to lattice match the substrate [48].

3.1.3 Low dimensional structures

In this work, structures of different dimensionalities are described. In order to distinguish the difference between different growth dimensions of growth modes (see Section 3.1.2) and dimensions from the point of view of quantum physics, the following conventions were applied:

1)   Growth mode dimensions are shown as 2-d and 3-d.

2)   Quantum size dimensions are shown as 3D, 2D, 1D and 0D.

Semiconductor charge carriers (electrons and holes) have a density of states $\rho_E(E)$ in three dimensional space (3D)

$$\rho_E^{3D}(E)dE = \frac{1}{2\pi^2}\left(\frac{2m}{\hbar^2}\right)^{\frac{3}{2}} E^{\frac{1}{2}} dE \,, \tag{3.13}$$

where E is the energy of the particle, m is an effective mass and $\hbar$ is Planck's constant divided by 2π. By decreasing the film thickness d it is possible to reach a state where $d \approx \lambda_c$, λ_c is the de Broglie wavelength. Size quantization appears for one direction (2D) and energy dispersion becomes discrete:

$$\rho_E^{2D}(E)dE = \frac{1}{\pi}\left(\frac{m}{\hbar^2}\right)dE \,. \tag{3.14}$$

Size limitation from two directions leads to the case where the only one dimension remains non-quantized (1D). In this particular state the density of states is equal

$$\rho_E^{1D}(E)dE = \frac{1}{2\pi}\left(\frac{2m}{\hbar^2}\right)^{\frac{1}{2}} E^{-\frac{1}{2}} dE \,. \tag{3.15}$$

If all three dimensions are quantized (0D), the density of states is presented as discrete, sharp energies (Fig. 3.6).

Usually 3D structures are named heterostructures, 2D quantum wells (QWs), 1D quantum wires (QWis) and 0D quantum dots (QDs).
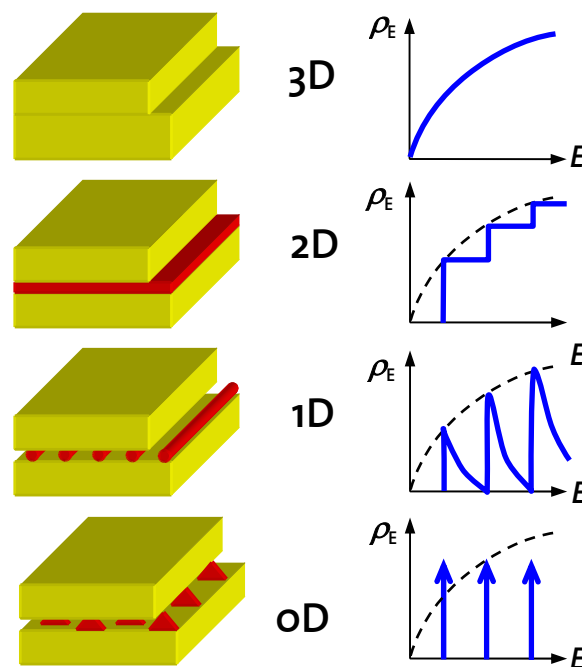

Fig. 3.6. Schematic diagram of structures with different dimensionalities (left) and corresponding density of states functions $\rho_E(E)$ (right).

3.2 MBE growth

In molecular beam epitaxy (MBE), molecular beams generated by effusion cells impinge upon a heated substrate. Ultra high vacuum (UHV) conditions inside the MBE chamber ensure a very low contamination. In addition, the mean free paths are much larger than the distance between an effusion cell and the substrate. MBE also makes possible to evaporate substances from different sources in order to obtain different chemical compounds and to vary doping. Molecular beam epitaxy is useful for making low dimensional structures. Shutters above the sources allow to precisely control the flux within thicknesses below one monolayer.

In this chapter the main growth conditions for fluorides and IV-VI materials are described. Different substrates (BaF_2, Si), dimensions of growth (3-d, 2-d) and materials were used to achieve different properties of grown structures.

3.2.1 MBE experimental set-up

All epitaxy experiments were made in two MBE chambers which are connected by an UHV tunnel (Fig. 3.7). In the first chamber calcium and barium fluoride layers are grown on Si substrates. Thin layers of CaF_2 and/or BaF_2 were used as buffer layers for compatibility.
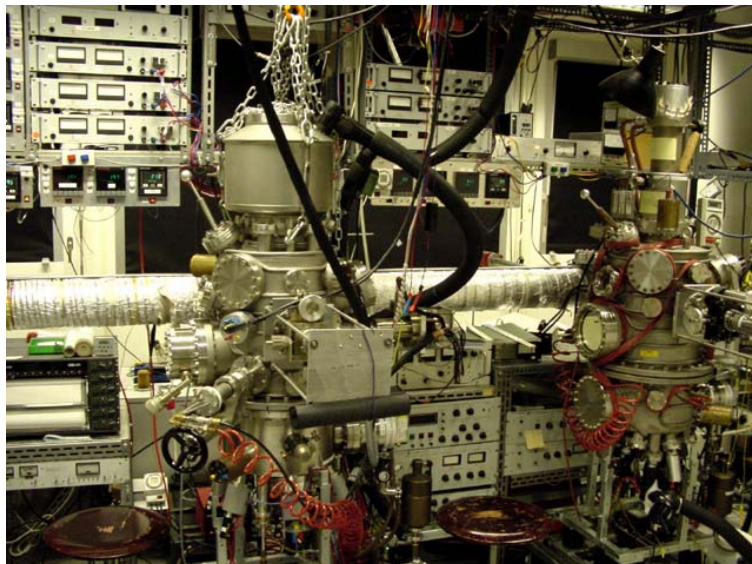

Fig. 3.7. Fluoride (right) and IV-VI (left) MBE chambers connected
with the UHV tunnel.

Fig. 3.8 shows a schematic drawing of the second MBE chamber, which is mainly used for the IV-VI material epitaxy. The chamber contains seven effusion cells: PbTe, Te, PbSe, Se, Eu, Bi_2Te_3 and BaF_2. These effusion cells utilize the principle of molecular effusion (demonstrated by Knudsen in 1909). The material to be deposited is heated to provide a suitable vapour pressure in an isothermal enclosure. The deposition rate is extremely stable being determined by the temperature of the furnace. All sources are controlled by the temperature. Temperature fluctuations of the sources are typically not more than ±1°, and molecular fluxes are stable during the whole MBE run. All sources are equipped with individual shutters, which can be manipulated by the operator. An additional main shutter is situated near the substrate.
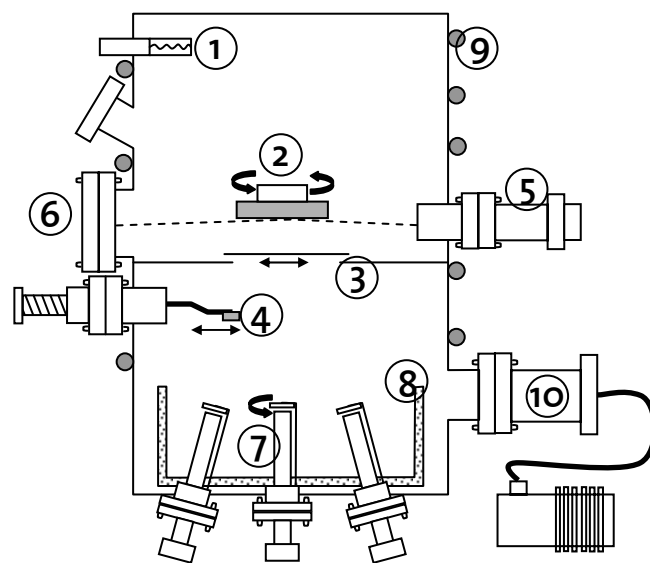
Fig. 3.8. Schematic drawing of the IV-VI MBE chamber.
(1). Ionisation manometer, (2). Heatable substrate holder, (3). Main shutter, (4). Crystal thickness monitor, (5). RHEED electron gun, (6). Fluorescent screen, (7). Effusion cells, (8). Liquid nitrogen cooled shield, (9). External water cooling, (10). Turbo molecular UHV pump with fore-pump.

The substrate holder for the 3 inch samples can be rotated, samples can be heated up to 1173 K. Material fluxes are controlled by crystal thickness monitors. To control the CaF_2 deposition rate, flux was controlled all the time, since the 2 nm CaF_2 buffer layer thickness is very critical. For the other materials usually it is not necessary to measure the fluxes continuously: The quartz monitor is introduced in the flux centre only before and after the MBE growth. During epitaxy the crystal monitor is taken out from the active zone of the flux in order not to shade the epitaxy area. RHEED (reflection high-energy electron diffraction) allows to produce *in situ* surface analysis. UHV turbo molecular pump and internal liquid nitrogen shield make possible to work in the 10^{-9} mbar range.

3.2.1.1 Crystal quartz monitor

The quartz crystal deposition monitor (QCM) utilizes the sensitivity of the frequency of a quartz monitor crystal to added mass. This mass sensitivity is used to control the deposition rate and final thickness of a vacuum deposition process. When mass is added to the face of a resonating crystal, the resonance frequency F_q is reduced by ΔF. This change in frequency can be transferred to first order by

$$\frac{\Delta m}{m_q} = \frac{\Delta F}{F_q} \qquad (3.16)$$

to a mass change $\Delta m = m_c - m_q$, where m_c and m_q are the masses of the coated and uncoated quartz, respectively [49].

The Z-Match™ equation introduced by Lu and Lewis in 1972 [50] allows to take into account the acoustic properties of the resonating quartz and film system by introducing the Z-factor (acoustic impedance ratio):

$$Z = \sqrt{\frac{\rho_q \sigma_q}{\rho_f \sigma_f}}, \qquad (3.17)$$

ρ is the density and σ is the shear modulus of quartz (q) and the deposited film (f). The film thickness d deposited to the quartz monitor is calculated as

$$d = \frac{F_{AT} \rho_q}{\pi \rho_f F_c Z} \arctan\left(Z \tan\left[\frac{\pi \Delta F}{F_q} \right] \right), \qquad (3.18)$$

where F_{AT} is the frequency constant. Non-linearities introduced by the arctan term are important for thick deposited layers only.

For the measurements a QCM XTC/2 from Leybold with F_q=6 MHz was used to control the fluxes Φ of all evaporated materials in both MBE chambers. The measured fluxes Φ (Å/sec) are related with the impinging deposition rate J_{imp} (ML/sec) by the molar weight and density of deposited material which is a function of the crystal orientation. For example, one monolayer of (111) oriented PbSe contains 6.15×10^{14} atoms/cm^2.

3.2.1.2 RHEED

Reflection high-energy electron diffraction (RHEED) is generally used as an *in situ* observation method of growth, which can be applied during growth. Surface disorder and different growth modes (2-d, 3-d) are observable as well. Moreover, this method is surface sensitive, reflection takes place in the very top atomic planes [51]. The RHEED instrument

consists of easy-to-handle parts: An electron gun (see (5) in Fig. 3.8) with the possibility to deflect the 5÷50 keV beam into different directions and a fluorescent screen for the registration of the reflection (6). The substrate (2) is inclined to the beam at angles below 3°.

   A useful geometrical representation of the diffraction conditions is the Ewald sphere construction, shown in Fig. 3.9 and Fig. 3.10. There the 2-d reciprocal lattice of the crystal surface is depicted as rods. The wave vector $\vec{k}_0$ represents the incoming beam. All wave vectors of the same magnitude as $\vec{k}_0$ define a sphere of radius $|\vec{k}_0|$ centred at $-\vec{k}_0$ from the origin in reciprocal space. Wherever this sphere intersects a reciprocal lattice rod (green points in Fig. 3.10), the conditions for diffraction defined above are satisfied, and the vector $\vec{k}$ to that point on the Ewald sphere is the wave vector of an allowed diffraction beam.
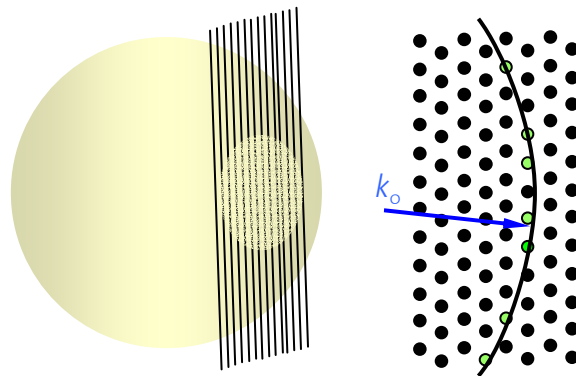

Fig. 3.9. The Ewald sphere and intersected reciprocal rods as a 3-d view (left), and top view with the lattice net (right). Those lattice points that will be visible on the RHEED screen are shown green.
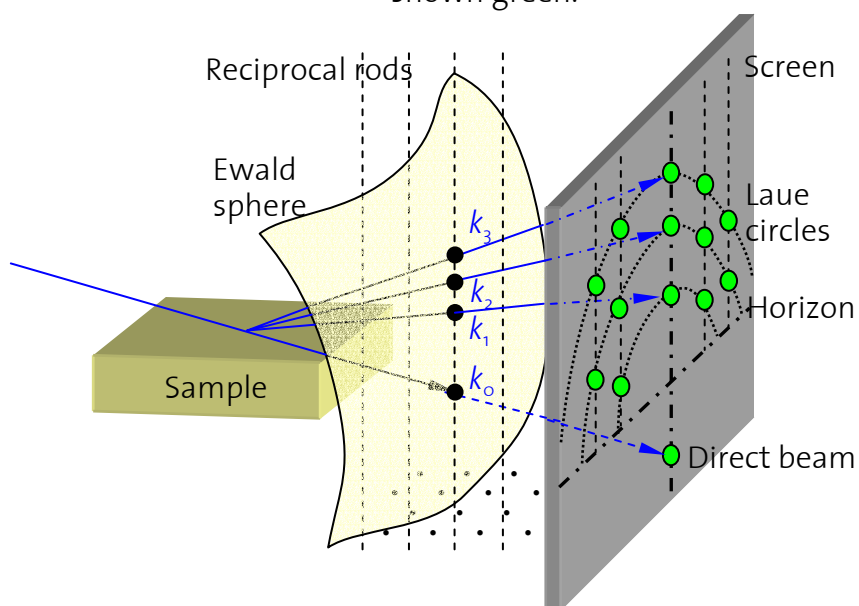

Fig. 3.10. The Ewald construction for an ideal 2-d surface in RHEED geometry.

Deviations from the ideal 2-d surface influence a lot the appearance of the electron diffraction image [52]. Examples of different RHEED patterns depending on the surface morphology are shown in Fig. 3.11. The diffraction spots from the "ideal" surface ((1) in Fig. 3.11) are all located on the Laue circles. For a "real" 2-d surface, the points elongate to streaks, but remain at the same position ((2) in Fig. 3.11). Contrary to 2-d smooth surfaces, the diffraction image of a 3-d rough layer ((3) in Fig. 3.11) results as an intersection of the Ewald sphere with the 3-d reciprocal lattice points. The streaks are situated not on the Laue circles any more. For textured microstructure or different crystal orientations point-like images are replaced by semicircles ((4) in Fig. 3.11).

In this work the RHEED method was used for three main reasons:

- To evaluate substrate quality for the further successful growth.

- To determine a crystal orientation of a film (single/polycrystalline, (100)/(111) orientation), which was especially helpful for the epitaxy on (100) silicon substrates.

- To control surface behaviour during the growth (2-d/3-d) in order to reach the desired results (3-d for quantum dots and CaF_2 nanostructures, 2-d for active laser regions).

As an example of a 3-d growth, a RHEED image of EuSe growth on $Pb_{0.95}Eu_{0.05}Se/BaF_2$ (111) is shown in Fig. 3.12.

3.2.2 Fundamental aspects of IV-VI growth

The beam fluxes in solid-source MBE are produced by thermal evaporation in effusion cells. The evaporation rate from the cell is determined by the cell temperature T_{cell}. For the Knudsen cell the rate Γ_{eff} of molecules emitted from the cell into the environment can be calculated according to the Hertz-Knudsen equation [53]

$$\Gamma_{eff}\left[\frac{Molecules}{sec}\right] = \frac{A_e P_v}{\sqrt{2\pi m k_B T_{cell}}} = 2.639 \times 10^{22} \frac{A_e\left[cm^2\right]P_v\left[mbar\right]}{\sqrt{M\left[\frac{g}{mol}\right]T_{cell}}}, \qquad (3.19)$$

where P_v is the vapour pressure of the material inside the cell, M the molecular mass and A_e the area of the orifice. The vapour pressure is

$$P_v[mbar] = \exp\left(B - \frac{A}{T_{cell}}\right), \qquad (3.20)$$

where A is a constant proportional to the vaporization free enthalpy and B is a material constant.
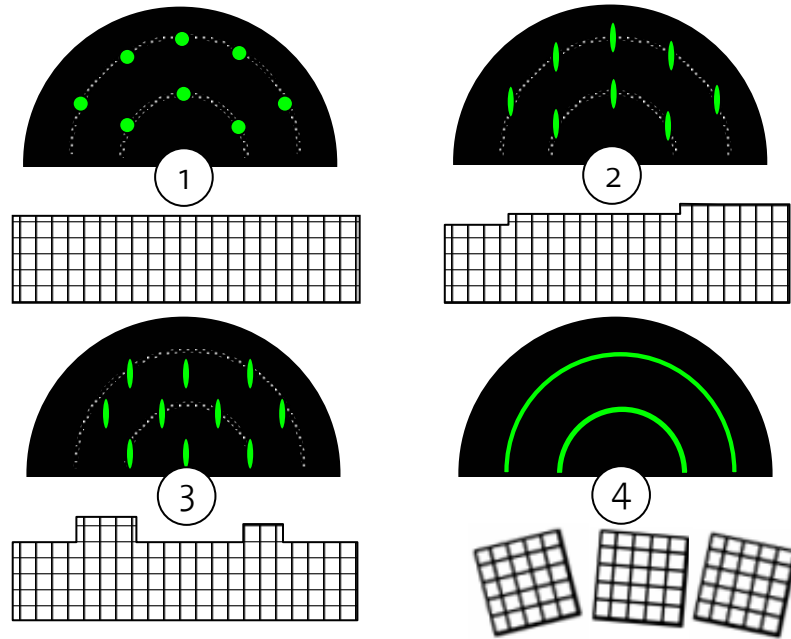
Fig. 3.11. Schematic presentation of RHEED patterns diffracted on four different surfaces. RHEED reflections are shown in green, Laue circles-dashed white.
(1). Ideal smooth surface, (2). 2-d smooth surface, (3). 3-d growth mode, (4). Polycrystalline or textured structure.

Fig. 3.12. EuSe on $Pb_{0.95}Eu_{0.05}Se/BaF_2$ (111) RHEED image ([-110] azimuth).

The flux rate density J_{imp} of molecules impinging onto the substrate at a distance l from the orifice on a symmetry axes is given by:

$$J_{imp}\left[\frac{\text{Molecules}}{\text{cm}^2\text{sec}}\right] = \frac{A_e P_v}{\pi l^2 \sqrt{2\pi m k_B T_{cell}}} = 8.4\times10^{21}\frac{A_e\left[\text{cm}^2\right]P_v\left[\text{mbar}\right]}{l^2\left[\text{cm}^2\right]\sqrt{M\left[\frac{\text{g}}{\text{mol}}\right]}T_{cell}}.$$ (3.21)

In Fig. 3.13 typical evaporation properties of the materials used for MBE in this work are shown. For simplicity, the flux rates are given in monolayers per second (ML/sec), where 1 ML=5.5×10^{14} atoms/cm², which is

the atomic density for the PbTe (111) surface. Typical growth conditions (temperatures T_{cell} and fluxes J_{imp}) are marked with the circles.

The surface diffusion constant D is given by the formula

$$D = v_a d_0^2 \exp\left[\frac{-E_d}{k_B T_W}\right]$$ (3.22)

where v_a stands for the jump frequency, d_o is the atomic distance, T_W the substrate temperature and E_d the surface diffusion energy. For IV-VI material growth, a typical D is of the order of magnitude 10^{-4} cm²/sec, the typical frequency is $v_a=10^{13}$ sec^{-1} [45] and $E_d=0.3$ eV.

The reevaporation rate from the surface into the UHV environment is given by

$$J_{reevap}\left[\frac{\text{Molecules}}{\text{cm}^2\text{sec}}\right] = \alpha_v \frac{P_v}{\sqrt{2\pi m k_B T_W}} = 2.639 \times 10^{22} \frac{P_v[\text{mbar}]}{\sqrt{M\left[\frac{\text{g}}{\text{mol}}\right] T_W}},$$ (3.23)

where α_v is the evaporation coefficient [53]. For PbSe this coefficient is equal to $\alpha_v=0.5$ and for quite a high substrate temperature $T_W=673$ K PbSe reevaporates with the rate $J_{reevap}=0.05$ ML/cm²sec.

The critical size of PbSe nuclei on PbTe (111) is not known exactly. But usually it is reported to be 2÷10 molecules. Moreover, in a recent work of Wiesauer [54] it was found that critical nuclei sizes for PbTe on PbTe (111) are $i=1.15>1$. This means that islands with a number of atoms larger than one are stable.
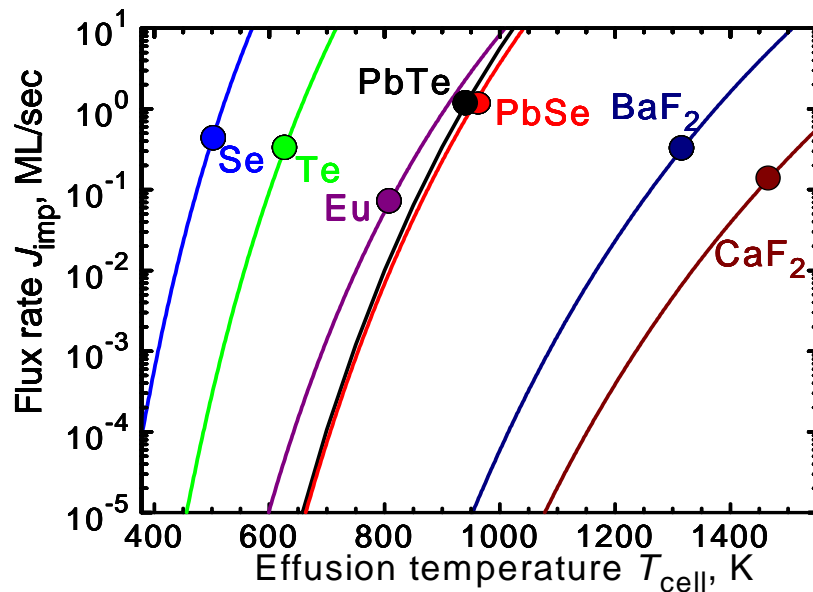

Fig. 3.13. The flux rates of the materials used in this work versus the temperatures of the cells. Typical growth condition regions are shown with the circles.

3.2.3 Substrates

Two materials were used as a substrate for the heteroepitaxy: silicon and barium fluoride. Different surface orientations and for some experiments structured substrates were used (Fig. 3.14). All of them have their advantages and disadvantages. Silicon, as the main material of microelectronics, is commercially available, inexpensive and can be up to 12 inch in size. For IV-VI materials it gives an opportunity to combine read-out electronics and infrared detectors in one monolithic approach [55]. Si is an easy-to-handle material, but its lattice constant a_o is 19% smaller and its thermal expansion coefficient β_{exp} is seven times lower than for IV-VI materials. In spite of these mismatches lead chalcogenide films on Si have reasonable quality [56, 57]. Barium fluoride is more suitable for the lead chalcogenide compounds from the point of view of matching parameters (lattice mismatch is only +4% with PbTe, no thermal expansion mismatch), therefore very high quality IV-VI layers were grown on BaF_2 [e.g. 58]. It is not a problem to grow 25 μm thick layer stacks on BaF_2 [59]. BaF_2 is brittle, relatively expensive and usually available only in small sizes. Other physical properties can be found in Table 2.1.
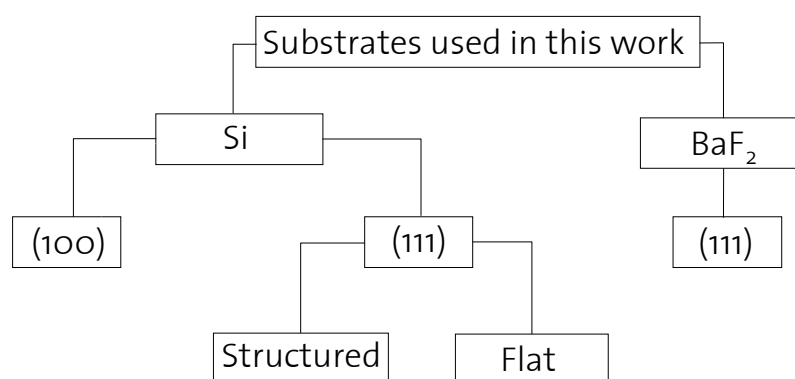
Fig. 3.14. Schematic overview of substrate types used for epitaxy in this work.

3.2.3.1 Silicon substrates

As shown in the schematic overview (Fig. 3.14), silicon wafers of two different orientations were used: (111) and (100). Standard silicon wafers used in the MBE procedure are 3 inch (76.2 mm) in diameter and 280÷370 μm thick. They are produced by the float zone method with n-type doping, 1 kΩ·cm resistivity and prime mirror polishing for the epitaxy side with a roughness less than 1 nm. Single side or double side polished Si substrates were taken for the processing according to the purpose of growth.

To clean the wafers a standard wet chemical process invented by Shiraki [60] is used. More information about this method is found in Appendix A. After the cleaning procedure, ready-to-grow Si (111) substrates exhibit the 7×7 and Si (100) the 2×1 reconstruction (Fig. 3.15).
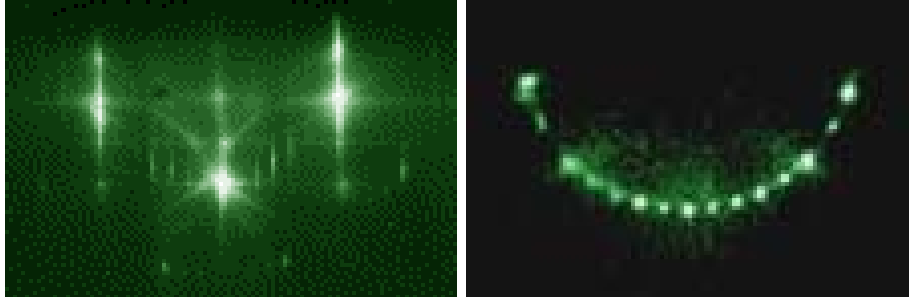
Fig. 3.15. RHEED pattern of Si (111) surface with 7×7 reconstruction (left) and Si(100) 2×1 reconstruction (right) ([10-1] azimuth).

Structured substrates were used for the preparation of edge-emitting lasers. Structures with different shapes (sizes 3÷1000 μm, height 25 μm) were prepared by reactive ion etching (RIE). An etched substrate ready for film deposition is shown in Fig. 3.16.
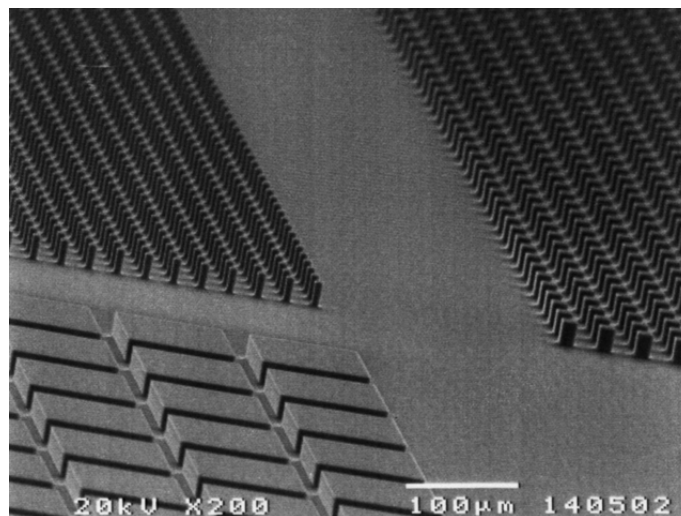
Fig. 3.16. SEM image of a structured Si substrate. Etching depth is 25 μm.

3.2.3.2 BaF$_2$ substrates

Barium fluoride has a (111) cleavage plane. Suitable substrates are obtained just by cleaving a single crystal along this plane. In this work, five 10×8×0.5 mm^3 single crystal pieces clamped in 3 inch metal substrate holder were used for the growth and device manufacturing.

Substrates were cleaved in air shortly before growth. After introduction into the growth chamber, the BaF$_2$ crystals were kept for 20 minutes at the temperature T_w=473 K to evaporate the adsorbed water and for 30 seconds at T_w=823 K to desorb the oxygen [61]. RHEED images show that after these treatments the surface becomes smoother (Fig. 3.17).

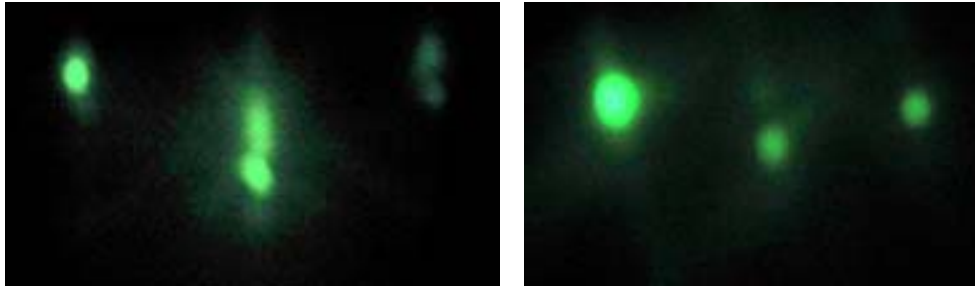Fig. 3.17. RHEED pattern of the BaF$_2$ (111) surface after 20 minutes of T_w=473 K treatment (left) and after the short heating up to T_w=823 K (right) ([-1-12] azimuth).

3.2.4 Growth conditions

3.2.4.1 Growth on Si (111)

In order to diminish the influence of thermal and lattice mismatch between IV-VI layers and the Si substrate a buffer layer of CaF$_2$ [62, 63], CaF$_2$/BaF$_2$ [56, 64, 65] or porous silicon [66, 67] seems to play an important role. In some cases, the buffer can be even omitted [68]. Results of CaF$_2$ epitaxial growth on Si (111) [69] were used by our group in different conditions. The best results for IV-VI epitaxy on Si (111) were achieved with a CaF$_2$ buffer layer with a thickness just below the critical thickness for the formation of misfit dislocations [63]. This thickness is about 2 nm for a growth temperature T_w=923 K [34]. The lattice misfit with Si is rather small (2%) at this temperature.

After the preparation of the silicon surface for the fluoride epitaxy (see Appendix A), CaF$_2$ deposition takes place at T_w=923 K and at a very slow rate Φ=0.1÷0.2 Å/sec, total thickness is 20 Å. The lattice orientation of the CaF$_2$ is *type B*, which means the lattice of the CaF$_2$ is rotated by 180° around the surface normal with respect to the Si substrate [13]. The surface energy γ_A of CaF$_2$ (111) is about 1/3 that γ_S of Si (111) [16], so CaF$_2$ was initially expected to wet the Si surface. But actually, everything depends on the growth conditions: All three basic morphologies (SK, VW, FM) have been observed for the initial growth [16]. In this work the MBE parameters were chosen in such a way that 2 nm CaF$_2$ shows 2-d RHEED patterns after growth (Fig. 3.18).
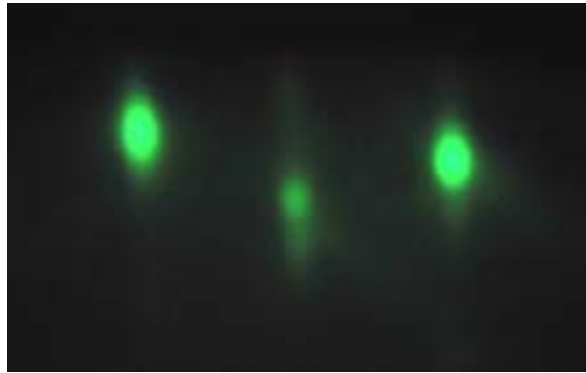
Fig. 3.18. RHEED image of 2 nm thick CaF$_2$ layer deposited on
Si (111) ([-1-12] azimuth).

After CaF$_2$ deposition, the substrate is moved to the second chamber for IV-VI epitaxy. As described in Section 3.2.1, it is transferred through the UHV tunnel and therefore the surface is not exposed to air or another contaminating environment.

The next MBE deposition steps depend on the desired structure design. As an example, a resonant cavity infrared detector (RCD) structure (Fig. 3.19) is described from the point of view of growth conditions (see also Section 8.4).

IV-VI layers grow *type B*, i.e. 180° rotation with respect to the CaF$_2$ lattice. The Pb$_{0.95}$Eu$_{0.05}$Se layer is deposited with a constant flux Φ=1 µm/hour and T_w=673 K using PbSe, Eu and Se solid sources with source temperatures 1033 K, 733 K and 463 K, respectively. It was experimentally found that the ratio between europium and selenium fluxes should be as large as 1:2. The flux ratio PbSe:Eu determines the Eu content. For the present work, the europium content varies in the range of 5%<x<12%. The typical detected fluxes Φ PbSe:Se:Eu are for example 150:32:18 for ≈10% and 295:33:19 for ≈5% of Eu. In the beginning of growth Pb$_{0.95}$Eu$_{0.05}$Se tends to grow 3-d, but

Fig. 3.19. Schematic profile of a resonant cavity infrared detector
(part grown by MBE). The 2 nm CaF$_2$ buffer layer is shown white.

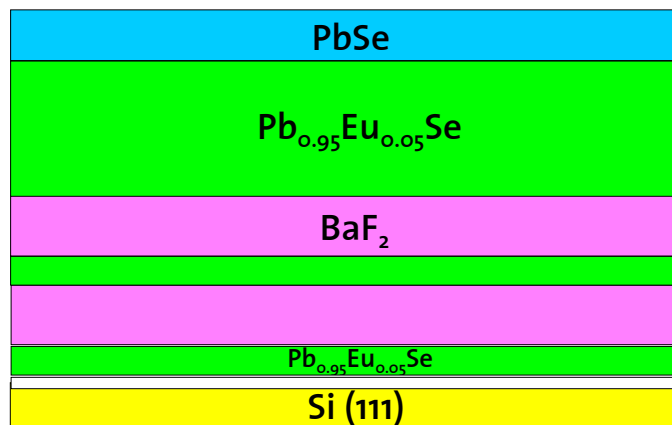after 50 nm it switches to the 2-d growth mode (Fig. 3.20).
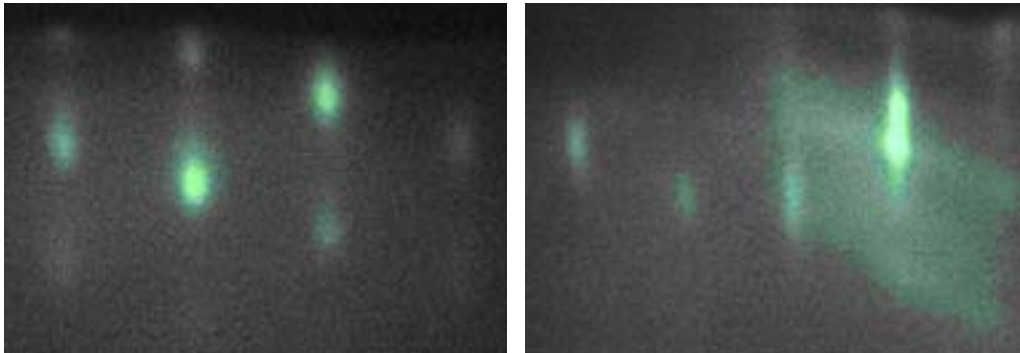
Fig. 3.20. RHEED pattern of $Pb_{0.95}Eu_{0.05}Se/Si$ (111) surface after deposited 5 ML (left) and 50 nm (right) ([1-10] azimuth).

To achieve 2-d growth of BaF_2 on $Pb_{1-x}Eu_xSe$, very low fluxes $\Phi \approx 4 \div 6$ Å/min were used in the beginning. Then the flux was slowly increased during 15 minutes up to the working flux of $70 \div 80$ Å/min at a source temperature of 1533 K. Growth conditions were selected in such a manner that not only growth was 2-d (Fig. 3.21) but also $BaF_2/Pb_{1-x}Eu_xSe$ multistacks appeared as crack-free after epitaxy.
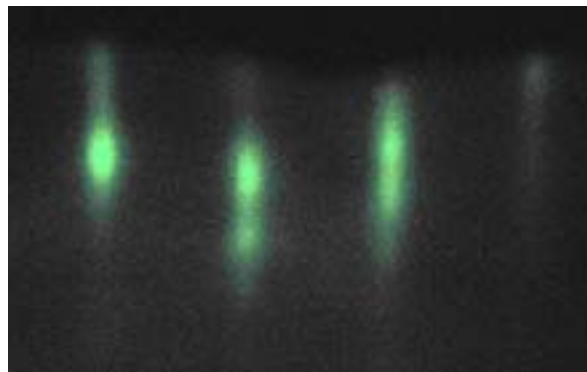
Fig. 3.21. 700 nm thick BaF_2 layer on $Pb_{0.95}Eu_{0.05}Se/Si$ (111) ([1-10] azimuth).

Epitaxy of binary compounds (PbSe, PbTe) is possible not only on "usual" Si (111) substrates but even on Si (111) substrates with active read-out electronics [70]. PbSe thin seed layers can be used as an initial buffer for PbTe (111) growth [71]. Usually $\Phi \approx 1$ μm/hour and $T_w = 573 \div 673$ K are used as the growth conditions. To achieve p-type conductivity of the layers, additional chalcogen fluxes (Se or Te) are supplied. It was possible to obtain smooth IV-VI surfaces with very good electronic properties (low temperature Hall mobilities μ_{sat}(15 K)=350000 cm^2/Vsec at $p=2 \times 10^{17}$ cm^{-3}).

EuSe is always used as a top layer of laser structures or resonant cavity emitters (see Chapter 8). The micro roughness of its surface does not play

any role in device functioning. This top layer can be even polycrystalline [72]. As it was already shown in Fig. 3.12, EuSe layers on IV-VI tend to grow 3-d.

Low-dimensional structures such as two-dimensional PbSe quantum wells embedded in $Pb_{1-x}Eu_xSe$ cladding layers are grown according to the standard procedure described above just by closing and opening the shutter of the europium source. Zero-dimensional structures (PbSe quantum dots on PbTe (111)) are grown at somewhat higher substrate temperature for PbSe deposition (T_w=713 K) at low flux ($\Phi\approx0.2$ Å/sec) after the 5÷7 μm thick PbTe layer growth at T_w=573 K and $\Phi\approx2.5$ Å/sec.

3.2.4.2 Growth on Si (100)

Some laser structures used for emission in the 3÷5 μm wavelength range were grown on Si (100) substrates (see also Chapter 8). It is important to note that (100) is the natural growth mode for IV-VI materials, at least as long as another orientation is not dictated by a strong interface to the substrate [13]. Growth conditions for the (100) growth were taken according to previous results [73, 74, 75]. To grow the structure shown in Fig. 3.22, 10 nm CaF_2 and 200 nm BaF_2 layers were deposited at T_w=723 K, and as can be seen in the RHEED images, that growth is 3-d (Fig. 3.23). Some rapid thermal annealings at T_w=923 K for several seconds help
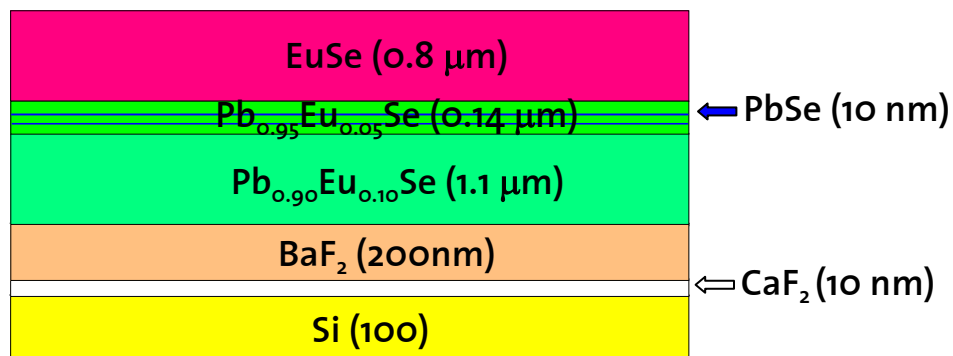
Fig. 3.22. Schematic profile of a laser structure with two quantum wells grown on Si (100) with CaF_2/BaF_2 buffer layers.

to smooth the surface of fluorides. The best results were received by applying low evaporation fluxes such as $\Phi(CaF_2)\approx0.2$ Å/sec and $\Phi(BaF_2)\approx0.5$ Å/sec. After UHV transfer of the silicon wafer covered with the buffer layer to the IV-VI chamber, the same procedure described above is used for the chalcogenide deposition. It is possible to achieve a two dimensional growth of IV-VI materials, as shown in Fig. 3.24. Because of the strain, cooling down of the structure from the deposition temperature to room

temperature should be very slow (ΔT_w=5 min^{-1}) to avoid peeling off of the layers.
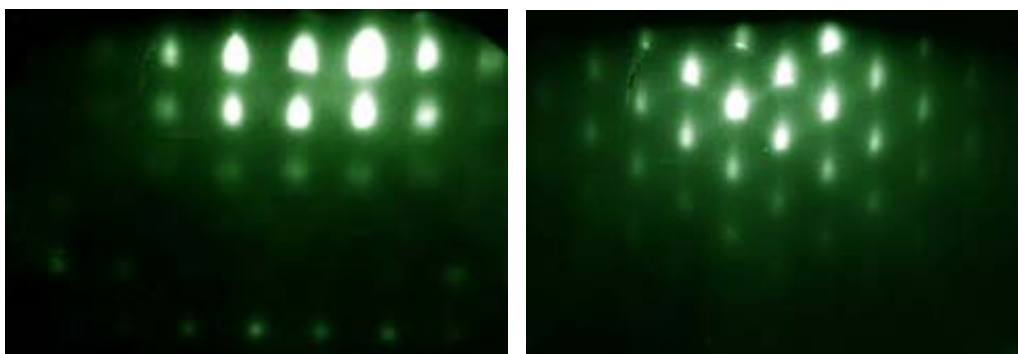
Fig. 3.23. RHEED image of BaF$_2$ layer on CaF$_2$/Si (100) with the [001] azimuth (left) and [011] (right).

Fig. 3.24. Smooth surface RHEED patterns of Pb$_{0.9}$Eu$_{0.1}$Se/BaF$_2$/CaF$_2$/Si (100) ([011] azimuth).

Si (100) substrates were used to grow nanosized self-assembled layers of CaF$_2$/BaF$_2$ structures. Long and narrow (5 μm × 10 nm) stripes of fluorides can be grown on silicon under the certain conditions. The results obtained are discussed in Chapter 7.

3.2.4.3 Growth on BaF$_2$ (111)

There is no big difference between the IV-VI epitaxy parameters (fluxes, substrate temperatures) on Si (111)/(100) and BaF$_2$ (111). As depicted in Fig. 3.25, no fluoride buffer layer is needed as compared to growth on silicon. Since the (111) free surface energy of the lead salts is much larger than that of BaF$_2$, epitaxial growth always starts in 3-d Volmer-Weber growth mode. As indicated by RHEED growth studies, coalescence usually starts at layer thickness below 100 nm. However, a completely streaked RHEED pattern indicating formation of a smooth 2-d surface is not observed below 500 nm thickness [32].
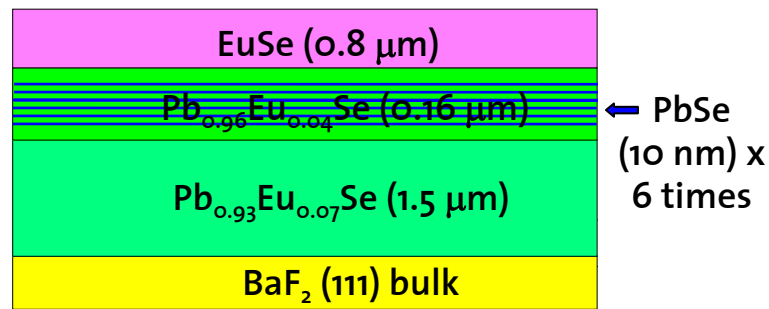
Fig. 3.25. Schematic profile of a laser structure grown on a
BaF$_2$ (111) substrate.

In contrast to MBE of pure lead salts, complete layer coalescence occurs as early as at 50 nm layer thickness for ternary Pb$_{1-x}$Eu$_x$Te/ Pb$_{1-x}$Eu$_x$Se on BaF$_2$ (111). Some typical RHEED images of Pb$_{1-x}$Eu$_x$Se growth on BaF$_2$ are shown in Fig. 3.26. Our experiments thus sustain the prior finding, that IV-VI materials tend to grow 3-d in the beginning and the growth transforms to 2-d after a certain thickness is reached. This thickness (50÷100 nm) is smaller than described by Springholz *et al.* [32].
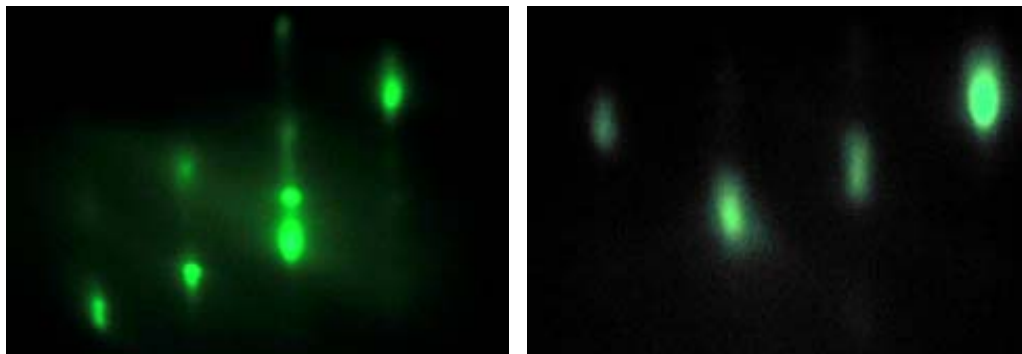
Fig. 3.26. RHEED images of Pb$_{0.93}$Eu$_{0.07}$Se/BaF$_2$ (111) surface in the beginning of growth (left) and after 200 nm (right) ([1-10] azimuth).

3.3 Hall measurements

Hall measurements are a standard method for epitaxial semiconductor layers. Some general issues as well as some specific experiments based on the Hall principle are described in this section.

3.3.1 The Hall Effect and the Lorentz Force

When a magnetic field is applied to a conductor carrying a current in a direction at right angles to the current, an electronic field appears across the conductor in a direction perpendicular to the current and to the magnetic field. This effect was discovered by E. H. Hall in 1879 in thin metallic foils and was named as the Hall effect. Now it is a very important method for the investigation of electrical properties of semiconductors.

Fig. 3.27 shows a magnetic field $\vec{B}$ applied along the z-axis and an electric field $\vec{E}$ applied along the x-axes. When holes (consider a p-type semiconductor) move in a conducting layer that is introduced in a magnetic field, a Lorentz force $\vec{F}_L$ appears:

$$\vec{F}_L = q(\vec{E} + \vec{v} \times \vec{B}),$$

(3.24)

where q is the charge ($q=|e|$, e is elementary charge) and $\vec{v}$ the velocity. If electrodes are placed across the transverse dimension of the layer, a voltage V_H, called the Hall voltage, will appear.
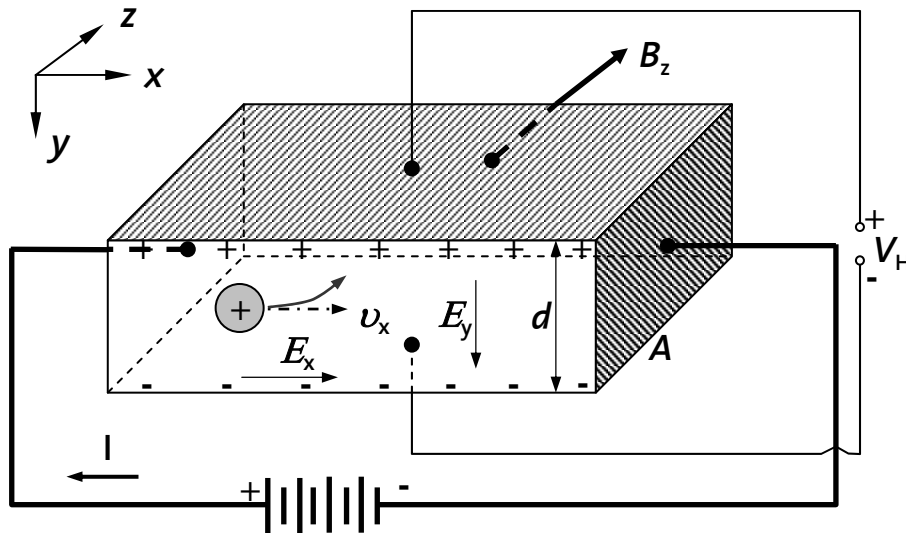
Fig. 3.27. Hall effect measurement setup.

For an ideal plate geometry, the Hall voltage can be written

$$V_H = \frac{IB}{qpd} = R_H \frac{IB}{d},$$

(3.25)

where I is the current, B the magnetic field component transverse to the current, p is charge carrier density, d is the thickness of the layer, and

$$R_H \equiv \frac{1}{qp}$$

(3.26)

is the Hall coefficient.

A similar result can be obtained for an n-type semiconductor, except that the Hall coefficient is negative:

$$R_{\text{H}} \equiv -\frac{1}{qn}.$$ (3.27)

A measurement of the Hall voltage for a known current and magnetic field yields

$$p = \frac{1}{qR_{\text{H}}} = \frac{IB_z d}{qV_{\text{H}} A},$$ (3.28)

where A is the cross-section of the sample. All the quantities in the right-hand side of the equation can be measured. The majority carrier concentration and carrier type can be obtained directly from the Hall measurement [76].

3.3.2 Van der Pauw method for the Hall measurements

In order to determine both the mobility μ and the sheet density $p_s=p/d$, a combination of a resistivity measurement and a Hall measurement is needed. The van der Pauw technique is widely used in semiconductor analysis for this purpose [77]. The sample of thickness d may have any shape, but:

• The contacts are at the circumference of the sample

• The contacts are sufficiently small

• The sample is homogeneous in thickness and composition

• The surface of the sample is singly connected, i.e., the sample does not have isolated holes.

The objective of the resistivity measurement is to determine the sheet resistance R_S. There are two characteristic resistances R_1 and R_2, associated with the contacts shown in Fig. 3.28. R_1 and R_2 are related to the sheet resistance R_S through the van der Pauw equation

$$\exp\left(-\frac{\pi R_1}{R_s}\right) + \exp\left(-\frac{\pi R_2}{R_s}\right) = 1; \ R_1 = \frac{V_{\text{DC}}}{I_{\text{AB}}}, \ R_2 = \frac{V_{\text{BC}}}{I_{\text{AD}}}, R_s = \frac{\rho}{d},$$ (3.29)

where ρ is the electrical resistivity. This equation can be solved numerically for R_S.

The objective of the Hall measurement in the van der Pauw technique is to determine the sheet carrier density p_s by measuring the Hall voltage V_{H}. To measure the Hall voltage V_{H}, a current I is forced through the opposing
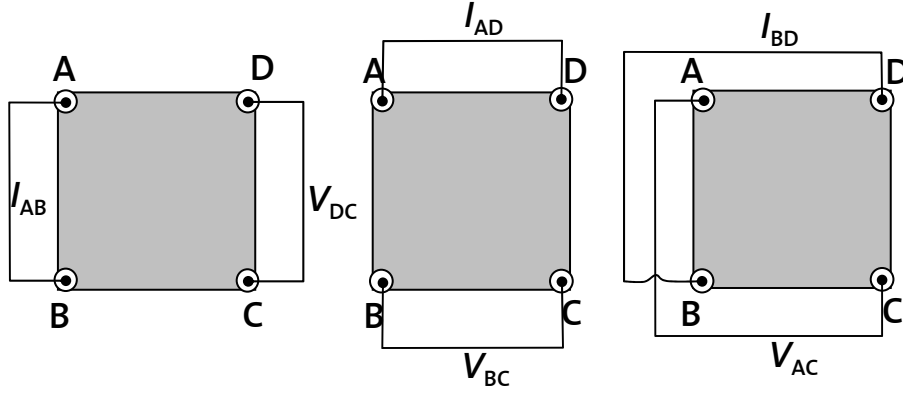
Fig. 3.28. A schematic square van der Pauw configuration.

pair of contacts B and D and the Hall voltage V_H (=V_{AC}) is measured across the remaining pair of contacts A and C with and without the magnetic field B (in Fig. 3.28 magnetic field is perpendicular to the page plane). Once the Hall voltage V_H is established, the resistance R_3 can be calculated via

$$\Delta R_3 = \frac{\Delta V_{AC}}{I_{BD}} = \frac{R_H B}{d} \ , \tag{3.30}$$

where $\Delta V_{AC}=V_{AC}$ (measured voltage between A and C with magnetic field)- V_{AC} (without magnetic field).

For the carrier density it can be written

$$p = \frac{1}{R_H q} \ , \tag{3.31}$$

and in the case of highly doped semiconductors

$$\rho = \frac{1}{qp\mu_H} \ . \tag{3.32}$$

The Hall mobility μ_H can be found as

$$\mu_H = \frac{1}{qp\rho} = \frac{R_H}{\rho} \ . \tag{3.33}$$

R_H and ρ can be found from the four resistance measurements

$$R_H = \frac{d\Delta R_3}{B} \ , \tag{3.34}$$

$$\rho = \frac{\pi d}{\ln 2} \frac{R_1 + R_2}{2} f_{vdP} \ , \tag{3.35}$$

where f_{vdP} is a correction factor which depends on contact symmetry. For a square sample f_{vdP}=1.

3.3.3 Investigation of a layered samples using the Petritz model

Hall mobility measurements are a standard tool for investigation of electronic properties of semiconductor thin films. But it is in most cases impossible to investigate single layers in a sandwich structure containing many layers. Unfortunately, there are only few non-destructive methods for this case (for example, acoustic microscopy or X-ray analysis). If one wants to know the electrical properties of an internal layer of such a structure, one must rather use a destructive layer-by-layer measurement method.

In Fig. 3.29 a structure with 3 different layers is presented: An upper (or surface) layer s with the electrical parameters σ_s (conductivity), μ_s (mobility), n_s (concentration), a bottom layer b with σ_b, μ_b, n_b and a bulk, which has dielectric properties (σ_s, $\sigma_b \gg \sigma_{bulk}$). One of the possibilities to determine the electric characteristics of the surface layer s is to apply the Petritz model for the Hall measurements [78].

Fig. 3.29. Schematic cross-section of the structure with 3 layers.

In Fig. 3.30 one of the possible measurement techniques is shown: The magnetic field B is perpendicular to the broad area of the sample, Hall voltages of surface V_s and bottom V_b layers are acting in parallel, and bias currents I_b and I_s are in parallel. The equivalent circuit is shown in Fig. 3.31.

The individual Hall voltages and currents are

$$V_b = \frac{I_b R_{Hb} H}{d_b}, \; V_s = \frac{I_s R_{Hs} H}{d_s}, \tag{3.36}$$

$$I_b = \frac{\sigma_b d_b I}{\sigma_b d_b + \sigma_s d_s}, \; I_s = \frac{\sigma_s d_s I}{\sigma_b d_b + \sigma_s d_s}, \tag{3.37}$$

$$I = I_b + I_s, \; d = d_s + d_b, \tag{3.38}$$

where the subscripts b and s refer to the bottom and surface layers, respectively, σ is the conductivity, R_H Hall coefficient, d layer thickness, and H the magnetic field. The open-circuit Hall voltage is
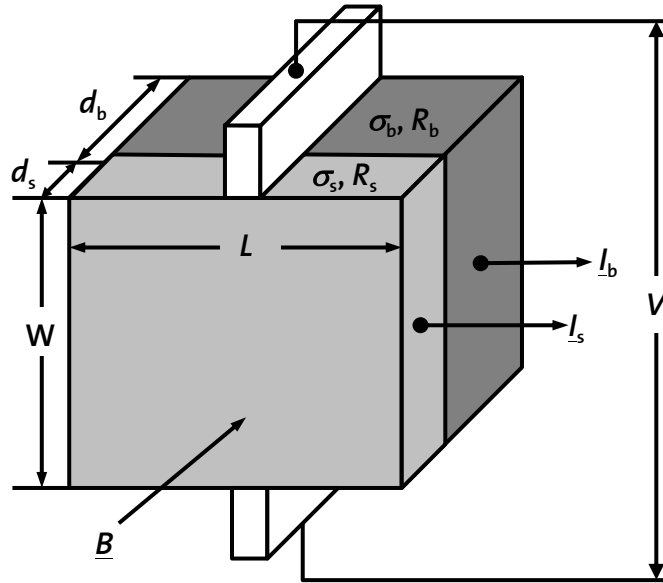
Fig. 3.30. Possible configuration for Hall measurements. Currents in parallel and Hall voltages in parallel.
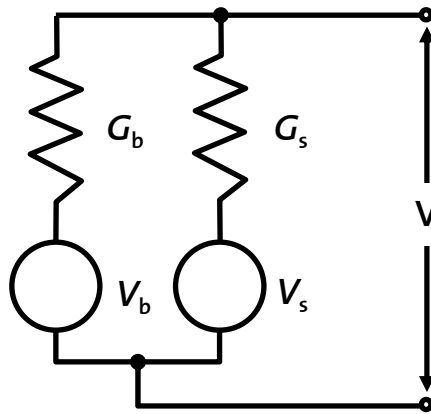
Fig. 3.31. Equivalent electric circuit to Fig. 3.30.

$$V = \frac{IHR_H}{d} = \frac{V_b G_b + V_s G_s}{G_b + G_s} \quad , \tag{3.39}$$

where the conductances G are given as a function of length L and width W of a sample

$$G_b = \frac{\sigma_b d_b L}{W}, \ G_s = \frac{\sigma_s d_s L}{W}. \tag{3.40}$$

Solving (3.39) with the help of (3.36), (3.37) and (3.40), one finds for the Hall coefficient and conductivity of the total sample,

$$R_H = \frac{d(R_{Hb}\sigma_b^2 d_b + R_{Hs}\sigma_s^2 d_s)}{\sigma_b d_b + \sigma_s d_s}, \tag{3.41}$$

$$\sigma = \frac{\sigma_b d_b + \sigma_s d_s}{d}. \tag{3.42}$$

From these equations, an expression for the Hall mobilities μ and carrier concentration n is easy to get,

$$\mu = \frac{\mu_s^2 n_s d_s - \mu_b^2 n_b d_b}{\mu_s n_s d_s + \mu_b n_b d_b},$$

(3.43)

$$n = \frac{(\mu_s n_s d_s + \mu_b n_b d_b)^2}{d(\mu_s^2 n_s d_s - \mu_b^2 n_b d_b)}.$$

(3.44)

It is important to note that for the Petritz method $\mu B \ll 1$ is assumed.

3.4 Infrared Spectroscopy

Infrared spectroscopy is a powerful method to characterize structures based on IV-VI narrow band materials. The transmission and reflection measurements made in this work were made by Fourier Transform Infrared Spectroscopy (FTIR) and grating spectroscopy for the visible wavelength range. The wavelength range of the instruments used in this work was $0.45 \div 25$ µm:

- Reflection properties of the laser structures are important for the optical pumping procedure. Different semiconductor lasers with the emission wavelengths (λ_{pump}) $0.87 \div 1.55$ µm were used as an excitation source. It is significant to know the reflection of the incoming beam from the material surfaces in this range. These measurements are done in order to achieve the best device design with the minimum reflectivity at a given λ_{pump}.

- For the structures grown on silicon substrates the transmission measurements are limited by the cut-off wavelength ($\lambda_{cut-off}$) of silicon, $\lambda_{cut-off}$ (300 K) ≈ 1.1 µm.

- For the BaF$_2$ substrates $\lambda_{cut-off}$ is in the ultraviolet range ($\lambda_{cut-off}$(300 K)$\approx$ 0.1 µm). But it is not possible to reach these numbers anyway: The lowest cut-off value of the materials used in the experiments is for EuSe with $\lambda_{cut-off}$ (300 K)$\approx$0.69 µm.

- Usually quite a narrow wavelength window ranging from 2 to 6 µm only is of importance for the experiments, most of the devices described in this work were designed for this range.

3.4.1 Fourier transform infrared spectroscopy

The concept of a Fourier transform spectrometer is based on Michelson's design of an interferometer in which a beam of monochromatic light is

split into two approximately equal parts which follow different paths before being brought together again [79]. In Michelson's interferometer the beam of the source (1) in Fig. 3.32 is divided by the beam splitter (2) to the fixed mirror (3) and the moving mirror (4), at distances L and $L+\delta/2$, respectively (where δ is the difference in path length between the two arms). The recombined beam is focused on the detector (5), which measures the intensity I as a function of the mirror displacement $\delta/2$.

If δ is an integer multiple of the wavelengths λ ($\delta=\kappa\lambda$, $\kappa=1, 2, 3, ...$), constructive interference is observed and the signal component of this wavelength at the detector is at maximum; for $\delta=(2\kappa+1)\lambda/2$ the beams interfere destructively and the signal component is minimal. The instrument measures $I(\delta)$, the intensity of the registered signal is a function of the optical path difference. In other words, the interferometer converts the frequency dependence of the spectrum $B(\nu)$ into a spatial dependence of the detected intensity $I(\delta)$, which is represented by a sum of $\sin^2$ functions for all wavelengths. From this information, it is possible to reconstruct mathematically the source $B(\nu)$ [79, 80].

The electric field at the beam splitter can be described as

$$E(x,\nu)d\nu = E_0(\nu)e^{i(2\pi x\nu-\omega t)}d\nu, \tag{3.45}$$

where $\nu=1/\lambda$ is the wavenumber of the radiation and x is the coordinate of the axis parallel to the mirror movement. Each of the two beams which
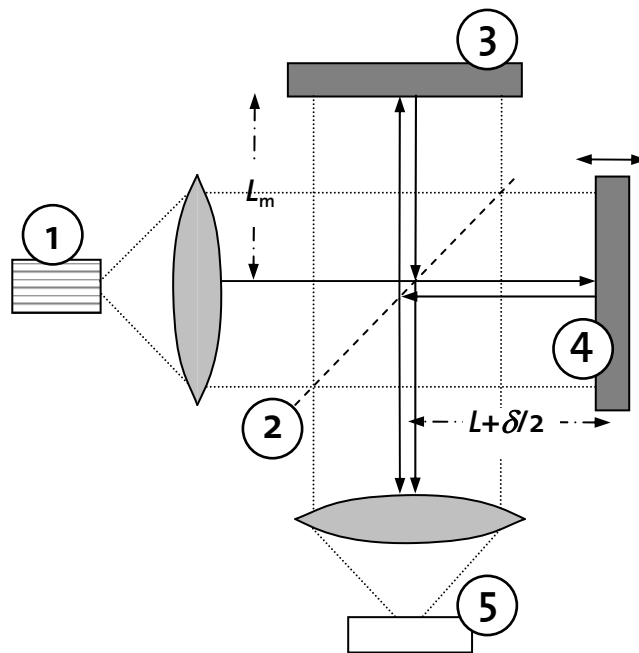

Fig. 3.32. Basic outline of a Michelson interferometer.
(1). Source of emission, (2). Beam splitter, (3). Fixed mirror, (4). Moving mirror, (5). Detector.

reach the detector has to undergo one reflection and one transmission at the beam splitter. And therefore one can consider their amplitudes to be equal. If one light beam travels a distance $2L$ to the fixed and the other a distance $2L+\delta$ to the moving mirrors, then the reconstructed field E_R is

$$E_R(\delta,\nu)d\nu = \left|r^*\right|\left|t^*\right|E_0(\nu)(e^{i(4\pi\nu L-\omega t)} + e^{i(2\pi\nu(2L+\delta)-\omega t)})d\nu , \tag{3.46}$$

where r^* and t^* are the complex reflection and transmission coefficients of the beam splitter. For a given spectral range, the intensity is proportional to the complex square of the electric field $E_R E_R^*$. The equation (3.46) then gives

$$I(\delta,\nu)d\nu \propto E_0^2(\nu)(1+\cos(2\pi\nu\delta))d\nu , \tag{3.47}$$

and the total intensity from all wavenumbers at a particular path difference δ is

$$I(\delta) \propto \int_0^{+\infty} E_0^2(\nu)(1+\cos(2\pi\nu\delta))d\nu . \tag{3.48}$$

Equation (3.48) is usually presented in a slightly different form:

$$(I(\delta)-\frac{1}{2}I(0)) \propto \int_0^{+\infty} E_0^2(\nu)\cos(2\pi\nu\delta)d\nu , \tag{3.49}$$

often referred to as the interferogram. Finally, from equation (3.49) and using the fact that $B(\nu)\approx E_0^2(\nu)$ it is possible to write the inverse Fourier transformation

$$B(\nu) \propto \int_0^{+\infty}(I(\delta)-\frac{1}{2}I(0))\cos(2\pi\nu\delta)d\delta . \tag{3.50}$$

Thus, $I(\delta)$ can be measured with the interferometer and then $B(\nu)$ can be obtained from the Fourier transform. As an example, the transmission spectrum of air as a function of δ and ν is shown in Fig. 3.33.

3.4.2 Matrix method

The matrix method is a good method to understand the transmission and reflection mechanisms in stacked thin films. This method is universal and can be applied for any wavelength from ultraviolet to far infrared. In Fig. 3.34 a thin layer with thickness d and refractivity index n_1 is depicted [81]. Waves with wavelength λ and the incidence angle θ in the direction of incidence are marked with the symbol "+" (positive-going) and wave in the opposite direction by "-" (negative-going). There is no negative-going wave in the substrate, which is taken to be of infinite extent, and the waves in the film can be summed into one resultant positive-going wave
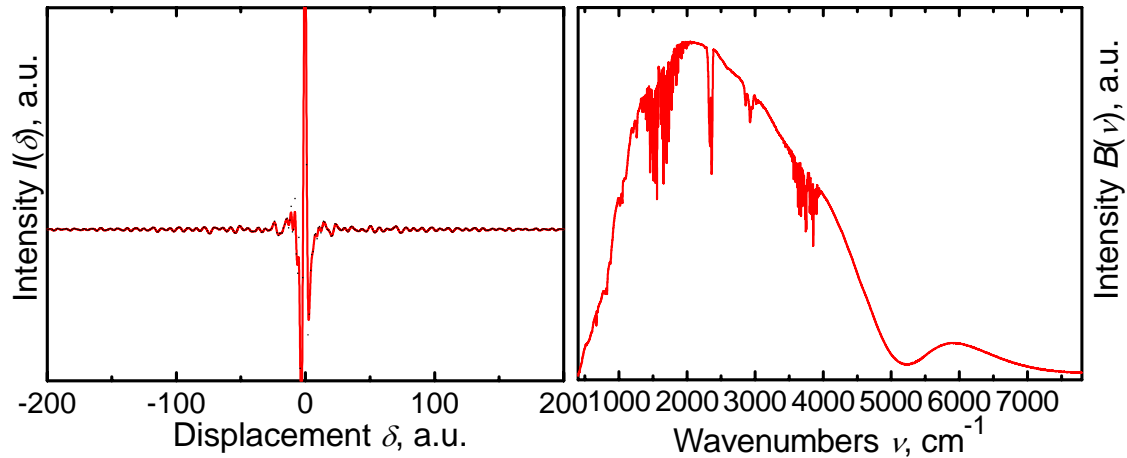
Fig. 3.33. Transmission spectrum of Zurich air recorded by the interferometer (left, only a part of the measurement around $\delta{=}0$ is shown) and its Fourier transform (right, full range).

and one resultant negative-going wave. At the interface thin film/ substrate b the tangential components of $\vec{E}$ and $\vec{H}$ are

$$E_{\mathrm{b}} = E_{1\mathrm{b}}^{+} + E_{1\mathrm{b}}^{-},\tag{3.51}$$

$$H_{\mathrm{b}} = \eta_1 E_{1\mathrm{b}}^{+} - \eta_1 E_{1\mathrm{b}}^{-},\tag{3.52}$$

where η is optical admittance $\eta = \dfrac{H_{\mathrm{II}}}{E_{\mathrm{II}}}$ and E_{b} and H_{b} represent the resultants. Hence

$$E_{1\mathrm{b}}^{+} = \frac{1}{2}(\frac{H_{\mathrm{b}}}{\eta_1} + E_{\mathrm{b}})\tag{3.53}$$

$$E_{1\mathrm{b}}^{+} = \frac{1}{2}(\frac{H_{\mathrm{b}}}{\eta_1} + E_{\mathrm{b}})\tag{3.54}$$

$$H_{1\mathrm{b}}^{+} = \eta_1 E_{1\mathrm{b}}^{+} = \frac{1}{2}(H_{\mathrm{b}} + \eta_1 E_{\mathrm{b}})\tag{3.55}$$
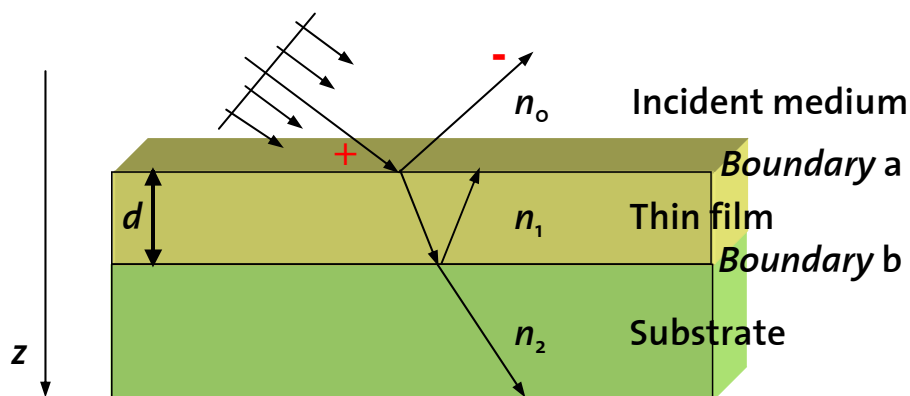
Fig. 3.34. Plane wave incident on a thin film.

$$H_{1b}^- = -\eta_1 E_{1b}^- = \frac{1}{2}(H_b - \eta_1 E_b).$$

(3.56)

The fields at the other interface (boundary a) between incidence medium and thin film can be determined by altering the phase factors of the waves to allow for a shift in the z coordinate from 0 to −d. The phase factor of the positive-going wave will be multiplied by $e^{i\delta}$ where $\delta = 2\pi n_1 d\cos\theta_1/\lambda$, while the negative-going phase factor will be multiplied by $e^{-i\delta}$. The values of $\vec{H}$ and $\vec{E}$ at the interface a are now

$$E_{1a}^+ = E_{1b}^+ e^{i\delta} = \frac{1}{2}(\frac{H_b}{\eta_1} + E_b)e^{i\delta}$$

(3.57)

$$E_{1a}^- = E_{1b}^+ e^{-i\delta} = \frac{1}{2}(-\frac{H_b}{\eta_1} + E_b)e^{-i\delta}$$

(3.58)

$$H_{1a}^+ = H_{1b}^+ e^{i\delta} = \eta_1 E_{1b}^+ e^{i\delta} = \frac{1}{2}(H_b + \eta_1 E_b)e^{i\delta}$$

(3.59)

$$H_{1a}^- = H_{1b}^- e^{-i\delta} = -\eta_1 E_{1b}^- e^{-i\delta} = \frac{1}{2}(H_b - \eta_1 E_b)e^{-i\delta}.$$

(3.60)

After these the sums of positive and negative components are

$$E_a = E_{1a}^+ + E_{1a}^- = E_b\left(\frac{e^{i\delta} + e^{-i\delta}}{2}\right) + H_b\left(\frac{e^{i\delta} - e^{i\delta}}{2}\right) = E_b\cos\delta + H_b\frac{i\sin\delta}{\eta_1}$$

(3.61)

$$H_a = H_{1a}^+ + H_{1a}^- = E_b\eta_1\left(\frac{e^{i\delta} - e^{-i\delta}}{2}\right) + H_b\left(\frac{e^{i\delta} + e^{i\delta}}{2}\right) = E_b i\eta_1\sin\delta + H_b\cos\delta.$$

(3.62)

This can be written in matrix notation as

$$\begin{bmatrix} E_a \\ H_a \end{bmatrix} = \begin{bmatrix} \cos\delta & i\sin\delta\eta_1^{-1} \\ i\eta_1\sin\delta & \cos\delta \end{bmatrix}\begin{bmatrix} E_b \\ H_b \end{bmatrix}.$$

(3.63)

This relationship connects the tangential components of $\vec{E}$ and $\vec{H}$ which are transmitted. The 2×2 matrix is known as the characteristic matrix of the thin film.

If one defines the input optical admittance as $Y = H_a/E_a$ then the reflectance of a interface between an incident medium of admittance η_0 and a medium of admittance Y is

$$\rho = \frac{\eta_0 - Y}{\eta_0 + Y} \text{ or } R = \left(\frac{\eta_0 - Y}{\eta_0 + Y}\right)\left(\frac{\eta_0 - Y}{\eta_0 + Y}\right)^*.$$

(3.64)

Then the matrix can be written

$$E_a\begin{bmatrix} 1 \\ Y \end{bmatrix} = \begin{bmatrix} \cos\delta & i\sin\delta\eta_1^{-1} \\ i\eta_1\sin\delta & \cos\delta \end{bmatrix}\begin{bmatrix} 1 \\ \eta_2 \end{bmatrix}E_b.$$

(3.65)

Normally, *Y* is the parameter which is of interest and the matrix product gives sufficient information for calculating it:

$$\begin{bmatrix} B \\ C \end{bmatrix} = \begin{bmatrix} \cos\delta & i\sin\delta\,\eta_1^{-1} \\ i\eta_1\sin\delta & \cos\delta \end{bmatrix} \begin{bmatrix} 1 \\ \eta_2 \end{bmatrix}, \tag{3.66}$$

where $\begin{bmatrix} B \\ C \end{bmatrix}$ is the characteristic matrix of the assembly. Clearly, $Y = C/B$.

If the structure consists of *m* thin layers, then for the whole structure the equation is

$$\begin{bmatrix} B \\ C \end{bmatrix} = \prod_{j=1}^{m} \begin{bmatrix} \cos\delta_j & i\sin\delta_j\big/\eta_j \\ i\eta_j\sin\delta_j & \cos\delta_j \end{bmatrix} \begin{bmatrix} 1 \\ \eta_{\text{sub}} \end{bmatrix}. \tag{3.67}$$

From the matrix elements *B* and *C* it is possible to extract the reflection *R* and transmission *T*:

$$Y = \frac{C}{B} \longrightarrow R(\lambda) = \left|\frac{\eta_0 - Y}{\eta_0 + Y}\right|^2, \ T(\lambda) = \frac{4\eta_0 Y}{(\eta_0 + Y)^2}. \tag{3.68}$$

These formulas do not depend on the polarization of the incoming wave for the normal incidence ($\theta = 0$ and $\delta_i = 2\pi n_i d/\lambda$).

In this work the matrix method is used to calculate the parameters of the wavelength transformers, resonant cavity diodes and laser structures (see Chapter 8) as well as to fit the results of FTIR-spectra for Eu content determination (see Chapter 4).

3.4.3 Experimental set-up

Fig. 3.35 illustrates the optical path in the Perkin Elmer 16PC spectrometer used in most experiments of the present work. The infrared beam is emitted at the source coil (3). A fixed toroidal mirror (9) collimates the beam from the source and directs it to the interferometer (4-7, 10-11). The beam from a helium neon (He-Ne) 633 nm laser (1) follows the IR beam through the interferometer. This beam tracks the position of the moving mirror (5) (optical path difference) and forms reference wavelength for adjustments. To put the beam to a sample for measurements (14) the toroidal mirror (11) is used. From the sample area the beam travels through two toroidal mirrors to the detector (13).

A total spectral range covered is $100 \div 7800$ cm^{-1} ($1.28 \div 100$ μm), the resolution is <2 cm^{-1}. The spectrometer can operate in ratio or single beam mode. It is possible to carry out the experiments at room temperature in air or in gases like N_2. The Fourier transform of interferograms is performed using a Fast Fourier Transform algorithm.

This spectrometer is mainly used for the transmission measurements. Reflection measurements can be realized using a special additional mirror system too. The disadvantage of reflection measurements is that the incidence angle of the beam can not be smaller than 15°.
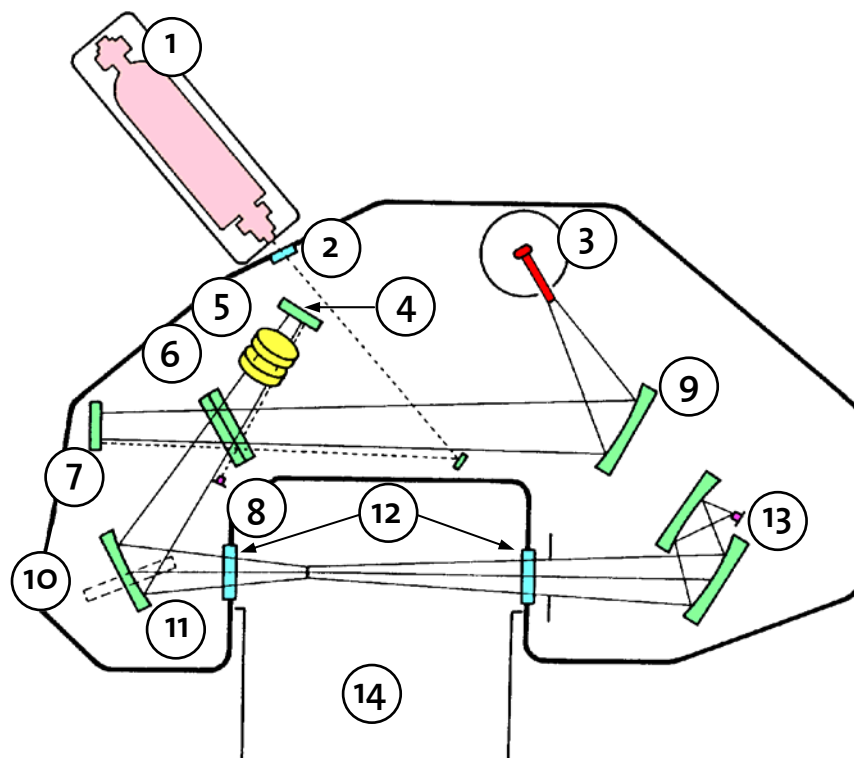
Fig. 3.35. Perkin Elmer 16PC FTIR spectrometer optical system.
(1). He-Ne Laser, (2). Glass window, (3). IR source, (4). Interferometer flat mirror,
(5). Interferometer scan mirrors, (6). Beam splitter, (7). Interferometer flat mirror,
(8). Laser fringe detector, (9). Fixed toroidal mirror, (10). Adjustable flat mirror,
(11). Adjustable toroidal mirror, (12). KBr windows, (13). IR detector system with
fixed toroidal mirrors, (14). Sample area.

Fig. 3.36. Reflection measurement configuration.
(1). Optical source, (2). Waveguide of the incidence beam, (3).
Surface for measurement, (4). Waveguide of the reflected beam,
(5). Detector.

3.4.4 Reflection measurements

Additional reflection measurements were made with a Carl Zeiss MCS 500 spectrometer for the wavelengths 450÷1100 nm. The advantage of this instrument is the possibility to easily access a sample surface. This spectrometer system has different broad band sources (for example, Xe lamp); gratings cover a wavelength range from ultraviolet to near infrared. In Fig. 3.36 the main parts of the Carl Zeiss equipment are shown. The beam from the source (1) is illuminating the sample surface (3) through a waveguide (2). The second waveguide (4) leads the reflected beam from the surface to a detector (5). The instrument is calibrated with Al mirror with known reflectivities.

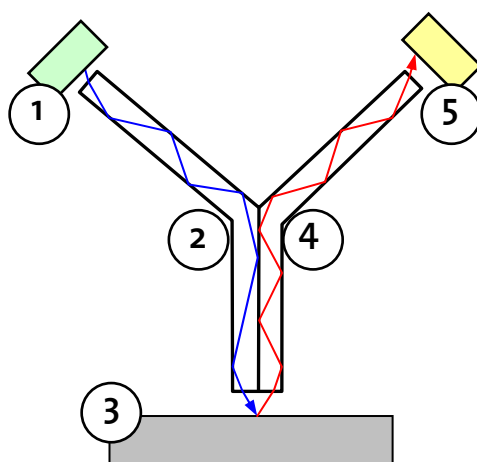## 3.5 X-ray measurements

X-ray measurements were performed in this work in order to determine europium concentrations (see Chapter 4) and to analyse the quality of the grown IV-VI layers (see Chapter 5). In this section some basics of X-ray analyses are shown.

3.5.1 X-ray measurement geometry

The three basic components of an X-ray diffractometer are the X-ray source, specimen and X-ray detector. In the bisecting mode the angle between the surface of the specimen and the incident beam is θ. The angle between the incident beam direction and the detector is 2θ (Fig. 3.37). For
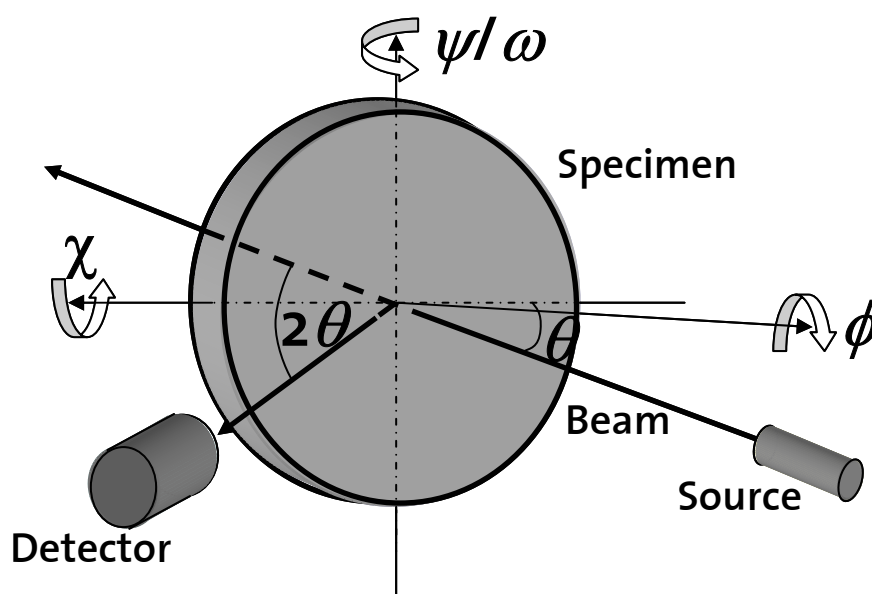

Fig. 3.37. Geometry of an X-ray diffractometer.

this reason the X-ray diffraction patterns produced with this geometry are often known as θ-2θ scans [e.g. 82]. In the θ-2θ geometry both the X-ray source and the detector move in the vertical plane around the centre of the specimen. The specimen can be rotated about the ψ, χ and ϕ-axes. In some forms of X-ray diffraction analysis the sample is tilted about an axis ψ. This scan, often known as an ω scan or rocking curve employs a wide entrance slit of the detector (see Chapters 4 and 5).

3.5.2 Coplanar X-ray diffraction

Different scattering geometries can be applied for structural investigations. The conventional coplanar X-ray diffraction (XRD) method is characterised by a plane normal to the surface in which the incident k_i and scattered k_f beams are propagating (Fig. 3.38). Varying the incidence angle via ω and the scattering angle 2θ, the scattering vector components $Q_{x,z}$ are scanned [e.g. 83]. This geometry is sensitive to lattice strains, and the sensitivity increases with the length of the scattering vector $\vec{Q} = \vec{k}_f - \vec{k}_i = (Q_x, 0, Q_z)$ (Fig. 3.39). From scans along Q_z, information on the strain in the layer can be obtained (the penetration depth depends on the incidence angle θ and material properties). Scans along Q_x give information about mosaicity of the structure. The coplanar rocking curve measurements can determine a "tilt" of the mosaic blocks. Tilt stands here for block rotations around an axis parallel to the surface (axes x and y in Fig. 3.38).
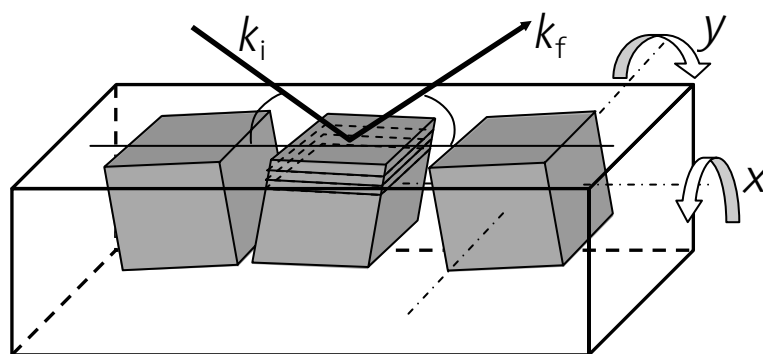

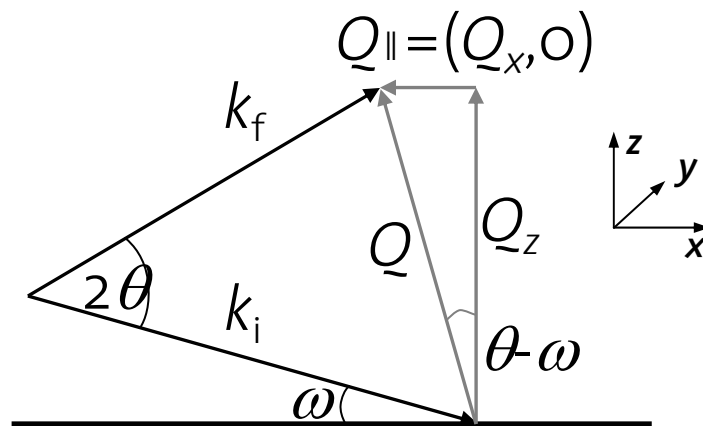Fig. 3.38. Example of the XRD (coplanar) scattering method.

Fig. 3.39. Coplanar geometry for XRD in reciprocal space.

3.6 Atomic force microscopy

The atomic force microscope (AFM), developed in the middle 1980s by Binnig and Quate [84], uses a sharp probe to investigate surface features with high spatial resolution. With the AFM, it is possible to image an object's surface topography with extremely high magnifications, up to 1,000,000 times. Further, the magnification of an AFM is in three dimensions, the horizontal x-y plane and the vertical z dimension.

3.6.1 Atomic force microscopy tapping mode

The AFM functioning principle is very simple. A sharp Si_3N_4 or Si tip is scanned across a surface with piezo-electric scanners. The tip is controlled to remain at a constant force (to obtain height information), or height (to obtain force information) above the sample surface. The AFM employs an optical detection system: A diode laser is focused onto the back of a reflective cantilever. As the tip scans the surface of the sample, moving up and down with the contour of the surface, the laser beam focused onto the back side of a cantilever is deflected into a dual element photodiode. The photodetector measures the difference in light intensities between the upper and lower photodetectors, this signal is used for a computer control.

Tapping mode is a reliable feature of AFM with good image resolution and gentle sample handling. A schematic view of the tapping mode functioning is shown in Fig. 3.40. Tapping mode imaging is implemented in air by the cantilever (3) oscillating with a high amplitude ($\approx$20 nm) at or near its resonant frequency using a piezoelectric crystal (4) and a frequency generator (5). During scanning, the vertically oscillating tip

contacts the surface (taps it) and lifts off, generally at a frequency 50,000-500,000 cycles per second. When the cantilever touches the surface (2), its oscillation amplitude is reduced owing to energy loss. The reduction in oscillation amplitude can be identified and measured with the help of a beam (7) emitted by a laser (6). The beam is reflected by the cantilever and a mirror (8) and registered in a position- sensitive detector (9).
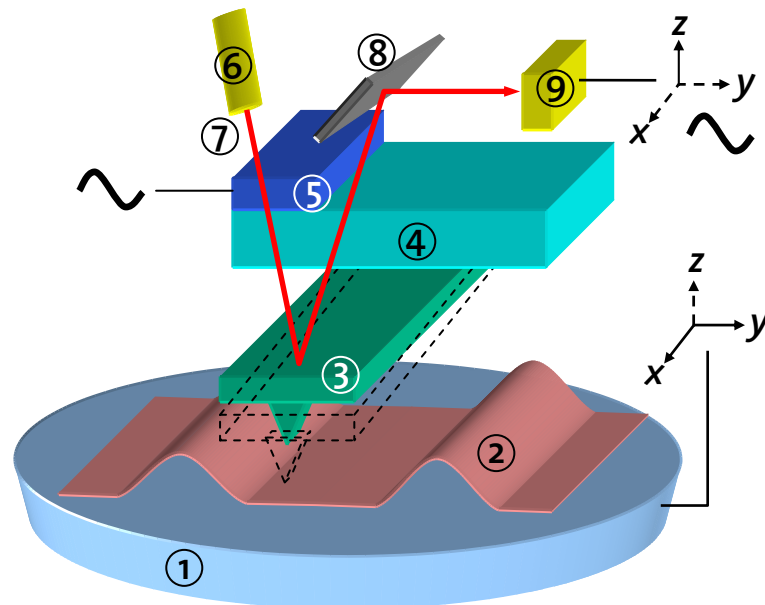
Fig. 3.40. Schematic view of the AFM tapping mode operation.
(1). X-y piezo driver, (2). Sample surface, (3). Oscillating cantilever with tip, (4). Piezo actuator, (5). Frequency generator, (6). Laser diode, (7). Laser beam, (8). Mirror, (9). Photodetector.

Four types of the tapping mode data can be distinguished: plane position, height, phase and amplitude.

- Position in *x-y* plane: The tip coordinates are determined from the *x-y* piezo driver (1).

- Height (*z*-direction): The vertical position of the probe tip is monitored by noting changes in the optical signal (6-9).

- Phase: This type of imaging describes the change in phase offset, or phase angle, of the input drive signal with respect to the phase offset of the oscillating cantilever. The phase of the drive signal (5) is compared with the phase of the cantilever response signal on the photo diode detector (9). The phase offset between the two signals is defined as zero for the cantilever oscillating freely in air. As the probe tip touches sample surface, the phase offset of the oscillating cantilever changes depending on the local properties of the surface.

- Amplitude: The amplitude of the cantilever is monitored by the photo diode detector. The root mean square value of the laser signal on the *x*-axis of the detector is recorded for each of the 512 segments on a given raster of the probe tip. These values are plotted as an amplitude map of the sample surface. Amplitude images tend to show edges of surface features well.

3.6.2 Tip broadening

The AFM imaging process is a result of an interaction between tip and sample. Tip broadening arises when the radius of curvature of the tip is comparable with or greater than the size of the imaged object. Fig. 3.41 shows an example of tip broadening for an object with triangular shape. The size of the base and the sides is affected by the radius *R* of the AFM tip. It leads to the broadening $\Delta W = W\text{-}w$ of the image taken. For a rectangular shape of the height *h* this broadening can be calculated [85] as

$$\Delta W = 2\sqrt{h(2R - h)}, \tag{3.70}$$

and for a spherical element with the diameter *d* [86] as

$$\Delta W = 2\sqrt{2Rd} - d. \tag{3.71}$$

In case of a triangular structure, an analysis of the tip broadening becomes not an easy task. It is hard to derive an universal formula for the pyramids with different bases and sides. For the measurements in this work (Chapter 6), the tip broadening ΔW is 16 nm (e.g. $h \approx 15$ nm, base side $w \approx 36$ nm and tip radius $R \approx 15$ nm). However, the heights of the pyramids *h* are determined accurately because they are not affected by the shape and size of the tips.
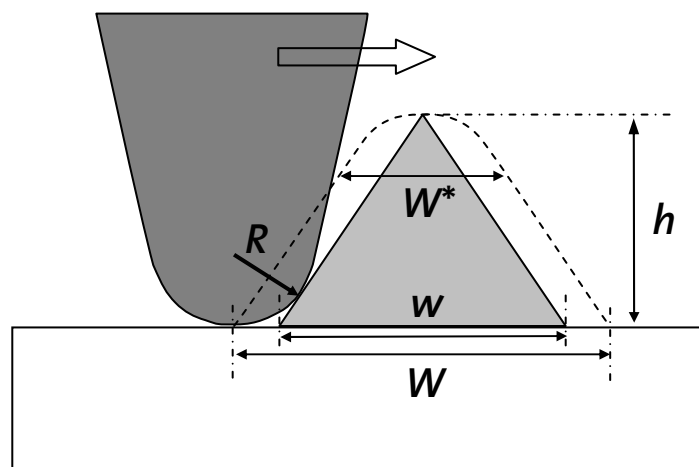

Fig. 3.41. Tip broadening of the image *W* for the triangular structure with base *w*.

Chapter 4

Determination of europium content in IV-VI materials

As was already discussed in Section 2.4, with different Eu content one can vary energy gap (Fig. 2.7(a), Fig. 2.8(b)), lattice constant (Fig. 2.7(b), Fig. 2.8(a)) and refractive index of the IV-VI layers (Fig. 2.9). Even a few percent of Eu suffice to increase the band gap energy appreciably for $Pb_{1-x}Eu_xA$ (where A is Se or Te). This property is useful for band gap engineering such as for quantum well applications (Fig. 4.1). As shown in the figure, these quantum wells are of *type I* band alignment, and have a close to symmetric offset between valence and conductance band for low Eu contents [87]. With increasing Eu concentration the lattice constant a_o increases as well. This can be considered another advantage: The higher the Eu concentration x, the closer a_o of $Pb_{1-x}Eu_xSe$ approaches a_o of BaF_2. However, the lattice mismatch between PbSe and EuSe is only $\Delta a_o/a_o$=1%. Europium decreases the refractive index of a ternary alloy (as usual with increasing band gap), which is an advantage for optoelectronic device manufacturing.
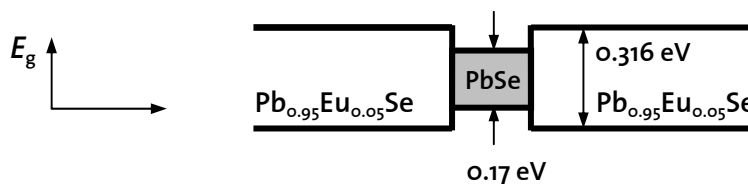
Fig. 4.1. Schematic drawing of the band alignment of a PbSe/ $Pb_{0.95}Eu_{0.05}Se$ structure

Eu admixture causes some disadvantages to IV-VI material properties. First, the Hall mobility decreases drastically with increasing Eu concentration (Fig. 4.2 shows LTHM for $Pb_{1-x}Eu_xTe$ layers). The decrease is caused by alloy scattering. At x>10%, a metal-to-insulator transition takes place [88]. Second, strain relaxation by dislocation glide occurs at low europium concentrations as well as at high (EuTe), while $Pb_{1-x}Eu_xTe$ films on silicon with x=30÷40% lose their plasticity and crack during cooling down from the deposition to room temperature.

According to all the points mentioned above, Eu concentration has to be controlled in a proper way in order to use the advantages and minimise the disadvantages of the element. In the following, several possibilities to determine x in ternary $Pb_{1-x}Eu_xTe$ and $Pb_{1-x}Eu_xSe$ alloys are described.
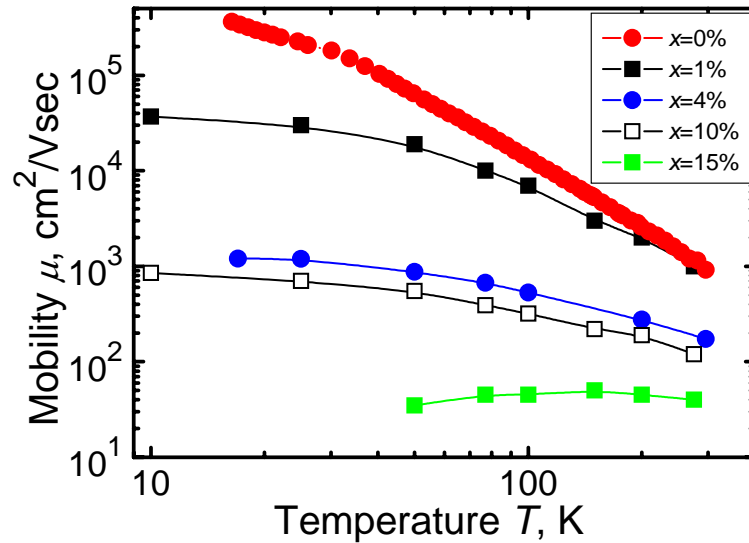
Fig. 4.2. Mobility as a function of temperature for $Pb_{1-x}Eu_xTe$ with various Eu concentrations x. Circles show results of own measurements of layers on Si (111), squares are taken from [89] for layers grown on BaF_2 (111).

4.1 Flux ratio

One of the easiest ways to measure the Eu concentration x in $Pb_{1-x}Eu_xSe$ or $Pb_{1-x}Eu_xTe$ is to check the fluxes during the growth in the MBE chamber. As already mentioned in Section 3.2, PbSe, Eu and Se, or PbTe, Eu and Te sources, were used for $Pb_{1-x}Eu_xSe$ and $Pb_{1-x}Eu_xTe$ epitaxy, respectively. The flux ratio $\Phi_{\text{Lead chalcogenide}}/\Phi_{\text{Europium}}$ determines the europium content in the alloys. A few MBE runs are needed to calibrate the actual Eu concentration (Fig. 4.3). To this end, fluxes were measured by the oscillating quartz
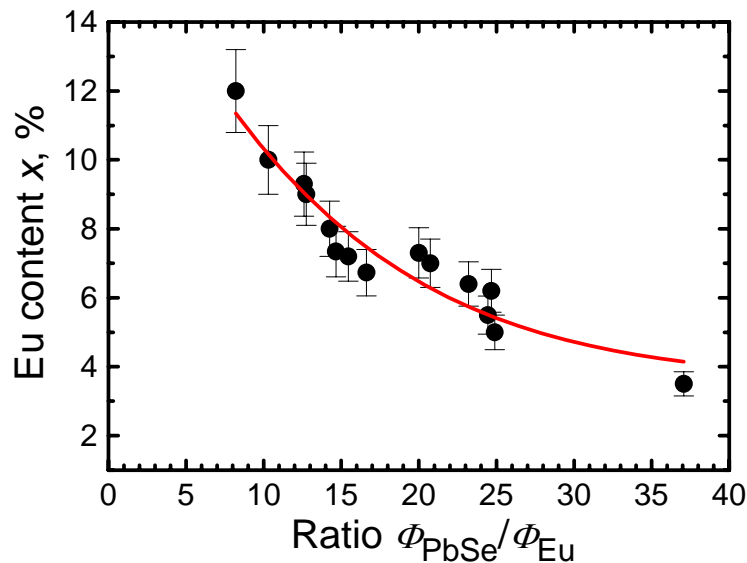
Fig. 4.3. Europium content x in $Pb_{1-x}Eu_xSe$ layers as a function of the PbSe/Eu flux ratio as measured with the crystal quartz monitor.

monitor, the Eu content in the layers was obtained afterwards mainly by determining the absorption edge with FTIR. The possibility to control and change the Eu concentration *in situ* during and even before growth is an advantage of this method. The calibration slightly depends on the substrate temperature because of reevaporation.

4.2 Hall measurements

As already mentioned above, the mobility of carriers decreases with increasing Eu content. For example, $Pb_{1-x}Eu_xTe$ samples with $x>0.3$ could not be measured because the electrical resistivity was too high (resistivity for $x>0.15$ increases for decreasing temperatures and $\rho_o(T=50$ K$)=8000$ Ωcm for $Pb_{0.7}Eu_{0.3}Te$) [88, 89]. As an example, the Hall mobilities for $Pb_{1-x}Eu_xSe$ layers with different europium concentrations are shown in Fig. 4.4. Structures consisting of layers of different x can be analysed with the help of the Petritz method (see Chapters 3 and 5). Measurement problems at higher x and interpretation of the results of complex structures where QWs are embedded in bulk $Pb_{1-x}Eu_xA$ (A=Se, Te) are the main disadvantages of the method. Moreover, mobility values depend on the substrate and carrier type, on the thickness of the measured layers, and they are sensitive to temperature annealings.
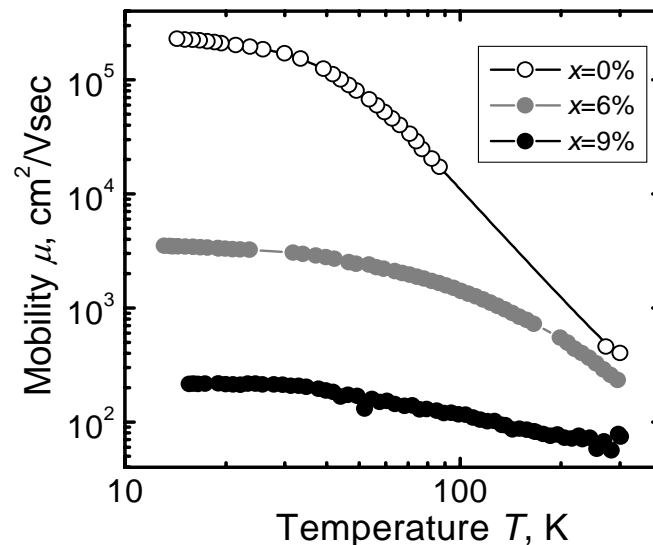
Fig. 4.4. Hall mobilities of $Pb_{1-x}Eu_xSe$ p-type layers on Si (111) with different Eu concentrations x as a function of temperature.

4.3 XRD measurements

The lattice constant a_o increases with increase in Eu content (Chapter 2) and can therefore be determined by X-ray diffraction measurements (XRD). The separation of the angular peaks of multilayer structures in the diffractogram are given by the Eu concentration x. One of the samples with $Pb_{1-x}Eu_xSe$ bottom, PbSe middle and EuSe top layers is shown as an example (Fig. 4.5). The analysis was performed at the FIRST Lab, ETHZ. A Θ-2Θ scan of the 444 reflections is shown in Fig. 4.6. The peaks from materials with larger a_o appear more to the left than those with smaller a_o. EuSe with the largest a_o appears at the left side, followed by $Pb_{1-x}Eu_xSe$ and PbSe.

Bragg's law for a small change in $\Delta\Theta$ is

$$\Delta\Theta = -\frac{\Delta d}{d}\tan\Theta .$$ (4.1)
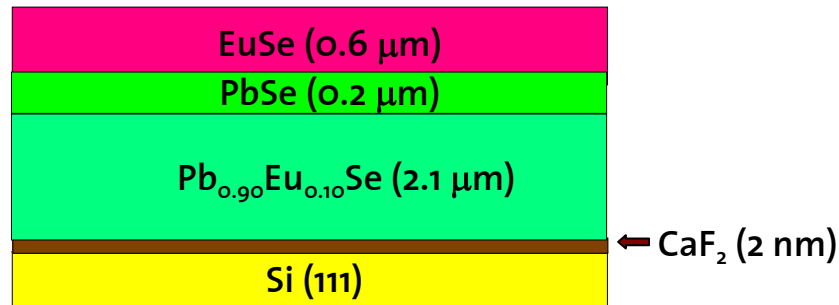
Fig. 4.5. Schematic profile of the structure containing EuSe, PbSe and $Pb_{0.9}Eu_{0.1}Se$ layers on Si (111). x=10% was found from FTIR measurements.
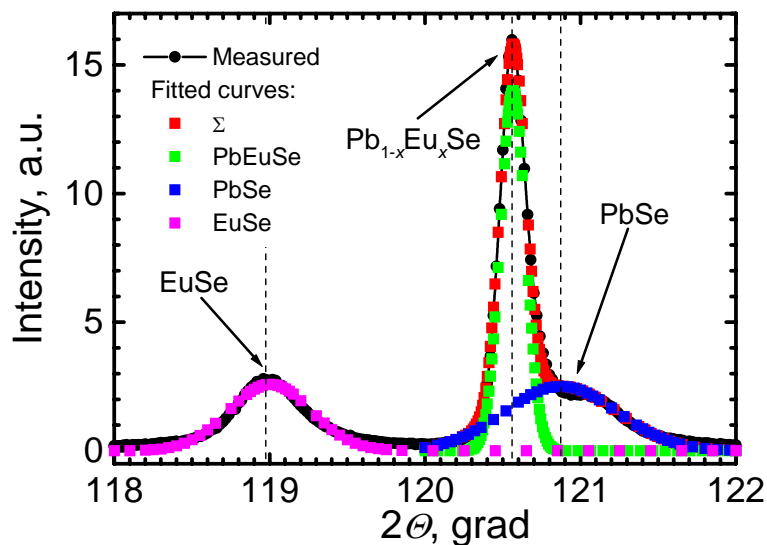
Fig. 4.6. 444 X-ray Θ-2Θ scan of the structure shown above. Measured values are shown with connected circles, the fitted curves are shown with squares.

Using the lattice constants for PbSe and EuSe, one finds $\Delta d/d$=1.21%, $\Delta\Theta$=1.23° or $\Delta(2\Theta)$=2.46°. This means that the shift of the EuSe peak (100% Eu) with respect to PbSe is 2.46° for unstrained layers. The actual value for the strained layer was found to be $\Delta(2\Theta)$=1.9°. In order to determine this value, several fitting procedures were applied (see dots in Fig. 4.6) for all three peaks.

The $Pb_{1-x}Eu_xSe$ peak has an experimental shift $\Delta(2\Theta)$=0.31° from PbSe. The europium content is calculated as the ratio $\Delta(2\Theta)_{PbSe-PbEuSe}/\Delta(2\Theta)_{PbSe-EuSe}$, and is equal to 16.3% (assuming a linear dependence of the lattice constant change with Eu content). But this concentration is valid for the unstrained layers only. Recalculation for the compressed structure gives a value x=12.6±3.15%.

The method described above is based on the comparison of the peak positions on Θ-2Θ scans. It is useful for layers with homogeneous Eu distribution and x>5%. Moreover, since it is a "comparison" method, the presence of europium chalcogenide or lead chalcogenide layers in the structure is required.

There are at least two other methods to determine the concentration of Eu from X-ray measurements. The first method employs direct calculation of the lattice constant from the diffraction pattern, from which x is determined. This requires the measurement of absolute angles with very high precision. Another method correlates the increase of the full widths at half maximum (FWHM) with the increase in Eu concentration. The latter was described for $Pb_{1-x}Eu_xSe$ [22, 90] and $Pb_{1-x}Eu_xTe$ [91]. In Fig. 4.7 two example dependences of these FWHMs are shown. Grown on silicon (111) $Pb_{1-x}Eu_xSe$ samples were measured at 333 Bragg reflections [90], and grown on BaF_2 (111) $Pb_{1-x}Eu_xTe$ samples were measured at 222 reflections [91].

4.4 FTIR

Fourier Transform Infrared Spectroscopy (FTIR) (see Section 3.4) is most suited to determine the europium concentration even in multiple layers with different Eu contents. This method is very sensitive, and absolute values $\Delta x \leq 1\%$ are distinguished without any problems. FTIR suits the experiments described in this work for many reasons. BaF_2 or Si, which are used as substrates, are transparent in the IR range. The europium content in the structures does not exceed 15% (except EuSe), therefore the lower 1.28 μm wavelength limit of the spectrometer employed is sufficient for all measurements. A typical spectrum and a fitted curve of the structure for the optically pumped laser (Fig. 4.5) are presented in Fig. 4.8. The fitting procedure will be discussed in the next section.
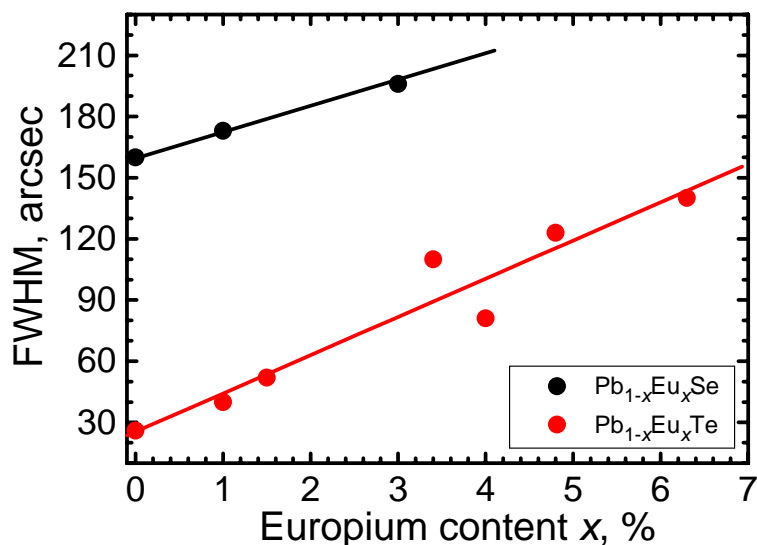
Fig. 4.7. FWHM of the X-ray rocking curve of lead europium
chalcogenides with different x. Results are taken after [90] and [91].
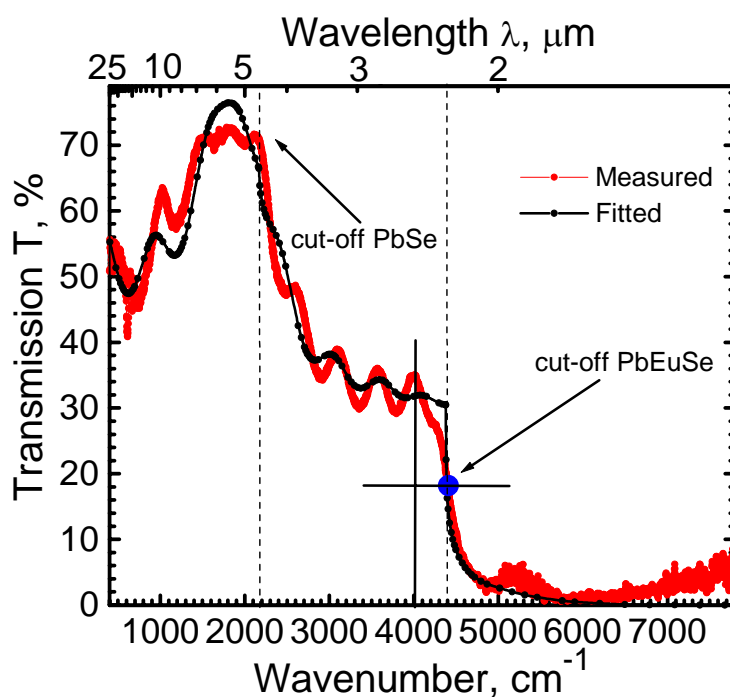
Fig. 4.8. FTIR spectrum of the laser structure with two cut-off
wavelengths $\lambda_{cut-off}$ for PbSe and $Pb_{0.9}Eu_{0.1}Se$. Measured and fitted
curves.

As already discussed in Chapter 2, the band gap E_g of ternary alloys
depends on x. The cut-off wavelength can be determined from the
spectrum. An exact point of onset is not defined, so that comparison with
the theoretical curves is required. In many cases however one uses specific
empirical absorption features with reasonable uncertainties. In this work,
the cut-off wavelength was determined as the point on the spectral curve

which is located at half height after the last maximum (blue dot in Fig. 4.8). The refractive index of the whole structure can be directly calculated from the spectrum (neglecting dispersion):

$$n = \frac{1}{2d\Delta z},$$
(4.3)

where d is layer thickness (usually measured by a profilometer), n is the refractive index and Δz is the distance between two nearest extrema.

Another advantage of FTIR is a good spatial resolution giving the possibility of a direct and simultaneous comparison of x, $\lambda_{cut-off}$, n and d values across the samples. Most of the structures were grown on Si 3 inch substrates and deviations in thickness and composition are expected along the 76.2 mm diameter. Deviations can be determined by comparison of the spectra from different locations of the wafer. As an example, two measurements made at different locations of a Si (111)/Pb$_{1-x}$Eu$_x$Te/PbTe/ EuTe structure with six QWs are shown in Fig. 4.9. One can immediately estimate that $x_{border} > x_{centre}$ and $d_{border} < d_{centre}$. For the properly aligned MBE sample holder relative to the molecular fluxes, the differences between the $\Delta x/x$ and $\Delta d/d$ values near the centre and near the border are less than 6%.
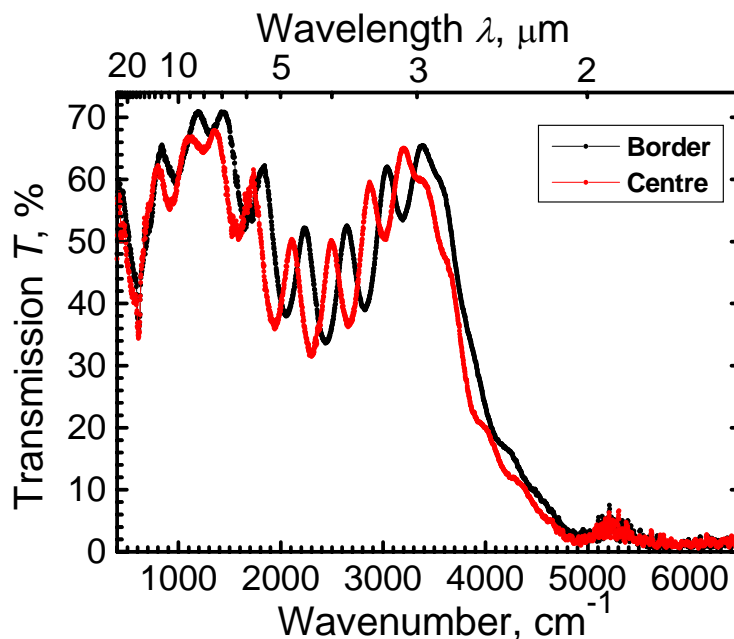
Fig. 4.9. FTIR spectra of a laser structure containing Pb$_{1-x}$Eu$_x$Te layers in the centre (red) and near the border (black) of the 3 inch Si substrate.

For wavelengths larger than 3 μm interference in the structures is observed. As shown in the enlarged spectrum of the same measurement in Fig. 4.10, these oscillations can be explained by the interference fringes

from the double side polished Si substrate. According to equation (4.3) it is found that d is equal to 300 μm for a refractive index n=3.42 (Si). It corresponds to the actual thickness of the Si substrate. This effect does not occur for single side polished wafers. One can avoid these fringes by tilting the sample a few degrees during the measurement.

To know only the total thickness of the structure is not always sufficient since there can be three or four different layers with different thicknesses d_i as well as x_i and/or QWs. For such kind of structures special fitting programmes can be applied.
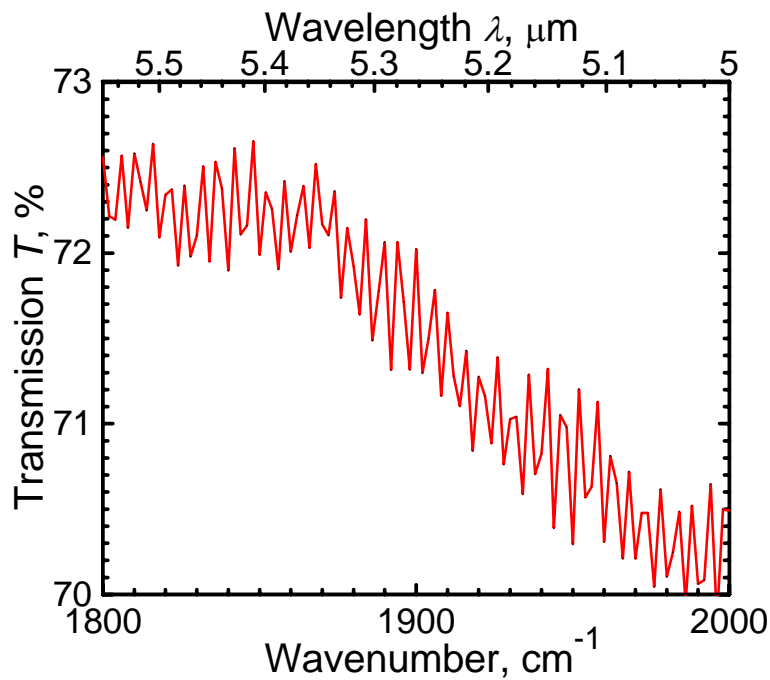
Fig. 4.10. Enlarged part of the FTIR spectrum shown in Fig. 4.8. Interference fringes are due to the Si substrate.
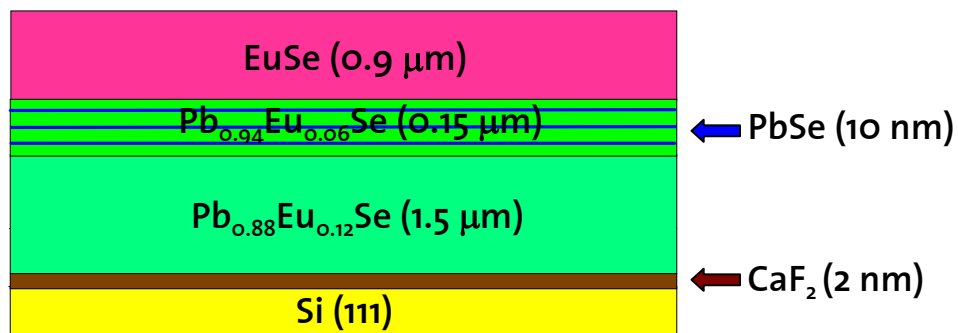
Fig. 4.11. Cross-section of the laser structure with the wave guiding and three different europium concentrations x.

4.4.1 Matrix method application for FTIR measurements

A home written program for thin films was employed to fit the FTIR spectra. The program is based on the matrix method described in Section 3.4. As an example, FTIR measurements and a fitting curve of a lead chalcogenide laser structure (Fig. 4.11) is shown. This structure consists of a thin active $Pb_{0.94}Eu_{0.06}Se$ layer with three 10 nm PbSe QWs between bottom cladding $Pb_{0.88}Eu_{0.12}Se$ and top cladding EuSe layers. This means that 9 films should be described in the fitting programme (the 10th layer- 2 nm CaF_2 buffer film is not taken into consideration because of its minimum influence; the 11th component is the Si substrate). To calculate spectral transmission or reflection 9 thicknesses of the structure components d_j and 10 refractivity indexes n_j (9 films+ $n_{substrate}$) are involved. As mentioned before, refractivity indices depend on the europium content in the layers. An assumption of the Eu amount x_j for each component is a good way to reach positive results. For the calculations, the values $x=0.12$ for the bottom layer, $x=0.06$ for claddings in the active layer, $x=0$ for QWs and $x=1$ for the top EuSe film were used.

After FTIR measurements and profilometer or scanning electron microscope thickness measurements, one may proceed with an attempt to fit the experimental values. In general all parameters (in this particular case there are eleven: nine thicknesses and two Eu contents of the bottom and the active layers) can be fitted in one non-linear fit. But usually 3-4 parameters suffice. An example of a fit with four parameters (thicknesses of the bottom and top layers and Eu contents in the active and bottom layers) is shown in Fig. 4.12.

As can be seen in the graph, there are some deviations of the fit from the initial measurement. The most crucial parts of the fit are uncertainties in the absorption coefficients of the layers containing Eu.

4.5 Spectral response measurements

This method of europium determination is suitable for structures with only one x value. The main principle of spectral response measurements (SR) includes manufacturing of photovoltaic devices like Schottky diodes or p-n diodes and a measurement of spectral response. Like in the case of FTIR measurements, the cut-off wavelength gives here a value of Eu content. As an example, a spectral response measurement of a $Pb_{1-x}Eu_xSe/Pb$ Schottky diode with $x \approx 6\%$ is presented in Fig. 4.13.
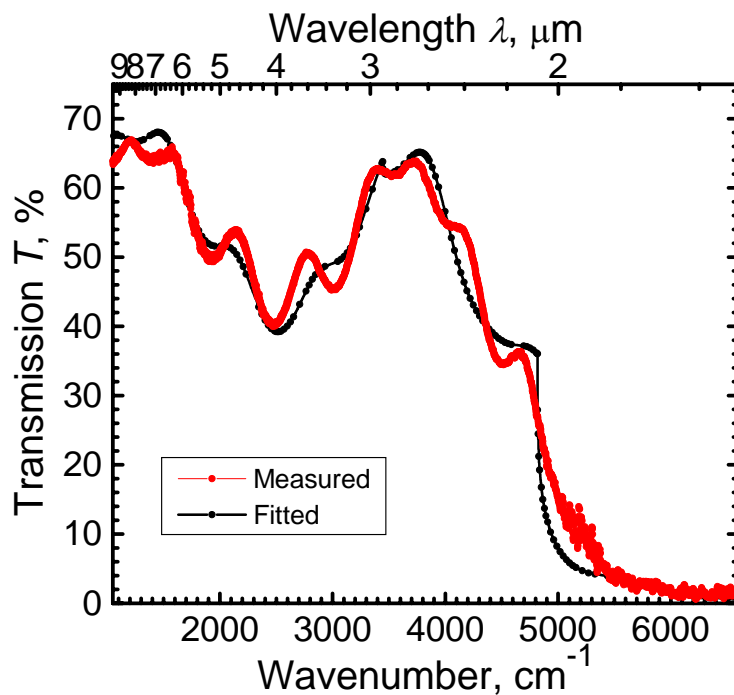
Fig. 4.12. FTIR measurements (red curve) and fitted values (black curve) of the laser structure based on $Pb_{1-x}Eu_xSe$ with top and bottom cladding layers and 3 quantum wells.
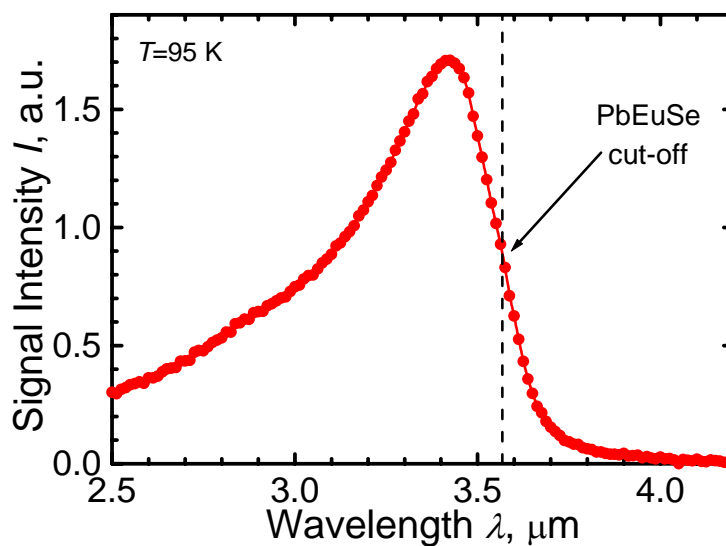
Fig. 4.13. Spectral response of a Schottky diode based on a $Pb_{1-x}Eu_xSe/Pb$ junction at T=95 K. Cut-off wavelength corresponds to x=6%.

4.6 Conclusion

Several methods of europium determination in ternary lead chalcogenide layers were discussed in this chapter. The main advantages and disadvantages of each experimental method are summarized in Table 4.1. Not all methods mentioned above have a small detection error. As shown in Fig. 4.14, the best detection precision is obtained with spectral response and FTIR measurements. The flux ratio and FTIR spectra method were the most valuable and often used type of analysis for the determination of the Eu content in IV-VI ternary alloys.

Table 4.1. Comparison of Eu concentration analyses in IV-VI layers

	Flux ratio	LTHM	XRD	FTIR	SR
x detection limits*: minimum x maximum x minimum thickness	<1% >95% no	no ≈30% 50 nm	≈5% ≈95% 50 nm	no 27% <10 nm	no 11% 100 nm
x_i detection in multilayers, $x_i \neq x_j$	yes	yes (Petritz)	yes ($x_i \gg x_j$)	yes (Matrix)	no
Influence of substrate	no	yes (σ_{sub})	yes (mismatch)	yes ($\lambda_{cut-off, sub}$)	yes ($\lambda_{cut-off, sub}$)
Special conditions	*in situ*	cooling	no	no	cooling

* These x detection limits are due to the finite resolution and/or detectivity range of the equipment used in this work.
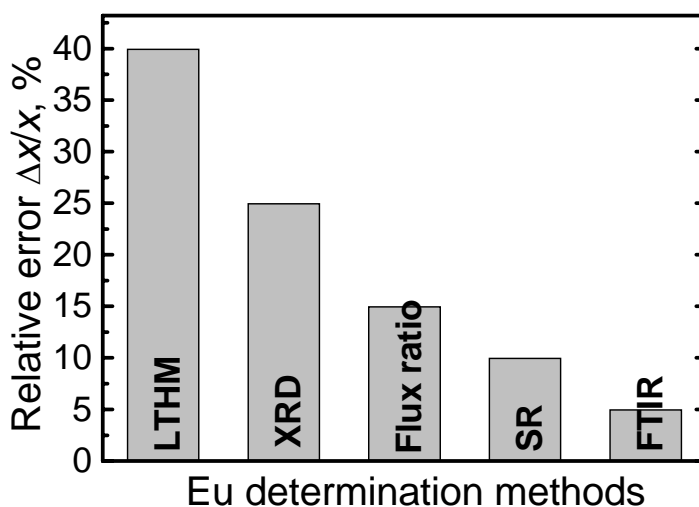
Fig. 4.14. Diagram of the relative error in Eu concentration analyses for the five methods described in this chapter.

Chapter 5

Structural quality of IV-VI layers

Structural quality is one of the most important factors for a reliable and outstanding performance of IV-VI mid-infrared devices. Such mid-IR devices like emitters (edge-emitting lasers and wavelength transformers) and detectors (resonant cavity detectors, RCDs) are described in Chapter 8. High quality of grown layers allows to achieve higher operation temperatures and output powers for lasers, better detectivities for detectors and a more efficient conversion coefficient for wavelength transformers. Layer quality depends on such parameters as layer thickness, presence of Eu atoms, type of substrate, lattice mismatch and growth parameters. All structures were grown epitaxially on Si and BaF_2 substrates. For both types of substrate, a lattice mismatch is presented. In addition, a very large thermal expansion mismatch occurs for Si substrates. Moreover, multistacks containing materials with different lattice constants a_o were used, too. This means that dislocations appear in the layers and their densities can be as high as $10^7 \div 10^9$ cm^{-2}.

Several methods were applied to assess the properties of structures grown in this work. First, methods such as AFM, SEM and TEM are useful and reliable for the characterization of thin films (Section 5.1 for AFM). Second, some electronic properties of the structure were determined (Section 5.2). Third, X-ray analysis was used to investigate grown layers (Section 5.3). In addition, the performance of the device itself can be correlated with properties of the layers it consists of (see Chapter 8).

5.1 Characterization of the layers with AFM

As discussed in Section 3.6, atomic force microscopy (AFM) images the structure of a sample surface with very high magnification. Inclusions, surface roughness and other structures with sizes less than one nanometer are easily seen with AFM. The threading ends of dislocations coming to the surface can be detected, too. As an example, an AFM image of the surface of a PbTe layer grown on silicon is shown in Fig. 5.1. Small holes can be found on the surface with density $\rho_{hole} \approx 1.3 \times 10^8$ cm^{-2}. If one assumes that all these holes correspond to threading dislocations ending at the layer surface, then $\rho_{disl} = \rho_{hole}$. This assumption is supported by low temperature saturation Hall mobility measurement (see Section 5.2) where the same dislocation density was obtained.
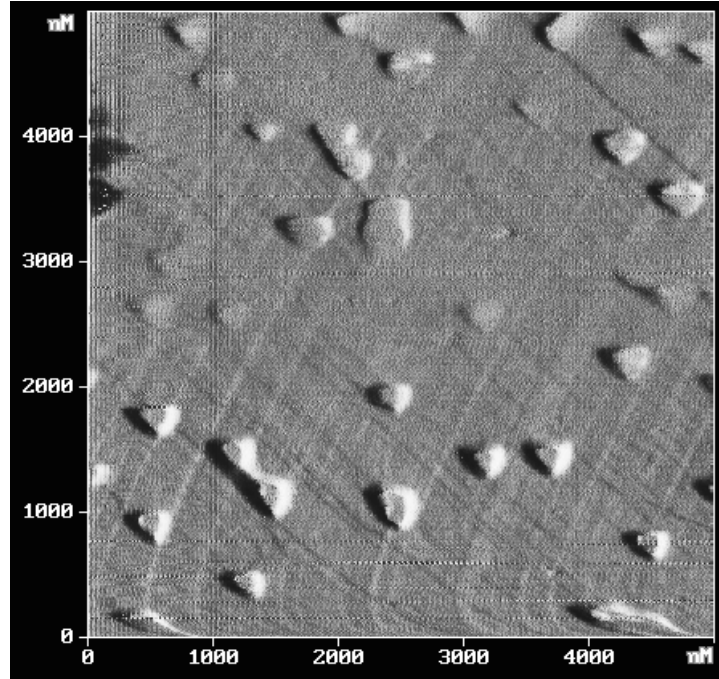
Fig. 5.1. AFM image of a PbTe surface with holes resulting from the threading
dislocation ends (image by M. Gerke, Vladimir State University, Russia).

5.2 Characterization of the layers by Hall measurements

Low temperature Hall measurements (see Section 3.3 for basics) were
used in this work not only for europium content determination (see
Chapter 4) but for structural investigations as well. As stated by Allgaier
and Scanlon [92], the low-temperature saturation Hall mobilities μ_{sat} in IV-
VI materials are not caused by ionized impurity scattering (as in III-V, II-VI
or IV-IV semiconductors) but by dislocations. Therefore, μ_{sat} is controlled by
the mean distances between dislocations L_{disl}

$$L_{disl}[\mu m] = \frac{1}{\sqrt{\rho_{disl}}} = 1.29 \times 10^{-5} \mu_{sat} \sqrt[3]{\frac{n}{10^{18}}} \, , \tag{5.1}$$

where ρ_{disl} dislocation density in cm^{-2}, n carrier density in cm^{-3} and μ_{sat} in
cm^2/Vsec [93]. This means that the density of dislocations in the layer can
be calculated from Hall measurements at low (< 15 K) temperatures. Fach
[94] experimentally found a correlation between L and μ_{sat} for IV-VI
materials on silicon with carrier concentrations in the low 10^{17} cm^{-3} range:

$$L_{disl}[\mu m] = \frac{1}{\sqrt{\rho_{disl}}} = 9.09 \times 10^{-6} (\mu_{sat} + 34000) \, . \tag{5.2}$$

Equation (5.2) was used to determine properties of the layers in this work.
It was found that thicker IV-VI layers have higher LTHM and therefore,

lower dislocation densities. This experiment is in conformance with results of [53], where the author investigated different thicknesses of PbTe deposited on BaF$_2$ (111) substrates.

Another possibility to increase mobilities is to use a buffer layer. For example, a 1.8 μm thick Pb$_{0.94}$Eu$_{0.06}$Se buffer layer with μ_{sat}=3150 cm^2/Vsec increases mobilities in the top PbSe layer up to three times (Table 5.1).

Table 5.1. Low-temperature saturation Hall mobilities for PbSe layers with different thicknesses grown with and without a Pb$_{0.94}$Eu$_{0.06}$Se buffer layer. All layers were grown on Si (111) with a thin (2 nm) CaF$_2$ buffer layer.

	Pb$_{0.94}$Eu$_{0.06}$Se d=1.8 μm	PbSe d=120 nm	PbSe d=240 nm
μ_{sat} without buffer	no buffer	12200 cm^2/Vsec	29000 cm^2/Vsec
μ_{sat} with buffer	3150 cm^2/Vsec	36300 cm^2/Vsec	41300 cm^2/Vsec

For structures consisting of two and more conducting layers (like most of the lasers, RCDs and structure from Table 5.1) the Petritz method was applied for LTHM measurements (see Section 3.3.3 for basics). This is a good method to investigate electronic properties of multilayers with two restrictions: Firstly, the inequality μB<<1 has to be fulfilled and secondly, the difference in mobilities must not be larger than a factor 100.

In Fig. 5.2 one of the edge-emitting laser structures is depicted. It consists of a thin active PbSe layer between bottom cladding Pb$_{0.92}$Eu$_{0.08}$Se and top cladding EuSe (the latter is not conductive). For this experiment, first the EuSe layer was etched away by chemical etching. The EuSe etchant does not harm the active PbSe layer. Afterwards, a Hall measurement yielded μ and n of the combination PbSe + Pb$_{0.92}$Eu$_{0.08}$Se. Then the PbSe was etched away (PbSe and Pb$_{1-x}$Eu$_x$Se have different etching rates) and the Pb$_{0.92}$Eu$_{0.08}$Se bottom layer was measured and the parameters μ_b and n_b were extracted from the Hall data (Fig. 5.3, left).

Using equation (3.42), where b corresponds to Pb$_{0.92}$Eu$_{0.08}$Se (bottom), and s to PbSe (surface) layers and with $\sigma = ne\mu$ for the stack, one obtains the Hall mobility of the active layer

$$\mu_s = \frac{\mu\sigma d - \mu_b\sigma_b d_b}{\sigma d - \sigma_b d_b}.$$
(5.3)

According to this equation, the result for the surface layer (PbSe) is approximately equal to the values of two-layer measurements (PbSe + Pb$_{0.92}$Eu$_{0.08}$Se) if the bottom layer has very low mobility values (Fig. 5.3, right). The calculated saturation value of the PbSe active layer μ_{sat}(15 K) equals 21000 cm^2/Vsec, and the dislocation density according to equation (5.2) is $\rho_{disl} \approx 4\times10^8$ cm^{-2}.

Fig. 5.2. Cross-section of the laser double heterostructure with PbSe active layer.
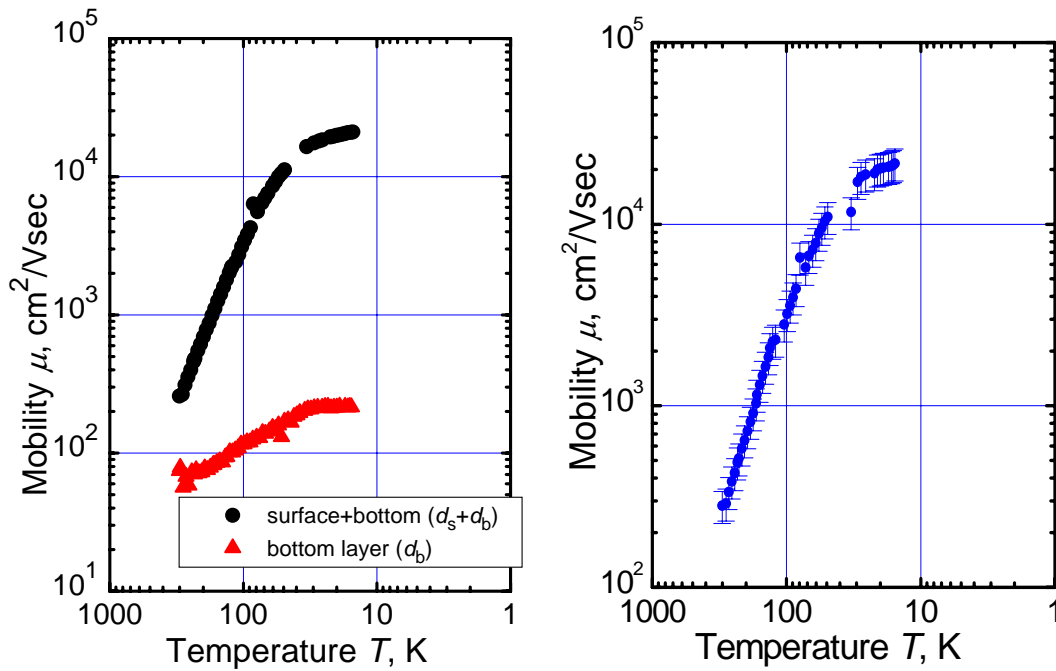
Fig. 5.3. Hall mobilities for surface and bottom layers (black), only for bottom (red) (both to the left) and according to the Petritz method calculated mobilities of the surface layer (blue, right).

5.3 X-ray measurements of dislocation densities

The full widths at half maximum (FWHM) β_{FWHM} of intensity of Θ-2Θ scan depend on the structural quality of the layers. The dislocation density ρ_{disl} is proportional to $(\beta_{FWHM})^2$ (assuming a homogeneous Gaussian distribution of the threading dislocations across the layer thickness):

$$\rho_{disl} = \frac{\beta_{FWHM}^2}{4.36 b^2},$$ (5.4)

where b is the length of the Burgers vector [e.g. 95]. This formula applies for layers much thicker than the X-ray absorption length. If the layer is thin, a peak broadening $\Delta\theta$ occurs:

$$\Delta\theta = \frac{\lambda}{2d_{Layer}\cos\theta}\,, \qquad\qquad (5.5)$$

where λ is wavelength of the X-ray source, d_{Layer} layer thickness and θ the Bragg angle. For the case of a DH laser structures with d_{Layer}=150 nm, Cu K_α radiation and θ=60.5° for the 444 reflection, the natural peak width is calculated as 144 arcsec, which is larger than values found in layers in the micrometer thickness range. This means, that the XRD method is useful for thick IV-VI layers only.

PbTe-on-Si (111) homostructures with thicknesses d=3.5÷11 µm have been examined at the European Synchrotron Radiation Facility (ESRF). Main aims of these measurements were to reveal the distribution of dislocations across the sample's volume, prove a β_{FWHM}=$f(d)$ correlation and find the influence of thermal cyclings on structural properties of high quality layers. Investigating structures with different incoming angles θ (Fig. 5.4, left), it was found that the FWHM (and calculated from the equation (5.4) dislocation density) is independent of θ within the accuracy of the measurements. The dislocation density is therefore constant in the top part of the PbTe layers (about 2÷3 µm for the 333 reflection). This means that the reduction of the threading dislocation density takes place mainly near the PbTe/CaF$_2$/Si interfaces. Unfortunately, this region is not accessible with X-rays for thick layers.
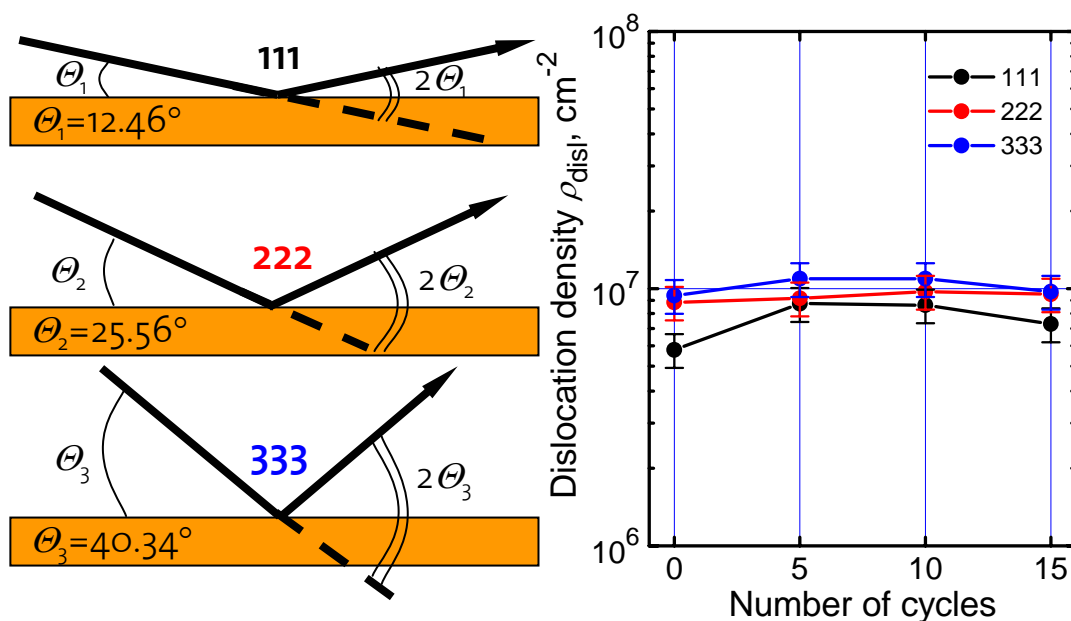

Fig. 5.4. Schematic drawing of the experiment with different incoming angles (left) and ρ_{disl} dependence on the number of cycles (right).

The dislocation behaviour after temperature cycling was investigated as well. For these experiments annealings were performed by heating from RT to 573 K (2 min) and back to RT (10 min) 5, 10 and 15 times. The annealing was made in air. A slight increase for all FWHM was observed after the first anneal cycles of 5 times (Fig. 5.4, right). Then, we observed a small decrease for the measurements after 10 and 15 cycles, but not more than 15%. This is in contrast to earlier temperature cycle measurements, where a drastic decrease of dislocation densities after some similar thermal cycles was found. However, initial dislocation densities were at least 10 times higher in these earlier investigations than in the present work [13].

The narrowest width of a thick sample of thickness d=11 μm is about 35 arcsec. This corresponds to a dislocation density ρ_{disl}=5×10^6 cm^{-2}. For a 3.5 μm thick layer β_{FWHM}=220 arcsec and ρ_{disl}=2×10^8 cm^{-2} were found.

From equations (5.2) and (5.4) follows

$$\mu_{sat} \propto \frac{1}{\sqrt{\rho_{disl}}} \propto \frac{1}{\beta_{FWHM}}.\qquad\qquad(5.6)$$

The XRD β_{FWHM} values are compared with LTHM measurements in Fig. 5.5 for different layers with different thicknesses. Fitting equation (5.6) to the data, we find a slope of -0.85, with an acceptable fitting range of ±0.29.

Generally, the dislocation density of lattice mismatched epitaxial layers decreases with increasing thickness according a power law

$$\rho_{disl} \propto d^{-s}\qquad\qquad(5.7)$$
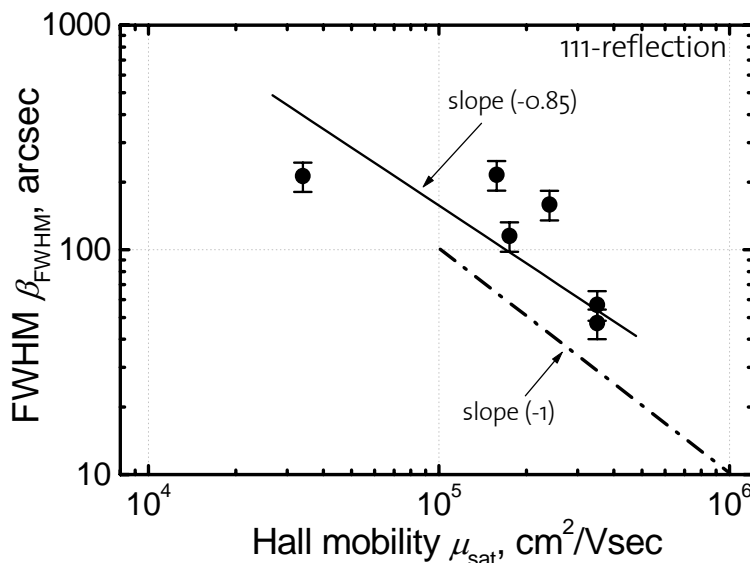
Fig. 5.5. Correlation between saturation Hall mobilities and widths of the X-ray Bragg peaks. Red line shows a power law dependence with a negative slope 0.85. Slope with the power -1 is shown in dashed.

where s is around 1 [96]. According to Springholz [53], the threading dislocation density in IV-VI materials grown on BaF_2 (111) substrates decreases with increasing thickness and roughly follows a power law dependence with a negative exponent of 1.2, $\rho_{disl} \propto d^{-1.2}$.

Fig. 5.6 shows the dependence of full widths at half maximum of the Bragg peaks versus the layer thickness. It can be approximated by $\beta_{FWHM} \propto d^{-1.3}$ or $\rho_{disl} \propto \beta_{FWHM}^2 \propto d^{-2.6\pm0.4}$. The value $s=2.6\pm0.4$ is slightly higher than obtained with etch pit counting for IV-VI materials on Si (111) $s=2$ [33]. Presently, there is no explanation for such a high s value.
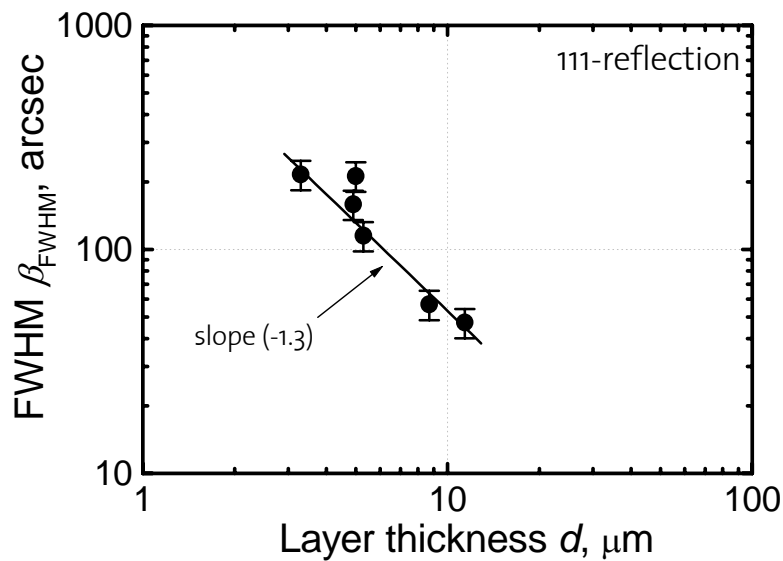
Fig. 5.6. FWHM of PbTe layers with different thicknesses. The line shows a power law dependence with negative slope, this fit results in the slope 1.3±0.2.

5.4 Conclusion

Structural quality plays a very important role in device manufacturing and performance. AFM, LTHM and XRD are the main methods for layer characterization employed in this work. The same dislocation densities were obtained within measurement accuracy with all three methods described above. The thicker the IV-VI (111) oriented layer, the lower is the dislocation density. The lowest dislocation density $\rho_{disl}=5\times10^6$ cm^{-2}, which was obtained for a 11 μm thick PbTe layer on Si (111), proves that layers with quite high structural and electronic quality can be grown even on Si substrates. High dislocation densities (up to 10^9 cm^{-2}) limit the characteristics of infrared devices. Dislocation density remains constant

across the top (2÷3 μm) part of a IV-VI layer on Si (111), but the densities follow the layer thickness with a power law $d^{-2.6\pm0.4}$.

Chapter 6

Zero-dimensional structures: PbSe quantum dots on PbTe/Si (111)

Quantum dots (QDs) exhibit discrete sharp energy values with equal number of states. Self-assembled dot matrixes have been in use since a long time for systems like III-V, II-VI or Si-Ge [97, 98]. Zero dimensional structures may become useful as the active elements in addressable arrays for nanoscale computation and memory, and as dense arrays in active regions of optoelectronic devices.

The typical width of the size distribution of self-assembled QDs is 20÷50%. The randomness of spatial nucleation and unavoidable size variation of dots cause a large spread in the energies of electronic states [99]. Even artificially influencing the QD growing using specially prepared substrates (patterning, structuring, electron beam *in situ* lithography, etc.) [99, 100] or superlatticing does not lead to the "ideal" narrow height distribution. A broadening of about 7% after III-V growth on patterned surfaces is reported in [99]. Using different multilayers as a buffer it was possible to grow InAs dots with a width of the size distribution of less than 4% [101].

In this work a very narrow quantum dot size distribution (2÷3%) was achieved for the system PbSe/PbTe (111) without any artificial influence [102, 103, 104]. Growth and measurement procedures as well as an explanation are described below.

6.1 Growth and measurements

The structures were grown on 3 inch Si (111) substrates by molecular beam epitaxy in a two chamber system. First, a 2 nm CaF_2 buffer layer was grown for compatibility. Then, a 4÷5 μm thick layer of PbTe was deposited in the second chamber (a description of the growth conditions can be found in Chapter 3). Immediately after PbTe epitaxy, 3÷4 monolayers (MLs) of PbSe were deposited with a low flux rate of less than 0.1 ML/sec on the PbTe quasi-substrate at a slightly higher substrate temperature. A schematic view of the structure is shown in Fig. 6.1.
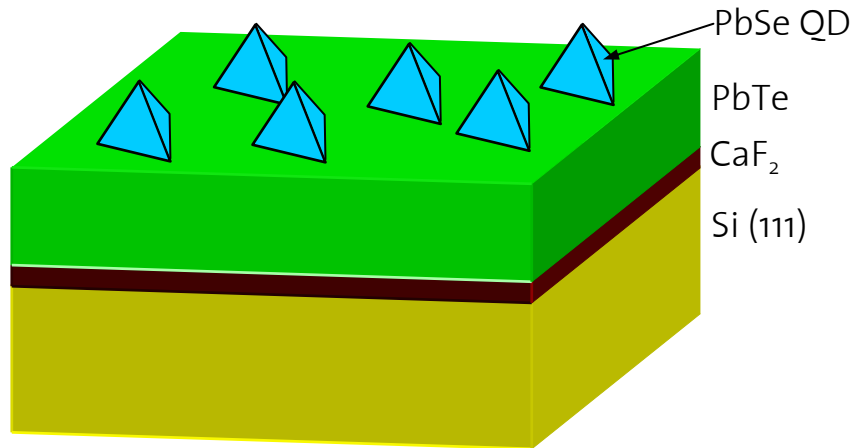
Fig. 6.1. Schematic view of PbTe quasi-substrate with PbSe quantum
dots on top.

The samples were investigated by atomic force microscopy (AFM *Nanoscope IIIa*) in air within a few days after growth. It was found that all dots have pyramidal shape with three (100) oriented side facets and a (111) oriented base, which corresponds to the earlier results obtained by other groups [e.g. 105]. This shape can be explained by referring to the lowest free energy surfaces of IV-VI materials. Typical AFM images (made in tapping mode, see Section 3.6) are presented in Fig. 6.2.
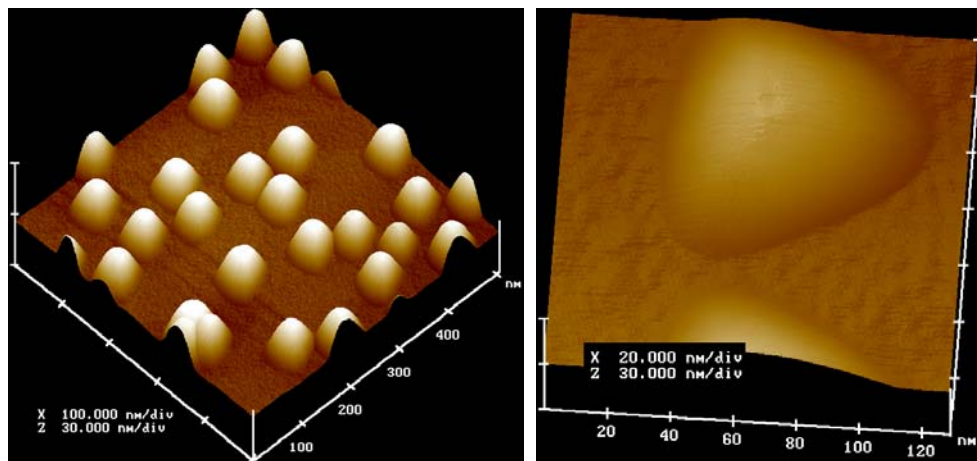
Fig. 6.2. 0.5×0.5 µm² three-dimensional image of IV-VI QDs (left) and
enlarged view of a single dot (right).

It is important to emphasize that the AFM tip has an influence on the measured lateral size of a dot, but not on its height (see Section 3.6). Only the terrace structure of the PbTe surface limits the accuracy of the experiment. An example of height measurements is shown in Fig. 6.3.
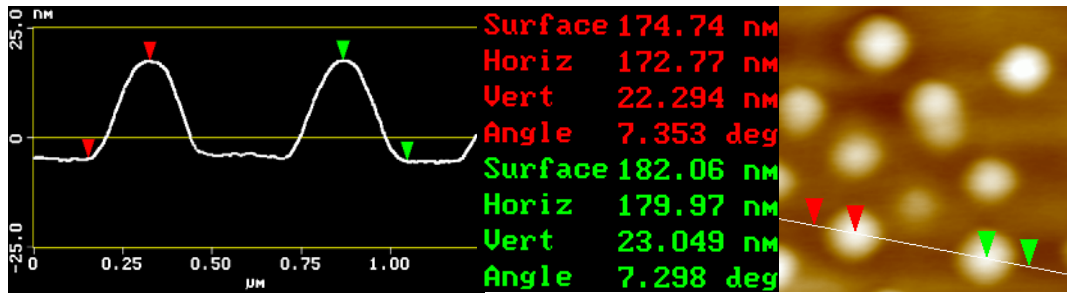
Fig. 6.3. Height determination according to AFM measurements.

6.2 Height distribution

Series of experiments with different growth parameters (flux rate, substrate temperature, properties of the bulk material, different Si substrates) were made in order to investigate the narrow height distributions of PbSe quantum dots on PbTe/Si (111) as initially reported by Alchalabi [102]. Different AFM microscopes and various AFM tips were used for this purpose. It was found that the standard deviation (std) of measured heights never exceeds 6.5%. This is in contrast to Pinczolits *et al.* [105], where a "remarkably narrow size distribution with a relative variation of height… as low as ±7%" was reported. Size distributions were within the 7÷17% range and growth was performed on BaF_2 substrates in this work.

The best results of the present work on silicon substrates were std=2÷3% [103, 104]. To the knowledge of the author, nobody has reported a narrower size distribution for self-assembled QDs for any material system. Two examples are shown in Fig. 6.4 and Fig. 6.5. The most important values obtained from the AFM images are summarized in Table 6.1.

Table 6.1. Main results of the measurements of QD structures 0717 and 0975.

Sample Number	Dot Density, cm^{-2}	Measured Dots	Mean Dot Height, nm	Dot Volume, nm^3	PbSe Molecules in a Dot	Standard Deviation std, %
0717	$1.1 \cdot 10^{10}$	113	18.76	8090	$(1\pm0.1)\times10^5$	3.11
0975	$0.85 \cdot 10^{10}$	48	15.06	4180	$(5\pm0.5)\times10^4$	2.08

For a well-defined three-sided pyramidal shape of the dot one can calculate the dot volume

$$V = \sqrt{\frac{3}{2}} h^3 \qquad\qquad (6.1)$$

and the number of PbSe molecules in one dot (see Table 6.1).

Fig. 6.4. AFM top view image (left) and height distribution (right) of QDs 0717 with std=3.1%.

Fig. 6.5. AFM image (left) and height distribution (right) of the sample 0975 with QDs, std=2.1%.

6.3 Explanation of the results

Statistical nucleation theory (see Section 3.1.1) was applied for the explanation of such a narrow size distribution of quantum dots. Two assumptions were made:
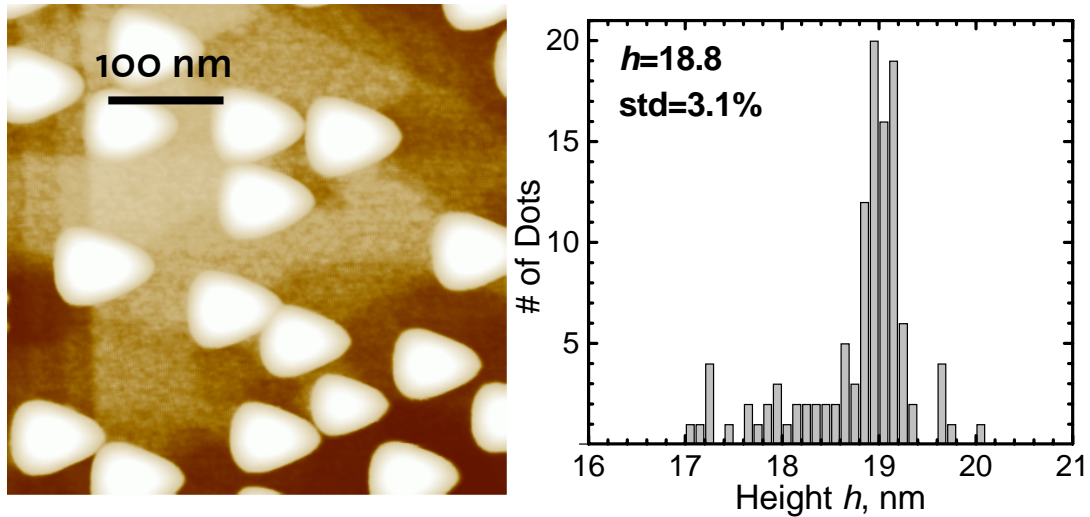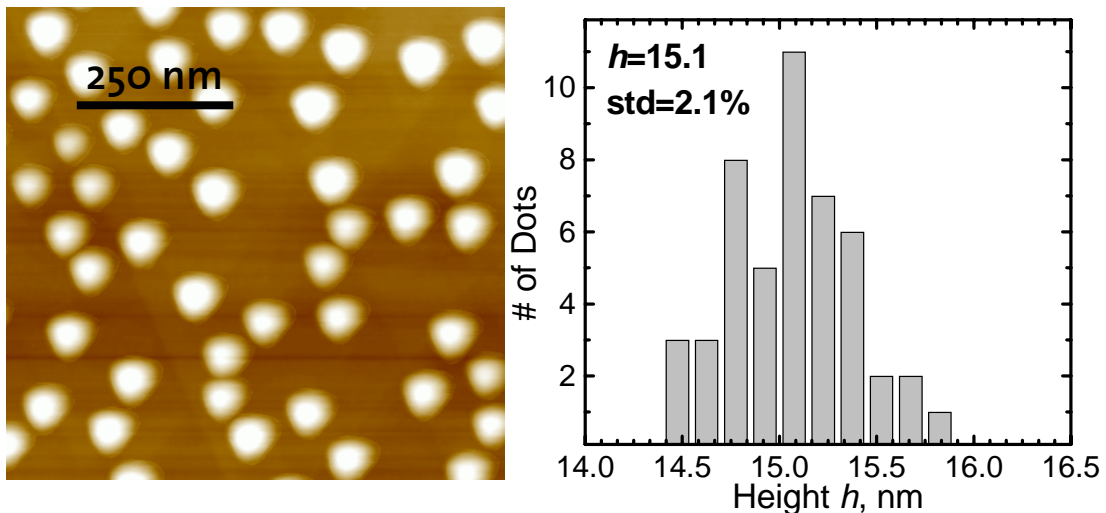
1.   All stable nuclei are formed at start of deposition within a time interval $t_{Formation} << t_{Total}$.

2.   The growth rate is the same for all stable nuclei [103].

6.3.1 First assumption

   As described in Section 3.2, the PbSe deposition rate was quite low F=0.05 ML/sec and deposition time was more than one minute for these experiments. AFM images show a mean distance between the QDs equal to $L_{Mean} \approx 100$ nm. According to these values it is easy to estimate that the minimal time needed to obtain stable nuclei containing 2÷10 molecules is $t_{Formation} \approx 1$ msec. Adsorption time τ (see also equation (3.1)) calculated by the equation

$$\tau = \frac{\lambda_a^2}{D},$$
(6.2)

where λ_a is the diffusion length (50 nm) and D is the diffusion coefficient (10^{-4} cm²/sec), is about 1 μsec. This means that the probability to have a stable cluster with $i \geq 2$ in the very beginning of nucleation is very low ($t_{Formation} >> \tau$). The formation of stable nuclei proceeds very slowly and can lead to different times of cluster appearances and afterwards to a wide size distribution.

   But this is true only for homogeneous condensation on a defect free surface. PbTe (111) quasi-substrates used for PbSe QD epitaxy have a rough surface on a nanometre scale. The nature of such roughnesses is discussed in Section 2.5. The densities of threading dislocations ρ_{disl} which end at the PbTe quasi-substrate surface used for these experiments are in the $10^7 ÷ 8 \times 10^7$ cm^{-2} range. These dislocations cannot explain synchronous dot nucleation, since dot densities are at least two orders of magnitude higher (see Table 6.1). Other possible surface defects are shown in Fig. 6.6: intersections of dislocation lines, terraces with steps, kinks, etc. From our experience we can expect that a strongly terraced structure of the PbTe surface already exists before PbSe deposition, because an appreciable difference in substrate temperature T_w during PbTe growth (T_w=573 K) and during PbSe evaporation (T_w=713 K) leads to relaxation of thermal misfit strains. To show that a high number of surface defects exist which act as nucleation centre for QD, an AFM image is presented in Fig. 6.7. It is a modified version of Fig. 6.4, with increased contrast in order to show triangular terraces and dislocation lines (shown with dashed lines).
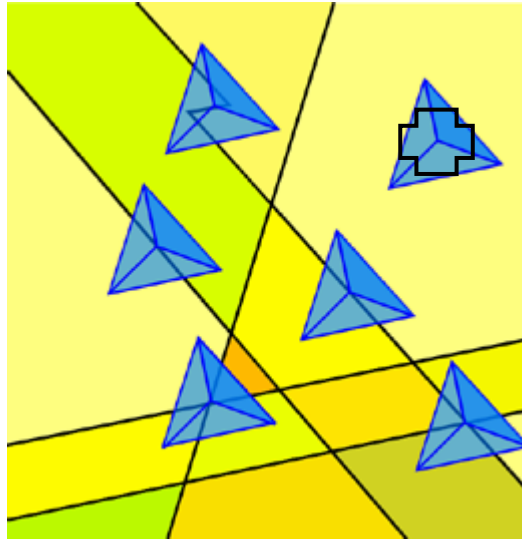
Fig. 6.6. Schematic drawing of quantum dots which nucleated at different defects of the PbTe surface: threading ends of dislocations, terrace surface steps, intersecting dislocation lines.
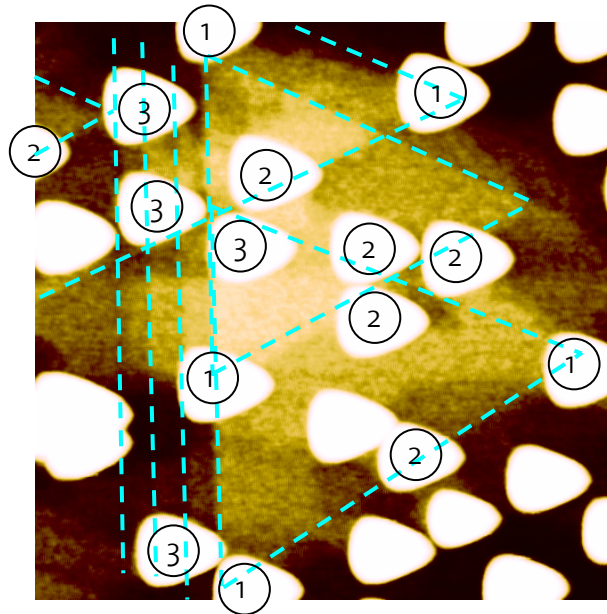
Fig. 6.7. Modified AFM image (same data as Fig. 6.4) to show surface steps, terraced structures and threading dislocations. Only the central part of the AFM picture was analysed because of imaging quality. (1). Dots on triangle apexes, (2). Dots on surface steps, (3). Dots on two or more dislocation lines.

6.3.2 Second assumption

To prove the second assumption and to make an explanation easier one adopts four approximations:

1.   For all QDs the diffusion range λ_a is smaller than half the distance L between dots ($2\lambda_a < L$) (Fig. 6.8).

2.   All PbSe molecules impinging outside a circle with radius λ_a reevaporate.

3.   PbSe molecules impinging inside this circle diffuse to the existing QD and are incorporated there.

4.   PbSe molecules impinging directly on a QD are incorporated in this dot [104].
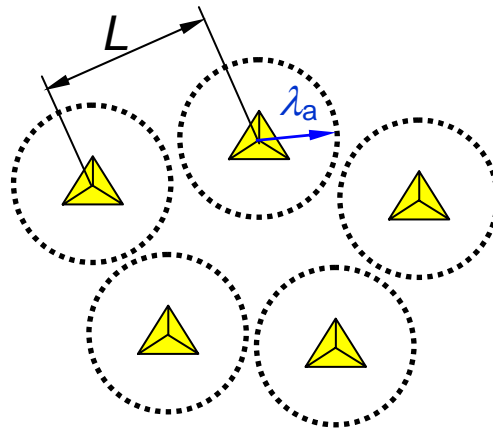
Fig. 6.8. Positioning of QDs on the substrate when distance between
2 dots L is larger than two diffusion lengths λ_a, $L > 2\lambda_a$.

Assuming isotropic diffusion on the PbTe surface, the probability to capture incoming molecules is the same for all quantum dots. This means that all QDs have the same growth rate. This leads to a very narrow size distribution. If λ_a becomes larger than L (Fig. 6.9), dot pairs with $L < 2\lambda_a$ grow
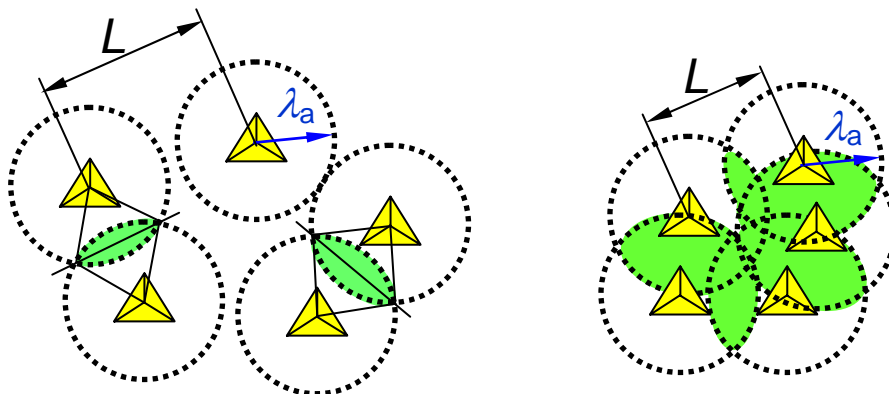
Fig. 6.9. QD growth arrangement if some diffusion radii overlap (left)
and general overlapping $L < 2\lambda_a$ (right). The shared areas are shown green.
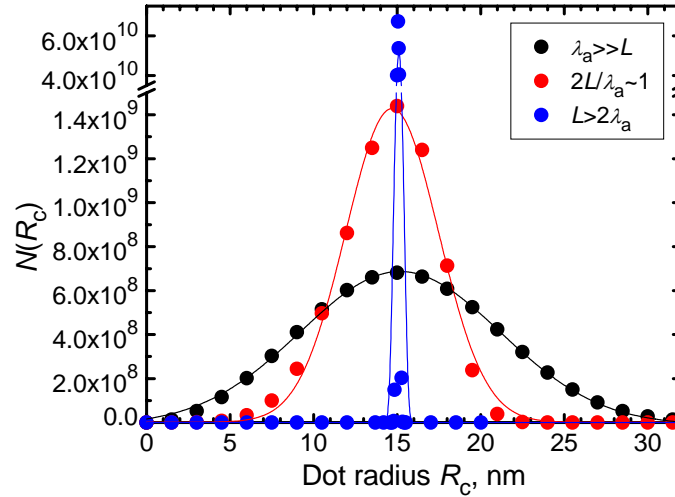
Fig. 6.10. Distribution functions $N(R_c)$ (dots) and Gaussian fits (lines) for different L and λ_a relations for sample 0975. Widths of size distribution are 79% for $\lambda_a \gg L$, 37.5% for $L/2\lambda_a \approx 1$ and only 0.078% for $2\lambda_a < L$.

less rapidly, and the size distribution becomes broader. It is easy to see in Fig. 6.4 (right) for the sample 0717 that diffusion radii overlapping for some dot pairs result in an asymmetrical size distribution towards lower h. Much broader distributions appear if for all QDs $L < 2\lambda_a$ (Fig. 6.9, right).

6.3.3 Numerical calculations of QD height distribution

In order to prove the assumption about the necessity of the inequality $2\lambda_a < L$ for narrow size distributions, some numerical calculations were made according to reference [46]. There are final equations (see (3.9)÷(3.11) in Chapter 3) which describe the size distribution of clusters $N(R_c)$ with different L and λ_a relations. Quantum dots of the sample 0975 were taken as an example. Defect density n_d was taken equal 10^{10} cm^{-2}, and the mean dot radius (assuming here that the dots have hemispherical shape) $R_{c,m}=15.06$ nm (see Table 6.1). The results are presented in Fig. 6.10. It is evident that the narrowest distribution belongs to the case $2\lambda_a < L$.

The size distribution broadens if some distances L are too small, $L < 2\lambda_a$. This can be taken into account individually for each pair of dots. The shared area for two too narrowly spaced dots has been calculated and after this, with

$$\begin{cases} h_{\text{corr}} = h \times \sqrt[3]{\dfrac{1}{2\pi(1-\arccos\left(\dfrac{\lambda_a}{2\lambda_{a,\text{corr}}}\right))}} \;,\; 2\lambda_a > L \\[4mm] h_{\text{corr}} = h \,,\; 2\lambda_a \leq L \end{cases} \qquad (6.3)$$

the height h can be "corrected" by the amount of changed diffusion area. This is done for different assumed diffusion lengths λ_a. With the values h_{corr}, the size distribution can be recalculated. One of the results (for sample 0717, std=3.1%) is presented in Fig. 6.11. The graph has a minimum at $\lambda_{a,corr} \approx 50$ nm, which, as expected, just corresponds to the experimentally determined half mean distance between two nearest dots.
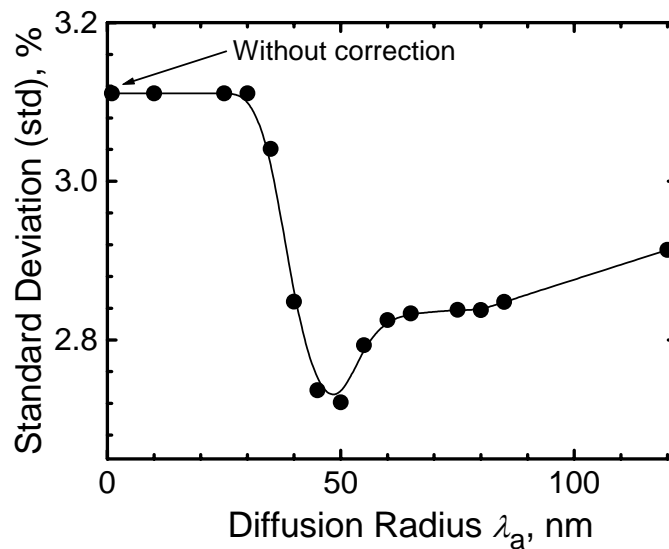
Fig. 6.11. Width of size distribution for the sample 0717 as a function of assumed diffusion length λ_a for those dots which are separated by $L < 2\lambda_a$.

6.4 Conclusion

The extremely narrow width (2÷3%) of the size distribution of self-assembled PbSe quantum dots on PbTe (111) quasi-substrates on Si (111) is understood on the basis of the existence of surface defects as nucleation centres and by the inequality $L > 2\lambda_a$. In the beginning of dot growth incoming molecules with the flux Φ nucleate at defects. There are obviously always enough nucleation sites on the PbTe surface due to dislocation glide steps caused by the relaxation of the thermal misfit strain. Molecules form stable clusters with the number of molecules $i > 1$ and then all clusters have the same probability to capture an incoming molecule within the diffusion radius λ_a. The results are in good agreement with the nucleation theory. To the knowledge of the author, there is no prior publication reporting such a narrow quantum dot size distribution for self-assembled quantum dots.

Chapter 7

One-dimensional structures: Fluoride template for quantum wires

One-dimensional structures are called quantum wires (QWis). Only few papers are dedicated to 1D structures based on IV-VI materials. Ordered PbSe crystalline nanowire arrays with diameters of about 50 nm and lengths up to 5 μm have been fabricated in the nanochannels of porous alumina membranes by electrodeposition [106]. The group in Linz fabricated quantum wires by plasma etching of $Pb_{0.94}Eu_{0.06}Te$ layers [107]. According to the knowledge of the author, there are no publications about IV-VI quantum wires grown by physical vapour deposition (PVD) including MBE. One way to grow IV-VI QWis epitaxially is deposition of lead chalcogenides on a templated surface. Such templates can be obtained in the fluoride-on-Si (100) system.

Si (100) substrates were used to grow nanosized self-assembled CaF_2/BaF_2 structures. As found by Pasquali *et al.* [108], under certain conditions it is possible to achieve a self-assembled MBE growth of nanostripes. For fluorides {111} planes are the planes with the lowest surface energy. Thin layers of CaF_2 tend therefore to form (111) facets on Si (100) surfaces. The formation of these facets is facilitated by thermal annealing. A similar behaviour can be found with polished BaF_2 (100) surfaces where during extended thermal anneal roughening of the surface can be observed (e.g. RHEED patterns indicate a change from a 2-d to a 3-d surface structure). High deposition temperature and low fluxes (T_w=923÷1073 K, $\Phi\approx$0.1 Å/sec) were chosen as growth parameters. Thick CaF_2 appears as a continuous layer with stripes (Fig. 7.1) [109].
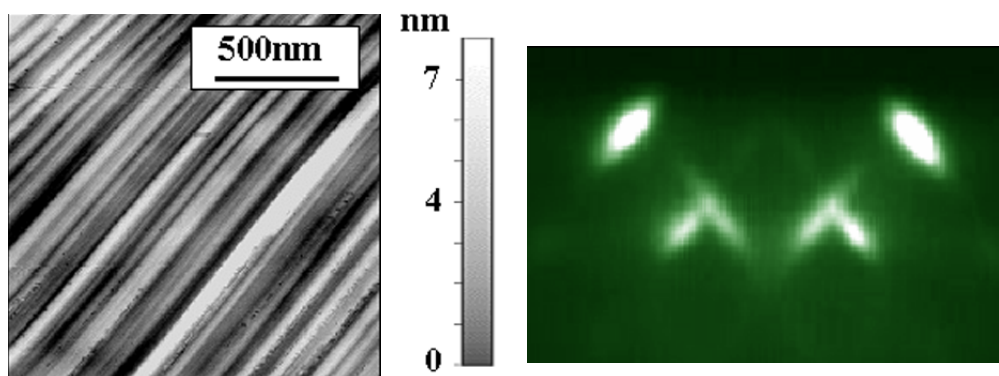
Fig. 7.1. AFM image (left) and RHEED pattern along [110] direction (right) of a 100 nm thick CaF_2 layer on Si (100). Inclined streaks of RHEED image indicate {111} faceting (by A. Banschikov, Ioffe Institute, Russia).

These unique properties of self assembling can be used for pattern manufacturing. As mentioned above, CaF_2 stripe-like surfaces can be applied as a growth template for quantum wire growth of other substances. Such CaF_2/Si (100) specimens were used as a substrate for IV-VI material deposition. The resulting overgrowth is presented in Fig. 7.2. It shows that the structure of the CaF_2 template is preserved. These results are the intermediate steps for the future use of fluoride templates for 1D growth of IV-VI materials.
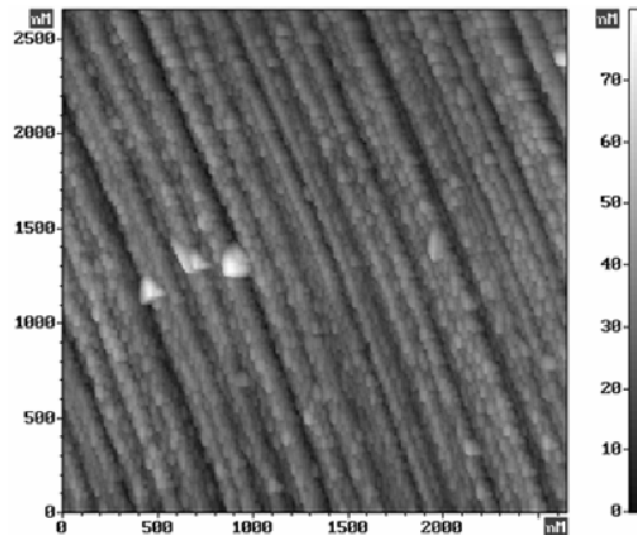
Fig. 7.2. CaF_2-on-Si (001) structure overgrown with PbSe (AFM image).

These results were achieved in cooperation with the Ioffe Institute. The fluoride layers were grown at the Ioffe Institute MBE fluoride equipment, and IV-VI MBE growth was performed at ETHZ. The same growth procedure for the fluoride at ETHZ led to different results. As shown in Fig. 7.3, two instead of one growth directions of fluoride stripes have appeared. Such a grid of perpendicular stripes was already observed before [110]. The differences can be traced back to the different miscuts of the silicon wafers (0.1° at Ioffe Institute and 1° at ETHZ) and slightly different cleaning procedures of the Si surface before epitaxy. This grid-type structure may be used as a template as well. Small sizes of the cells formed (< 100 nm) allow to grow low-dimensional structures by filling in the desired materials.

CaF_2/BaF_2 templates grown on Si (100) are therefore of great interest for the further formation of low-dimensional structures, including overgrowth with lead chalcogenides to form QDs and QWis. The above discussed results are the intermediate steps for the future use of fluoride templates for 0D or 1D growth of IV-VI materials.
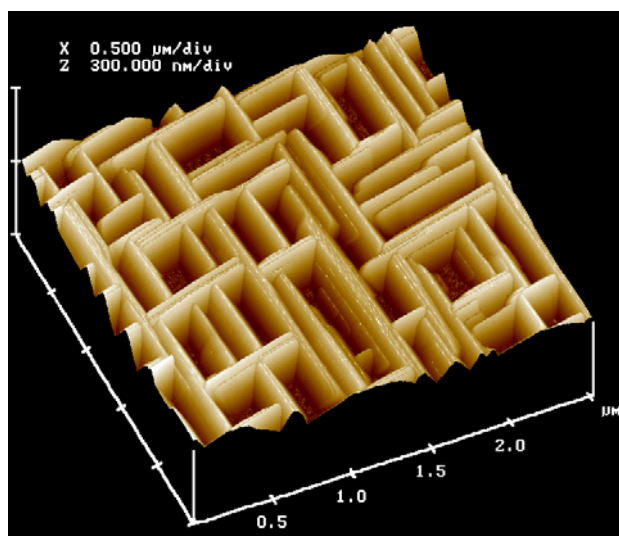
Fig. 7.3. AFM image of the morphology of a 50 nm thick CaF$_2$ layer on Si (100). The stripes have two possible orientations: [110] and [-110].

Chapter 8

Two- and three-dimensional structures: IV-VI optoelectronic devices for the mid-IR range

For a long time the infrared part of the electromagnetic spectrum with wavelengths 2÷100 μm has been either not covered by semiconductor devices or used for specific purposes only, as, for instance, military applications. One technical problem of the infrared range is that most semiconductor lasers have to be cooled. Today, there are some trends to obtain stimulated IR emission near or at room temperature. This can lead to a broad usage of the 2÷5 μm wavelength range, by employing novel devices like:

1. Double heterostructure lasers based on $Ga_{1-x}In_{1-y}As_xSb_y/Al_{1-z}Ga_{1-u}As_zSb_u$ materials [111].

2. *Type-I* multi quantum well (MQW) lasers based on $Ga_{1-x}In_{1-y}As_xSb_y/Al_{1-z}Ga_{1-u}As_zSb_u$ layers [112].

3. *Type-II* lasers, including:

   a. Multi quantum well lasers containing $InAs/In_{1-x}Ga_xSb$ [113].

   b. Lasers with $InAs/Ga_{1-x}In_xSb$ or $GaSb/Al_{1-x}As_xSb$ "W" shaped active regions [114].

4. Interband cascade lasers made from $AlSb/InAs/In_{1-x}Ga_xSb$ materials [115].

5. Intersubband quantum cascade lasers fabricated with $Ga_{1-x}In_xAs/In_{1-y}Al_yAs$ [116] or $GaAs/Al_{1-x}Ga_xAs$ [117] emitting components.

6. IV-VI lasers, including:

   a. Electrically pumped edge-emitting double heterostructures (DH) like $Pb_{1-x}Sr_xSe/PbSe/Pb_{1-x}Sr_xSe$ [118], or DH and MQW $Pb_{1-x}Sr_xS/PbS$ structures [119].

   b. Optically pumped vertical cavity surface-emitting lasers based on 0D $Pb_{1-x}Eu_xTe/PbSe$, 2D or DH $Pb_{1-x}Eu_xTe/PbTe$ active regions [120, 121], or 2D $Pb_{1-x}Sr_xSe/PbSe$ [122].

   c. Optically pumped edge-emitting lasers based on 2D or DH $Pb_{1-x}Eu_xSe/PbSe$ [123].

According to their output power characteristics, monomode/multimode operation, tunability, pulsed/continuous wave operation and other parameters, IR lasers can be used including the following:

- Environmental monitoring spectroscopy (Fig. 8.1 shows typical absorption lines of gases and vapors in the atmosphere),

- Industrial process control spectroscopy,

- Direct atmospheric communications (within the atmospheric transmission windows),

- Military applications (pump lasers, radars, lidars),

- Medicine needs (reconstructive surgery, ophthalmology).

IV-VI lasers satisfy all the requirements of an IR source for spectroscopy needs. The emission wavelength of lead chalcogenide lasers can be tuned by temperature over a wide mid-infrared range (see Fig. 2.6). For monomode emission, the temperature coefficient is still $\approx 3 \times 10^{-4}$ K^{-1}. The output power is high enough for spectroscopic analysis (spectroscopy works reliably with source powers above 1 mW for III-V lasers [124] and at even lower powers for IV-VI lasers [125]).
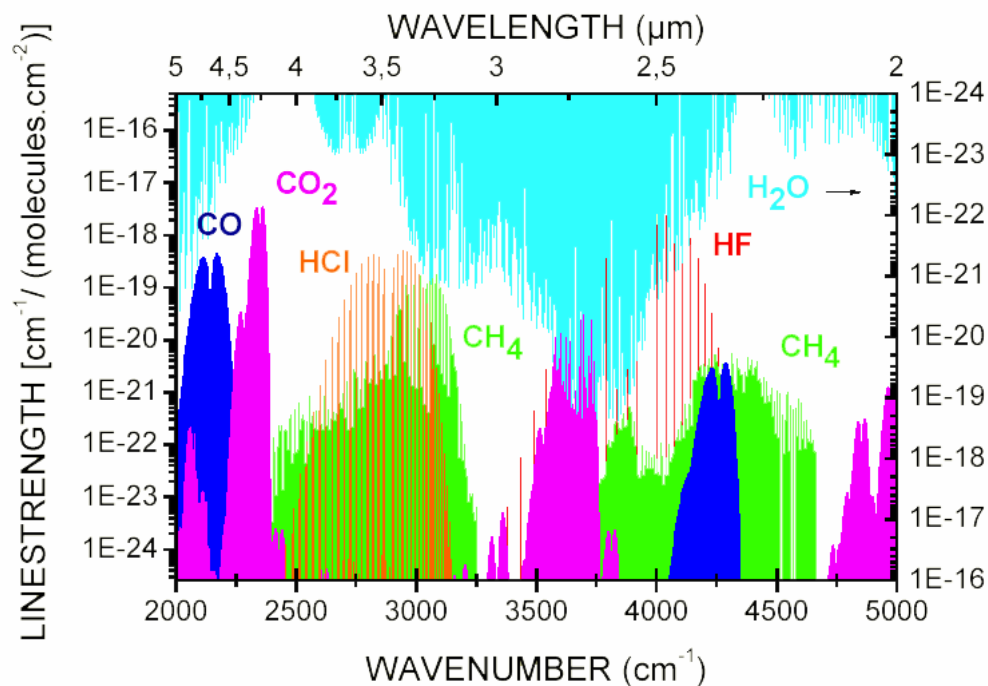
Fig. 8.1. Main absorption lines of important atmospheric gases (left scale) and water vapours (right scale) shown in the mid-IR range. From [124] with the kind permission of the author.

In Sections 8.2 and 8.3, two types of IV-VI infrared emitters operating above (lasers) and below ("wavelength transformers") the threshold will be described. In order to increase performance characteristics (for lasers) and to obtain cavities (for transformers), Bragg mirrors were introduced (Section 8.1).

In addition, Bragg reflectors play a very important role in manufacturing of high efficiency photovoltaic detectors with narrow band spectral response. This is discussed in Section 8.4. The performance of all these devices depends on the material quality. The optical properties of the layers are sufficient for applications of these devices. However, the electronic quality of the IV-VI materials essentially limits device performance. In Section 8.5, experiments are described how this quality is assessed and ways for further improvements are discussed.

8.1 Bragg mirrors

Simple metallic layers often give adequate performance for mirrors in optical instruments. For some applications, where the reflectance must be higher than can be achieved with simple metal layers (for example, for vertical cavity surface-emitting laser (VCSEL)), the reflectance can be increased by an addition of extra dielectric layers. Multilayer all-dielectric reflectors consisting of alternating films of high and low refractive index, which combine maximum reflectance with minimum absorption, are called Bragg reflectors (or mirrors) under certain conditions (discussed in Section 8.1.1). These reflector stacks are used as laser mirrors, resonant cavities, colour beam splitters, heat reflecting filters, solar cell covers and for many other applications. They are of high importance for optoelectronic devices in the infrared range as well.

8.1.1 Theoretical considerations

The high reflectivity of Bragg mirrors is achieved by constructive interference of all waves reflected at the different boundaries of a multilayer structure (Fig. 8.2). The interfaces are flat and layers with high (H) and low (L) refractivity indices alternate. For nonabsorbing materials there is no phase shift for the reflection in the layer with higher reflectivity index and 180° phase shift for the reflection in the lower refractivity index layer. If the thicknesses of the ith layer equals

$$d_i = \frac{\lambda_0}{4n_i},$$

(8.1)

with λ_0 the wavelength of the incoming wave and n_i the refractive index of the ith layer, or a multiple of this value, all reflected waves interfere constructively at λ_0 (so-called quarter wavelength $\lambda/4$ layers).

The mirror characteristics are governed by the refractive index contrast n_H/n_L and the number of $\lambda/4$ pairs N. At the design wavelength λ_o, the reflectivity R of a Bragg mirror consisting of N $\lambda/4$ pairs is given by:

$$R = \left(\frac{1 - \dfrac{n_t}{n_i}\left(\dfrac{n_L}{n_H}\right)^{2N}}{1 + \dfrac{n_t}{n_i}\left(\dfrac{n_L}{n_H}\right)^{2N}} \right)^2 , \tag{8.2}$$

where n_i and n_t are the refractive indices of the materials in front of and behind the multilayer stack [126].
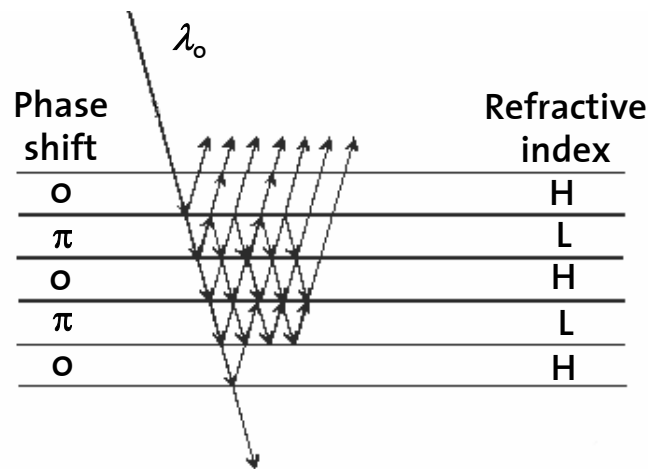
Fig. 8.2. Schematic view of the wave propagation in multifilm mirror.

If one takes H and L layers with a very high index contrast (e.g. a factor two) then even three pairs of H/L films yield a reflection of the system higher than 98%. An even better index contrast is obtained with lead chalcogenide and fluoride pairs. As an example, calculations of the spectral reflectivity R of $Pb_{0.96}Eu_{0.04}Te/BaF_2$ (n_H=5, n_L=1.45 at RT) pairs with different numbers N for the target wavelength λ_o=4.2 µm (CO_2 absorption peak) are shown in Fig. 8.3. The calculations are performed using the matrix method outlined in Section 3.4.2. From these matrix simulations follows that a very high reflectivity (R>99%) is achieved with already three pairs. This is a significant advantage of such a type of material combination, while Bragg multistacks with III-V material require 10÷30 pairs to show similar values in the infrared range (e.g. 11 pairs of $GaSb/AlAs_{0.08}Sb_{0.92}$ yield R≈99% at λ_o=3 µm [127]).

Moreover, due to the high index contrast, the Bragg mirror stop band is very broad, which gives more design freedom. Bragg mirrors can be obtained for any wavelength. In order to get high quality Bragg reflectors,

the thicknesses of the films have to be accurately controlled, and the layers have to be smooth and transparent in the wavelength range of interest.
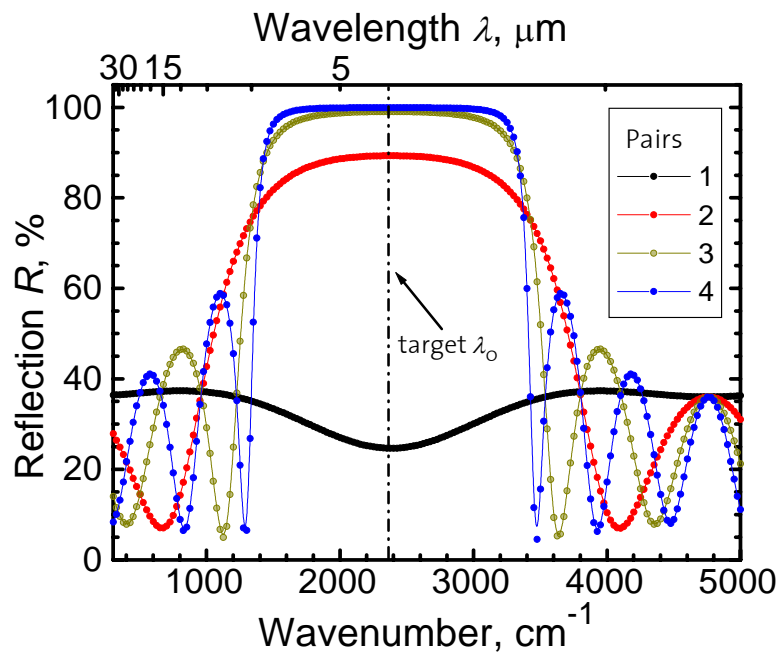
Fig. 8.3. Calculated spectral reflection for the target wavelength λ_o=4.2 µm for 1, 2, 3 and 4 Bragg $Pb_{0.96}Eu_{0.04}Te/BaF_2$ mirror pairs grown on Si. T=300 K.

8.1.2 Bragg mirrors for the mid-infrared range

In the present work, Bragg mirrors were used for:

1.   Edge-emitting lasers. λ_o/4 air grooves were etched for some structures to increase reflectivity of the mirrors (Appendix B and Section 8.2).

2.   Wavelength transformers. $Pb_{0.95}Eu_{0.05}Se/BaF_2$ pairs were grown as a bottom mirror and $EuSe/BaF_2$ or TiO_2/SiO_2 pairs as a top mirror (Section 8.3).

3.   Resonant cavity detectors. In order to obtain narrow band spectral photosensitive devices with high quantum efficiency, bottom mirrors $Pb_{0.95}Eu_{0.05}Se/BaF_2$ were applied (Section 8.4).

Separate single Bragg mirrors are useful for external cavity devices, as reflection coatings and as mirrors for general purposes. As an example, a 2.5-pair mirror with three high refractive index PbTe layers (n_H=5.7) and two low index BaF_2 layers (n_L=1.45) grown on Si (111) is shown in Fig. 8.4. The reflectivity (Fig. 8.5) of such a multistack is very high (R≈100% within the accuracy of the FTIR spectrometer).

n=5.7	PbTe
n=1.45	BaF$_2$
n=5.7	PbTe
n_L=1.45	BaF$_2$
n_H=5.7	PbTe
n_{sub}=3.42	Si (111)
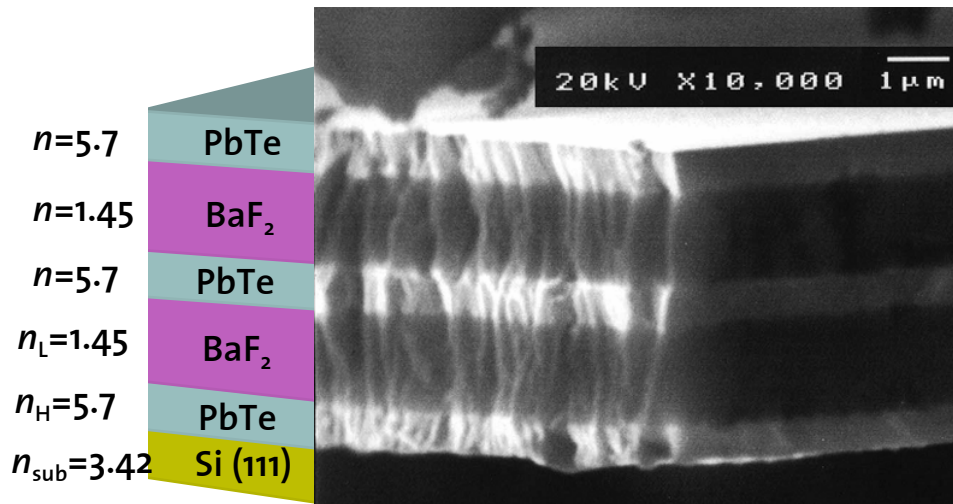
Fig.8.4. SEM image and schematic drawing of the mirror profile with five layers PbTe/BaF$_2$ designed for the wavelength λ_o=11 μm.
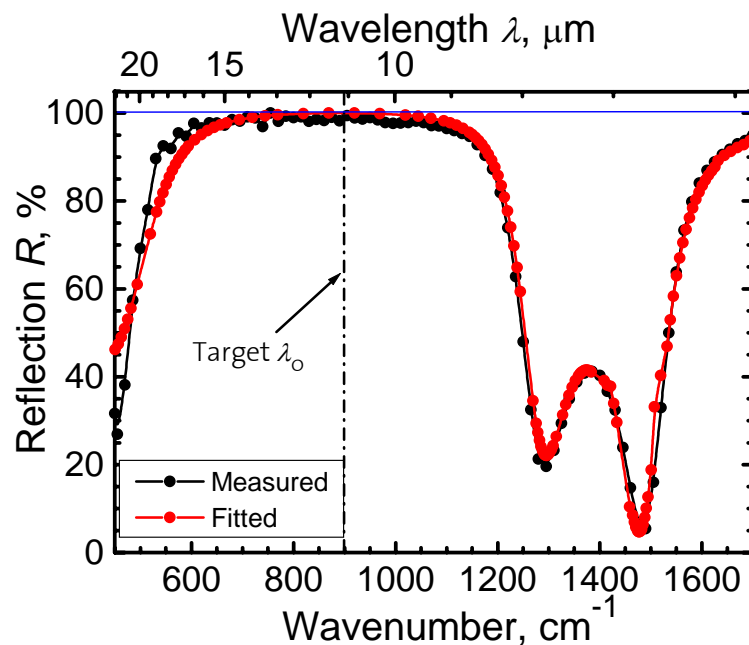
Fig. 8.5. Room temperature transmission spectrum of a 2.5-pair Bragg mirror designed for λ_o=11 μm, measured and fitted curves. The spectrum is not corrected relative to the Al calibration mirror reflection (R≈98%). T=295 K.

8.2 IV-VI edge-emitting lasers based on quantum wells and double heterostructures

Edge-emitting mid-IR IV-VI lasers are known for more than 30 years. A recent review is given by Ishida [129]. Nearly all lasers are fabricated on bulk PbA (A=S, Se, Te) substrates. Some companies fabricate IV-VI IR-lasers on a commercial basis. The company "Laser Components" (Germany)

produces electrically pumped lead chalchogenide IR lasers which typically operate at liquid nitrogen temperature [130]. The American company "Ekips Technology" sells electrically pumped 4÷7.5 μm emitting devices with maximum operation temperature of 115 K [131]. Another American company "Laser Photonics" reached the highest continuous wave (cw) operation temperature of 223 K [132] for electrically pumped devices.

Academic groups in Oklahoma and Linz fabricate optically pumped VCSEL structures grown on BaF_2 substrates. They achieved lasing at temperatures above 300 K: $Pb_{1-x}Eu_xTe/PbTe$ based VCSEL structures operate up to 316 K at λ=3.8 μm [120] and VCSELs containing $Pb_{1-x}Sr_xSe/PbSe$ multiple QW layers have laser emission up to 325 K for λ=3.8 μm [133]. For the excitation to achieve population inversion, both groups use bulky high power Nd:yttrium-aluminium-garnet lasers with 1÷2 μm wavelengths.

The main difference between optically pumped VCSEL and edge-emitters is shown in Fig. 8.6. VCSEL structures need high reflectivity mirrors (R>99%), and the active layer thickness has to fit the target wavelength exactly. Edge-emitters operate with much lower reflection mirrors and exact optical thicknesses are not critical. This means that the design freedom for edge-emitting lasers is higher.

In the present work, optically pumped edge-emitting IV-VI lasers on Si and BaF_2 substrates are described, which are pumped with low cost III-V based laser diodes. III-V laser diodes with wavelengths ranging from 870 nm to 1550 nm were used as a pump source. Typical pulse width was 150
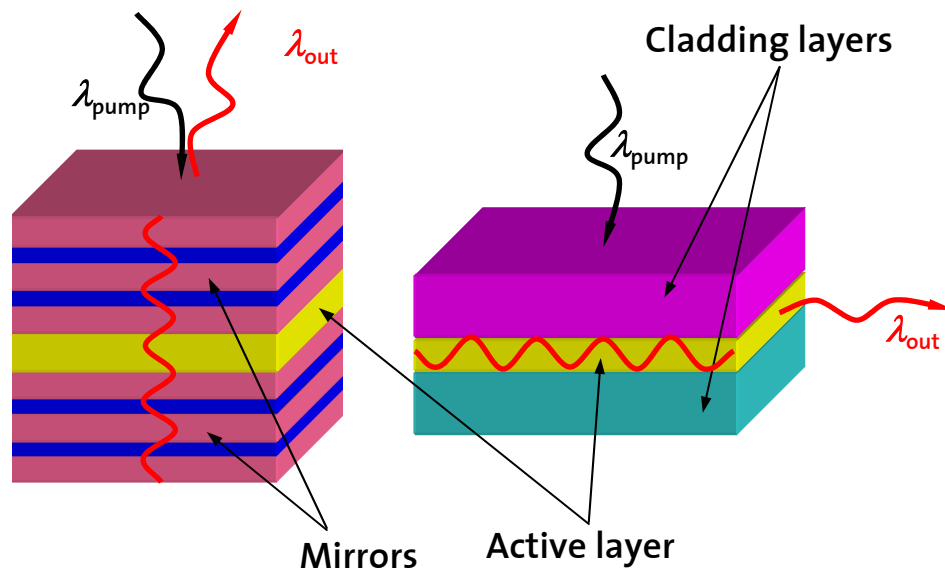
Fig. 8.6. Schematic presentation of an optically pumped VCSEL structure (left) and an edge-emitting laser (right). An amplified wave propagates in the same plane as the excitation beam in surface-emitters and perpendicular to the pumping beam in the edge-emitters.

ns with 8 kHz repetition frequency and maximum pump power was 5.5 W_p at the sample. The beam size on the sample surface is about 20×350 μm², it depends on the focusing of the measuring setup. With optical pumping, no p-n junctions with low ohmic contacts have to be fabricated.

The best results in the present work have been achieved by growing DH or QW structures. They consist of a bottom $Pb_{1-x}Eu_xA$ (A=Se, Te) cladding layer, the active QW (see Section 8.2.1) or DH (see Section 8.2.2) part and a top EuSe or EuTe cladding layer which is transparent to the incoming pump beam. Several procedures of mirror preparation are discussed in Appendix B. The thickness of the top cladding layer should be selected in a way that it reflects the lowest possible amount of laser pump radiation. In Fig. 8.7 a reflection spectrum of a IV-VI laser structure with a 700 nm thick EuSe top layer is shown. The lowest reflection is for λ_{pump}=920÷940 nm, while somewhat higher reflection occurs for 870 nm illumination.
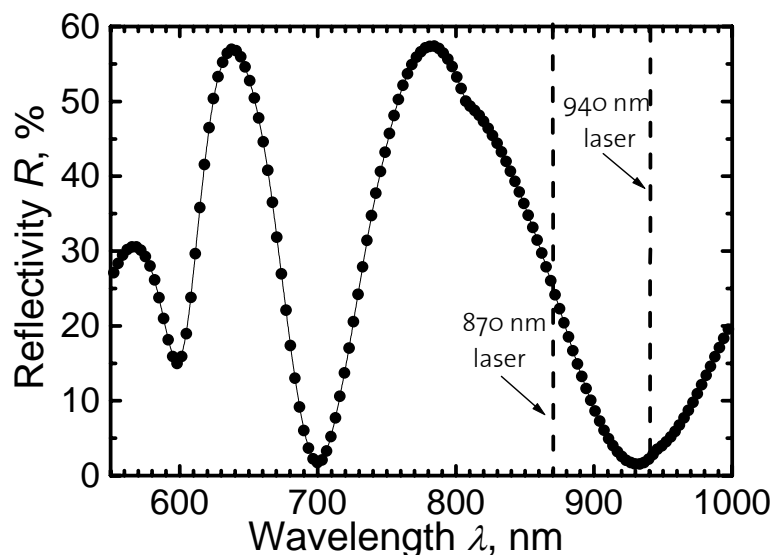
Fig. 8.7. Reflectivity of a laser structure with a 700 nm thick EuSe top cladding layer. At 870 nm wavelength, 30% of radiation is reflected, while when illuminated with a 940 nm laser, reflection is as low as 3%. T=295 K.

8.2.1. Quantum well lasers

Quantum well lasers comprise 2D structures in their active region. As discussed in Chapter 2, adding of europium allows to achieve electrical and optical confinement for the IV-VI layers. A four quantum well structure and its confinement diagrams are schematically shown in Fig. 8.8. 2D structures are used in order to improve the inversion characteristics: Lower

carrier densities are needed to get inversion [134] and Auger recombination is lower in comparison with DH structures [135]. Moreover, QWs lead to a blue shift (shift to shorter wavelengths) in comparison with bulk materials due to the additional quantization. The quantum size effect splits the four-fold degeneracy at the L point of both conduction band and valence band into a singlet longitudinal valley and triplet oblique valleys [136]. These transitions between low-density of states longitudinal valleys theoretically lead to lower threshold excitation powers and give a good possibility to tune the emission wavelength not only by temperature change, but also by band gap engineering.
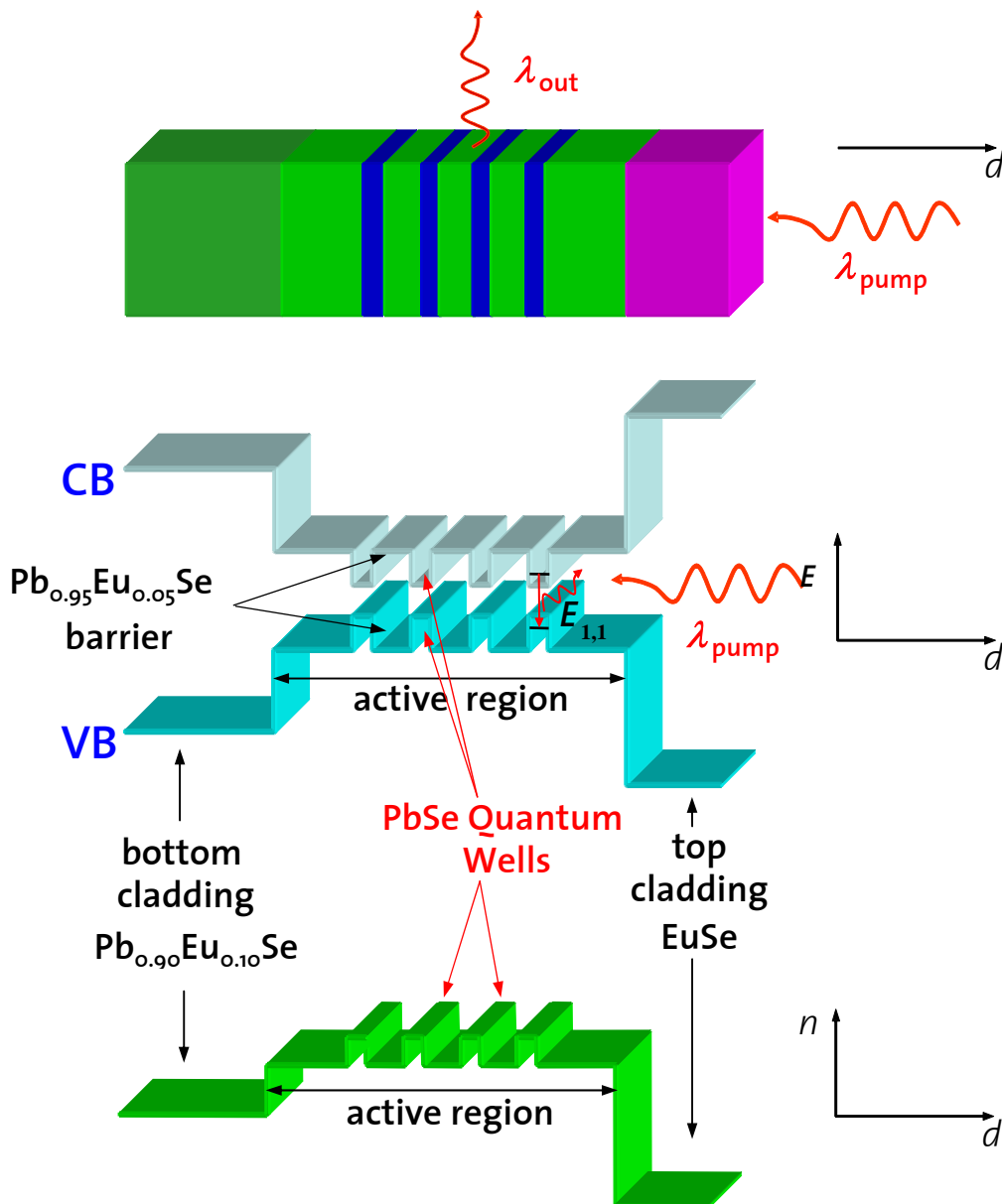
Fig. 8.8. Schematic presentation of a laser structure with four PbSe QWs in the active region separated by $Pb_{0.95}Eu_{0.05}Se$ layers (top) and electrical ($E_g(d)$, middle) and optical ($n(d)$, bottom) confinements. $Pb_{0.90}Eu_{0.10}Se$ and EuSe layers are bottom and top claddings, respectively, used for the waveguiding.

Changes of emission wavelengths due to quantum well energy level shifts are quite high. As an example, stimulated emission from a two quantum well PbSe/Pb$_{0.97}$Eu$_{0.03}$Se laser structure with d_{PbSe}=10 nm and barrier d_{PbEuSe}=20 nm was measured as a function of temperature (Fig. 8.9). The results are compared with the PbSe bulk values (Fig. 8.10) [137]. From the graph follows that the energy difference is the same for the
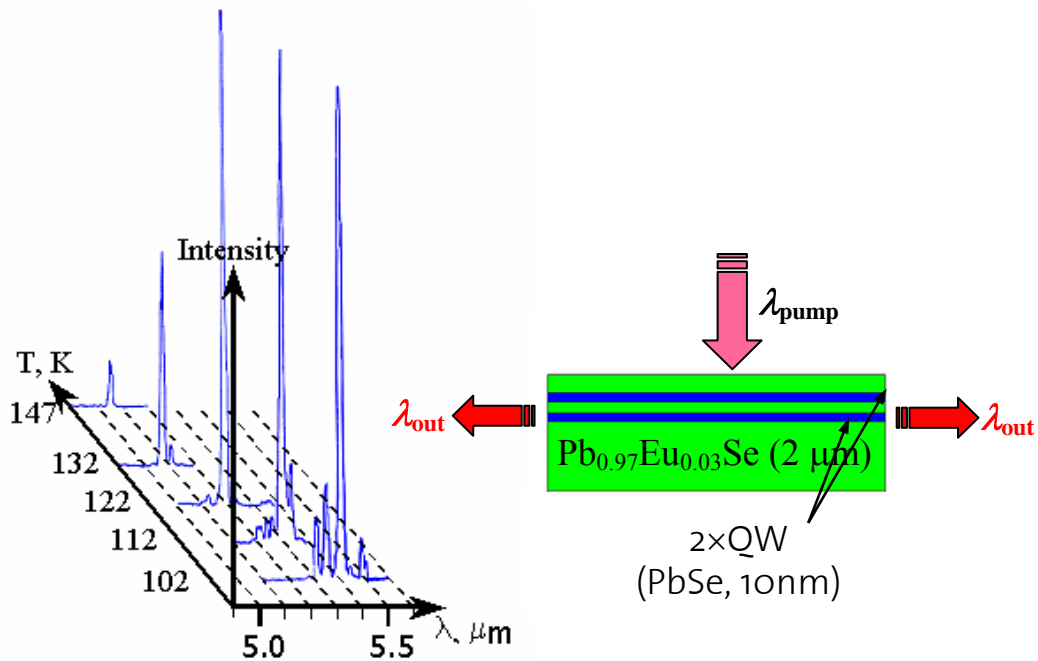
Fig. 8.9. Temperature dependence of emission intensity and emission wavelength (left) of a laser structure with 2 QWs (right). After [137] with the kind permission of the author.
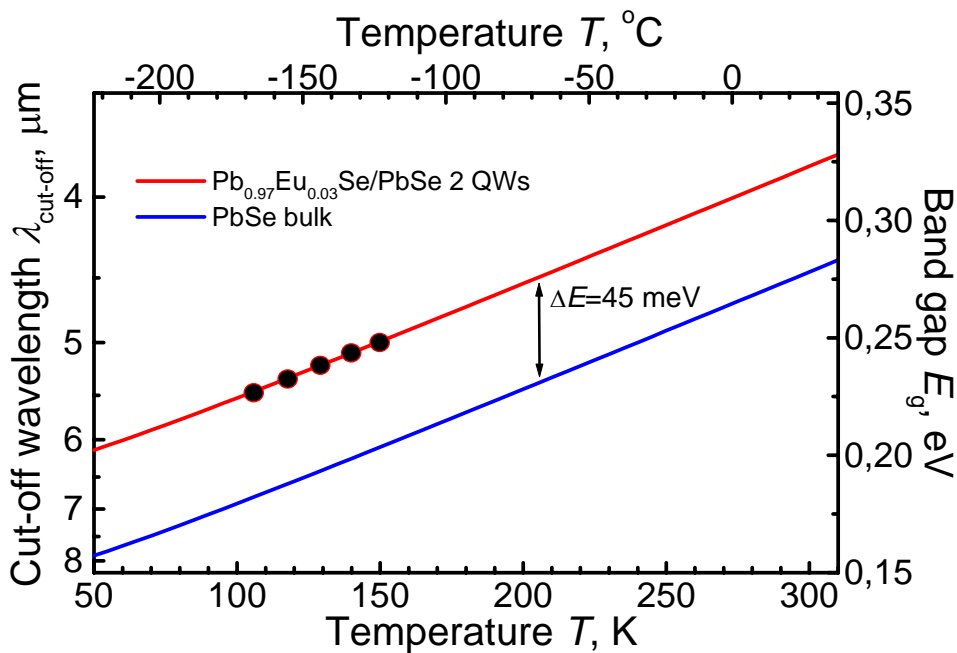
Fig. 8.10. Blue shift of the laser emission from a structure with Pb$_{0.97}$Eu$_{0.03}$Se/PbSe QWs in comparison with bulk PbSe.

temperature range measured and is as high as ΔE=45 meV. This value is in agreement with experiments made by Wu *et al.* [136], who described photoluminescence from multiple quantum wells based on PbSe/Pb$_{1-x}$Sr$_x$Se materials.

For optimal quality of QW lasers, interfaces between the quantum well and the barrier have to be abrupt and smooth, and Eu interdiffusion should be minimal. According to RHEED pictures, PbSe quantum wells thicker than 10 nm are growing 2-d on Pb$_{1-x}$Eu$_x$Se. A TEM image (Fig. 8.11) confirms the sharp interface between QW and barrier layers.
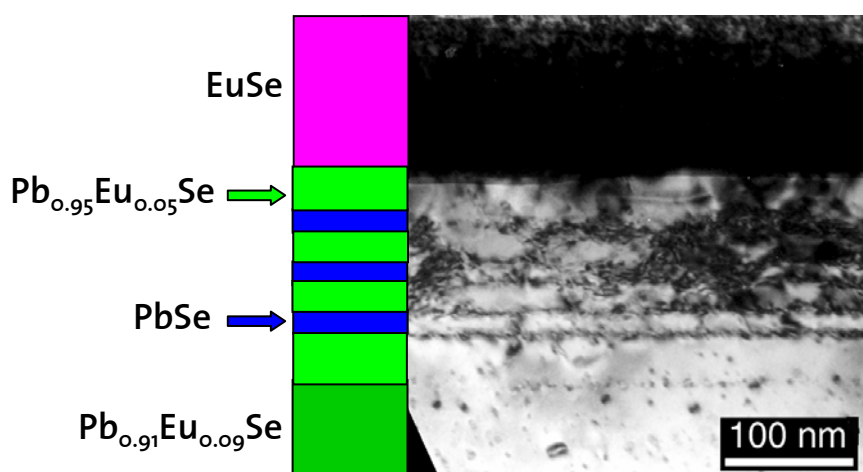
Fig. 8.11. TEM cross-section image of a structure with 3 PbSe quantum wells with Pb$_{0.95}$Eu$_{0.05}$Se barriers, EuSe top and Pb$_{0.91}$Eu$_{0.09}$Se bottom claddings. Image by P. Brunkov, Ioffe Institute, Russia.

The comparatively small Eu interdiffusion coefficient in the PbSe/Pb$_{1-x}$Eu$_x$Se system is D=4×10^{-18} cm²/sec for a substrate temperature T_w=643 K and D=8×10^{-18} cm²/sec for T_w=693 K, according to Springholz *et al.* [23]. Approximately the same values were obtained by Valeiko *et al.* [138]: The authors report about D=1×10^{-17} cm²/sec for a substrate temperature T_w=633 K. These values are smaller than those for tellurides (for the PbTe/Pb$_{1-x}$Eu$_x$Te D=1×10^{-16} cm²/sec for T_w=643 K [139]). At least for the diffusion values, the selenide system seems to be superior to the telluride system for the fabrication of QW structures.

For the design of the QW laser structures, suitable thicknesses of quantum wells and barriers have to be found. The following essential factors should be taken into consideration:

- The thickness of the well should correspond to 2D quantization conditions. Well thickness determines the well energy levels and for IV-VI materials should be below 50÷100 nm [136].

- Barrier heights should be higher than k_BT. The value for room temperature is $k_BT(300\ K)=25.8$ meV and for liquid nitrogen temperature $k_BT(77\ K)=6.6$ meV. The increase of the band energy is $\Delta E_g=27$ meV for $Pb_{1-x}Eu_xSe$ and $\Delta E_g=35$ meV for $Pb_{1-x}Eu_xTe$ per atomic percent x of europium. A europium concentration of $x=2\div3\%$ is therefore high enough to achieve QW conditions.

- Thickness of the barriers. On one hand, the barriers should not be too thin to avoid coupling with neighbour wells and tunnelling ($d_{barr}\sim1$ nm) [140]. On the other hand, for too thick barriers the mean free path of the free carriers in the barriers generated by the pump source can be smaller than the barrier width, recombination then occurs already in the barrier but not in the quantum well layer. A value $d_{barr}\approx20\div40$ nm for $Pb_{0.95}Eu_{0.05}Se$ barrier material was chosen [137].

- The strain induced in the quantum well. This strain is due to the lattice mismatch between the quantum well and the barrier layer. For the multiple quantum wells (MQW) $PbTe/Pb_{0.95}Eu_{0.05}Te$ structure the strain in the PbTe well decreased monotonically from an almost fully strained layer ($\varepsilon_\parallel=2.78\times10^{-3}$) to 26% strain relaxation as the well width increased from 2.3 to 20.6 nm for structures on BaF_2 (111) substrates [141]. A parallel strain in PbTe for a 20 nm thick well and 50 nm thick barrier was calculated as $\varepsilon_\parallel=1.89\times10^{-3}$. For selenides, a strain for the 20 nm thick PbSe well and 40 nm $Pb_{0.96}Eu_{0.04}Se$ barrier was reported as $\varepsilon_\parallel=1.97\times10^{-3}$ [138].

All these above-indicated four points have to be considered for a good design and have been applied in our structures. Illuminated with the III-V pumping lasers described above, the highest operation temperatures of QW lasers were above 230 K for $PbSe/Pb_{0.95}Eu_{0.05}Se$ structures with three quantum wells grown on BaF_2 (111) as well as on Si (111) (Fig. 8.12). A spectrum of the laser emission is shown in Fig. 8.13. More details of the device performance may be found in [72, 109, 137].
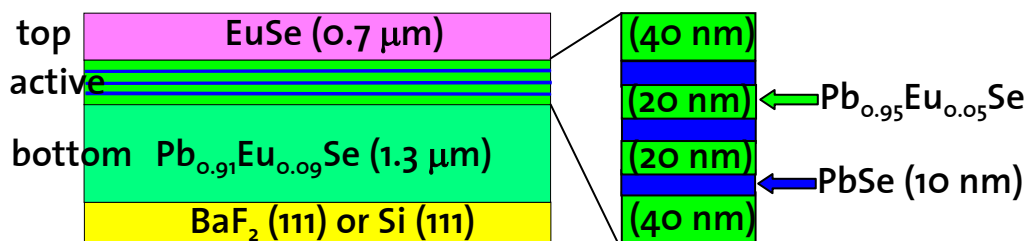
Fig. 8.12. Cross-section of a QW laser structure grown on BaF_2 or (111) with operation temperature up to 233 K. The active region is enlarged to show three 10 nm thick PbSe QWs between the $Pb_{0.95}Eu_{0.05}Se$ barriers.

8.2.2. Double heterostructure lasers

As already mentioned, the highest operation temperatures for edge-emitting lasers in the present work were obtained for double heterostructures. Experiments with continuous wave photoluminescence show that emission temperature up to 463 K and strong signals can be achieved with bulk PbSe and PbTe structures, but not with PbSe/$Pb_{1-x}Eu_xSe$ and PbTe/$Pb_{1-x}Eu_xTe$ multiple quantum well structures. Moreover, the luminescence signal of PbSe sample is twenty times higher than in PbTe measured under the same conditions [142]. The same tendency was found by Fürst *et al.* [121]: Bulk-like and QW VCSEL show comparable performance and there is no effective improvement achieved by the reduction of the dimensionality, contrary to III-V devices. All these measurements were done for structures grown on BaF_2 substrates.

Fig. 8.13. Spectrum of emission at T=115 K of a laser with the design given in Fig. 8.12.

For the edge-emitting laser structures grown on Si (111) and (100) as well as on BaF_2 (111) substrates of the present work the same was observed: DHs show the highest operating temperatures. The highest operating temperature T_{max}=250 K was measured for a PbSe double heterostructure between a bottom $Pb_{1-x}Eu_xSe$ and a top EuSe cladding layers (Fig. 8.14).

The experiments of Kellermann [137] with PbSe and PbTe based active layers grown by the author of this thesis support the results of Böberl *et al.* [142]: Lasers with PbSe active region have higher maximal operation temperature than PbTe (T_{max}(PbSe)=250 K vs. T_{max}(PbTe)=155 K) and the output intensity of PbSe lasers is higher than of the PbTe structures under the same excitation conditions.
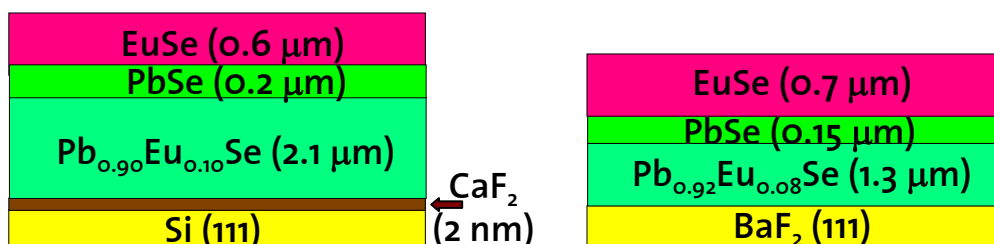
Fig. 8.14. Double heterostructure lasers based on a PbSe active layer and two cladding layers for the optical confinement grown on Si (left) and BaF_2 (right). These structures have shown the highest operation temperature T_{max}=250 K.

8.2.3 Comparison of structures with different types of mirrors

Four different methods of mirror fabrication were developed in the present work:

- Cleaving,

- Wet chemical etching,

- Reactive ion etching (RIE),

- Focused ion beam (FIB) etching.

They are described in Appendix B.

The best way to determine the properties of the mirrors is to measure laser characteristics such as: maximum operation temperature, threshold power and intensity of stimulated emission. All these parameters are described in details in [137]. Up to now, the best results were obtained with the lifted-off and cleaved structures for (100) orientation and FIB etched mirrors for (111) oriented lasers. Recent experiments show comparable laser characteristics for the same laser layers but different methods of mirror manufacturing. For example, the intensity of laser emission and its temperature behaviour looks identical for lasers with cleaved and FIB etched mirrors for both (100) and (111) oriented layers (Fig. 8.15 and Fig. 8.16). Most surprising results were obtained by measuring laser structures grown on BaF_2 (111): Inclined cleaved mirrors (see Fig. B.6) give the same intensity as perfectly FIB etched vertical facets (Fig. B.11), as shown in Fig. 8.16 [143].

Note that the inclination angle of the mirror ($\theta \approx 35°$) is above the critical angle for total reflection $\theta > \theta_c$ for a beam propagating parallel to the interface, where

$$\theta_c = \arcsin\left(\frac{n_{Air}}{n_{Laser}}\right) \approx 12° \tag{8.3}$$

for n_{Laser}=4.75 and n_{Air}=1. This is a demonstration of the fact that guided modes in planar open waveguides can be described as a set of plane waves running at an angle to the interface.

Fabrication of additional quarter wavelength grooves made by FIB (Fig. B.12, right) did not lead to better laser performance in comparison with lasers with only one groove (Fig. B.12, left). Both maximum operating temperature and intensity of emission remained the same despite a decrease of external losses α_{ext} by more than ten times (see Appendix B). This fact can be explained by formula (B.2), where threshold gain is determined by α_{ext} and α_{int}. Having $\alpha_{ext} \ll \alpha_{int}$, it is essential to consider
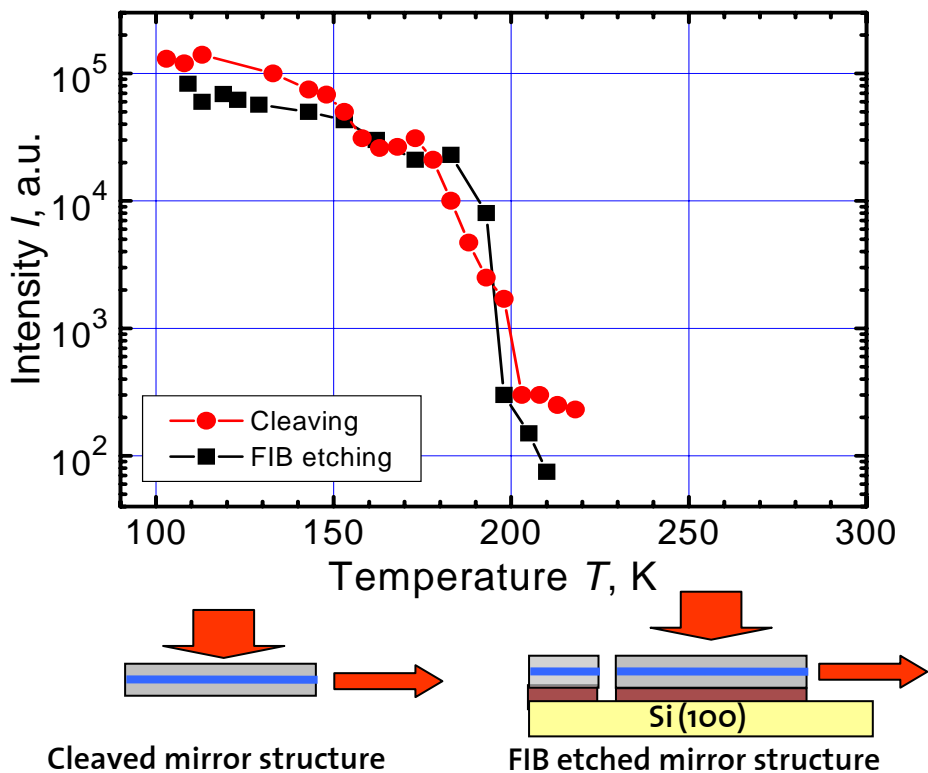
Fig. 8.15. Intensity of the laser emission as a function of temperature for the same structure but differently prepared mirrors: Circles stay for the lifted-off structure with cleaved laser facets by internal strain and squares for the focused ion beam etched facets.
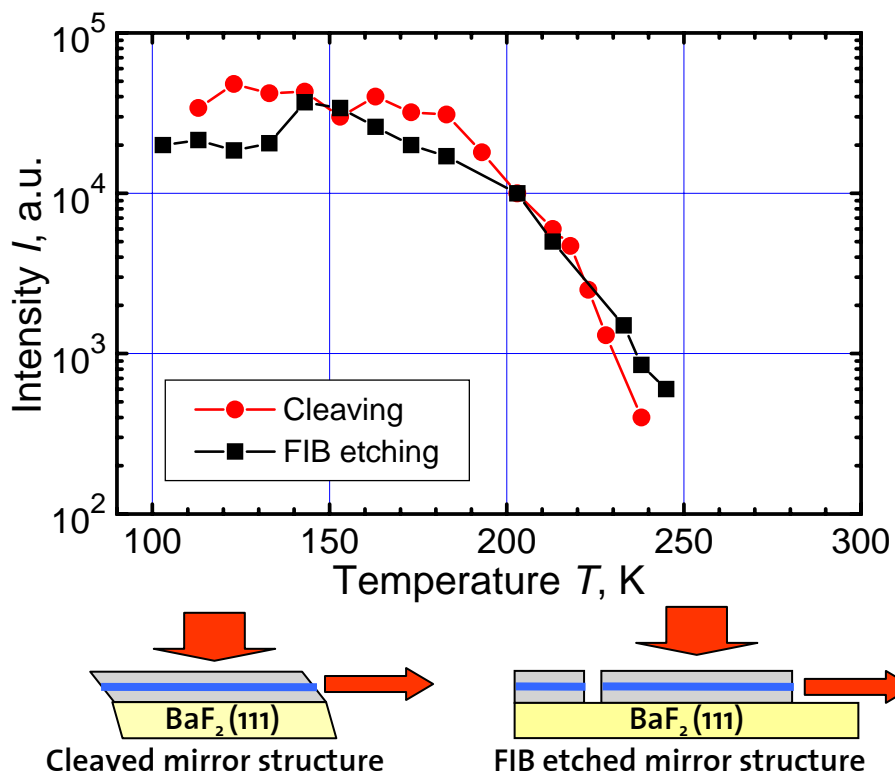
Fig. 8.16. Intensity of the laser emission as a function of temperature for the same structure but differently prepared mirrors: Circles stay for cleaved inclined laser facets (schematically shown left bottom) and squares for focused ion beam etched facets (right bottom).

internal losses as the main factor to affect the output parameters of a laser.

More suitable for mass production are wet chemical and RIE etching methods. However, these methods show somewhat less promising results and etching technology has to be developed further. RIE can introduce damage by reactive ions in regions near the surface [107]. Isotropic etching with wet chemicals leads to underetching. With successful development of these two procedures it will be possible to avoid such drawbacks in laser preparation as low yield (cleaving) and low etching speed (FIB).

8.3 Wavelength transformer

Vertical cavity surface-emitting devices (VCSEDs) operate below laser threshold and are based on photoluminescence properties. It was shown that the photoluminescence of lead chalcogenide structures is, according to Majumdar *et al.* [144], "high-power light emission" up to very high temperatures (463 K) [142]. Photoluminescence is usually broadband and extends over a wide emission angle. In order to obtain a narrow, peaked emission line, the material showing photoluminescence is placed inside a resonant cavity, thus forming an active cavity [145]. These cavity structures are based on Fabry-Pérot filters.

An active Fabry-Pérot filter (or "wavelength transformer") for the mid-infrared wavelength range can be constructed with IV-VI materials, too. As a Fabry-Pérot filter for resonance at wavelength λ_0, it consists of an active $\lambda_0/(2n)$ spacer layer between a high reflectivity bottom and top mirror. These mirrors may be Bragg mirrors as described in Section 8.1.

A wavelength transformer which converts part of the incoming $\lambda_{in}=970$ nm light emitted from a commercially available III-V laser to $\lambda_0=3\div5$ μm wavelength was realized. It has a similar structure as a VCSEL (vertical cavity surface-emitting laser), but lower reflectivity of the top and bottom mirrors for optimal performance: A $\lambda_0/2$ $Pb_{1-x}Eu_xSe$ active layer containing PbSe quantum wells at the antinodes of the standing wave pattern is sandwiched between the two Bragg mirrors. The top mirror can be formed either by single crystalline (BaF_2/EuSe layer pairs grown by MBE) or by polycrystalline (SiO_2/TiO_2 pairs grown by e-beam evaporation, Fig. 8.17), but it should be transparent to the incoming light. The bottom mirror consists of one (or more) pairs of $Pb_{1-x}Eu_xSe/BaF_2$ layers (Fig. 8.18).

The layers were grown by MBE on Si (111) or BaF_2 (111) substrates, which are transparent to the output beam and also act as a mechanical protection. FTIR measurements show a narrow peak separated by quite broad low-transmission regions (Fig. 8.19, left).

The device works at a room temperature in the subthreshold region. The line width is given by the resonator design, and is about 6% for the present design (Fig. 8.19, right). The power efficiency is above 10^{-4} [146]. The full widths at half maximum (FWHM) and efficiency depend on mirror reflectivities.

$\Leftarrow$ TiO$_2$ (n=2.4)

$\Leftarrow$ SiO$_2$ (n=1.45)

$\Leftarrow$ **Resonator**
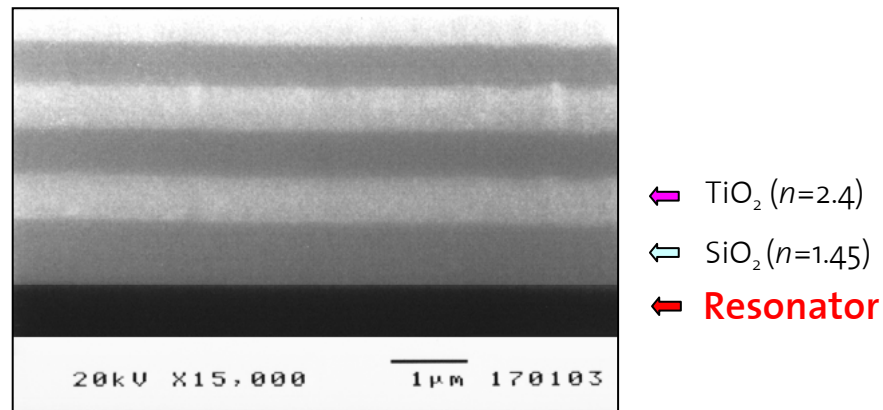
Fig. 8.17. SEM cross-section of a top Bragg mirror consisting of three SiO$_2$/TiO$_2$ pairs.

λ_{in}=970 nm

Top mirror
h
L
h
L
h
L

$\Leftarrow$ EuSe or TiO$_2$ (n=2.4)

$\Leftarrow$ BaF$_2$ or SiO$_2$ (n=1.45)

Resonator 2H

Bottom mirror { L H

$\Leftarrow$ **QW: PbSe (20 nm)**
$\Leftarrow$ Pb$_{0.95}$Eu$_{0.05}$Se ($n \approx 4.5$)
$\Leftarrow$ BaF$_2$
$\Leftarrow$ Pb$_{0.95}$Eu$_{0.05}$Se

Si (111) or BaF$_2$ (111) $\Leftarrow$ **Substrate**

λ_{out}=3÷5 µm
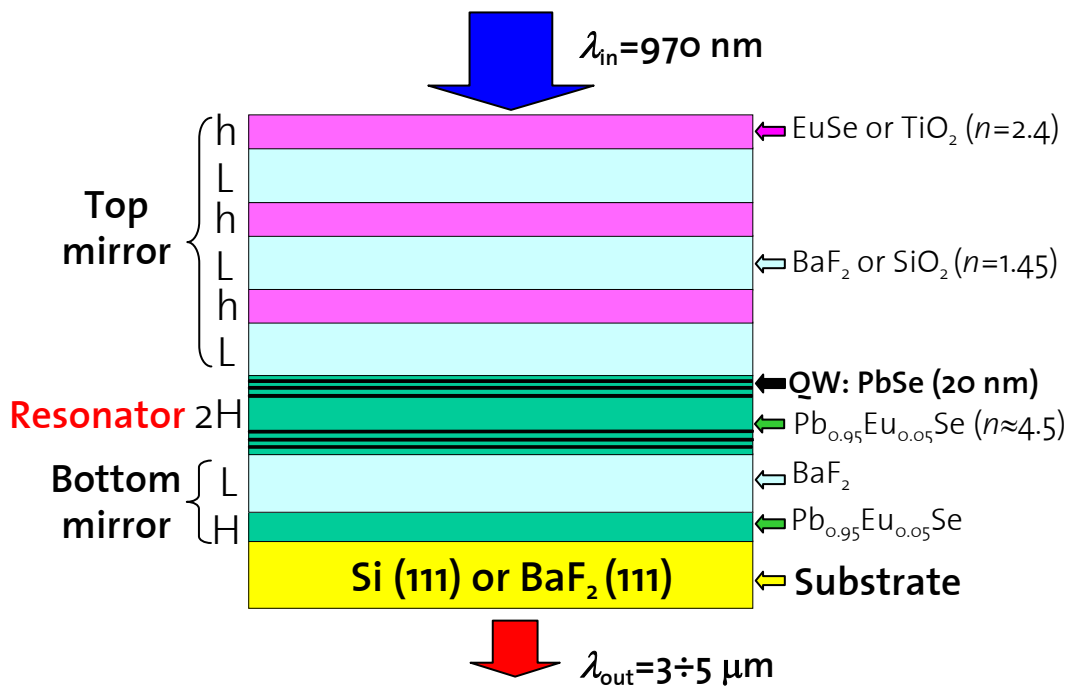
Fig. 8.18. Schematic cross-section of an optically pumped microcavity mid-IR emitter.
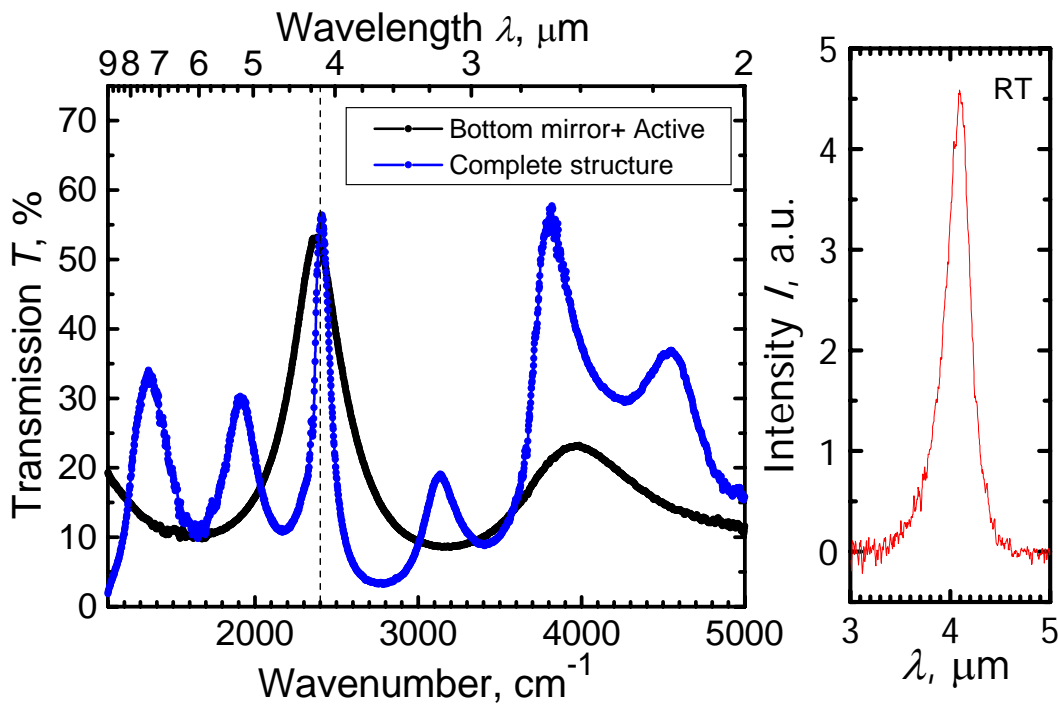
Fig. 8.19. FTIR transmission measurements of a wavelength transformer with target wavelength λ_o=4.1 μm (left). Black curve is for the VCSED without top mirror, blue curve for the complete structure. Emission characteristics of the wavelength transformer (right). T=295 K.

Calculations for FWHM and peak efficiency as functions of the design of the Bragg mirrors are presented in Table 8.2. For example, with a structure consisting of a 3 pair bottom and a 4 pair top mirror it is possible to achieve a very narrow (0.2%) line with 40 times higher intensity (above 4×10^{-3} power efficiency) line of subthreshold emission as compared to the 1 pair bottom and 2 pair top mirror structure. The output wavelength λ_o is

Table 8.2. Theoretical calculations of intensity and width of emission (FWHM) for a structure with different number of mirror pairs. Calculated for λ_o=4.2 (CO_2 absorption line).

Number of pairs in the bottom mirror	Number of pairs in the top mirror	Width of emission (FWHM)	Intensity of emission
1	2	5.5%	100%
2	3	1.3%	-
2	4	1.0%	700%
3	3	0.5%	-
3	4	0.2%	4000%

determined by the optical thickness of the resonator. The width of the QWs and energy band gap determine the wavelength range for optimum power efficiency.

The temperature dependence of λ_o is not defined by E_g, but by the optical thickness nd. As an example, the temperature dependence of VCSED emission is shown in Fig. 8.20. The shift of the peak wavelength is 3.3×10^{-4} µm/K. This low value mainly corresponds to the temperature dependence of the refractive indices, while the change of thicknesses due to thermal expansion is still lower, $\sim2\times10^{-5}$ K^{-1}.

Due to the ease of fabrication, these emitters allow application for low cost spectroscopic gas sensing of common gases like CO_2, CO or CH_4 at room temperature. This was the first VCSED fabricated with IV-VI materials, and a patent is pending [147].
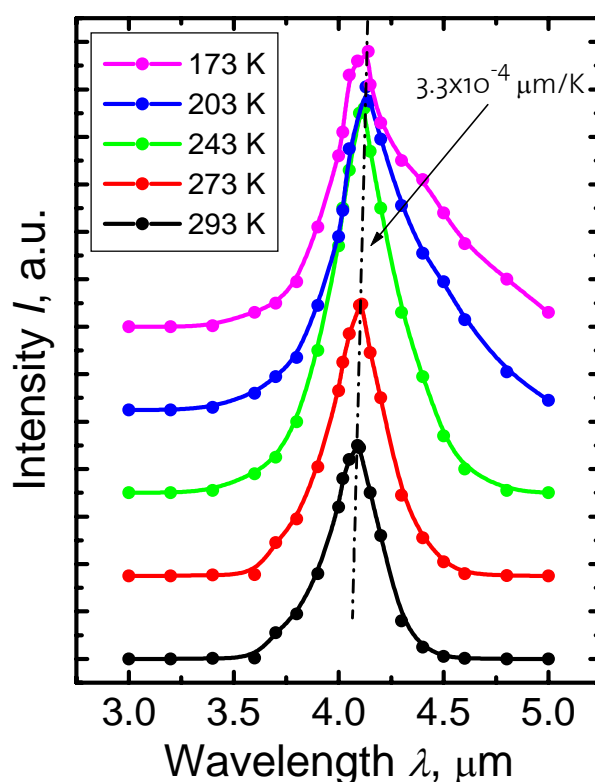
Fig. 8.20. Temperature shift of the emission peak of a VCSED from λ=4.1 µm at T=293 K to λ=4.14 µm at T=173 K. The shift of 3.3×10^{-4} µm/K is mainly due to the temperature dependence of n. The intensity scale is the same for all curves, the curves are vertically shifted.

8.4 Resonant cavity detectors

The aim of this section is to describe mid-IR photodetectors which are selectively sensitive to a specific narrow wavelength range. Resonant cavity detectors (RCDs) are optoelectronic devices whose performance is enhanced by placing the active device structure inside a Fabry-Pérot

resonant cavity. Such devices benefit from the wavelength selectivity and the large increase of the resonant optical field in the cavity. Off-resonance wavelengths $\lambda \neq \lambda_o$ are rejected by the cavity. Photodetector structures based on RCD can have very thin active layers [148]. This yields higher detectivities (smaller volume where noise carriers are generated), and, in addition, to faster devices. Moreover, high quantum efficiencies η result because the photon may be reflected many times before it is absorbed in the thin active layer. Here are described resonant cavity diodes with resonant wavelength λ_o in the 3÷5 µm wavelength range and high quantum efficiency η [143].

As a Fabry-Pérot resonator, a RCD consists of a cavity embedded between two mirrors (see also Section 8.3). Both the mirror and cavity material (except the active zone) must be non-absorbing at the target wavelength λ_o, and the reflectivity of the mirrors has to be high. A schematic drawing is shown in Fig. 8.21. Bragg mirrors are used for high reflectance with thicknesses of the individual layers $d_i = \lambda_o/4n_i$. The cavity length L has to comply with $L = \kappa \lambda_o/2n_c$, where $\kappa = 1, 2, 3, \ldots$ For resonances of higher order ($\kappa > 1$), the higher the κ values are, the narrower the cavity resonances become. The height of the resonance depends on κ, as well as on mirror reflectivities and properties of the absorption layer. The active absorption region H of the cavity is grown in a manner that its position extends to a maximum of the standing wave λ_o. Waves with different
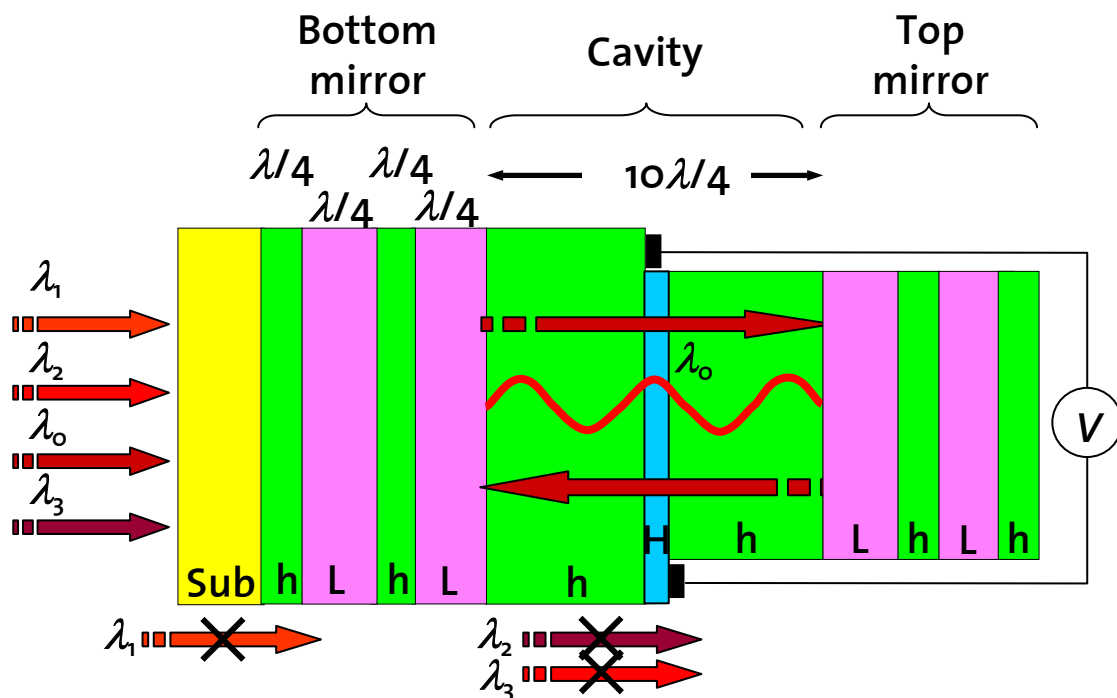
Fig. 8.21. Optoelectronic principle of RCDs designed for a narrow band detection at λ_o out of a broad band infrared radiation spectrum $\lambda_o \div \lambda_3$. The active absorption region H is shown in blue.

wavelength of the incoming radiation vanish due to destructive interference in the resonator or are absorbed in the substrate, mirrors or cavity. Only wavelengths with $\lambda = \lambda_0$, which satisfy equation (8.1), can be enhanced in a RCD. Several resonance modes are observed. The mode numbers m are given by

$$\lambda_m = \frac{nL}{m - \dfrac{\varphi_{top} + \varphi_{bottom}}{2\pi}} \; , \tag{8.4}$$

where n is refractive index, L cavity length, φ phase shift at bottom and top mirrors and λ_m wavelength of the mode.

The RCD structures described in the present work are based on the Schottky diode (Fig. 8.22). The top mirror is replaced by a reflecting metal (Pb in the present case) which forms a Schottky barrier with the IV-VI semiconductor. The whole resonant structure is grown on Si (111) by MBE except the Pb layer, which is deposited afterwards by thermal evaporation. The bottom mirror consists of two $\lambda_0/4$ $Pb_{0.95}Eu_{0.05}Se/BaF_2$ Bragg pairs, followed by a microcavity filled with a $7\lambda_0/2$ or $9\lambda_0/2$ thick $Pb_{0.95}Eu_{0.05}Se$ buffer layer. The active absorbing layer is a $\lambda_0/4$ IV-VI material.

The grown structures have smooth surfaces and do not contain inclusions or cracks even after thermal annealings up to $T=573$ K and several coolings down to $T=15$ K. This is contrary to [149], where cracks occurred in the IV-VI/BaF_2 multilayer structure after MBE growth.

The room temperature reflectance spectra in Fig. 8.23 refer to two measurements: The reflectivity R of the as-grown (without top mirror, in
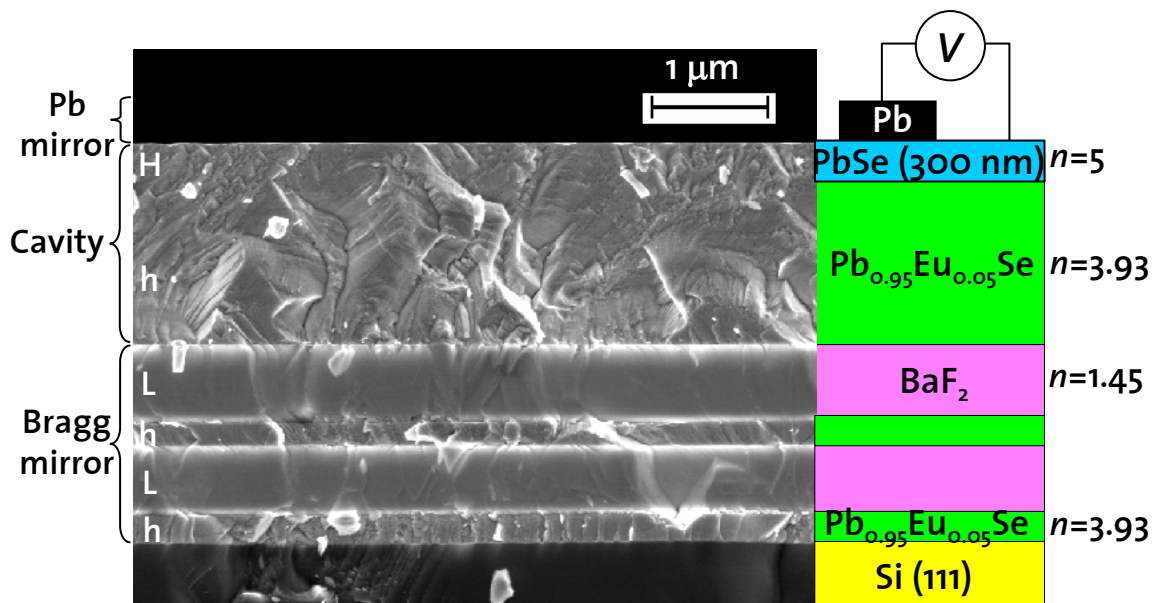
Fig. 8.22. SEM and schematic profile of the resonant cavity structure. The top PbSe layer can not be distinguished from $Pb_{0.95}Eu_{0.05}Se$ in the SEM. Image by P. Wägli, ETHZ.

red) and R for the complete RCD structure (in black). The spectra show the mirror stop band with five resonances $m=2 \div 6$. After deposition of lead, the cavity resonances become narrower, the transmission at λ_m increases and a blue shift occurs.
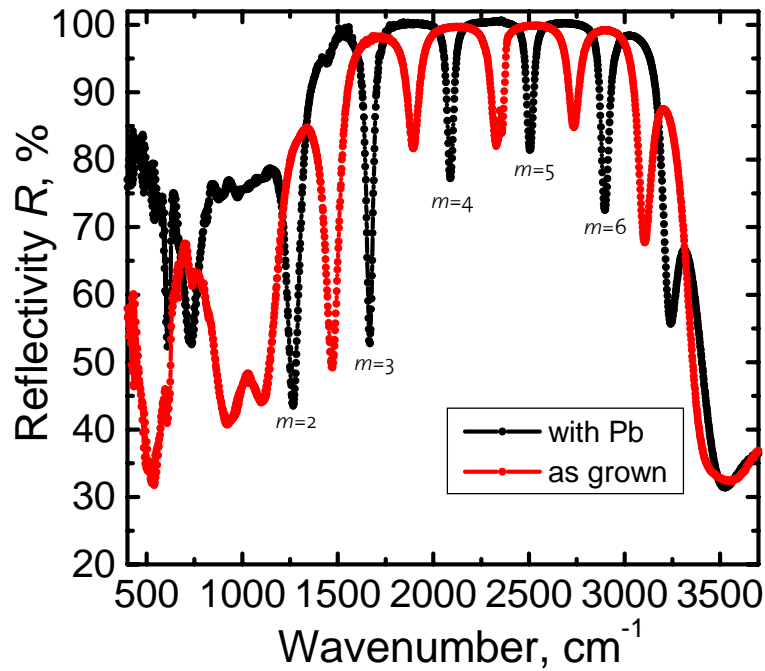
Fig. 8.23. Reflectance spectra of the RCD. Resonant cavity with $Pb_{0.97}Eu_{0.03}Se$ active layer and without top mirror (as grown) is shown in red. After deposition of the Pb top mirror, cavity resonances m shifted to shorter wavelengths (in black). $T=295$ K.

Spectral response measurements of the completed RCD were made at different temperatures $T=95 \div 250$ K. Several RCDs were designed in order to analyse the enhancement of the incoming radiation at the resonance wavelengths. The spectral response $\eta(\lambda)$ of the structure with a PbSe absorption layer is shown in Fig. 8.24. Three peaks ($m=3, 4, 5$) with quantum efficiencies up to 35% and FWHM equal to $4 \div 5$% are observed.

In order to block unnecessary modes, material properties of the absorbing layer may be changed. For example, by adding Eu to the PbSe absorbing layer, a blue shift of the cut-off wavelength $\lambda_{cut-off}$ occurs. There will be no sensitivity above $\lambda_{cut-off}$. A single mode ($m=5$) photoresponse of a detector at $\lambda_0=4.4$ μm is presented in Fig. 8.25. A $Pb_{0.97}Eu_{0.03}Se$ layer was used as an absorber with $\lambda_{cut-off}$(95 K)=4.6 μm, all modes with the lower orders are blocked. All modes with order higher than $m=6$ are cut by absorption in the bottom mirror or the buffer layer ($\lambda_{cut-off}$ (95 K)=3.8 μm for $Pb_{0.95}Eu_{0.05}Se$). This RCD has a high quantum efficiency ($\eta=32$%) and a very

narrow resonance peak (FWHM=0.8%) at 95 K. The latter value is much narrower than published for structure grown on BaF$_2$ [150]. The present photovoltaic RCDs were operated up to T=250 K. As in the case of wavelength transformers, the shift of the resonance wavelength is given
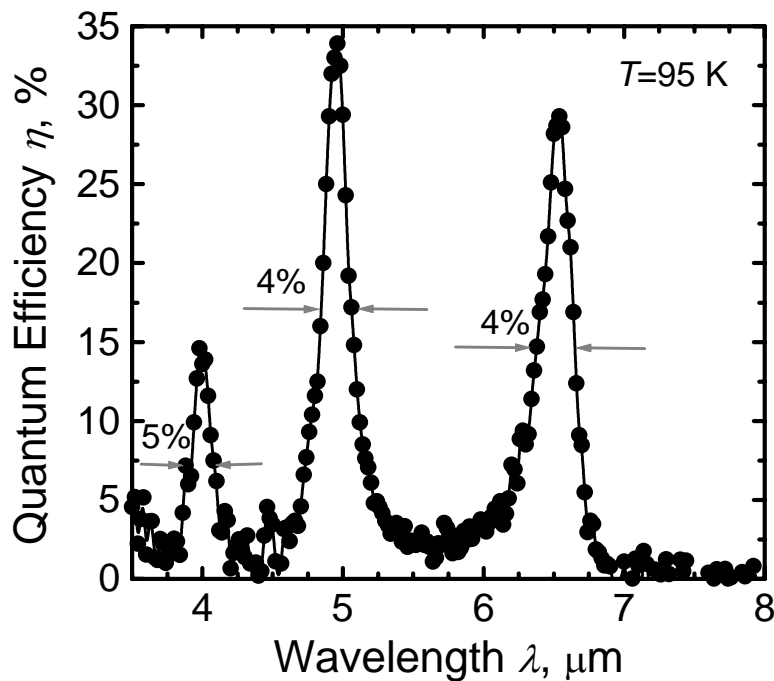
Fig. 8.24. Spectral response measurements of a structure with PbSe active layer and three cavity modes. T=95 K, full widths at half maxima of the peaks (FWHM) are 4÷5%. Measured by M. Arnold, ETHZ.
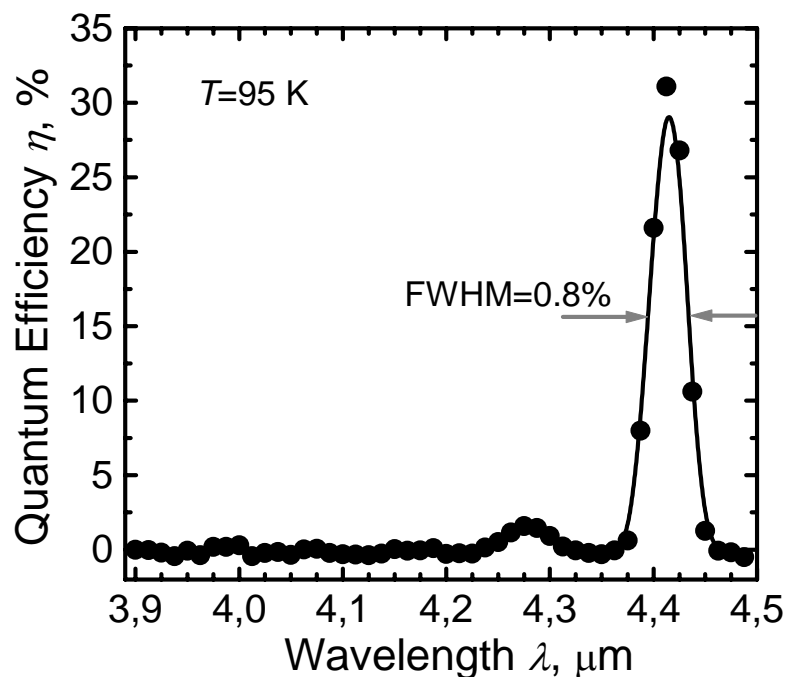
Fig. 8.25. Spectral response of a RCD structure from Fig. 8.23 sensitive to only one cavity wavelength λ_o≈4.4 µm. T=95 K, width of the peak (FWHM) is 0.8%. Measured by M. Arnold, ETHZ.

by the $n(T)$ dependence, but not by the change of cut-off wavelength.

The possibility to obtain a photovoltaic detector with sensitivity only within a narrow wavelength range at any desired wavelength in the mid-infrared range is the main advantage of this type of device. Applying modified designs (for example, top and bottom mirrors with higher reflectivities), still narrower resonance peaks and quantum efficiency close to the theoretical limit ($\eta \approx 100\%$ [151]) can be obtained.

8.5 Comparison of the device performance

Performance of the devices depends on the structural quality of the layers they consist of. Among others, the maximum operation temperature, threshold intensity and output intensity of emission are parameters which allow making a direct comparison of laser structures with similar design.

As shown by Kellermann [137], the threshold pump power densities at low temperatures of the lasers grown on BaF_2 (111) are about four times lower than those of lasers grown on Si (111). Similar results were obtained for maximum operating power and maximum operation temperature. Moreover, the degradation of laser characteristics observed after multiple cool-downs to T=100 K under illumination is less for BaF_2 (111) based lasers. There is an explanation for these observations. According to Table 2.1 and Fig. 2.1, BaF_2 has twelve times smaller relative lattice mismatch to PbSe than silicon. The linear thermal expansion coefficient β_{exp} of barium fluoride is approximately the same as in IV-VI materials. Both these factors lead to lower dislocation densities ρ_{disl} and therefore better characteristics of the light-emitting device on BaF_2 (111) substrate.

As has already been discussed in Section 2.5, dislocations can not move in the IV-VI layers grown on Si (100) substrate and densities were as high as ρ_{disl}=10^9 cm^{-2}. The lowest dislocation density in layers used for lasers on (111) oriented substrates was 5×10^7 cm^{-2}. Measurements show somewhat poorer performance of laser structures grown on (100) oriented substrates than those grown on (111) oriented substrates (concerning the maximum operation temperature and threshold intensities), compatible with the different dislocation densities for the different orientations.

Several other factors have to be taken into consideration for better laser performance. Most important of them are diffusion length of carriers L_{diff} and thickness of the active layer d_{act}. Firstly, structural properties of the layer depend on its thickness d: The thicker the layer, the lower is the dislocation density (see Section 5.3). Secondly, as it has been already discussed in Section 8.2, the optimal thickness d_{act} should correspond to a

high absorption of the pumping light. In semiconductors, the mean diffusion length L_{diff} is [76]:

$$L_{\text{diff}} = \sqrt{D\tau} = \sqrt{\frac{k_B T}{e}\mu\tau} \, ,$$ (8.5)

where D denotes diffusion coefficient, τ minority carrier lifetime, k_B Boltzmann´s constant, T temperature, e elementary charge and μ carrier mobility. Using a lifetime value τ=0.1 ns [123], diffusion lengths in the barriers can be calculated (Table 8.3). Diffusion lengths and mobilities in PbSe layers are larger than in $Pb_{1-x}Eu_xSe$ layers. This might be a reason why double heterostructure lasers have higher operation temperatures than QW lasers.

Table 8.3. Mean diffusion lengths of carriers in PbSe and its alloys with different europium content.

Material	T, K	μ, cm²/Vsec	L_{diff}, nm
PbSe	300	420	322
	100	10000	930
$Pb_{0.95}Eu_{0.05}Se$	300	250	254
	100	1400	350
$Pb_{0.92}Eu_{0.08}Se$	300	25	80
	100	115	240

All points mentioned above are consistent with the material properties of Eu containing ternary IV-VI alloys. Owing to alloy scattering, incorporated europium atoms at Pb sites behave as a "free carrier killers". This was already discussed in Chapter 4.

8.6 Conclusion

Several types of optoelectronic devices that were grown, structured and characterized in our laboratory were described in this chapter. All these emitters and detectors cover the 3÷6 μm mid-IR range.

Most of the work was dedicated to optically pumped edge-emitting IR-lasers grown on (100) oriented Si and (111) oriented Si and BaF_2 substrates. The highest operation temperature (T_{max}=250 K) was found for a double heterostructure laser with a lead selenide active layer and grown on a BaF_2 (111) single crystal substrates. Similar devices grown on Si substrates reach nearly the same operating temperature. FIB milling and cleaving were the most successful mirror preparation techniques for these laser

structures. Two-dimensional (QW) structures showed somewhat lower operation temperature, probably due to the barriers containing Eu. The main advantage of IV-VI lasers is a large tuning range by temperature change. Moreover, the use of an inexpensive and compact optical source is an additional advantage.

Wavelength transformers (or VCSEDs) work at room temperature and convert the incoming λ_{in}=940 nm pump beam to a narrow output beam with peak wavelength λ_{out}=3÷5 µm. It is based on the Fabry-Pérot resonator principle, the conversion is due to the strong photoluminescence of PbSe. The parameters of the outcoming beam (power efficiency, λ_{out}, width of the peak) depend on the design of the structure. This is the first VCSED grown with IV-VI materials for mid-IR range.

Resonant cavity detectors (RCDs) are based on the above-mentioned resonator, too. Photovoltaic devices, designed to be sensitive at the target wavelength λ_o only, show high quantum efficiencies at λ_o and very narrow spectral response peaks. Results described in this work can be claimed the best for all known RCDs covering 3÷6 µm wavelength range. Narrow linewidths of VCSEDs and RCDs are easily obtained because of the high-contrast Bragg mirror layers. It is possible to reach >99% reflection with a few IV-VI/BaF$_2$ quarter wavelength Bragg pairs only.

Structural quality plays a very important role in device manufacturing and performance. The high dislocation densities and Eu atoms limit the performance of the infrared devices.

Chapter 9

Conclusions

This work has been dedicated to the growth procedure, investigation of properties and quality control of IV-VI structures grown on Si and BaF_2 substrates. PbSe, PbTe and their ternary alloys with Eu were described as materials for optoelectronic devices (emitters and detectors) and low dimensional structures (QD, QWi, QW).

Eu atoms in grown $Pb_{1-x}Eu_xA$ (A=Se, Te) layers lead to significant changes in refractive indices, band gaps and electronic properties of alloys. Several methods of europium determination in ternary lead chalcogenide layers and their advantages and disadvantages were discussed. The more reliable results were obtained with spectral response and FTIR measurements. The flux ratio and FTIR spectra method were the most valuable and often used type of analysis for the determination of the Eu content in $Pb_{1-x}Eu_xA$.

Structural quality plays a very important role in device manufacturing and performance. Dislocation density ρ_{disl} is the main factor that limits the performance of mid-IR devices grown on lattice mismatched substrates. AFM, LTHM and XRD were described in this work as methods for determination of ρ_{disl}, which was in the $5 \times 10^6 \div 10^9$ cm^{-2} range.

The extremely narrow width (2÷3%) of the size distribution of self-assembled PbSe quantum dots on PbTe quasi-substrates on Si (111) was explained by referring to the existence of surface defects and the inequality $L > 2\lambda_a$, where λ_a is the diffusion radius and L the distance between two nearest dots. Incoming molecules nucleate at defects in the beginning of growth. There are always enough nucleation sites on the PbTe surface due to dislocation glide steps caused by the relaxation of the thermal misfit strain. Molecules form stable clusters that have the same probability to capture an incoming molecule within λ_a. The results are in good agreement with the nucleation theory. To the knowledge of the author, the samples grown in this work have by far the most narrow quantum dot size distribution for self-assembled quantum dots.

Low-dimensional IV-VI structures can be obtained by epitaxial deposition of lead chalcogenides on a templated surface of the fluoride-

on-Si (100) system. This system consists of long CaF_2 self-assembled nanostripes oriented in one direction or a grid of perpendicular stripes. The resulting overgrowth with IV-VI materials shows that the structure of the CaF_2 template is preserved.

Several types of grown, structured and measured optoelectronic devices were briefly described in this work: edge-emitting lasers, wavelength transformers, resonant cavity diodes and Bragg mirrors. All these emitters and detectors cover the 3÷6 μm mid-IR wavelength range.

Most of the work was dedicated to optically pumped edge-emitting IR-lasers grown on (100) oriented Si and (111) oriented Si and BaF_2 substrates. The highest operation temperature (T_{max}=250 K) when illuminated with a 5.5 W_p GaAs based laser diode was found for a double heterostructure laser with a lead selenide active layer and grown on a BaF_2 (111) single crystal substrate. Similar devices grown on Si substrates reach nearly the same operating temperature. FIB etching and cleaving were the most successful mirror preparation techniques for these laser structures. Two-dimensional (QW) structures showed somewhat lower operation temperature, probably due to the barriers containing Eu. The main advantages of these IV-VI lasers described are a large tuning range by temperature change and the use of an inexpensive and compact optical source.

Wavelength transformers (VCSEDs) are structures operated in sub-threshold and consist of a $PbSe/Pb_{1-x}Eu_xSe$ active resonant cavity with integrated top and bottom mirrors grown on Si (111) substrates. They transform the incoming λ_{in}=940 nm pump beam to a narrow output beam with peak wavelength λ_{out}=3÷5 μm. Wavelength transformers work at room temperature and are based on the Fabry-Pérot resonator principle. The wavelength conversion is due to the strong photoluminescence of PbSe. The parameters of the outgoing beam (power efficiency, λ_{out}, width of the peak) depend on the design of the structure.

Resonant cavity detectors (RCDs) are based on the above-mentioned resonator, too. RCDs consist of a $n\lambda/2$ cavity with a thin active $Pb_{1-x}Eu_xSe$ absorption layer, a bottom $Pb_{1-y}Eu_ySe/BaF_2$ Bragg mirror ($x<y$), and a Pb blocking contact. This Pb acts as top mirror and at the same time forms the photovoltaic metal-semiconductor detector. The spectral response shows a very narrow resonance peak, peak position and width are given by the design. For the example described, peak position is at about 4.4 μm wavelength, and FWHM 0.8%. These results can be claimed the best for all known RCDs covering 3÷6 μm wavelength range.

Narrow linewidths of VCSEDs and RCDs are easily obtained because of the high-contrast Bragg mirror layers. It is possible to reach >99% reflection with a few IV-VI/BaF$_2$ quarter wavelength Bragg pairs only. To further increase the performance characteristics of the devices containing cavities, improved electronic quality of the active regions is needed, especially still lower dislocation densities.

Chapter 10

Outlook

Despite the fact that IV-VI compounds are among the oldest known semiconductors, a lot of effort is still needed for investigation of lead salt materials and devices they consist of. Some possible future improvements of the results of the present work are listed below.

Structural quality

As shown in the present work, dislocation density of layers for optoelectronic devices is quite high ($\rho_{disl} \approx 10^8 \div 10^9$ cm^{-2}). This leads to a relatively short lifetime of the carriers, $\tau \approx 0.1$ ns [123]. Better understanding of the nature of dislocations in IV-VI single layers and multistacks, improved deposition characteristics and post-growth treatment would reduce the number of dislocations and increase structural quality. Thus, for instance, by using a more sophisticated cladding layer with graded composition design, it should be possible to decrease the dislocation density in the 200 nm thin active layer of a laser structure to 10^7 cm^{-2}. This will lead to longer τ up to ~1 ns with correspondingly reduced threshold intensities and, therefore, to considerably higher operation temperatures [123].

Zero-dimensional structures

There is an assumption that multistacks of PbSe quantum dots with certain thicknesses of PbTe spacer layers can lead to even narrower size distributions. Several preliminary experiments were made with 20-period PbSe/PbTe superlattices. According to a TEM image (Fig. 10.1), a layer-to-layer correlation of dots inclined under the angle $\approx 25°$ from the [111] direction is observed. The PbTe spacer layer is ≈ 25 nm thick. This thickness corresponds to the intermediate alignment position between vertical (0°) and trigonal fcc stacking (39° from [111] direction) types [152]. The width of the size distribution of such a type of structure corresponds to std$\approx 6 \div 7\%$. Under optimized growth conditions it should be possible to reach still smaller std values.
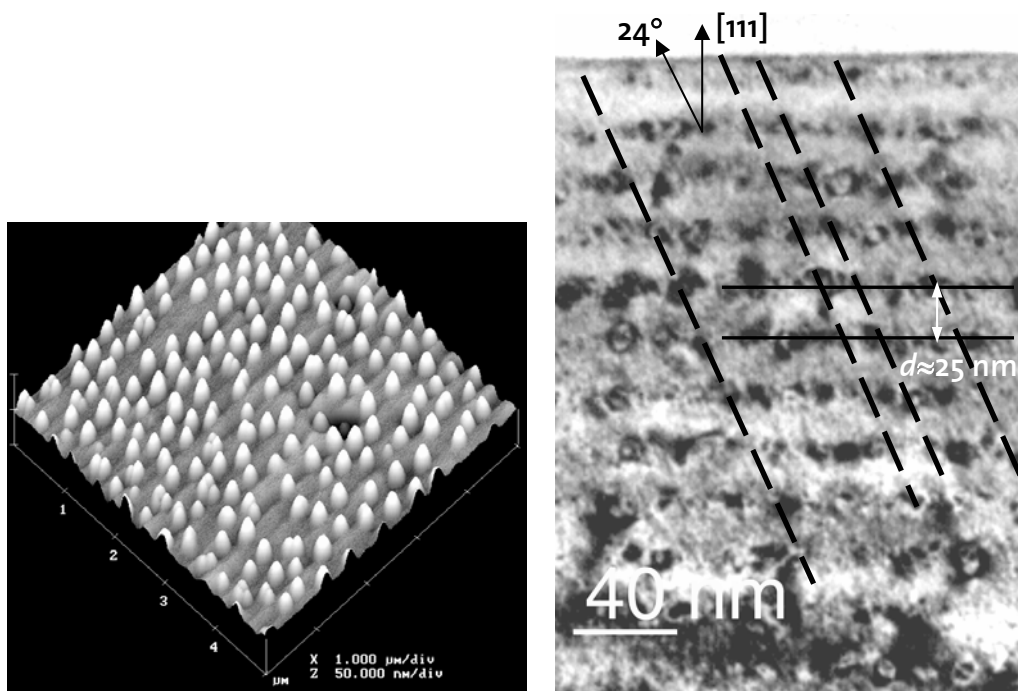
Fig. 10.1. AFM image of a top layer of the 20-period quantum dot PbSe/PbTe superlattice (left). TEM cross-section of the 20-period superlattice with 25 nm PbTe spacer. The inclined layer-to-layer dot correlations are indicated with red lines (right)(TEM image by P. Brunkov, Ioffe Institute, Russia).

One-dimensional structures

The overgrowth with PbSe and PbTe materials of CaF_2-on-Si (100) nanostripes shows that the structure of the CaF_2 template is preserved. Therefore, these fluoride templates grown on Si (100) are of a great interest for the further formation of low-dimensional structures, including overgrowth with lead chalcogenides to form QDs and QWis. These 1D structures can be used in active regions of lasers and wavelength transformers.

Edge-emitting lasers

Reaching room temperature operation is a main aim of future work. To achieve this goal, better layer quality (see above) and optimized design are needed. Moreover, a special design of the laser structure might be applied for additional tuning of the emission wavelength. If the active layers are grown with a tapered thickness, the laser emission may be continuously tuned over a wavelength range of up to several micrometers by moving the structure with respect to the pump beam (Fig. 10.2).
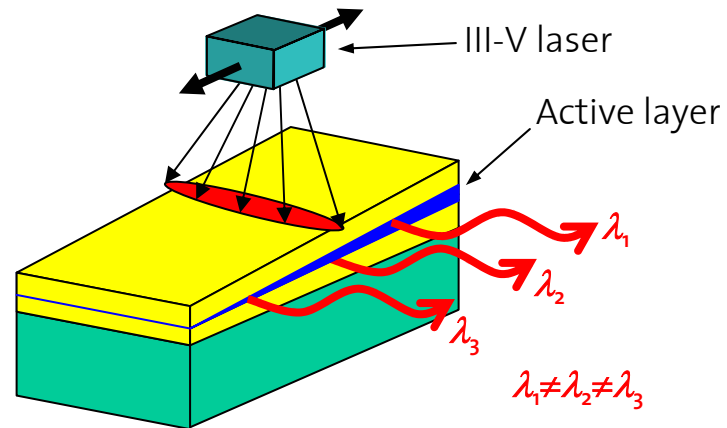
Fig. 10.2. Wavelength tuning by excitation of different regions of an edge-emitting laser with a tapered thickness of the active region. Tuning is possible by mechanical displacement of the pumping III-V laser.

Appendix A

Silicon substrate cleaning (Shiraki cleaning [60]) procedure

1. Removing of fat.

Isopropanol and aceton baths are applied in order to remove residuals of fat-containing contamination and large dust particles.

2. Cleaning in acid.

Silicon is immersed in a concentrated HNO_3 solution to avoid metallic particles on the Si surface.

3. Cleaning in alkali.

A special solution containing NH_3 and H_2O_2 is used to remove organics from silicon.

4. Oxide removing.

The thin oxide layer of SiO_x is dissolved by 5% HF solution.

5. Surface passivation.

Formation of so called "wet oxide" on the Si surface in HCl and H_2O_2 solution for surface passivation.

After these steps, the silicon substrates are considered to be clean and ready for prolonged storage without changes in surface properties. According to our experience, wafers stored three years in nitrogen atmosphere behave in the MBE growth as freshly cleaned ones.

6. Thermal removal of oxide

This operation takes place in the MBE chamber immediately before CaF_2 deposition. During substrate heating up to T_w>1173 K the oxide evaporates at temperatures T_w=933÷998 K. Oxide removal can be registered by the ion gauge (the pressure value becomes one order of magnitude worse) and change of Si colour (wafer becomes red). Fig. A.1 made through the MBE

window shows the silicon substrate after removing the oxide. After three minutes at the highest temperature (usually T_w=1178÷1193 K) and cooling to the deposition temperature T_w =923 K, a transition from a 1×1 to a 7×7 Si surface reconstruction for (111) oriented substrates is observed by RHEED (see also Section 3.2 and Fig. 3.15). This reconstruction change occurs at T_w ≈1123 K and can be considered a confirmation of successful cleaning and oxide removal [153].
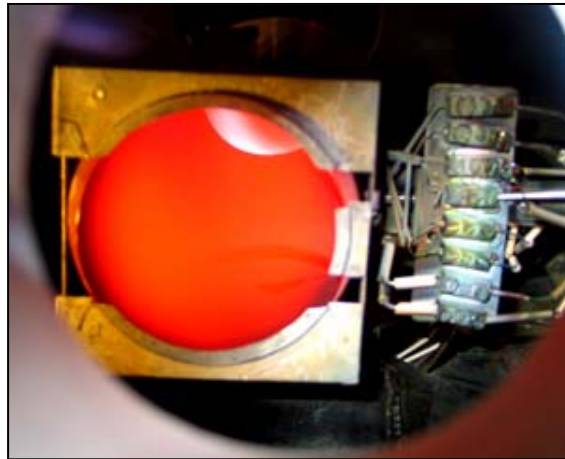
Fig. A.1. Red colour of Si as a result of oxide removing according to Shiraki procedure. The photo of the substrate held in the manipulator was made through the MBE window, T_w=1187 K.

Appendix B

Preparation of mirrors for edge-emitting lasers

To achieve laser emission suitable edge mirrors are needed. The mirrors should provide resonator stability and the reflectivity must be high enough. With refractive indices n_{PbSe}=4.92 and n_{Air}=1, the reflectivity is

$$R = \left(\frac{n_{\text{Active}} - n_{\text{Air}}}{n_{\text{Active}} + n_{\text{Air}}} \right)^2 \approx 44\% . \tag{B.1}$$

This value is higher than the reflectivity of III-V materials (R_{GaAs}=34%).
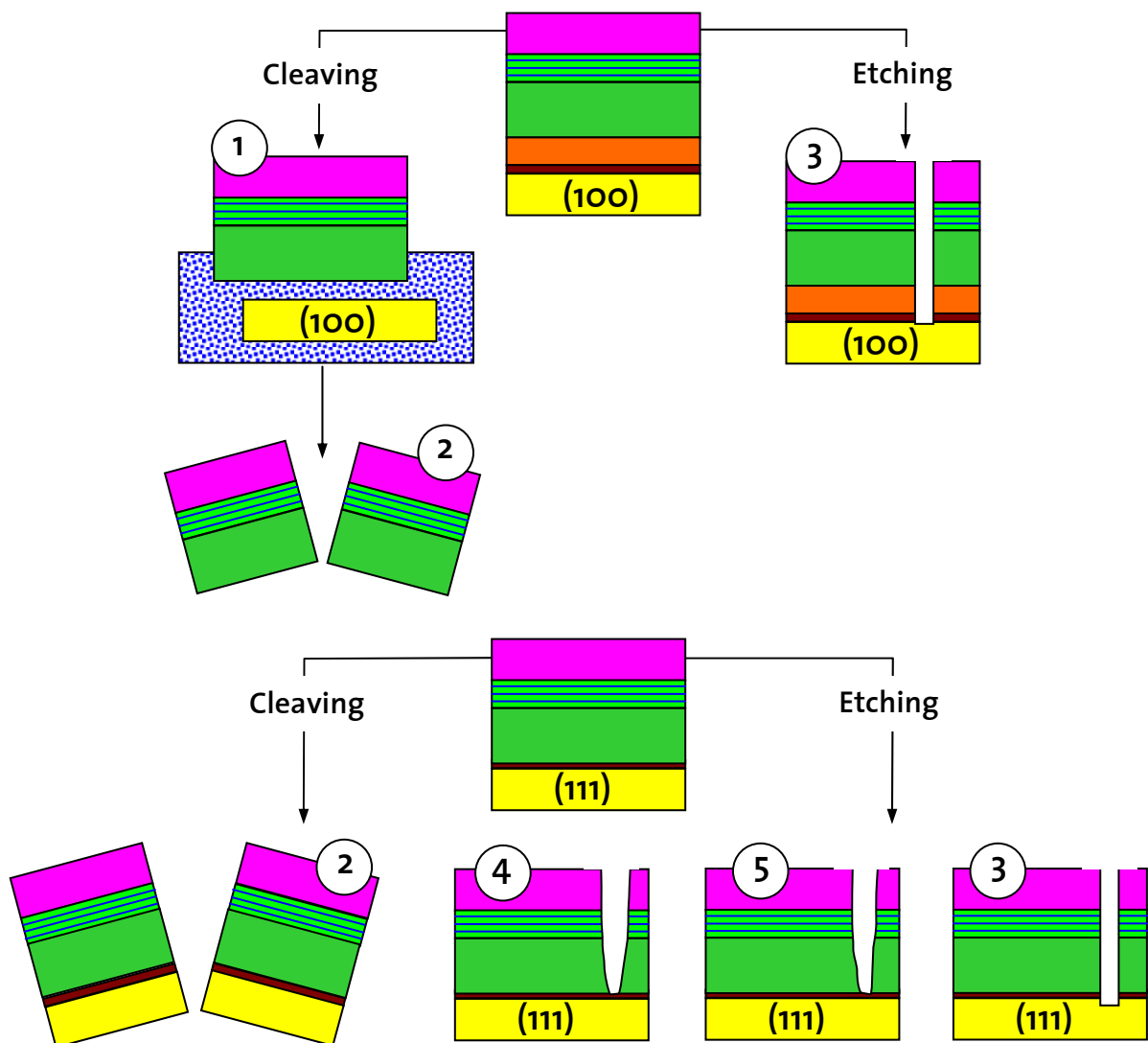
Fig. B.1. Preparation methods of edge-emitting laser from (100) and (111) oriented structures.(1). Lift-off process by BaF$_2$ dissolving in water. (2). Cleaving. (3). Focused ion beam etching. (4). Reactive ion etching. (5). Wet chemical etching.

There are different methods to fabricate mirrors for IV-VI edge-emitting lasers. The methods used in this work are sketched in Fig. B.1. Stress-induced (internal or external stress) cleaving and different types of etching such as a focused ion beam (FIB) etching, reactive ion etching (RIE) and wet chemical etching are discussed below.

B.1 Cleaved mirrors

Fabrication of in-plane lasers from epitaxially grown materials traditionally involves a wafer cleaving procedure to obtain Fabry-Pérot cavity structures. This procedure has not been significantly improved since it was first developed in the early 1960s. There were several attempts to develop a cleaving technique with the use of growth-substrate removal procedures, such as a selectively etchable AlAs release layer for III-V materials [154] or a water soluble BaF_2 buffer layer for IV-VI compounds [72, 155].

(100) oriented layers. Using (100) oriented silicon substrates, one can achieve cleaving induced by the internal stress of the layers. The surface of a structure after the MBE-run is shown in Fig. B.2. The layer is ~3 μm thick and growth temperature was T_w=633 K. The layer is cracked since strain relief by dislocation glide is not efficient for (100) oriented layers (see Section 2.5). These cracks can be considered "useful"- they are oriented along two perpendicular directions only, and after the lift-off process they decompose into small pieces which form parallelepipeds of the sizes 20÷200 × 1500÷2500 μm^2. Cleavage planes formed by these cracks are of {100}-type.

After removal from the substrate, suitable pieces are clamped to a sample holder [137]. This lift-off method was applicable only for (100) oriented layers grown on silicon. Quite good results have been achieved for this orientation even for structures with very high dislocation densities
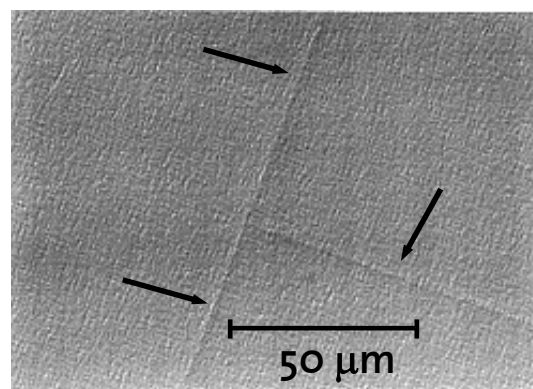
Fig.B.2. Nomarski light microscope image of successfully grown (100) structure. Arrows show crack lines.

(ρ>10^8 cm^{-2}) and limited range of crack-free (2.5÷3.5 μm) thicknesses. Note that strictly vertical mirrors ideal for lasers may be formed by cleavage (Fig. B.3).
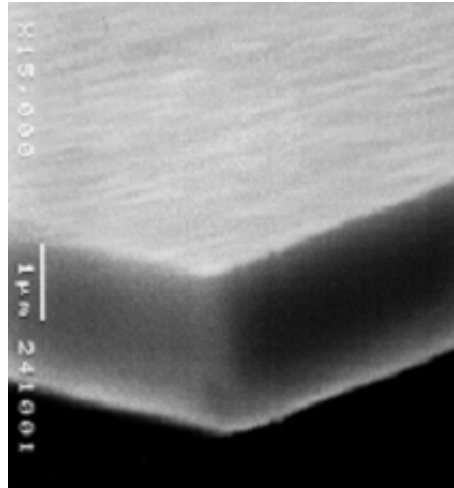
Fig. B.3. Scanning electron microscopy image of the lifted-off (100) structure. Cleaved facets are of {100}-type, strictly perpendicular to the surface and to each other, and perfectly smooth.

<u>(111) oriented layers</u>. (111) oriented layers can be cleaved for laser purposes, too. In contrast to (100) oriented structures where the internal strains in the layers already cause cleavage, an external mechanical force is needed. Both Si (111) and BaF$_2$ (111) substrates exhibit {111} cleavage planes. IV-VI materials cleave in a different way on these substrates:

<u>(111) oriented layers on Si</u>. According to the SEM images of cleaved (111) structures, vertical cleavage planes form for PbTe as well as PbSe. The orientation is (-1-12) (Fig. B.4 and Fig. B.5).

<u>(111) oriented layers on BaF$_2$</u>. The usual (100)-type cleavage plane was found for (111) oriented IV-VI layers on BaF$_2$ (111) substrates. The (100) mirror surfaces are 35° inclined to the (111) surface (Fig. B.6). Suprisingly, these structures show laser performance comparable to those with vertical oriented mirrors (see Section 8.2.3).

<u>Cleaving methods</u>. Quite simple methods were used for the cleavages described above. Structures on BaF$_2$ were cleaved with a blade. For lasers grown on Si (111), the back side of the Si substrate was scribed with a diamond and then cleaved by mechanical stress. The yield of such kind of preparation is very low. In order to improve the output, deep cutting (down to 100 μm) of the silicon back side was made with a circular saw (Fig. B.7a). This brought several advantages such as: 1) More precise size definition of the laser structures; 2) Easier cleaving procedure along the preferred directions; 3) Improved yield (up to 25%). In Fig. B.7b, one of the cleaving experiments is shown- silicon (111) is to cleave along a <110> direction (in
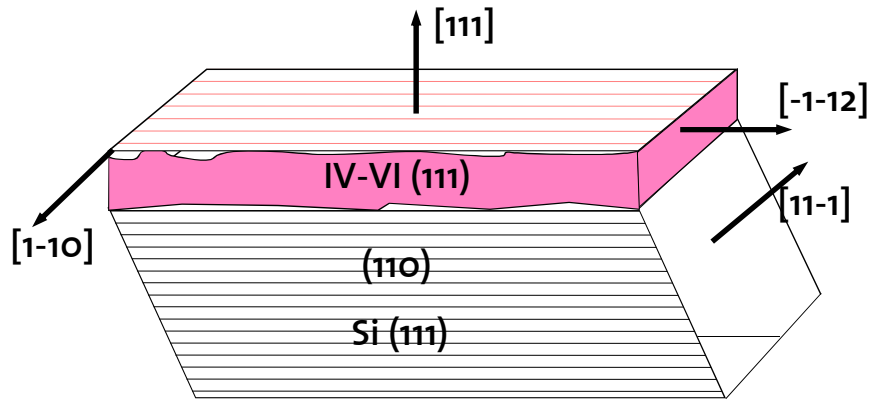
Fig. B.4. Schematic view of the cleavage planes for Si (111)/IV-VI (111) combinations. Lead chalcogenides cleave vertical to the surface along the (112) plane.
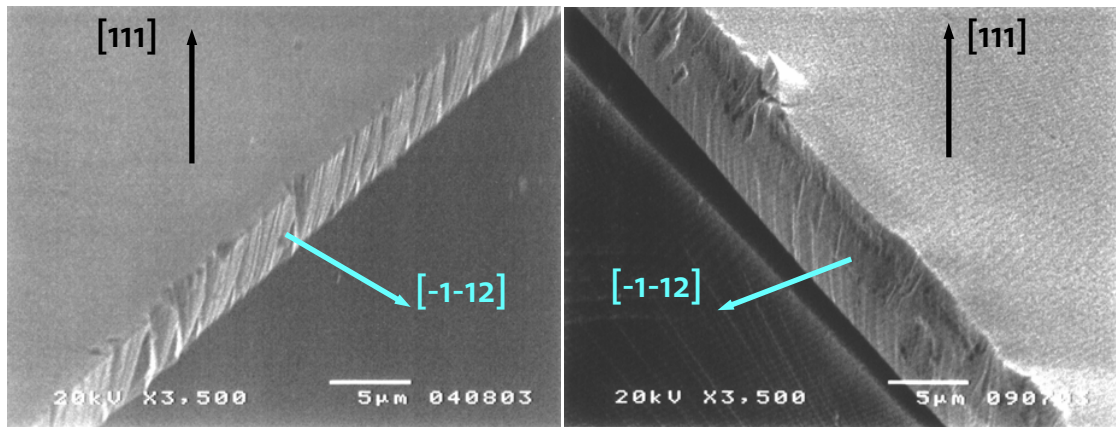
Fig. B.5. SEM image of cleaved PbTe (left) and PbSe (right) layers on Si (111).
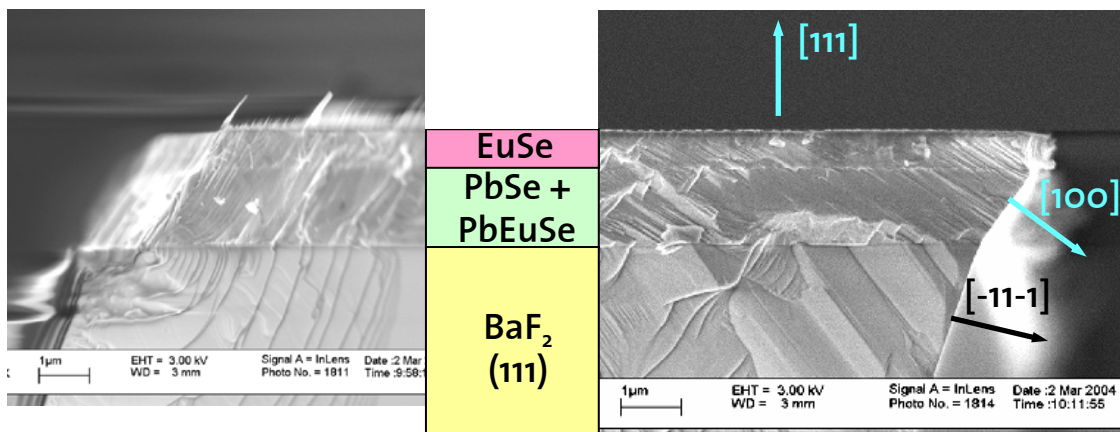
Fig. B.6. SEM profile of a cleaved laser structure grown on BaF_2 (111). Cleavage plane of the BaF2 substrate is (-11-1), inclined $\approx 18°$ with respect to the (111) surface, while that of the IV-VI layer is (100), inclined $\approx 35°$ to (111).

the figure one of these directions is along the longer side of the bars). A ready-to-measure right-angled device is shown in Fig. B.7c. In this image it is easy to note that above the sawn part, the silicon cleaves along a (111) cleavage plane.
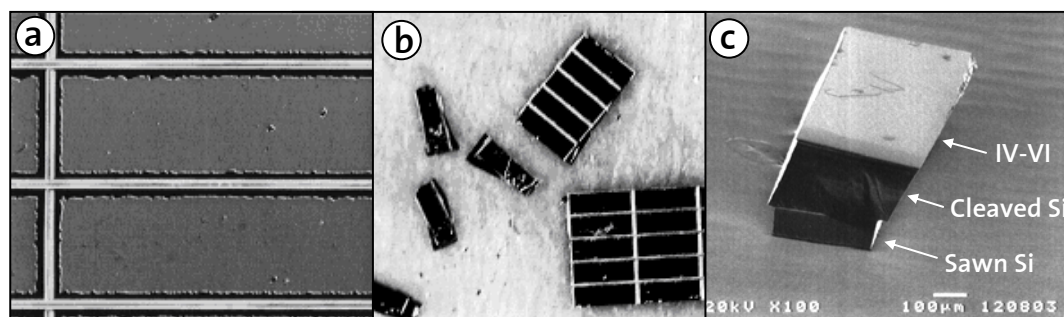
Fig. B.7. The back sawn side of Si (111) with IV-VI layer with piece size of 1000×350 µm (a). Separated-by-cleaving laser structures from the sawn wafer (b). Sawn, cleaved and ready-to-measure laser (c) (60° tilt view).

B.2 Etched mirrors

For mirror fabrication, etching rather than cleaving is the preferred method. Three methods of mirror fabrication (besides cleaving) were developed for IV-VI mirror etching: (1) wet chemical etching, (2) reactive ion etching (RIE) and (3) focused ion beam (FIB) etching.

The etching rate of ternary IV-VI alloys containing Eu decreases drastically with increasing Eu content x. This behaviour was observed by Schwarzl et $al.$ [107] by plasma etching of $Pb_{1-x}Eu_xTe$ alloys. The same property was found by etching of the structures described in the present work.

(1) <u>Wet chemical etching</u> is an inexpensive way to obtain laser mirrors. No special equipment such as plasma or focused electron sources is needed. Standard photolithographic procedures are applied to protect specified surface areas with photoresist from etching. A three-component etching solution similar to the one used for fabrication of two dimensional focal plane arrays [102] was developed. The best etching results were achieved with binary PbSe and PbTe compounds grown on (111) oriented silicon. The 4 µm thick PbSe laser structure in Fig. B.8 has vertically oriented mirrors. Wet chemical etching of ternary layers with homogeneously distributed europium is slower, especially for $Pb_{1-x}Eu_xTe$. But vertical mirrors can be achieved as well in this case. Multilayer lasers like those shown in Fig. 8.12 and Fig. 8.14, are most complex structures for wet etching. Having different x concentrations in the layers, etch rates are different for each composition. Moreover, etching with the chosen chemicals is isotropic. This means, the edges of wet-etched lasers suffer
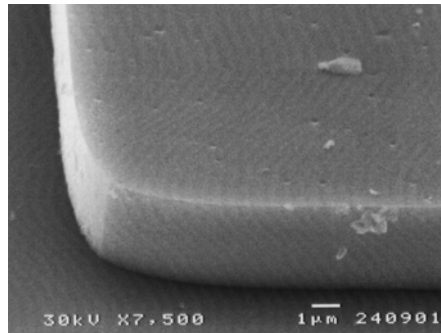
Fig. B.8. Cross-section of a PbSe (111) on Si (111) laser structure obtained by
wet chemical etching.

from roughness through underetching. EuSe and EuTe do not react with
the etching solutions used, therefore the etching process consists of two
stages in this case: First, the europium chalcogenide layer is etched with an
etchant containing HNO_3. Afterwards, this etched top layer can be used as
a mask for the further etching steps.

Despite the different etching rates for different Eu concentrations, an
optimised wet chemical etching process for selenides allowed to fabricate
acceptable mirrors. As an example, a multilayer laser structure which is
ready for measurements is shown in Fig. B.9. This PbSe based structure on
Si (111) was wet etched, then the silicon substrate was cut and mounted on
a copper heat sink. It is important to note that wet chemical etching is
suitable only for structures grown on Si (111). This is due to the aggressive
environment of the etchants: BaF_2 (as a buffer layer or a substrate) is
rapidly etched away in this chemical solution.
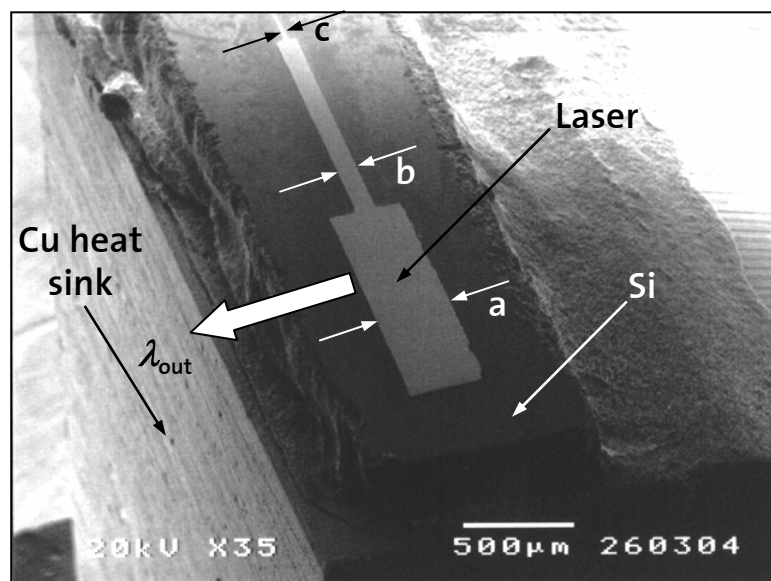
Fig. B.9. SEM top view of a wet chemically etched PbSe on Si laser
structure mounted on the copper heat sink. The stripe widths L of the
laser are: a) 300 μm, b) 80 μm, c) 25 μm.

(2) <u>Reactive ion etching</u> (RIE) is a suitable method for anisotropic material removal. RIE is a variation of plasma etching in which during etching a semiconductor wafer is placed on a radio frequency (ν=13.2 MHz) powered electrode. The wafer is charged to a potential where etching species extracted from the plasma are accelerated towards the etched surface, therefore, the chemical etching reaction is preferentially taking place in the direction normal to the surface.

Different RIE techniques as well as different gases were used to etch suitable mirror facets. Problems arose finding a suitable mask material, while the etching of IV-VI alloys itself does not cause difficulties. An etched mirror which was successfully used in a laser structure is shown in Fig. B.10.
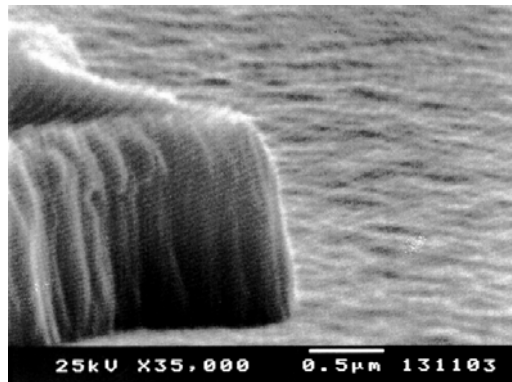
Fig. B.10. SEM image of a laser structure profile etched by
RIE. Sample is 70° tilted.

(3) <u>Focused ion beam etching</u> (FIB etching) is another dry processing technique to fabricate mirrors. This functions as follows. A focused gallium (Ga) ion gun is employed. The heavy Ga ions, perfectly focused and accelerated, remove atoms from the surfaces by sputtering. Typical resolution of the equipment at EMPA, Dübendorf, which was used for the present work, is better than 50 nm. Therefore, FIB allows structuring in the submicron range. Very precise grooves for the $\lambda_o/4$ Bragg mirror design were made using this method. Milling of a $\lambda_o/4$ groove in the material increases the reflectivity of the Fabry-Pérot resonator mirrors from 44% (IV-VI/air interface) to 85% (IV-VI/air groove/IV-VI). Moreover, FIB etching of the mirrors can be made in any part of the laser structure, giving more freedom in choosing of the laser length b and width L.

Before FIB was applied, a rough wet chemical etching was used to coarsely define the edges of the laser structure. Afterwards, rough milling of the front mirror was performed with the focused ion beam. This was done to remove a 10-15 μm wide stripe of the laser material near the edge influenced by the rough wet etching and to avoid regions with underetching. Precise etching of the front facet and the back Bragg groove

are done at the end. The Bragg groove designed for improved reflectivity at λ_o=4.8 µm is shown in Fig. B.11. As can be seen from this image, deviation of facet planes from the normal to the surface is minimal, and the air/IV-VI interfaces appear very smooth.
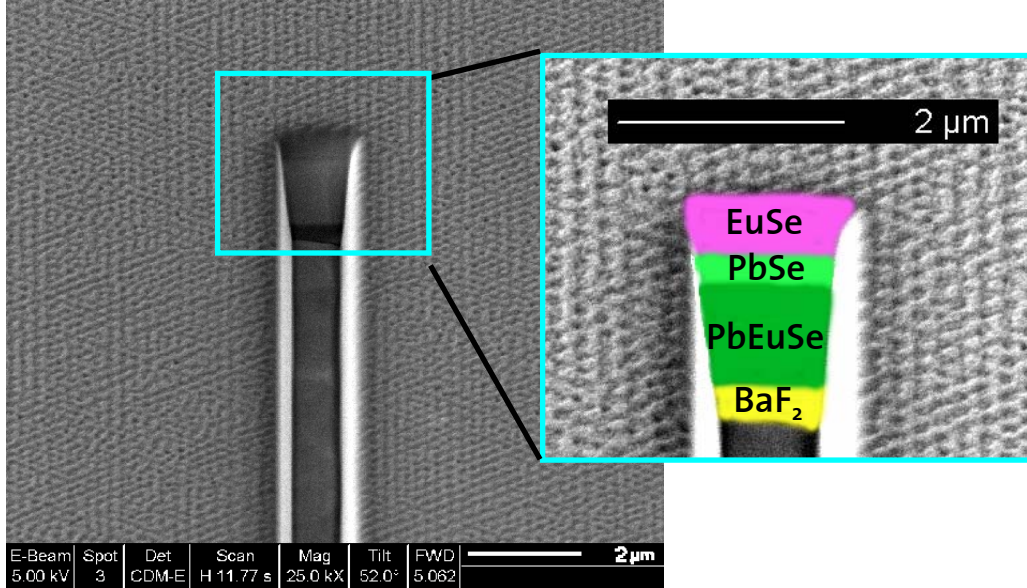
Fig. B.11. Image of the back Bragg $\lambda_o/4$ mirror groove made by FIB (52° tilt view) obtained by scanning ion microscopy (SIM)(Ph. Gasser, EMPA). The enlarged part shows a cross-section of a completely etched through (in this case-down to the BaF_2 substrate) groove. The rough features with three-fold symmetry of the EuSe surface are probably due to dislocations. A RHEED showing a 3-d surface image of this structure is shown in Fig. 3.12.

One of the most important characteristics of laser structures, the threshold gain γ_{th} is a function of resonator losses:

$$\gamma_{th} = \alpha_{int} + \alpha_{ext} = \alpha_{int} - \frac{1}{2b}\ln(R_{Front}R_{Back}), \qquad (B.2)$$

where α_{int} is internal loss, α_{ext} external loss, b resonator length and R_{Front} and R_{Back} are reflectivities of the resonator mirrors. Lower losses lead to lower threshold gain, which makes laser performance better. Internal losses α_{int}, which depend on the material properties (Section 8.2), are higher than external losses, however.

External loss is a function of laser length b and reflectivities of the mirrors R. Therefore, the higher reflectivities are, the less is the external loss for the same laser length. FIB etching of additional grooves was applied in order to increase the R values. One additional $\lambda_o/4$ groove in IV-VI materials (see Fig. B.12) increases the reflectivity of the front mirror R_{Front} from ≈44% to ≈97% and that of the back mirror R_{Back} from ≈85% to ≈99%. These improvements decrease the external loss α_{ext} from 16 cm^{-1} to 0.7 cm^{-1}.

These calculated values correspond to a $Pb_{1-x}Eu_xSe$ DH laser with $b=300$ μm. Scanning ion microscopy (SIM) images of laser structures with three FIB etched stripes are shown in Fig. B.13.
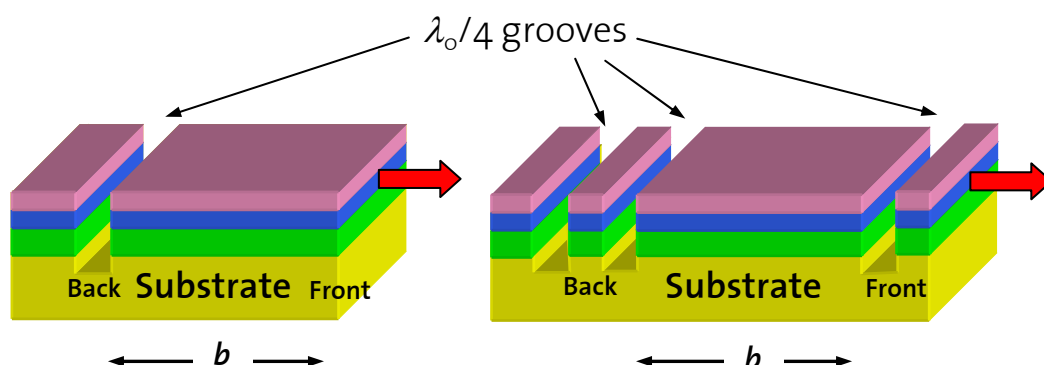
Fig. B.12. Schematic cross-section of the FIB etched structures. A laser structure with length b, only one groove in the back and $\alpha_{ext}\approx16$ cm^{-1} is shown left. A laser with two grooves in the back and one groove in front with $\alpha_{ext}\approx0.7$ cm^{-1} is shown right.
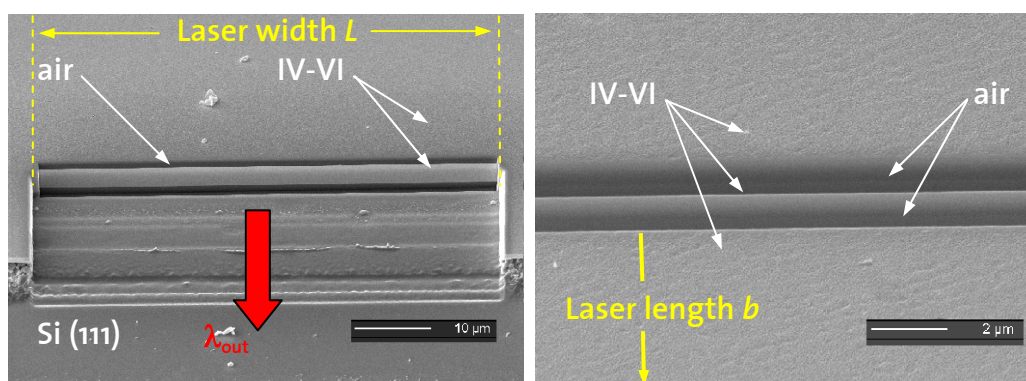
Fig. B.13. SIM images of laser mirrors etched with FIB (top view with 52° tilt). $\lambda_o/4$ Bragg grooves increase the reflectivity of the mirrors. Front mirror with $R\approx97\%$ (left) and back mirror with $R\approx99\%$ (right).

Growth on patterned silicon structures. The two step process of etching (FIB after the coarse wet etching definition of the laser) can be modified to only one operation. This becomes possible if the layers are grown on structured silicon substrates (see Section 3.2.3 for more details). After the MBE growth, layers useful for posterior handling are available on the top of the silicon structures (Fig. B.14). No wet chemical etching is needed, while material grown on Si "columns" is roughly self defined in size. The structure is ready for the fine FIB milling of the facets. IV-VI lasers fabricated with these patterned substrates showed comparable performance with respect to lasers on flat substrates.
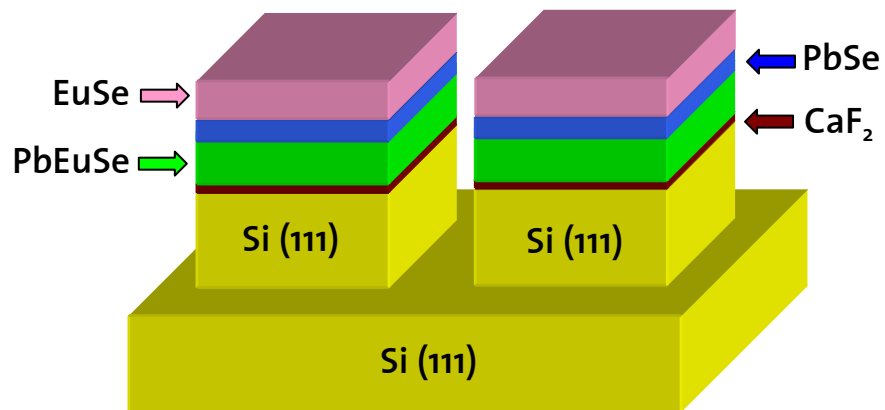
Fig. B.14. Schematic drawing of a laser structure grown on a structured Si (111) substrate. Etch depth of Si is 25 μm. The laser structure is 3 μm thick. Material deposited at the bottom of the structured wafer is not shown.

References

[1] H. Zogg, K. Alchalabi, D. Zimin, K. Kellermann "Two-dimensional monolithic lead chalcogenide infrared sensor arrays on silicon read-out chips and noise mechanisms", *IEEE Transactions Electron Devices*, vol. 50(1), p. 209, 2003.

[2] X. Zhang; S. A. Jenekhe "Light-emitting diodes with voltage-switchable colors from semiconducting polymer/polymer heterojunctions", *Proceedings of IV Symposium on Electrical, Optical and Magnetic Properties of Organic Solid State-Materials*, p. 539, 1998.

[3] J. Faist, C. Sirtori, F. Capasso, D. L. Sivco, J. N. Baillargeon, A. L. Hutchinson, A.Y. Cho "High-power Long Wavelength (~11.5 m) Quantum Cascade Lasers Operating Above Room Temperature", *IEEE Photonics Technology Letters*, vol. 10, p. 1100, 1998.

[4] A. Rogalski "Infrared Photon Detectors", *SPIE Optical Engineering Press*, Washington, 644 pp., 1995.

[5] J. R. Meyer, C. L. Felix, W. W. Bewley, I. Vurgaftman, E. H. Aifer, L. J. Olafsen, J. R. Lindle, C. A. Hoffman, M.-J. Yang, B. R. Bennett, B. V. Shanabrook, H. Lee, C.-H. Lin, S. S. Pei, R. H. Miles "Auger coefficients in type-II InAs/Ga$_{1-x}$In$_x$Sb quantum wells", *Applied Physics Letters*, vol. 73(20), p. 2857, 1998.

[6] P. C. Findlay, C. R. Pidgeon, R. Kotitschke, A. Hollingworth, B. N. Murdin, C. J. G. M. Langerak A. F. G. van der Meer, C. M. Ciesla, J. Oswald, A. Homer, G. Springholz, G. Bauer "Auger recombination dynamics of lead salts under picosecond free-electron-laser excitation", *Physical Review B*, vol. 58, p. 12908, 1998.

[7] Zh. I. Alferov "The history of heterostructure lasers"-chapter from the book "Nano-Optoelectronics: Concepts, Physics and devices" (ed. M. Grundmann), *Springer*, Berlin, 442 pp., 2002.

[8] Crystal structure images were taken from the Internet page www.webelements.com (with permission).

[9] N. B. Brandt, V. P. Dubkov, E. P. Skipetrov, E. A. Ladigin "Resonant Defect States in PbSnSe (x=0.125) Irradiated with Electrons", Solid State Communications, vol. 65(12), p. 1489, 1988.

[10] D. R. Lide "CRC Handbook of Chemistry and Physics", *CRC Press*, 74th ed., 1993-94.

[11] W. L. Wolfe, G. J. Zissis "The infrared handbook", *Environmental Research Institute of Michigan*, 3[d] ed., 1989.

[12] A. Mauger, C. Godart "The magnetic, optical, and transport properties of representatives of a class of magnetic semiconductors: The europium chalcogenides", *Physics Reports*, vol. 141(2-3), p. 51, 1986.

[13] H. Zogg "Lead Chalcogenide Infrared Detectors Grown on Silicon Substrates"-chapter from the book "Lead Chalcogenides: Physics and Application (ed. D. Khokhlov)", *Taylor and Francis Books*, New York, 697 pp., 2003.

[14] G. Bauer, H. Krenn "Lead Selenide (PbSe)" and "Lead Telluride (PbTe)"- chapters from the book "Handbook of Optical Constants of Solids (ed. E. D. Palik)", *Academic Press*, New York, 711 pp., 1985.

[15] A. Rogalski "IV-VI Detectors", chapter from the book "Infrared Photon Detectors (ed. A. Rogalski)", *SPIE Optical Engineering Press*, Bellingham, 644 pp., 1995.

[16] M. A. Olmstead "Heteroepitaxy of Disparate Materials: From Chemisorption to Epitaxy in CaF$_2$/Si(111)"- chapter from the book "Thin Films: Heteroepitaxial Systems (ed. W. K. Liu, M. B. Santos)", *World Scientific*, Singapore, 688 pp., 1999.

[17] D. R. Lide "CRC Handbook of Chemistry and Physics", *CRC Press*, 84th ed., 2003-04.

[18] S-H. Wei, A. Zunder "Electronic and structural anomalies in lead chalcogenides", *Physical Review B*, vol. 55 (20), p. 13605, 1997.

[19] Y. I. Ravich "Lead Chalcogenides: Basic Physical"- chapter from the book "Lead Chalcogenides: Physics and Application (ed. D. Khokhlov)", *Taylor and Francis Books*, New York, 697 pp., 2003.

[20] T. Story "Semimagnetic Semiconductors Based on Lead Chalcogenides"- chapter from the book "Lead Chalcogenides: Physics and Application (ed. D. Khokhlov)", *Taylor and Francis Books*, New York, 697 pp., 2003.

[21] M. Iida, T. Shimizu, H. Enomoto, H. Ozaki "Experimental studies on the Electronic structure of Pb$_{1-x}$Eu$_x$Te", *Japan Journal of Applied Physics*, vol. 32(10), Pt.1, p. 4449, 1993.

[22] T. Maurice, F. Mahoukou, G. Breton, S. Charar, P. Masri, M. Averous, R. Bisaro "Mid Infrared Optical Investigations of Pb$_{1-x}$Eu$_x$Se/BaF$_2$ Thin Films Grown by MBE", *Phys. Stat. Sol. (b)*, vol. 209, p. 523, 1998.

[23] G. Springholz, A. Holzinger, H. Krenn, H. Clemens, G. Bauer, H. Böttner, P. Norton, M. Maier "Interdiffusion in Pb$_{1-x}$Eu$_x$Se/PbSe multi-quatum well structures", *Journal of Crystal Growth*, vol. 113, p. 593, 1991.

[24] A. Lambrecht, N. Herres, B. Spanger, S. Kuhn, H. Böttner, M. Tacke, J. Evers "Molecular beam epitaxy of Pb$_{1-x}$Sr$_x$Se for the use in IR devices", *Journal of Crystal Growth*, vol. 108, p. 301, 1991.

[25] B. Halford, Y. Guan, M. Tacke "Pb$_{1-x}$Eu$_x$Se photodiodes for the 3-5 μm ranges", *Infrared Physics*, vol. 31, p. 255, 1991.

[26] K. H. Herrmann, V. Melzer, U. Müller "Interband and intraband contributions to refractive index and dispersion in narrow-gap semiconductors", *Infrared Physics*, vol. 34(2), p. 117, 1993.

[27] L. Vegard "Die Röntgenstrahlen im Dienste der Erforschung der Materie", *Zeitschrift für Kristallographie*, vol. 67, p. 239, 1928.

[28] S. Yuan, H. Krenn, G. Springholz, Y. Ueta, G. Bauer, P. J. McCann "Magnetoreflectivity of $Pb_{1-x}Eu_xTe$ epilayers and $PbTe/Pb_{1-x}Eu_xTe$ multiple quantum wells", *Physical Review B*, vol. 55, p. 4607, 1997.

[29] K. H. Herrmann "Narrow-Gap Alloys (Pb,Sr)Se and (Pb,Eu)Se for Optoelectronic Devices", *Proceedings of SPIE 3182*, p. 192, Ukrainian Chapter, International Conference "Material Science and Material Properties for Infrared Optoelectronics", 30 Sept.-2 Oct. 1996, Uzhgorod, Ukraine.

[30] D. L. Partin "Lead salt quantum effect structures", *IEEE Journal of Quantum Electronics*, vol. 24(8), p. 1716, 1988.

[31] H. Zogg, C. Maissen, S. Blunier, S. Teodoropol, R. M. Overney, T. Richmond, J. W. Tomm "Thermal-mismatch strain relaxation mechanisms in heteroepitaxial lead chalcogenide layers on Si substrates", *Semiconductor Science and Technology*, vol. 8(1S), p. S337, 1993.

[32] G. Springholz, Z. Shi, H. Zogg "Molecular Beam Epitaxy of Narrowgap IV-VI Semiconductors"- chapter from the book "Thin Films: Heteroepitaxial Systems (ed. W. K. Liu, M. B. Santos)", *World Scientific*, Singapore, 688 pp., 1999.

[33] P. Müller, H. Zogg, A. Fach, J. John, C. Paglino, A.N. Tiwari, M. Krejci, G. Kostorz "Reduction of threading dislocation densities in heavily lattice mismatched PbSe on Si(111) by glide", *Physical Review Letters*, vol. 78, p. 3007, 1997.

[34] H. Zogg, S. Blunier, A. Fach, C. Maissen, P. Müller, S. Teodoropol, V. Meyer, G. Kostorz, A. Dommann, T. Richmond "Thermal-mismatch-strain relaxation in epitaxial CaF_2, BaF_2/CaF_2, and $PbSe/BaF_2/CaF_2$ layers on Si(111) after many temperature cycles", *Physical Review B*, vol. 50(15), p. 10801, 1994.

[35] K. Takayanagi, K. Kobayashi, K. Yagi, G. Honjo "Heteroepitaxy of chalcogenite compounds: Misfit dislocation formation in monolayer overgrowths", *Thin Solid Films*, vol. 21, p. 325, 1974.

[36] C. Maissen "Epitaktische Bleisalz-Schmalhalbleiter auf Siliziumsubstraten", *Diss. ETH Nr. 9930*, Zurich, 1992.

[37] A. Foitzik, W. Skrotzki, P. Haasen "Slip on {111} planes in lead sulphide", *Materials Science and Engineering A*, vol. 132, p. 77, 1991.

[38] G. Springholz, A. Y. Ueta, N. Frank, G. Bauer "Spiral growth and threading dislocations for molecular beam epitaxy of PbTe on BaF_2 (111) studied by scanning tunneling microscopy", *Applied Physics Letters*, vol. 69, p. 2822, 1996.

[39] A. Y. Ueta, G. Springholz, G. Bauer "Improved nucleation and spiral growth of PbTe on BaF_2 (111)", Journal of Crystal Growth, vol. 175-176, p. 1022, 1997.

[40] C. Ratsch, J. A. Venables "Nucleation Theory and the Early Stages of Thin Film Growth", *Journal of Vacuum Science and Technology A*, vol. 21(5), p. S96, 2003.

[41] G. Zinsmeister "Theory of thin film condensation. Part B: Solution of the simplified condensation equation", *Thin Solid Films*, vol. 2 (5-6), p. 497, 1968.

[42] J. D. Weeks, G. H. Gilmer, K. A. Jackson "Analytical theory of crystal growth", *Journal of Chemical Physics*, vol. 65(2), p. 712, 1976.

[43] M. F. Gyure, C. Ratsch, B. Merriman, R. E. Caflisch; S. Osher, J. J. Zinck, D. D. Vvedensky "Level-set methods for the simulation of epitaxial phenomena", *Physical Review E*, vol. 58(6), p. R6927, 1998.

[44] H. Brune, G. S. Bales, J. Jacobsen, C. Boragno, K. Kern "Measuring surface diffusion from nucleation island densities", *Physical Review B*, vol. 60(8), p. 5991, 1999.

[45] C. Ratsch, M. Scheffler "Density-functional theory calculations of hopping rates of surface diffusion", *Physical Review B*, vol. 58(19), p. 13163, 1998.

[46] S. Stoyanov "Nucleation on point defects", *Journal of Crystal Growth*, vol. 24-25, p. 293, 1974.

[47] E. Bauer, H. Poppa "Recent advances in epitaxy", *Thin Solid Films,* vol. 12(1), p. 167, 1972.

[48] J. A. Venables "Atomic Interactions and Surface Processes in Heteroepitaxy"- chapter from the book "Thin Films: Heteroepitaxial Systems (ed. W. K. Liu, M. B. Santos)", *World Scientific*, Singapore, 688 pp., 1999.

[49] "XTC/2, XTC/C Operator's Manual", *Leybold Inficon Inc.*, East Syracuse, NY, 1991.

[50] C. Lu, O. Lewis "Investigation of film-thickness determination by oscillating quartz resonators with large mass load", *Journal of Applied Physics*, vol. 43(11), p. 4385, 1972.

[51] P. J. Dobson, B. A. Joyce, J. H. Neave, J. Zhang "Current understanding and applications of the RHEED intensity oscillation technique", *Journal of Crystal Growth*, vol. 81(1-4), p. 1, 1987.

[52] M. Henzler, W. Göpel "Oberflächenphysik des Festkörpers", *B. G. Teubner Verlag*, Stuttgart, 641 pp., 1991.

[53] G. Springholz "MBE of IV-VI Heterostructures and superlattices"- chapter from the book "Lead Chalcogenides: Physics and Application (ed. D. Khokhlov)", *Taylor and Francis Books*, New York, 697 pp., 2003.

[54] K. Wiesauer "Dislocation Structures in Epitaxial IV-VI Semiconductor Heterostructures", *Diss. Johannes Kepler University*, Linz, 2003.

[55] H. Zogg, K. Alchalabi, D. Zimin "PbTe IRFPAs for low cost thermal imaging", *Compound Semiconductors*, vol. 7(8), p. 86, 2001.

[56] A. Belenchuk, O. Shapoval, V. Kantser, A. Fedorov, P. Schunk, Th. Schimmel, Z. Dashevsky "Growth of (111)-oriented PbTe thin films on vicinal Si(111) and on Si(100) using fluoride buffers", *Journal of Crystal Growth*, vol. 198-199, p. 1216, 1999.

[57] D. Zimin, K. Alchalabi, H. Zogg "Heteroepitaxial PbTe-on-Si pn-junction IR-sensors: Correlations between material and device properties", *Physica E*, vol. 13, p. 1220, 2002.

[58] G. Springholz, G. Bauer, G. Ihninger "MBE of high mobility PbTe films and PbTe/ $Pb_{1-x}Eu_xTe$ heterostructures", *Journal of Crystal Growth*, vol. 127, p. 302, 1993.

[59] G. Springholz, T. Schwarzl, W. Heiss, M. Aigle, H. Pascher "Molecular beam epitaxy of lead salt-based vertical cavity surface emitting lasers for the 4-6 µm spectral region", *Journal of Crystal Growth*, vol. 227-228, p. 722, 2001.

[60] A. Ishizaka, Y. Shiraki "Low temperature surface cleaning of silicon and its application to silicon MBE", *Journal of the Electrochemical Society: Electrochemical Science and Technology*, vol. 133(4), p. 666, 1986.

[61] H. C. Snyman, G. J. Gouws, R. J. Muller "A TEM investigation of the nucleation, growth and structure of HWE grown lead-tin telluride films", *Journal of Crystal Growth*, vol. 70(1-2), p. 373, 1984.

[62] P. J. McCann, X. M. Fang, W. K. Liu, B. N. Strecker, M. B. Santos "MBE growth of PbSe/CaF$_2$/Si(111) heterostructures", *Journal of Crystal Growth*, vol. 175-176, p. 1057, 1997.

[63] H. Zogg, A. Fach, C. Maissen, J. Masek, S. Blunier "Photovoltaic lead-chalcogenide on silicon infrared sensor arrays", *Optical Engineering*, vol. 33(5), p. 1440, 1994.

[64] J. Masek, A. Ishida, H. Zogg, C. Maissen, S. Blunier "Monolithic photovoltaic PbS-on-Si infrared-sensor array", IEEE Electron Device Letters, vol. 11(1), p. 12, 1990.

[65] H. Zogg, M. Hüppi "Growth of high quality epitaxial PbSe onto Si using a (Ca,Ba)F$_2$ buffer layer", *Applied Physics Letters*, vol. 47(2), p. 133, 1985.

[66] S. P. Zimin, M. N. Preobrazhensky, D. S. Zimin, R. F. Zaykina, G. A. Borzova, V. V. Naumov "Growth and properties of PbTe films on porous silicon", *Infrared Physics & Technology*, vol. 40(4), p. 337, 1999.

[67] V. I. Levchenko, L. I. Postnova, V. P. Bondarenko, N. N. Vorozov, V. A. Yakovtseva, L. N. Dolgyi "Heteroepitaxy of PbS on porous silicon", *Thin Solid Films*, vol. 348, p. 141, 1999.

[68] P. Müller, A. Fach, J. John, A. N. Tiwari, H. Zogg, G. Kostorz "Structure of epitaxial PbSe grown on Si(111) and Si(100) without a fluoride buffer layer", *Journal of Applied Physics*, vol. 79(4), p. 1911, 1996.

[69] L. J. Schowalter, R. W. Fathauer "Growth and characterization of single crystal insulators on silicon", *CRC Critical Reviews in Solid State and Materials Sciences*, vol. 15(4), p. 367, 1989.

[70] H. Zogg, K. Alchalabi, D. Zimin "Two-dimensional monolithic lead-chalcogenide on active Si-substrate IR-FPA", *Proceedings SPIE*, vol. 4820-47, p. 429, 2002.

[71] M. Arnold "Molecular Beam Epitaxy of IV-VI Narrow Band Gap Semiconductors on Silicon for P-N Infrared Photodiode Focal Plane Arrays", *Diplomarbeit in experimenteller Festkörperphysik ETH*, Zurich, 2003.

[72] K. Kellermann, D. Zimin, K. Alchalabi, Ph. Gasser, H. Zogg "Optically pumped lead chalcogenide infrared emitters on silicon substrates", *Physica E*, vol. 20, p. 536, 2004.

[73] S. Blunier "Einkristalline Gruppe-IIA-Fluoridschichten auf Silizium (111)- und (100)-Substraten", *Diss. ETH Nr. 9776*, Zurich, 1992.

[74] S. Blunier, H. Zogg, H. Weibel "Epitaxial BaF_2-CaF_2 stacks on Si(111) and Si(100)", *Material Research Society Symposium Proceedings*, vol. 116, p. 425, 1988.

[75] A. N. Tiwari, W. Floeder, S. Blunier, H. Zogg, H. Weibel "Molecular beam epitaxial growth if (100) oriented CdTe on Si (100) using BaF_2-CaF_2 as a buffer", *Applied Physics Letters*, vol. 57(11), p. 1108, 1990.

[76] S. M. Sze "Semiconductor devices, physics and technology", 2nd ed., *John Wiley & Sons*, New York, 564 pp., 2001.

[77] L. J. van der Pauw "A method of measuring specific resistivity and Hall effect of discs of arbitrary shape", *Philips Research Reports*, vol. 13, p. 9, 1958.

[78] R. L. Petritz "Theory of an Experiment for Measuring the Mobility and Density of Carriers in the Space-Charge Region of a Semiconductor Surface", *Physical Review*, vol. 97, p. 641, 1955.

[79] M. Dressel, G. Gruener "Electrodynamics of solids: Optical Properties of Electrons in Matter", *Cambridge University Press*, Cambridge, 474 pp., 2002.

[80] P. Griffiths, J. A. de Haseth "Fourier Transform Infrared Spectrometry", *John Wiley & Sons*, New York, 656 pp., 1986.

[81] H. A. Macleod "Thin Film Optical Filters", *Institute of Physics Publishing*, Bristol, 641 pp., 2001.

[82] C. Suryanarayana, M. Grant Norton "X-Ray diffraction: a practical approach", *Plenum Press*, New York, 273 pp., 1998.

[83] J. Stangl, V. Holy, G. Springholz, G. Bauer, I. Kegel, T. H. Metzger "Self- organized semiconductor nanostructures: shape, strain and composition", *Materials Science and Engineering C*, vol. 19, p. 349, 2002.

[84] G. Binnig, C. F. Quate, Ch. Geber "Atomic Force Microscope", *Physical Review Letters*, vol. 56(9), p. 930, 1986.

[85] V. Francke, T. Mangel, K. Müllen, P. Samorí, J. P. Rabe "Poly-para-phenylene-ethynylene assemblies for a potential molecular nanowire: An SFM study", *Optical Materials*, vol. 9, p. 390, 1998.

[86] R. Lazzaroni "Principles of Atomic Force Microscopy", *Workshop LAMINATE short course on Scanning Probe Microscopies*, Mons, Belgium, 2001.

[87] S. Yuan, H. Krenn, G. Springholz, G. Bauer, "Large refractive index enhancement in $PbTe/Pb_{1-x}Eu_xTe$ multiquantum-well structures", *Applied Physics Letters*, vol. 62(8), p. 885, 1993.

[88] A. Prinz, G. Brunthaler, Y. Ueta, G. Springholz, G. Bauer, G. Grabecki, T. Dietl "Electron localisation in n-$Pb_{1-x}Eu_xTe$", *Physical Review B*, vol. 59(20), p. 12983, 1999.

[89] H. Krenn, W. Herbst, H. Pascher, Y. Ueta, G. Springholz, G. Bauer "Interband Faraday and Kerr rotation and magnetization of $Pb_{1-x}Eu_xTe$ in the concentration range $0<x\le1$", *Physical Review B*, vol. 60(11), p. 8117, 1999.

[90] X. M. Fang, I-Na Chao, B. N. Strecker, P. J. McCann, S. Yuan, W. K. Liu, M. B. Santos "MBE Growth of PbEuSe on CaF_2/Si(111)", from Proceedings of the Eighth International Conference on Narrow Gap Semiconductors (ed. S. C. Shen, D. Y. Tang, G. Z. Zheng, G. Bauer), *World Scientific*, Singapore, 472 pp., 1998.

[91] G. Springholz "Molecular Beam Epitaxy and in situ Reflection High-Energy Electron Diffraction of IV-VI Semiconductor Heterostrutures", *Diss. Johannes Kepler University*, Linz, 1994.

[92] R. S. Allgaier, W. W. Scanlon "Mobility of Electrons and Holes in PbS, PbSe, and PbTe between Room Temperature and 4.2 K", *Physical Review*, vol. 111, p. 1029, 1958.

[93] R. S. Allgaier "Evolving perspectives and unifying characteristics of the IV-VI semiconductors", *Proc. SPIE*, vol. 285 *Infrared Detector Materials*, p. 2, 1981.

[94] A. Fach "Der Einfluss von Defekten in einkristallinen $Pb_{1-x}Sn_xSe$- Schichten auf die Eigenschaften von Infrarotdioden", *Diss. ETH Nr. 11682*, Zurich, 1996.

[95] J. E. Ayers "The measurement of threading dislocation densities in semiconductor crystals by X-ray diffraction", *Journal of Crystal Growth*, vol. 135(1-2), p. 71, 1994.

[96] H. Kroemer, T-Y. Liu, P. M. Petroff "GaAs on Si and related systems: Problems and prospects", *Journal of Crystal Growth,* vol. 95(1-4), p. 96, 1989.

[97] N. N. Ledentsov, D. Bimberg "Growth of self-organized quantum dots for optoelectronics applications: nanostructures, nanoepitaxy, defect engineering", *Journal of Crystal Growth,* vol. 255(1-2), p. 68, 2003.

[98] F. Henneberger, J. Puls, Ch. Spiegelberg, A. Schulzgen, H. Rossman, V. Jungnickel, A. I. Ekimov "Optical and electro-optical properties of II-VI quantum dots", *Semiconductor Science and Technology*, vol. 6, p. A41, 1991.

[99] R. R. Li, P. D. Dapkus, M. E. Thompason, C. K. Harrison, P. M. Chaikin, R. A. Register, D. H. Adamson "Dense Arrays of Ordered GaAs Nanostructures by Block Copolymer Lithography", *Applied Physics Letters*, vol. 76(13), p. 1689, 2000.

[100] T. Ishikawa, S. Kohmoto, K. Asakawa "Site control of self-organized InAs dots on GaAs substrates by in situ electron-beam lithography and molecular-beam epitaxy", *Applied Physics Letters*, vol. 73(12), p. 1712, 1998.

[101] H. Saito, K. Nishi, S. Sugou "Shape transition of InAs quantum dots by growth at high temperature", *Applied Physics Letters*, vol. 74(9), p. 1224, 1999.

[102] K. Alchalabi "Eigenschaften und Anwendung epitaktischer IV-VI Schichten", *Diss. ETH Nr. 14419*, Zurich, 2001.

[103] K. Alchalabi, D. Zimin, G. Kostorz, H. Zogg "Self-Assembled Semiconductor Quantum Dots with Nearly Uniform Sizes", *Physical Review Letters*, vol. 90(2), p. 026104, 2003.

[104] K. Alchalabi, D. Zimin, H. Zogg "Self Assembled PbSe Quantum Dots with Almost Equal Sizes Grown by MBE on PbTe/Si(111)", *Quantum Confined Semiconductor Nanostructures,* Proceedings of Mater. Res. Soc. Symposium, vol. 737, p. 37, 2003.

[105] M. Pinczolits, G. Springholz, G. Bauer "Direct formation of self-assembled quantum dots under tensile strain by heteroepitaxy of PbSe on PbTe (111)", *Applied Physics Letters*, vol. 73(2), p. 250, 1998.

[106] X. S. Peng, G. W. Meng, J. Zhang, X. F. Wang, C. Z. Wang, X. Liu, L. D. Zhang "Strong quantum confinement in ordered PbSe nanowire arrays", *Journal of Material Research*, vol. 17(6), p. 1283, 2002.

[107] Th. Schwarzl, W. Heiss, G. Kocher-Oberlehner, G. Springholz "CH_4/H_2 plasma etching of IV-VI semiconductor nanostructures", *Semiconductor Science and Technology*, vol. 14, p. L11, 1999.

[108] L. Pasquali, S. D`Addato, G. Selvaggi, S. Nannarone, N. S. Sokolov, S. M. Suturin, H. Zogg "Formation of CaF_2 nanostructures on Si (001)", *Nanotechnology*, vol. 12, p. 403, 2001.

[109] N. S. Sokolov, S. M. Suturin "MBE growth of calcium and cadmium fluoride nanostructures on silicon", *Applied Surface Science*, vol. 175-176, p. 619, 2001.

[110] D. Loretto, F. M. Ross, C. A. Lucas "Quasi-one-dimensional CaF_2 islands formed on Si(001) by molecular beam epitaxy", *Applied Physics Letters*, vol. 68(17), p. 2363, 1996.

[111] H. K. Choi, S. J. Eglash, G. W. Turner "Double-heterostructure diode lasers emitting at 3 µm with a metastable GaInAsSb active layer and AlGaAsSb cladding layers", *Applied Physics Letters*, vol. 64(19), p. 2474, 1994.

[112] H. Lee, P. K. York, R. J. Menna, R. U. Martinelli, D. Z. Garbuzov, S. Y. Narayan, J. C. Connolly "Room-temperature 2.78 *µ*m AlGaAsSb/InGaAsSb quantum-well lasers", *Applied Physics Letters*, vol. 66(15), p. 1942, 1995.

[113] R. Kaspi, G. C. Dente, J. Chavez, M. L. Tilton, D. Gianardi "High power and high brightness from an optically pumped InAs/InGaSb type-II midinfrared laser with low confinement", *Applied Physics Letters*, vol. 81(3), p. 406, 2002.

[114] C. L. Felix, W. W. Bewley, I. Vurgaftman, L. J. Olafsen, D. W. Stokes, J. R. Meyer, M. J. Yang "High-efficiency midinfrared "W" laser with optical pumping injection cavity", *Applied Physics Letters*, vol. 75(19), p. 2876, 1999.

[115] Rui Q. Yang, J. L. Bradshaw, J. D. Bruno, J. T. Pham, D. E. Wortman , R. L. Tober "Room temperature type-II interband cascade laser", *Applied Physics Letters*, vol. 81(3), p. 397, 2002.

[116] D. Hofstetter, M. Beck, T. Aellen, J. Faist, "High-temperature operation of distributed feedback quantum-cascade lasers at 5.3 µm", Applied Physics Letters, vol. 78(4), p. 396, 2001.

[117] C. Sirtori, P. Kruck, S. Barbieri, P. Collot, J. Nagle, M. Beck, J. Faist, U. Oesterle "GaAs/Al_xGa_{1-x}As Mid-Infrared (λ= 9.4 µm) Quantum Cascade Lasers", *Applied Physics Letters*, vol. 73(24), p. 3486, 1998.

[118] U. P. Schiessl, J. Rohr "60°C lead salt laser emission near 5-µm wavelength", *Infrared Physics & Technology*, vol. 40(4), p. 325, 1999.

[119] A. Ishida, N. Sakurai, K. Aikawa, H. Fujiyasu "PbSrS MQW lasers and the effect of quantum well on operation temperature", *Solid-State Electronics*, vol. 37(4-6), p. 1141, 1994.

[120] W. Heiss, T. Schwarzl, G. Springholz, K. Biermann, K. Reimann "Above-room-temperature mid-infrared lasing from vertical cavity surface emitting PbTe quantum-well lasers", *Applied Physics Letters*, vol. 78(7), p. 862, 2001.

[121] J. Fürst, H. Pascher, T. Schwarzl, M. Böberl, W. Heiss, G. Springholz, G. Bauer "Mid-infrared IV-VI vertical-cavity surface-emitting lasers with zero-, two- and three-dimensional systems in the active regions", *Applied Physics Letters*, vol. 81(2), p. 208, 2002.

[122] F. Zhao, H. Wu, A. Majumdar, Z. Shi "Continuous wave optically pumped lead-salt mid-infrared quantum-well vertical-cavity surface-emitting lasers", *Applied Physics Letters*, vol. 83(25), p. 5133, 2003.

[123] K. Kellermann, D. Zimin, K. Alchalabi, Ph. Gasser, N. A. Pikhtin, H. Zogg, "Optically pumped lead-chalcogenide mid-infrared lasers on Si-substrates", *Journal of Applied Physics*, vol. 94, p. 7053, 2003.

[124] A. Joullié "Faut-il développer une nanooptoélectronique moyen infrarouge?", *Presentation at "Développement et applications industrielles des nanotechnologies"*, OPTO 2003, Paris Expo, France, 2003.

[125] M. Tacke "Lead-salt lasers", *Philosophical Transactions: Mathematical, Physical and Engineering Sciences*, vol. 359(1780), p. 547, 2001.

[126] W. Heiss, T. Schwarzl, J. Roither, G. Springholz, M. Aigle, H. Pascher, K. Biermann, K. Reimann "Epitaxial Bragg mirrors for the mid-infrared and their applications", *Progress in Quantum Electronics*, vol. 25, p. 193, 2001.

[127] C. L. Felix, W. W. Bewley, I. Vurgaftman, J. R. Meyer, L. Goldberg, D. H. Chow, E. Selvig "Midinfrared vertical-cavity surface-emitting laser", *Applied Physics Letters*, vol. 71(24), p. 3483, 1997.

[129] H. Zogg, A. Ishida "IV-VI (Lead Chalcogenide) Infrared Sensors and Lasers"- chapter from the book "Infrared Detectors and Emitters: Materials and Devices (ed. P. Capper, C. T. Elliott)", *Kluwer Academic Publishers*, Boston, 478 pp., 2000.

[130] Information is taken from the internet site www.lasercomponents.de.

[131] Information is taken from the internet site www.ekipstech.com.

[132] Z. Feit, M. McDonald, R. J. Woods, V. Archambault, P. Mak "Low threshold PbEuSeTe/PbTe separate confinement buried heterostructure diode lasers", *Applied Physics Letters*, vol. 68(6), p. 738, 1996.

[133] H. Z. Xu, F. Zhao, A. Majumdar, L. Jayasinghe, Z. Shi "High power mid-infrared optically pumped PbSe/PbSrSe multiple-quantum-well vertical-cavity surface-emitting laser operation at 325 K", *Electronics Letters*, vol. 39(8), p. 659, 2003.

[134] G. Bauer, M. Kriechbaum, Z. Shi, M. Tacke "IV-VI quantum wells for infrared lasers", *Journal of Nonlinear Optical Physics and Materials*, vol. 4(2), p. 283, 1995.

[135] F. Lemke, M. Mocker "Theoretical investigation of Auger recombination in PbSnTe structures", *Physica Status Solidi B*, vol. 167(1), p. 219, 1991.

[136] H. Z. Wu, P. J. McCann, O. Alkhouli, X. M. Fang, D. McAlister, K. Namjou, N. Dai, S. J. Chung, P. H. O. Rappl "Molecular beam epitaxial growth of IV-VI multiple quantum well structures on Si(111) and BaF$_2$(111) and optical studies of epilayer heating", *Journal of Vacuum Science and Technology B*, vol. 19(4), p. 1447, 2001.

[137] K. Kellermann "Optically pumped lead-chalcogenide mid infrared lasers grown on Si and BaF$_2$- substrates", *Diss. ETH Nr. 15470*, Zurich, 2004.

[138] M. V. Valeiko, I. I. Zasavitskii, B. N. Matsonashvili, Z. A. Rukhadze, A. V. Shirkov "Size-quantization and deformation effects in PbSe/Pb$_{1-x}$Eu$_x$Se structures grown by the molecular beam epitaxy method", *Soviet Physics of Semiconductors*, vol. 24(8), p. 900, 1990.

[139] D. L. Partin "Lead-europium-selenide-telluride grown by molecular beam epitaxy", *Journal of Electronic Materials*, vol. 13(3), p. 493, 1984.

[140] M. F. Khodr, P. J. McCann, B. A. Mason "Optimizing and Engineering EuSe-PbSe$_{0.78}$Te$_{0.22}$-EuSe Multiple-Quantum-Well Laser Structures", *IEEE Journal of Quantum Electronics*, vol. 34(9), p. 1604, 1998.

[141] E. Abramof, P. H. O. Rappl, A. Y. Ueta, P. Motisuke "Strain determination in PbEuTe/PbTe multi-quantum wells", *Journal of Applied Physics*, vol. 88(2), p. 725, 2000.

[142] M. Böberl, W. Heiss, T. Schwarzl, K. Wiesauer, G. Springholz "Midinfrared continuous-wave photoluminescence of lead–salt structures up to temperatures of 190 °C", *Applied Physics Letters*, vol. 82(23), p. 4065, 2003.

[143] H. Zogg, M. Arnold, D. Zimin, K. Alchalabi, K. Kellermann "Optically excited lead-chalcogenide mid IR emitters and resonant cavity detectors on Si-substrates", oral presentation at the MIOMD VI Conference (invited), *6th International Conference on Mid-Infrared Optoelectronic Material and Devices*, St. Petersburg, Russia, 28 June–1 July 2004.

[144] A. Majumdar, H. Z. Xu, S. Khosravani, F. Zhao, L. Jayasinghe, Z. Shi, "High power light emission of IV–VI lead salt multiple-quantum-well structure grown by molecular-beam epitaxy on ‹111› BaF$_2$ substrate", *Journal of Applied Physics*, vol. 82(4), p. 493, 2003.

[145] H. Benisty, H. De Neve, C. Weisbuch, "Impact of planar microcavity effects on light extraction-Part I: basic concepts and analytical trends", *IEEE Journal of Quantum Electronics*, vol. 34, p. 1612, 1998.

[146] H. Zogg, K. Kellermann, K. Alchalabi, D. Zimin "Optically pumped lead-chalcogenide mid-infrared emitters on silicon substrates", *Infrared Physics and Technology*, 2004, in press.

[147] Patent by H. Zogg, K. Alchalabi, K. Kellermann, D. Zimin "Schmalbandige modulierbare Infrarot-Strahlungsquelle", *Swiss Patent Application*, Nr 2002 0596/02, 2002.

[148] M. S. Ünlü, S. Strite "Resonant cavity enhanced photonic devices", *Journal of Applied Physics*, vol. 78(2), p. 607, 1995.

[149] X. M. Fang, H. Z. Wu, Z. Shi, P. J. McCann, N. Dai "Molecular beam epitaxy of periodic BaF_2/PbEuSe layers on Si(111)", *Journal of Vacuum Science and Technology B*, vol. 17(3), p. 1297, 1999.

[150] W. Heiss, M. Böberl, T. Schwarzl, G. Springholz, J. Fürst, H. Pascher "Applications of lead-salt microcavities for mid-infrared devices", *IEE Proceedings in Optoelectronic*, vol. 150(4), p. 332, 2003.

[151] M. S. Ünlü, private communications.

[152] G. Springholz, M. Pinczolits, V. Holy, P. Mayer, K. Wiesauer, T. Roch, G. Bauer "Self-organized growth of three-dimansional IV-VI semiconductor quantum dot crystals with fcc-like vertical stacking and tunable lattice constant", *Surface Science*, vol. 454-456, p. 657, 2000.

[153] K. Miki, K. Sakamoto, T. Sakamoto "Surface preparation of Si substrates for epitaxial growth", *Surface Science*, vol. 406(1-3), p. 312, 1998.

[154] E. Yablonovitch, T. Gmitter, J. P. Harbison, R. Bhat "Extreme selectivity in the lift-off of epitaxial GaAs films", *Applied Physics Letters*, vol. 51(26), p. 2222, 1987.

[155] P. H. O. Rappl, P. J. McCann "Development of a Novel Epitaxial-Layer Segmentation Method for Optoelectronic Device Fabrication", *IEEE Photonics Technology Letters*, vol. 15(3), p. 374, 2003.

List of publications and presentations

Publications

Archival journals

1. K. Kellermann, D. Zimin, K. Alchalabi, Ph. Gasser, N. Pikhtin, H. Zogg "Optically pumped lead-chalcogenide mid-infrared lasers on Si-substrates", *Journal of Applied Physics*, vol. 94(11), p. 7053, 2003.

2. K. Alchalabi, D. Zimin, G. Kostorz, H. Zogg "Self-Assembled Semiconductor Quantum Dots with Nearly Uniform Sizes", *Physical Review Letters*, vol. 90, p. 026104, 2003.

3. H. Zogg, K. Alchalabi, D. Zimin, K. Kellermann "Lead chalcogenide on silicon infrared sensors: Focal plane array with 96×128 pixels on active Si-chip", *Infrared Physics and Technology*, vol. 43, p. 251, 2002.

4. H. Zogg, K. Alchalabi, D. Zimin "PbTe IRFPAs for low cost thermal imaging", *Compound Semiconductors*, vol. 7(8), p. 86, 2001.

5. K. Alchalabi, D. Zimin, H. Zogg "Monolithic heteroepitaxial PbTe-on-Si infrared focal plane array with 96×128 pixels", *Electron Device Letters*, vol. 22(3), p. 110, 2001.

Conference proceedings

6. K. Kellermann, D. Zimin, K. Alchalabi, Ph. Gasser, H. Zogg "Optically pumped lead-chalcogenide infrared emitters on Si-substrates", *Physica E*, vol. 20(3-4), p. 536, 2004.

7. H. Zogg, K. Alchalabi, D. Zimin, K. Kellermann, W. Buttler "Two-dimensional monolithic lead-chalcogenide infrared sensor array on silicon read-out chip", *Nuclear Instruments and Methods in Physics Research A*, vol. 512, p. 440, 2003.

8. K. Alchalabi, D. Zimin, H. Zogg "Self Assembled PbSe Quantum Dots with Almost Equal Sizes Grown by MBE on PbTe/Si(111)", *Material Research Society Symposium Proceedings*, vol. 737, p. 37, 2003.

9. K. Kellermann, D. Zimin, K. Alchalabi, N. Pikhtin, H. Zogg "Optically pumped lead-chalcogenide IR-emitters", *IEE Proceeding- Optoelectronics*, vol. 150, p. 337, 2003.

10. H. Zogg, K. Alchalabi, D. Zimin, K. Kellermann "Two-dimensional monolithic lead chalcogenide infrared sensor arrays on silicon read-out chips and noise mechanisms", *IEEE Transactions on Electron Devices*, vol. 50(1), p. 209, 2003.

11.   H. Zogg, K. Alchalabi, D. Zimin "Two-dimensional monolithic lead-chalcogenide on active Si-substrate IR-FPA", *Proceedings SPIE*, vol. 4820, p. 429, 2003.

12.   H. Zogg, K. Alchalabi, D. Zimin, K. Kellermann "Two-dimensional monolithic lead chalcogenide infrared sensor array on silicon read-out chip", *Proceedings SPIE*, vol. 4746(1), p. 21, 2002.

13.   H. Zogg, K. Alchalabi, D. Zimin, K. Kellermann "Two- dimensional monolithic lead chalcogenide infrared sensor array on silicon read-out chip", in "Physics of semiconductor devices" ed. V. Kumar, P.K. Basu, *Allied Publishers LTD*, p. 21, 2002.

14.   D. Zimin, K. Alchalabi, H. Zogg "Heteroepitaxial PbTe-on-Si pn-junction IR-sensors: Correlations between material and device properties", *Physica E*, vol. 13, p. 1220, 2002.

15.   K. Alchalabi, D. Zimin, H. Zogg "Lead chalcogenide on silicon infrared focal plane arrays for thermal imaging", *Defence Science Journal*, vol. 51(1), p. 53, 2001.

16.   K. Alchalabi, D. Zimin, K. Kellermann, H. Zogg "Lead chalcogenide on silicon infrared sensor arrays: Noise mechanisms and 2-d array on active chips", *Proceedings of the 10th International Conference on Narrow Gap Semiconductors NGS10*, Institute of Pure and Applied Physics, p. 51, 2001.

17.   K. Alchalabi, D. Zimin, H. Zogg, W. Buttler "Heteroepitaxial 96×128 lead chalcogenide on silicon infrared focal plane array for thermal imaging", *Proceedings SPIE*, vol. 4369, p. 405, 2001.

Journals in print

18.   K. Kellermann, K. Alchalabi, D. Zimin, H. Zogg "Optically pumped mid-infrared lasers on Si-substrates", *Spectrochimica Acta A*, in print.

19.   H. Zogg, K. Kellermann, K. Alchalabi, D. Zimin "Optically pumped lead-chalcogenide mid-infrared emitters on silicon substrates", *Infrared Physics and Technology*, in print.

Presentations at conferences based on the present work

(the presenting authors are underlined)

1.   M. Arnold, D. Zimin, K. Alchalabi, H. Zogg "Lead salt mid-IR photodetectors with narrow linewidth", MBE-2004, International Conference on Molecular Beam Epitaxy 2004, Edinburgh, GB, 23-27 August 2004.

2.   H. Zogg, M. Arnold, D. Zimin, K. Alchalabi, K. Kellermann "Optically excited lead-chalcogenide mid IR emitters and resonant cavity detectors on Si-substrates", MIOMD-VI, 6th International Conference on Mid-Infrared Optoelectronic Materials and Devices, S.-Petersburg, Russia, 28 June- 2 July 2004.

3.   M. Arnold, D. Zimin, K. Kellermann, K. Alchalabi, H. Zogg "Bleichalkogenid IR-Detektoren mit schmaler Bandbreite", 34. IR-Kolloquium, Freiburg i. Br., Germany, 20-21 April 2004.

4.   H. Zogg, K. Kellermann, D. Zimin, M. Arnold, K. Alchalabi "Optisch gepumpte Bleichalkogenid IR-Laser auf Si und BaF$_2$ Substraten", 34. IR-Kolloquium, Freiburg i. Br., Germany, 20-21 April 2004.

5.   M. Arnold, K. Alchalabi, D. Zimin, H. Zogg "Bleisalz-Infrarot-Sensor-Array auf CMOS-Substrat", Deutscher MBE Workshop 2003, München, Germany, 16-17 October 2003.

6.   K. Alchalabi, K. Kellermann, D. Zimin, H. Zogg "Bleisalz-Infrarot-Emitter auf Si-Substraten", Deutscher MBE Workshop 2003, München, Germany, 16-17 October 2003.

7.   H. Zogg, K. Kellermann, K. Alchalabi, D. Zimin "Optically pumped lead chalcogenide infrared emitters on Si-substrates", 7th AITA workshop, 7th International Workshop on Advanced Infrared Technology and Applications, Pisa, Italy, 9-11 September 2003.

8.   K. Kellermann, K. Alchalabi, D. Zimin, H. Zogg "Optically pumped mid-infrared lasers on Si-substrates", TDLS-2003, Tunable Diode Laser Spectroscopy conference, Zermatt, Switzerland, 14-18 July 2003.

9.   K. Kellermann, D. Zimin, K. Alchalabi, Ph. Gasser, H. Zogg "Optically pumped lead chalcogenide infrared emitters on silicon substrates", NGS-11, 11th International Conference on Narrow Gap Semiconductors, Buffalo NY, USA, 16-20 June 2003.

10.   K. Kellermann, D. Zimin, K. Alchalabi, H. Zogg "Optisch gepumpte Bleichalkogenid Infrarotlaser auf Si-Substraten", 33. IR-Kolloquium, Freiburg i. Br., Germany, 8-9 April 2003.

11.   K. Kellermann, K. Alchalabi, D. Zimin, H. Zogg "Optically pumped lead chalcogenide infrared emitters on Si-substrates", 12th Euro-MBE Workshop, Bad Hofgastein, Austria, 16-19 February 2003.

12.   D. Zimin, K. Alchalabi, H. Zogg "Self assembled PbSe quantum dots with nearly uniform sizes on PbTe/Si (111)", 12th Euro-MBE Workshop, Bad Hofgastein, 16-19 February 2003.

13.   D. Zimin, K. Alchalabi, O. Anisimov, A. Banshchikov, N. Sokolov, S. Suturin, H. Zogg "Self-assembled CaF$_2$-on-Si (001) nanostructures", 12th Euro-MBE Workshop, Bad Hofgastein, 16-19 February 2003.

14.   K. Alchalabi, D. Zimin, H. Zogg "Self Assembled PbSe Quantum Dots with Almost Equal Sizes Grown by MBE on PbTe/Si(111)", MRS Fall 2002, Materials Research Society Fall Meeting, Boston MA, USA, 1-6 December 2002.

15.   K. Alchalabi, K. Kellermann, D. Zimin, H. Zogg "Optically pumped lead-chalcogenide IR-emitters", ISCS 2002, 29th International Symposium on Compound Semiconductors 2002, Lausanne, Switzerland, 7-10 October 2002.

16.   <u>D. Zimin</u>, K. Alchalabi, H. Zogg "Self assembled PbSe quantum dots with almost equal sizes on PbTe/Si(111)", ISCS 2002, 29th International Symposium on Compound Semiconductors 2002, Lausanne, Switzerland, 7-10 October 2002.

17.   <u>D. Zimin</u>, K. Alchalabi, H. Zogg "Self assembled semiconductor IV-VI quantum dots with extremely narrow size distribution", 2002 Workshop on Nanoscience, Twannberg, Switzerland, 30 September- 4 October 2002.

18.   K. Kellermann, D. Zimin, K. Alchalabi, N. Pikhtin, <u>H. Zogg</u> "Optically pumped lead-chalcogenide IR-emitters", MIOMD-V, 5th International Conference on Mid-Infrared Optoelectronic Materials and Devices, Annapolis MD, USA, 8-11 September 2002.

19.   K. Alchalabi, D. Zimin, K. Kellermann, <u>H. Zogg</u> "A 2-d Monolithic PbTe-on-Active-Si Infrared Focal Plane Array for Thermal Imaging", MIOMD-V, 5th International Conference on Mid-Infrared Optoelectronic Materials and Devices, Annapolis MD, USA, 8-11 September 2002.

20.   <u>H. Zogg</u>, K. Alchalabi, D. Zimin "Two-dimensional monolithic lead-chalcogenide on active Si-substrate IR-FPA", SPIE International Symposium on Optical Science & Technology, Infrared Technology and Applications XXVIII, Seattle WA, USA, 7-11 July 2002.

21.   <u>H. Zogg</u>, K. Alchalabi, D. Zimin, K. Kellermann "Two-dimensional monolithic lead chalcogenide infrared sensor array on silicon read-out chip", New Developments in Radiation Detectors, 9th European Symposium on Semiconductor Detectors, Schloss Elmau, Germany, 23-27 June 2002.

22.   <u>K. Kellermann</u>, D. Zimin, K. Alchalabi, H. Zogg "Optisch gepumpte Bleichalkogenid Infrarotemitter auf Si-Substraten", 32. IR-Kolloquium, Freiburg i. Br., Germany, 23-24 April 2002.

23.   <u>K. Alchalabi</u>, D. Zimin, H. Zogg "Photovoltaische Bleichalkogenid-auf-Silizium Infrarotsensoren-Arrays", 32. IR-Kolloquium, Freiburg i. Br., Germany, 23-24 April 2002.

24.   <u>H. Zogg</u>, K. Alchalabi, D. Zimin, K. Kellermann "Two-dimensional monolithic lead chalcogenide infrared sensor array on silicon read-out chip", IWPSD 2001, 11th International Workshop on Physics of Semiconductor Devices, Delhi, India, 11-15 December 2001.

25.   <u>K. Alchalabi</u>, D. Zimin, K. Kellermann, H. Zogg "Herstellung von IR-Dioden mittels Elektrodeposition von Pb auf epitaktischen PbTe(111) Schichten", Deutscher MBE-Workshop, Berlin, Germany, 17-18 September 2001.

26.   <u>D. Zimin</u>, K. Alchalabi, H. Zogg "Heteroepitaxial PbTe-on-Si pn-junction IR-sensors: Correlations between material and device properties", MSS10, 10th International Conference on Modulated Semiconductor Structures, Linz, Austria, 23-27 July 2001.

27.   D. Zimin, <u>F.-J. Haug</u>, K. Alchalabi, H. Zogg "Strain relaxation mechanisms in thermal expansion mismatched PbTe-on-Si(111) substrates", E-MRS Spring Meeting, Symposium M. Stress and Strain in Heteroepitaxy, Strasbourg, France, 5-8 June 2001.

28. K. Alchalabi, D. Zimin, K. Kellermann, <u>H. Zogg</u> "Lead chalcogenide on silicon infrared sensor arrays: Noise mechanisms and 2-d array on active chips", NGS10, 10th International Conference on Narrow Gap Semiconductors, Ishikawa, Japan, 27-31 May 2001.

29. <u>D. Zimin</u>, K. Alchalabi, H. Zogg "Correlation of material and device properties of PbTe-on-Si p-n$^+$ infrared sensors", Swiss Physics Society SPG-Tagung, Dubendorf, Switzerland, 2-3 May 2001.

30. <u>K. Alchalabi</u>, D. Zimin, H. Zogg, W. Buttler "Eigenschaften von heteroepitaktischen PbTe-auf-Si IR-Sensoren und Fabrikation eines 96×128 Matrixarrays auf aktiven Si-Substrat", 31-IR Kolloquium, Freiburg i. Br., Germany, 25-26 April 2001.

31. K. Alchalabi, D. Zimin, <u>H. Zogg</u> "Heteroepitaxial 96×128 lead chalcogenide on silicon infrared focal plane array for thermal imaging", Infrared Technology and Applications XXVII Conference, Orlando FL, USA, 16-20 April 2001.

32. K. Alchalabi, <u>D. Zimin</u>, H. Zogg "Heteroepitaxial 96×128 lead chalcogenide on silicon infrared focal plane array for 3-5 µm thermal imaging", MIOMD-2001, 4th International Conference on Mid-Infrared Optoelectronics Materials and Devices, Montpellier, France, 2-4 April 2001.

33. <u>D. Zimin</u>, K. Alchalabi, H. Zogg "Correlation between noise currents and dislocation densities of PbTe-on-Si p-n$^+$ Mid-IR-sensors", MIOMD-2001, 4th International Conference on Mid-Infrared Optoelectronics Materials and Devices, Montpellier, France, 2-4 April 2001.

34. <u>D. Zimin</u>, K. Alchalabi, H. Zogg "Correlation between noise currents and dislocation densities of PbTe-on-Si p-n+ IR-sensors", 11th Euro-MBE Workshop, Hinterzarten, Germany, 4-7 February 2001.

35. <u>K. Alchalabi</u>, D. Zimin, H. Zogg "Heteroepitaxial 96 x 128 lead chalcogenide on silicon infrared focal plane array for thermal imaging", 11th Euro-MBE Workshop, Hinterzarten, Germany, 4-7 February 2001.

36. <u>K. Alchalabi</u>, D. Zimin, H. Zogg "Use of dislocation properties for MBE Growth and device application in IV-VI materials", Fundamental Aspects of Surface Science, Castelvecchio Pascoli, Italy, 7-12 October 2000.

37. <u>D. Zimin</u>, K. Alchalabi, H. Zogg "Heteroepitaxial PbTe-on-Si p-n- junctions for mid-IR sensor arrays", Deutscher MBE Workshop 2000, Bochum, Germany, 25-26 September 2000.

38. <u>K. Alchalabi</u>, D. Zimin, H. Zogg "Herstellung eines monolithischen Infrarotdiodenarrays in mittleren Infrarot mittels MBE", Deutscher MBE Workshop 2000, Bochum, Germany, 25-26 September 2000.

39. <u>K. Kellermann</u>, D. Zimin, H. Zogg "Hoch reflektierende heteroepitaktische PbTe/BaF$_2$ Bragg-Spiegel auf Silizium zur Spurengasanalyse im mittleren Infrarot", Deutscher MBE Workshop 2000, Bochum, Germany, 25-26 September 2000.

Acknowledgments

First of all, I would like to thank Prof. Dr. Gernot Kostorz, Head of the Institute of Applied Physics, ETHZ, for being my supervisor, lecturer, teacher of scientific English and for the acceptance of my PhD-thesis.

I acknowledge and appreciate Prof. Dr. Maurus Tacke, Director of FGAN-FOM (Research Institute for Optronics and Pattern Recognition of the Research Establishment for Applied Science), Ettlingen, Germany, for being the external examiner of this thesis.

Most of all, I am thankful to PD Dr. Hans Zogg, Head of the Thin Film Physics Group, ETHZ, for giving me a chance to work in his Group, his readiness to help me at all times as well as his ultimate support.

I would also like to acknowledge all present and former members of the Thin Film Physics Group, who helped me to make experiments and feel myself comfortable in the laboratory. They are: Daniel Abou-Ras (thank you for TEM and EDX), Dr. Karim Alchalabi (thank you for being my mentor, friend, room neighbour and the king of the clean room), Martin Arnold (thank you for your support, explanations and jokes), Dr. Derk Bätzner, David Brémaud (thank you for a nice company during long MBE runs), Dr. Franz-Josef Haug (thanks for the help in computers and science, and for a nice pizza), Mark Kaelin (thank you for being a friend, for the specific jokes and for readiness to help in anything), Thomas Kämpfer (thanks for technical help, "golden hands" and discussions), Dr. Klemens Kessler (thank you for telling the secrets of SiO_x deposition), Dr. Klaus Kellermann (thank you for being a collaborator, a friend and a guide to Allgaeuer), Dr. Gennadiy Khrypunov (whose cheerfulness and sence of humor cannot but be admired), Dr. Fedor Kurdesau (thank you for being my friend), Michael Leopold (thanks for technical help, "golden hands", Si cleaning and orderings), Paulette Pfammatter, Dr. Alessandro Romeo (thank you for scientific and automobile discussions), Dr. Dominik Rudmann (thank you for being always amiable to me, and scientific and technical support), Gaby Strahm (thank you for being a very nice and helpful group's secretary and a room neighbour), Dr. Mathias Terheggen, Prof. Dr. Ayodya Nath Tiwari (thank you for fruitful scientific discussions and conversations in the coffee room).

I am grateful to Peter Wägli, ETHZ, for great SEM images, Philippe Gasser, EMPA, Dübendorf, Switzerland for a perfect operation with FIB and SIM, Dr. Pavel Brunkov, Ioffe Institute, Russia for TEM images, Dr. Miron Gerke, Vladimir State University, Russia for AFM images, and Pavel Lepshin,

Curriculum Vitae

Name: Zimin
Vorname: Dmitry
Adresse: Kaltackerstrasse 46, CH-8908 Hedingen
Geboren am: 22. April 1977 in Yaroslavl (Russland)

Schule:
11-jährige Mittelschule N 37 in Yaroslavl 1984-1994

Hochschule:
Physikstudium an der Staatlichen Universität in Yaroslavl 1994-1999
Abschluss: Ingenieurdiplom in Mikroelektronik und Halbleitergeräte 1999
Abschluss: Bakkalaureus der Physik 1998
Doktorarbeit an der ETH Zürich 2000-2004

Praktische Tätigkeiten:
Wissenschaftlicher Mitarbeiter im Institut für Mikroelektronik, russische Wissenschaftsakademie, Yaroslavl 1998-1999
Wissenschaftlicher Mitarbeiter als Bundesstipendiat an der ETH Zürich 1999-2000
Wissenschaftlicher Mitarbeiter (Doktorand) an der ETH Zürich 2000-2004